Neural control strategies for a complex biomechanical system: primary motor cortex and the hand.

A DISSERTATION
SUBMITTED TO THE FACULTY OF THE GRADUATE SCHOOL
OF THE UNIVERSITY OF MINNESOTA
BY

Jodi Fae Prosise

IN PARTIAL FULFILLMENT OF THE REQUIREMENTS
FOR THE DEGREE OF
DOCTOR OF PHILOSOPHY

Timothy J. Ebner, adviser
William K. Durfee, co-adviser

March 2010

Acknowledgements

I owe my deepest gratitude to my adviser, Tim Ebner, for his advising and support and for pushing me to think deeper about my research. I would also like to thank Claudia Hendrix for teaching me so many of the skills necessary to complete my research as well as her continuous moral support. I am also grateful to Mike McPhee for all of his hard work and technical support as well as everyone else in the Ebner lab for their help throughout my time there. Finally, this thesis would not have been possible without the encouragement and love from my friends and family, especially my husband, Eric, and daughter, Anna.

Abstract

The hand is a complex biomechanical apparatus with 27 bones, 18 joints, and 39 intrinsic and extrinsic muscles, resulting in over 20 degrees of freedom. Despite significant mechanical coupling between the joints of the hand, humans and non-human primates are able to perform both simple and highly intricate movements of the hand and fingers. Much of this ability is attributed to the neural control mechanisms. Although a large number of cortical and subcortical systems are involved in prehension, the primary motor cortex (M1) plays a critical role in reaching to and grasping an object. The strategy utilized by M1 to control movements of the hand is of considerable interest in the fields of neuroscience and engineering. A major area of debate is whether M1 explicitly controls individual degrees of freedom or more global patterns of movement. To test this hypothesis, two rhesus monkeys were trained to reach and grasp a set of 23 different objects that were designed to systematically vary hand shape. Fourteen joint angles and angular velocities of the hand and fingers were monitored simultaneously with the recording of 81 single cells in the hand area of M1. The joint angles were significantly different across objects during the *reach* and *grasp epochs*, indicating that the hand preshaped to match properties of the object to be grasped. There were fewer instances of significant differences in joint angular velocities across objects than for the joint angles, especially during the *premove* and *grasp* epochs. Singular value decomposition (SVD) analyses defined a dominant hand shaping pattern that was similar across sessions and monkeys that consisted of simultaneous extension/flexion of the MCP and IP joint angles. The majority of the variation in hand shaping was captured by

only a few lower-order eigenvectors (EVs), suggesting that they represent major patterns of hand shaping. In contrast, the higher-order EVs characterize the more detailed movements of the hand because of the smaller amount of variance captured. Linear regression analysis revealed that the firing of many M1 cells (up to 38.6%) was highly correlated with individual joint angles with only limited correlation to joint angular velocities. Typically, a cell's firing was correlated with multiple joints. The firing of M1 cells was also highly correlated to the lower-order temporal weighting vectors (TWs) derived from SVD analyses. Higher-order TWs were not well-represented. In addition, most cells displayed high R^2-values for multiple lower-order TWs. Correlations were improved most often by incorporating a temporal lead in the neural firing. This suggests that M1 is involved with the control of dominant hand shaping patterns rather than explicitly controlling details. These findings could be used to develop brain-machine interface algorithms in which signals from M1 are used to control robotic or virtual hands.

Table of Contents

List of Tables

List of Figures

Chapter 1: Background

Manual dexterity, or the ability to coordinate complex grasp postures and individuate finger movements, is a highly evolved skill possessed by few species. The ability to make intricate movements of the hand and digits is one of the many advantages of humans and non-human primates. This skill allows humans to perform simple actions such as using a tool or picking up a small piece of food, as well as highly sophisticated actions such as playing a musical instrument, typing, or communicating using sign language. In addition, there is a high degree of coordination of the hand and arm to accomplish reaching and grasping tasks. Several factors contribute to this ability, including the complexity of the system as well as its powerful control mechanism, the central nervous system (CNS). The goal of this thesis is to examine the involvement of the primary motor cortex (M1) in this complex system through individual degrees of freedom or patterns in hand kinematics. This chapter begins by discussing the complexity of the systems, both musculoskeletal and neuronal, involved with the behavior of reaching and grasping. Because synergies are a common tool for describing hand postures and control mechanisms, principal component analysis methods are explored. Next the neural control mechanisms for reaching and grasping are surveyed, including parieto-frontal networks as well as other circuits, culminating in a detailed investigation of the involvement of M1 in prehension.

1.1 Reaching and grasping behavior

1.1.1 The hand

One main factor that contributes to the ability of humans and non-human primates to make intricate movements of the hand is its complexity, including its many bones, joints, and muscles (MacKenzie and Iberall, 1994). The human hand is made up of 27 bones, 14 joints, and 39 muscles, resulting in over 20 degrees of freedom (Pagowski and Piekarski, 1977; Soechting and Flanders, 1997). There are more than 19 intrinsic muscles and at least 14 extrinsic muscles involved with digit movement that cross the wrist and insert in the forearm (Martini et al., 2006). In addition, there is an array of tendons and tendinous structures that add to the complexity of the hand (Kilbreath et al., 2002; Keen and Fuglevand, 2003; Schweitzer and Rayan, 2004). This complexity allows highly individuated and detailed movements of the hand and fingers.

The anatomical intricacy of the hand contributes to the dexterity of human beings, but also creates coupling of joints and biomechanical constraints. For example, because of tendon connections, flexion of the wrist causes passive extension of the fingers, and when the wrist extends, finger flexors passively pull the fingers to flex (Popovic, 2003). Although the thumb and index fingers have a high level of individuation for most tasks, movements of the remaining fingers tend to be coupled (Schieber, 1991; Soechting and Flanders, 1997). Therefore, in endeavoring to understand the control of the primate hand, one has to consider both its biomechanical capacity for intricate movements and the constraints that limit complete independence of movement.

The coupling of degrees of freedom in the hand can also be attributed to factors beyond joint and muscle anatomy. The squirrel monkey has similar anatomical constraints as humans and macaque monkeys, but their manual dexterity is significantly limited in comparison (Lawrence, 1994). Therefore, other factors are involved in the degree to which fingers and joints can be individually controlled. The first of many such factors is the motor unit. A motor unit is defined as the group of muscle fibers a motor neuron innervates, and several motor units make up an entire muscle. Many motor neurons innervate multiple muscle fibers (Kilbreath et al., 2002; Reilly et al., 2004), resulting in near simultaneous contraction of muscle fibers from a single spinal cord motor neuron. Muscles important for extension and flexion of the human hand, such as the flexor digitorum profundus and extensor digitorum communis, contain motor units that extend to multiple digits (Kilbreath et al., 2002; Keen and Fuglevand, 2003). Additionally, motor units receive common inputs from spinal networks and descending systems (Sears and Stagg, 1976; Kirkwood, 1979), further contributing to a high degree of coupling in movements of the hand and digits.

One prominent hypothesis is that the ability to individuate finger movements is directly correlated to the amount of monosynaptic connections from the cortex to α-motoneurons (Nakajima et al., 2000). There are several routes by which α-motoneurons receive signals from the cerebral cortex, but the corticospinal tract is the largest and most significant descending pathway (Lemon, 2008). The corticospinal tract also contains both direct and indirect projections to motoneurons. Direct corticomotoneuronal (CM) connections are most abundant in primates and are completely absent in non-primates

such as the cat, whose corticospinal projections are relayed by indirect connections via propriospinal neurons (Illert et al., 1977). In addition, the number of CM connections increases in accordance with an increase in dexterity. For example, squirrel monkeys are less dexterous than macaque monkeys, apes, or humans, and have far fewer CM connections (Nakajima et al., 2000). Control of coordination and dexterity is dependent on more than the architecture of the hand; therefore, it is important to understand the neural mechanisms underlying the control of grasping. This thesis examines the role of primary motor cortex in complex movements of the hand, particularly whether the firing of M1 neurons is correlated with individual degrees of freedom or patterns in hand kinematics.

1.1.2 Prehension

Prehension is defined as the act of grasping an object, including all actions of the hand leading to the final posture required to properly accomplish a task (MacKenzie and Iberall, 1994). This is one of the most common motor activities carried out by humans and non-human primates. Prehension is typically subdivided into two major phases that are temporally coupled: reaching and grasping (Jeannerod, 1984; MacKenzie and Iberall, 1994). Reaching consists of the unrestrained movement to transport the hand to its destination. This movement is typically rapid and includes opening of the hand. Grasping begins after peak aperture (distance between thumb and forefinger) has been achieved and the arm and hand slow to properly prepare the final grasp shape. Grasping is completed when contact is made with an object and the desired task is accomplished, which usually includes applying forces to the object for various purposes (Jeannerod,

1984; MacKenzie and Iberall, 1994). Because it is a natural behavior, reaching and grasping provides an excellent construct to examine the neural mechanisms underlying the control of voluntary movement.

It is well known that hand shaping evolves throughout reaching in a predictable manner (Jeannerod, 1984; Paulignan et al., 1990; Chieffi and Gentilucci, 1993; Bootsma et al., 1994; MacKenzie and Iberall, 1994). In both humans and non-human primates, preshaping of the hand begins early in reach, even before the hand approaches maximum grasp aperture (Jeannerod, 1984; Santello and Soechting, 1998; Roy et al., 2000; Mason et al., 2001; Hu et al., 2005), and continues throughout the second half of the reach (Santello and Soechting, 1998; Santello et al., 2002). In general, the maximum grasp aperture is linearly related to the size of the object to be grasped (Jeannerod, 1981; Paulignan et al., 1991a; Chieffi and Gentilucci, 1993). While the progression of hand postures for different objects differs during the second half of the reach, final grasp posture is not achieved until contact is made (Santello and Soechting, 1998; Mason et al., 2004). Preshaping of the hand is dependent on many properties of the object to be grasped including size (Fraser and Wing, 1981; Jeannerod, 1984; Marteniuk et al., 1990; Bootsma et al., 1994; Roy et al., 2000; Roy et al., 2002; Mason et al., 2004), shape (Santello and Soechting, 1998; Mason et al., 2001; Mason et al., 2004), fragility (Savelsbergh et al., 1996), contact surface area (Bootsma et al., 1994), texture (Weir et al., 1991), and weight (Johansson and Westling, 1988; Gordon et al., 1991; Weir et al., 1991). Therefore, the factors that contribute to hand shaping during prehension have

been extensively studied. However, less is known about the underlying neural mechanisms, the focus of this thesis.

Hand shaping during reach is also affected by the final goal of the task (Klatzky et al., 1987; Rosenbaum et al., 1992; Ansuini et al., 2006; Petit et al., 2006). Gradual shaping of the entire hand is utilized primarily when the end-goal is to perform small manipulations. When the goal is to place an object in a large target, the ring and little finger do not preshape during reach (Ansuini et al., 2006). Similarly, the parameters of movement, including arm velocity and grasp aperture, are affected by the goal such as whether the subject is lifting, throwing, raising, or placing an object (Armbruster and Spijkers, 2006). Finger positions during reach are modified for different tasks with the same object (Ansuini et al., 2008). Prehension is a highly developed skill in which the shaping of the hand and movements of the fingers are controlled to achieve the task goal.

The speed of the arm, hand, and fingers during reach to grasp are important parameters of movement in general. Therefore, it is necessary to examine the timing and speed of the components of prehension to understand the neural control strategies (Zhang et al., 1998; Mon-Williams and Tresilian, 2001; Braido and Zhang, 2004). The velocity of the arm and hand during reach-to-grasp has been examined extensively. The common bell-shaped velocity profile of the arm and hand during reaching is unaffected by changes in amplitude of the movement, goal of the task, or object to be grasped, although peak velocity does change in relationship to these factors (Jeannerod, 1984; Jakobson and Goodale, 1991; Bootsma et al., 1994; Roy et al., 2000; Roy et al., 2002). Although the speed of the joint angles of the fingers is critical to the proper timing of prehension, to

date, few studies have examined the speed of the joint angles of the fingers during grasping or neural control of hand shaping. An early study found that the joint angles and fingertip trajectories were highly variable during a rapid precision task, but the joint angular velocities remained relatively constant across trials and had bell-shaped velocity profiles (Cole and Abbs, 1986). This study had minimal task variation and started with the hand in the fully open position. In contrast, using a typical reach-to-grasp task, Vinjamuri and coworkers described joint angular velocities as increasing at the beginning of the task, followed by a decrease to a negative velocity, and then an increase to return to zero (Vinjamuri et al., 2007; Vinjamuri et al., 2009). This thesis examines joint angles and joint angular velocities during prehension and how the firing of M1 neurons is correlated with both of these parameters.

Movements of the hand and arm are also highly coupled during reaching and grasping. For example, maximum grasp aperture is temporally coupled with peak deceleration of the arm during transport (Jeannerod, 1981; Jeannerod, 1984; Arbib et al., 1985). When perturbations of object size, and subsequently the necessary grasp aperture, were presented during reaching, the time taken to reach the object was prolonged (Paulignan et al., 1991a; Castiello et al., 1993). An increase in task duration was observed during perturbations of object location as well (Paulignan et al., 1991b) but was accompanied by an additional change in hand shaping. Each change in direction of the wrist to accommodate a change in object location included a corresponding increase and decrease in grasp aperture (Paulignan et al., 1991b). The behavioral coupling of these

separate components suggests the presence of central control mechanisms for the coordination of the arm and hand during reaching and grasping.

1.1.3 Synergies

Synergies specify relationships (or patterns) between joint movements during complex motions, as defined by joint kinematics, forces, or muscle activation (Saltzman, 1979). Synergies provide a mechanism to reduce the degrees of freedom in complex movements by identifying patterns that describe the largest amount of variance in the data that can subsequently be used as building blocks to construct movements (Latash et al., 2002; D'Avella et al., 2003). Synergies are found in many classes of movements (Gelfand et al., 1971; Saltzman, 1979; Flash, 1990). Because of the inordinate number of degrees of freedom and movement possibilities, the hand is an attractive target for the application of the concept of synergies. In fact, the earliest descriptions of grasp defined classifications of hand shapes that could be interpreted as primitive or basic synergies (Napier, 1956). Many investigators have since searched for synergies or other simplifying patterns in hand movements (Santello et al., 1998; Valero-Cuevas, 2000; Mason et al., 2001; Santello et al., 2002; Jerde et al., 2003; Mason et al., 2004; Weiss and Flanders, 2004; Braido and Zhang, 2004; Theverapperuma et al., 2005; Klein et al., 2007; Ingram et al., 2008; Thakur et al., 2008; Vinjamuri et al., 2009).

A large variety of final grasp shapes can be described by scaling only a few hand postures defined by principal component or other dimension reduction analyses (Santello et al., 1998; Mason et al., 2001; Mason et al., 2004; Theverapperuma et al., 2005). These hand postures involve extensive covariation of the finger joint angles (Santello et al.,

1998; Santello and Soechting, 1998; Theverapperuma et al., 2005). Hand synergies have been defined for a variety of tasks, including static hand postures (Santello et al., 1998; Jerde et al., 2003), reaching and grasping objects (Mason et al., 2001; Mason et al., 2004; Braido and Zhang, 2004; Theverapperuma et al., 2005), and unconstrained movements (Ingram et al., 2008; Thakur et al., 2008). Fingertip force synergies have been defined (Shim et al., 2004; Gao et al., 2005; Shim et al., 2005; Niu et al., 2008), as well as muscle synergies (Holdefer and Miller, 2002; Weiss and Flanders, 2004; Brochier et al., 2004). Temporal coordination patterns of joint angles in hand shaping have also been identified (Soechting and Flanders, 1997; Santello and Soechting, 1998; Hager-Ross and Schieber, 2000; Mason et al., 2001; Mason et al., 2004; Braido and Zhang, 2004; Theverapperuma et al., 2005; Klein et al., 2007). A few studies have attempted to define synergies in joint angular velocities (Vinjamuri et al., 2007; Ingram et al., 2008; Vinjamuri et al., 2009). However, there has been no study that examined the synergies based on angles and angular velocities combined.

The most common method for defining synergies is principal component analysis (PCA). Principal component analysis is a form of factor analysis that is used to transform correlated variables into factors, or patterns, that are uncorrelated (Tabachnick and Fidell, 1996). The result of this analysis are vectors describing the contribution of each variable, or individual element, to orthogonal patterns (eigenvectors), and the amount of variance explained by each vector (eigenvalues) (Dunteman, 1989; Tabachnick and Fidell, 1996; Freund and Littel, 2000; Jolliffe, 2002; Jackson, 2003). The mathematical solutions require iterative processes and, therefore, are not precise. A principal component (PC) is

a reconstruction of the original data based on the linear combination of the weightings for each eigenvector (Dunteman, 1989; Jolliffe, 2002; Jackson, 2003). Singular value decomposition (SVD), a unique form of factor analysis, also identifies the singular values (i.e. vector scalings or factor scores) of the system (Jolliffe, 2002; Jackson, 2003). For instance, in the case of time series data, SVD identifies the weight of each eigenvector through time.

For many PCA-type analyses, the original input data is either centered or standardized before solving. Centering the data consists of subtracting the population average from the individual observations. This forces the variance of each component to be centered about zero, thus eliminating extra weighting for different amplitudes. Standardizing normalizes the variances by also dividing by the population standard deviation of each element, making the range of variances for each element similar. The advantage of centering or standardizing is debated and dependent on the application, but is necessary if analyzing components with differing units (Jolliffe, 2002; Jackson, 2003). If the data is not centered or standardized, the first eigenvector represents the mean of the data. If the mean of the data provides useful information for the application, this eigenvector is important to interpreting a data set (Jolliffe, 2002; Jackson, 2003).

One of the main purposes of PCA is to identify patterns in complex data. Analyses of hand shaping with PCA have consistently described one dominant hand shape based on the first principal component. Explaining between 60% and 90% of the variability of hand shaping, this pattern depicts the coordinated extension/flexion of the metacarpophalangeal (MCP) and interphalangeal (IP) joint angles and represents the

overall opening and closing of the hand (Santello et al., 1998; Mason et al., 2001; Mason et al., 2004; Braido and Zhang, 2004; Thakur et al., 2008). This hand shaping pattern has been found in both humans and non-human primates and can be considered a global shaping pattern. Additional patterns in hand shaping, or higher-order PCs, have not necessarily been consistent across studies. For example, in a human study of static grasping of common objects, the second PC consisted of the extension of the MCP joints with simultaneous flexion of the IP joints (Santello et al., 1998). In an unconstrained exploration task with human subjects, the second eigenvector was described as the flexion of the MCP angles of digits two and three and extension of the MCP angles of digits 4 and 5 (Thakur et al., 2008). In non-human primates performing a reach-to-grasp that controlled grasp force, the second eigenvector was hyperextension of the MCP and IP joint angles (Mason et al., 2004). Therefore, to date, PCAs have resulted in describing a global hand shaping pattern in the first eigenvector. However, the remaining components differ and appear to depend on the task (Santello et al., 1998; Thakur et al., 2008; Vinjamuri et al., 2009). Nonetheless, the higher-order PCs appear important and have been argued to transmit additional information beyond the lower-order PCs that is not simply noise or random variability (Santello et al., 1998). In addition, not all movements of the hand, such as pinch hand shapes or American Sign Language postures, can be accurately described by using a subset of PCs (Thakur et al., 2008; Vinjamuri et al., 2009). The higher-order PCs capture the versatility of the primate hand during prehension by describing the details and differences across and within a task.

The second goal of PCA is to remove correlation, or colinearity, between variables by defining orthogonal components. In reaching and grasping tasks, the kinematics of the hand covary (Santello et al., 1998; Santello and Soechting, 1998). Force control of the hand is also not individuated, but is shared between fingers (Li et al., 1998; Burstedt et al., 1999; Flanagan et al., 1999; Rearick et al., 2003). This high degree of covariation complicates attempts at understanding how neural or muscle activity is related to the kinematics or forces of the fingers. For instance, what is the interpretation of a significant linear relationship between neural firing and an MCP joint angle when there is a similar significant relationship between neural firing and an IP joint angle? Principal component analysis eliminates or reduces the covariation problem by transforming the data to a new coordinate system in which the components are independent. It is important to note, however, that only the resulting eigenvectors are orthogonal. Because the vector scalings are derived through direct multiplication of the eigenvectors with the variables, a degree of colinearity may be present in the vector scalings, but will be lesser than that found between the original parameters (Tabachnick and Fidell, 1996). In addition, when applied to biological sciences, the higher-level orthogonal variables that define small amounts of variability may or may not have significance.

Finally, PCA is used to reduce the degrees of freedom of a highly complex system. The first few eigenvectors explain the majority of the variance in hand shaping (Santello et al., 1998; Mason et al., 2001; Mason et al., 2004; Braido and Zhang, 2004; Thakur et al., 2008). Eigenvectors with smaller eigenvalues are considered to represent

patterns that are of less importance than eigenvectors with large eigenvalues. Often eigenvectors with smaller eigenvalues are driven by noise or outliers in the data (Freund and Littel, 2000), but this is not necessarily the case when the patterns are consistent across several repetitions. If the goal is only to reduce the degrees of freedom of a system, eigenvectors with smaller eigenvalues can be ignored (Dunteman, 1989; Freund and Littel, 2000; Jolliffe, 2002; Jackson, 2003). Several different criteria have been used to determine the number of eigenvectors to retain (Jolliffe, 2002; Jackson, 2003). One commonly used criterion is to retain eigenvectors that have eigenvalues greater than 1% (Freund and Littel, 2000; Jackson, 2003). A second is to define a desired cumulative variance (e.g. 90%) and keep all eigenvectors required to obtain that variance (Jackson, 2003). However, when reconstructing the data using a reduced set of PCs, small variations and details may be lost (Santello et al., 1998; Thakur et al., 2008).

To date, no studies have examined the neural correlates to principal components of hand shaping, although some authors suggest these patterns may be represented in the CNS (Ingram et al., 2008). There has been no evidence to support or contradict whether PCs, especially the higher-order definitions, are physiologically or neurologically relevant. The PCs that are highly consistent across sessions and subjects likely represent global patterns that are physiologically meaningful. However, despite being necessary to reconstruct all details of hand shaping (Santello et al., 1998; Thakur et al., 2008), it is not obvious that PCs that are highly variable across sessions are important to the CNS. In this thesis, I examine eigenvectors for a system of 14 joint angles, 14 joint angular velocities, and the combination of the two across multiple sessions and subjects. These

eigenvectors will then be used in regression analysis of firing from individual motor cortical cells.

1.2 Neural control of reaching and grasping

Several systems are involved with the neural coding of reaching and grasping, including the visual system for communicating extrinsic properties of the task (e.g. object shape and location), the somatosensory system for signaling intrinsic properties (location of the hand in space, texture, etc), and the motor system to execute the descending motor commands. Visuomotor transformations flow through two (dorsolateral and dorsomedial) streams of parieto-frontal circuits to convert visual input into a motor output (Jeannerod et al., 1995; Battaglia-Mayer et al., 1998; Castiello and Begliomini, 2008; Hendrix et al., 2009). Somatosensory information has a much more direct route to a motor command through extensive connections between the primary somatosensory, dorsal premotor, and primary motor cortices (Jones et al., 1978; Strick and Kim, 1978; Battaglia-Mayer et al., 1998). After sensory information has been processed, the primary motor cortex sends motor commands to the muscles via motoneurons and spinal cord networks (Asanuma et al., 1978; Shinoda et al., 1979; Lemon, 1988; Park et al., 2004). These cerebral cortical systems are also linked to the cerebellum and basal ganglia via the thalamus, which also play important roles in prehension (Georgopoulos et al., 1983; Alexander and Crutcher, 1990; Georgopoulos, 1991; Johnson and Ebner, 2000; Johnson et al., 2001; Mason et al., 2006).

1.2.1 Visuomotor transformation

Information about reach-to-grasp is often communicated through vision of the object and its surroundings. Humans and non-human primates use vision to guide preshaping of the hand to match object properties such as shape and size (Jeannerod, 1984; Wing et al., 1986; Paulignan et al., 1991a; Castiello et al., 1993; Santello and Soechting, 1998; Castiello et al., 1998; Roy et al., 2002). To generate the actual behavior, visual information must be transformed into the commands needed to control the muscles of the arm and hand. It is hypothesized that these visuomotor transformations are made through two separate, yet interconnected, streams; a dorsolateral circuit for grasping and dorsomedial circuit for reaching (Jeannerod et al., 1995; Castiello and Begliomini, 2008; Hendrix et al., 2009).

The dorsolateral circuit that is thought vital to the proper planning and execution of grasping primarily involves the anterior intraparietal area (AIP) of the posterior parietal cortex and ventral premotor cortex (PMv/area F5). Researchers suggest that object representations are encoded as object or shape schemas in AIP and are progressively transformed into movement-based coordinates in PMv (Taira et al., 1990; Murata et al., 2000). Object properties are one of many extrinsic properties because they are related to details outside the body, while geometries of movement such as muscle contraction or joint angles are intrinsic properties. The firing of neurons in AIP is modulated in relation to object shape rather than location, indicating that these cells encode aspects of the distal movements of the hand and fingers (grasping) instead of proximal movements of the arm (reaching) (Taira et al., 1990; Sakata et al., 1995; Murata et al., 2000). Visual stimuli, motor behavior, and the combination of the two, elicit

changes in the discharge of neurons in AIP, suggesting that AIP represents object properties as sensory-based plans (Murata et al., 2000). Chemical inactivation of AIP in monkeys severely impairs the subject's ability to properly preshape the hand for grasping of objects, but has little effect on reaching of the arm (Gallese et al., 1994). In addition, lesions (real or virtual) in humans reveal a temporal dissociation in the control of hand shaping (Davare et al., 2007) as well as a complete inability to preshape (Binkofski et al., 1998). These results support the hypothesis that AIP neurons are involved with the initial transformations of extrinsic properties into intrinsic commands important for hand shaping.

While some cells in AIP are modulated by the motoric components, movement-related responses are much more pronounced in PMv. The majority of cells in PMv are modulated early in the task for distal movements and are correlated to goal-related hand shaping rather than individuated finger movements (Rizzolatti et al., 1987; Rizzolatti et al., 1988; Murata et al., 1997; Umilta et al., 2007). This association with goal-related hand shapes is consistent with the selectivity of PMv neurons for one of three main grasp types, with precision grip being the most dominant (Rizzolatti et al., 1988; Murata et al., 1997; Davare et al., 2009). It is suggested that firing in PMv represents a vocabulary of basic hand shapes that can be used to construct a variety of complex movements (Rizzolatti et al., 1988; Jeannerod et al., 1995; Raos et al., 2004; Castiello and Begliomini, 2008). PMv processes the information received from AIP to participate in the early stages of hand shaping.

The visuomotor transformation for the transport component of reach-to-grasp is thought to flow through a dorsomedial circuit consisting of the occipital parietal sulcus (area VGA/areas V6 and V6A) and the dorsal premotor cortex (PMd/area F2) (Galletti et al., 1997; Tanne-Gariepy et al., 2002; Galletti et al., 2003). Neurons in VGA are tuned to both visual and motor properties of reaching (Galletti et al., 1997; Lacquaniti and Caminiti, 1998; Battaglia-Mayer et al., 1998). Galletti and coworkers found cells in VGA that are sensitive to several visual attributes, including size, orientation, and direction of movement of the stimuli (Galletti et al., 2003). In addition, VGA neurons are tuned to direction of reaching and position of the arm in space (Galletti et al., 1997; Lacquaniti and Caminiti, 1998). Similar to AIP for the dorsolateral circuit, VGA appears to begin the transformation of signals from extrinsic into intrinsic properties.

Area VGA projects to the reach-related area of PMd (Battaglia-Mayer et al., 1998). Neurons in PMd discharge in relation to several properties, including the direction, amplitude and speed of reach (Caminiti et al., 1990; Fu et al., 1993; Kalaska et al., 1997; Wise et al., 1997; Messier and Kalaska, 2000). However, the discharge of PMd cells is also related to distal movements (He et al., 1995; Dum and Strick, 2002; Raos et al., 2004; Stark et al., 2007a), including being modulated by hand shape (Hendrix et al., 2009). This suggests that PMd may communicate with PMv in planning hand shape during grasping (Castiello and Begliomini, 2008).

The areas involved with visuomotor transformation (e.g. AIP, PMv, VGA, PMd) have numerous neuronal interconnections (Battaglia-Mayer et al., 1998). Most researchers support the idea that the two streams for the control of reaching and grasping

actually work together for the proper implementation of prehension (Jeannerod et al., 1995; Tanne-Gariepy et al., 2002; Grol et al., 2007; Castiello and Begliomini, 2008; Hendrix et al., 2009). This is not unexpected, as behavioral research supports that timing of the opening and closing of the hand (grasping) is tightly coupled to the transport of the arm (reaching) in a highly predictable manner (Jeannerod, 1981; Jeannerod, 1984; Arbib et al., 1985; Paulignan et al., 1991a; Paulignan et al., 1991b; Castiello et al., 1993). The neural control of visually guided reaching and grasping is a highly complex system that has extensive cross-communications between the systems responsible for both sensory input and motor output (Georgopoulos, 1991).

1.2.2 Somatosensory and proprioceptive contribution to prehension

Reaching and grasping tasks can be completed successfully in the absence of vision of the object, with little or no change in the behavior (Jeannerod, 1984; Wing et al., 1986; Santello and Soechting, 1998; Santello et al., 2002; Winges et al., 2003; Mason et al., 2004; Hendrix et al., 2009). In fact, it has been argued that proprioception is more important than visual cues in proper completion of grasp and that proprioception alone can adjust for perturbations (Gentilucci et al., 1994). Both tactile feedback during grasping and proprioception during reaching contribute as feedforward mechanisms. The primary somatosensory cortex (S1/areas PE and PEa) is the major cortical area processing this information, and S1 provides the main parietal lobe input to M1 (Battaglia-Mayer et al., 1998). Inactivation of S1 results in an inability to coordinate the digits for a precision grip as well as the use of increased grip forces (Brochier et al., 1999). This suggests that cutaneous feedback is essential for the control of intricate grip

forces at the fingertips. During reaching and grasping, tactile and proprioceptive information is signaled to S1 predominantly at grasp initiation (Gardner et al., 2007a). However, neurons in S1 are tuned to movements as well as static posture of the arm (Kalaska et al., 1983; Georgopoulos et al., 1984), and their firing precedes the actual movement (Kalaska et al., 1983), indicating a role in planning and execution of movement rather than simply providing feedback. In addition, S1 has been argued to update future plans for reaching and grasping through connections to the posterior parietal cortex (Gardner et al., 2007b). Input from S1 to M1 is vital for constant updating of task information and proper implementation of prehension.

1.2.3 Basal ganglia and cerebellum

The ability of humans to properly execute complex reaching and grasping movements is also dependent on areas in the CNS beyond parietofrontal regions. The basal ganglia, a set of interconnected sub-cortical nuclei, are involved in scaling (Georgopoulos et al., 1983; Turner and Anderson, 1997; Prodoehl et al., 2009) and temporal coordination of motor output (Scarpa and Castiello, 1994; Jackson et al., 1995; Gentilucci and Negrotti, 1999). Areas within this region, such as the substantia nigra (DeLong et al., 1983), putamen (DeLong, 1973), and globus pallidus (Hamada et al., 1990), are modulated by movement of the joints, as well as movement direction, amplitude, and velocity (Georgopoulos et al., 1983; Turner and Anderson, 1997). Directly influencing the hand area of M1 through a pallidothalamic pathway, this suggests that the basal ganglia play an important role in prehension (Nambu et al., 1988; Holsapple et al., 1991). Patients with Parkinson's disease, which is characterized by loss

of substantia nigra pars compacta dopamine neurons and abnormal firing patterns in the basal ganglia, perform the transport and grasp components of prehension sequentially rather than simultaneously (Scarpa and Castiello, 1994; Ingvarsson et al., 1997; Alberts et al., 1998; Fellows et al., 1998; Nowak and Hermsdorfer, 2002). These patients also have difficulty with proper scaling and control of grip forces (Fellows et al., 1998; Nowak and Hermsdorfer, 2002; Wenzelburger et al., 2002; Spraker et al., 2007; Vaillancourt et al., 2007). Human functional imaging studies reveal that all the nuclei of the basal ganglia are activated during precision grasping. One view is that the anterior nuclei (e.g. caudate, anterior putamen, and external globus pallidus) are more activated for planning of movement and the posterior nuclei (e.g. posterior putamen, internal globus pallidus, subthalamic nucleus) for dynamic components such as force scaling (Prodoehl et al., 2009). Lesions in the basal ganglia result in increased grip force compared to controls and inappropriate scaling of forces applied during grasping (Dunnett et al., 1998; Jeyasingham et al., 2001; Dubrowski et al., 2005), further evidence that the basal ganglia are crucial in prehension.

The cerebellum is also essential for accurate prehension movements. Patients with cerebellar lesions display deficits primarily in the spatiotemporal coordination of reaching and grasping (Serrien and Wiesendanger, 2000; Rand et al., 2000; Zackowski et al., 2002), movements requiring multijoint coordination (Bastian et al., 1996; Timmann et al., 1999; Timmann et al., 2000), and the proper timing of force control (Mai et al., 1988; Muller and Dichgans, 1994). In particular, cerebellar patients show a deficit in anticipatory force control (Lang and Bastian, 1999; Serrien and Wiesendanger, 1999).

Studies using focal inactivation, functional imaging, and electrophysiology reveal that different regions within the cerebellar cortex and nuclei contribute to different components of prehension (Espinoza and Smith, 1990; Mason et al., 1998; Kawato et al., 2003). Cerebellar Purkinje cells signal several properties of reach, including direction, amplitude, and speed (Fortier et al., 1989; Fu et al., 1997; Coltz et al., 1999; Roitman et al., 2005). Cells in the cerebellum are also modulated in relation to several properties of grasp, including hand shape, grasp type, and force (Smith and Bourbonnais, 1981; van Kan et al., 1994; Kinoshita et al., 2000; Takasawa et al., 2003; Mason et al., 2006). One contemporary hypothesis is that the cerebellum is involved with the coordination of complex movements (e.g. prehension) by utilizing a feedforward internal model that compares the current state of the motor system with motor intent or future motor state (Kawato and Gomi, 1992; Kawato, 1999; Ebner and Pasalar, 2008; Roitman et al., 2009).

1.2.4 Primary motor cortex

As described earlier, extrinsic information flows through AIP and VGA and is gradually transformed into motor commands, which are initially encoded as goal-related hand shapes in PMv/PMd (Taira et al., 1990; Murata et al., 2000). Subsequently, PMv/PMd send goal-related motor signals about hand shape to M1, and a final transformation occurs before commands are sent through the corticospinal tract to the spinal cord and α-motoneurons (Brochier and Umilta, 2007). M1 also receives input from other areas in the CNS that are important for the feedback and feedforward control of the hand. This includes projections from S1 (Battaglia-Mayer et al., 1998) as well as inputs from the basal ganglia and cerebellum via the motor thalamus (Georgopoulos et

al., 1983; Alexander and Crutcher, 1990; Georgopoulos, 1991; Johnson and Ebner, 2000; Johnson et al., 2001; Mason et al., 2006). The abundant connections between M1 and other areas involved in controlling movements of the hand reinforce the importance of M1 in prehension.

M1 is essential for reaching and grasping, playing a major functional role in the execution of prehension. The majority of the direct axonal projections from the cerebral cortex to α-motoneurons, including those responsible for finger and hand movements, originate in M1 or premotor areas (Asanuma et al., 1978; Shinoda et al., 1979; Lemon, 1988; Palmer and Ashby, 1992; Bortoff and Strick, 1993; Maier et al., 1997; Park et al., 2004; Dum and Strick, 2005; Rathelot and Strick, 2006; Rathelot and Strick, 2009). CM cells, that is pyramidal cells with monosynaptic connections to α-motoneurons, are known to branch and innervate motor neuron pools of several muscles (Shinoda et al., 1979; Cheney and Fetz, 1980; Fetz and Cheney, 1980). Stimulation of individual motor cortical or CM cells facilitates EMG activity in multiple muscles (Asanuma and Rosen, 1972; Fetz and Cheney, 1980; Cheney and Fetz, 1985; Nudo et al., 1992; McKiernan et al., 1998; Beisteiner et al., 2001; Park et al., 2004). However, branching CM axons typically coactivate synergistic muscles. For example, stimulation of a single CM cell in the hand area of M1 activates the extensor muscles of three fingers nearly equally; the digitorum communis, digitorum 2/3, and digitorum 4/5 (Cheney and Fetz, 1985). The distribution and branching patterns of the connections between M1 and α-motoneurons implies a role in controlling more than just single joints or muscles, instead controlling more complex features of hand movements.

Transcranial magnetic stimulation (TMS) and functional magnetic resonance imaging (fMRI) studies in humans also illustrate the significance of M1 in reaching and grasping. TMS over the hand area of M1 in humans during complex manipulation tasks alters proper timing of grip force and digit closure (Lemon et al., 1995; Chouinard et al., 2005; Schabrun et al., 2008). In addition, the timing of the stimulation has different effects on different components of grasp shaping. Extrinsic muscles of the hand are predominantly effected when stimulation is applied throughout the reach period, while intrinsic muscles are most effected just before grasp initiation (Lemon et al., 1995). This demonstrates that M1 is engaged in all phases of reach-to-grasp. Finally, numerous fMRI studies have documented increases in M1 activity during reaching and grasping (Lemon et al., 1995; Sanes et al., 1995; Ehrsson et al., 2002; Takasawa et al., 2003; Kuhtz-Buschbeck et al., 2008).

The primary motor cortex's role in prehension can also be appreciated from the deficits produced by surgical removal, inactivation through chemical injection, or virtual lesion by TMS. Each results in severe motor deficits, including slow and weakened movements as well as complete inability to perform complex movements of the hand (Lawrence and Kuypers, 1968; Hoffman and Strick, 1995; Schieber and Poliakov, 1998; Rouiller et al., 1998; Brochier et al., 1999; Hummel and Cohen, 2005). These lesions affect dexterity and coordination of multijoint movements, resulting in awkward hand movements and improper timing during prehension. Most often, the deficits are characterized by the subjects' difficulty with individuated tasks such as precision grip (Schieber and Poliakov, 1998; Rouiller et al., 1998; Brochier et al., 1999), but whole-

hand grasping is also affected (Brochier et al., 1999). Therefore, the descending projections, stimulation, imaging, and lesion data demonstrate the importance of M1 in the coordination and completion of highly complex reaching and grasping tasks.

While it is clear that M1 is integral for prehension, its functional role is not fully understood. A classic debate regarding the function of M1 in voluntary movements has been whether it controls movement by encoding intrinsic or extrinsic properties (Thach, 1978; Kalaska and Crammond, 1992; Kakei et al., 1999). The discharge of M1 neurons modulates in relation to several aspects of arm and hand movement. Motor cortical firing is highly correlated with extrinsic properties such as movement direction (Georgopoulos et al., 1986; Caminiti et al., 1990; Fu et al., 1993; Georgopoulos et al., 1999), amplitude (Kalaska, 1991; Fu et al., 1993), force (Wannier et al., 1991; Georgopoulos et al., 1992; Cramer et al., 2002; Hendrix et al., 2009), and velocity (Reina et al., 2001). In addition, properties of the object being grasped modulate firing of M1 neurons (Picard and Smith, 1992b; Mason et al., 2002; Hendrix et al., 2009). M1 discharge is also correlated with intrinsic properties such as joint angles of the fingers (Schieber and Hibbard, 1993; Georgopoulos et al., 1999; Poliakov and Schieber, 1999; Theverapperuma et al., 2005). There is evidence that the primary motor cortex controls both extrinsic and intrinsic properties of movement (Scott and Kalaska, 1997; Kakei et al., 1999; Holdefer and Miller, 2002; Scott, 2008). For example, cells in the arm area of M1 that modulate preferentially for a certain direction of reaching (an extrinsic property) have altered directional tuning for changes in arm posture (an intrinsic property), despite movement along the same trajectory (Scott and Kalaska, 1997). These findings support the

hypothesis that the primary motor cortex is involved with the processing and control of multiple features of movements (Kakei et al., 1999; Johnson et al., 2001; Scott, 2008).

When examining the correlation of the firing of M1 neurons to movement parameters, the debate centers on whether M1 controls kinematic or kinetic parameters (Georgopoulos, 1991; Scott, 2008). Just as M1 neurons modulate for extrinsic kinematics of movement, these neurons also modulate in relation to extrinsic forces. This has been shown repeatedly for single (Evarts, 1968; Cheney and Fetz, 1980; Fetz and Cheney, 1980; Evarts et al., 1983; Maier et al., 1993; Hepp-Reymond et al., 1999) and multijoint reaching movements (Kalaska et al., 1989; Ashe, 1997; Cabel et al., 2001; Gribble and Scott, 2002). It is suggested that the correlation of firing of M1 neurons with kinetics reflects the descending motor commands to muscles (Cheney and Fetz, 1980; Ashe, 1997; Holdefer and Miller, 2002). However, only a fraction of cells in M1 modulate with "muscle-like" patterns (Thach, 1978; Kalaska et al., 1989; Crutcher and Alexander, 1990; Sergio and Kalaska, 1997; Ashe, 1997; Kakei et al., 1999). Post-spike facilitation (PSpF) of the firing of CM cells with muscle EMG activity show there is not a one-to-one relationship between neurons and muscle activity (Fetz and Cheney, 1980; Buys et al., 1986; Lemon et al., 1986; McKiernan et al., 1998). Furthermore, only a small percentage of M1 cells monosynaptically project to α-motoneurons (Schieber, 2001). As reviewed above, axons of CM cells branch to innervate several different motor neuron pools (Shinoda et al., 1979; Fetz and Cheney, 1980; Cheney and Fetz, 1985), making it difficult for a single cell to control a single muscle. While the issue has not been completely resolved, it is now generally accepted that descending signals from M1

are not exclusively controlling muscle activity (Georgopoulos, 1991; Ashe, 1997; Scott, 2008).

Another aspect of the debate that encompasses both the intrinsic vs. extrinsic and kinematics vs. kinetics arguments is whether M1 cells control these parameters as individual degrees of freedom (i.e. individual joints or muscles) or more complex elements (i.e. movements or synergies). Central to this debate is the somatotopic organization of M1, in which different body parts are mapped in an orderly topographic scheme on the M1 cortical surface (Penfield and Rasmussen, 1950; Woolsey, 1958). Early studies showed that focal stimulation of M1 evokes movement of limbs or muscles and these representations are organized somatotopically within M1 (Penfield and Rasmussen, 1950; Woolsey, 1958; Asanuma and Rosen, 1972). However, the spatial resolution of this somatotopic organization has been a source of much debate, as have the functional implications. A strict somatotopic map would support the theory that M1 controls individual degrees of freedom, while a less precise somatotopy would support alternate theories.

The anatomy of the primary motor cortex tends to support a coarse, rather than strict, somatotopic order. Cells involved with control of distal muscles of the hand are broadly distributed throughout the hand area of M1 and have representations that extensively overlap (Asanuma and Rosen, 1972; Shinoda et al., 1979; Lemon, 1988; Palmer and Ashby, 1992; Bortoff and Strick, 1993; Maier et al., 1997; Park et al., 2004; Dum and Strick, 2005; Rathelot and Strick, 2006; Rathelot and Strick, 2009). A strict somatotopic map would suggest that M1 cells project to and synapse on a scant group of

α-motoneurons. However, M1 cells make a host of intracortical, descending, and spinal connections in addition to the more direct corticomotoneuronal synapses. CM cells innervate motor neuron pools of several muscles (Fetz and Cheney, 1980; Shinoda et al., 1981; Buys et al., 1986; Lemon et al., 1986; McKiernan et al., 1998). M1 neurons also project to and synapse on interneurons in the spinal cord, in the intermediate gray, as well as the dorsal and ventral horns. Although most M1 intracortical connections are relatively local, within 1-2 mm (Landry et al., 1980; Keller and Asanuma, 1993), M1 neurons have longer projections that make connections throughout the upper extremity representation (Huntley and Jones, 1991; Tokuno and Tanji, 1993). Within M1 there are many interneurons, adding to the complexity of the network (DeFelipe and Jones, 1985; Jacobs and Donoghue, 1991; Kujirai et al., 1993). Therefore, the anatomy and connectivity do not support a strict somatotopic organization for M1.

Stimulation, imaging, and physiological studies also reveal a coarse somatotopic map in M1. Studies based on surface stimulation and intracortical microstimulation (ICMS) of M1 repeatedly support a general somatotopy, with mosaic-like mapping and significant overlap of muscle and digit representations (Kwan et al., 1978; Strick and Preston, 1978; Cheney and Fetz, 1985; Gould et al., 1986; Humphrey, 1986; Donoghue et al., 1992). Human fMRI (Sanes et al., 1995; Beisteiner et al., 2001) and magnetoencephalography (MEG) (Cheyne et al., 1991; Salenius et al., 1997) studies reveal a somatotopic organization in M1 during individuated finger movements, but with considerable overlap of activation for movements of adjacent digits. Adding to the complexity of this cortical map is that single M1 cells do not fire exclusively for a single

motor action. Single-cell recordings in monkeys show that most M1 neurons modulate for multiple movements during an instructed individuation task (Poliakov and Schieber, 1999). The extensive overlap of distal representations as well as the fact that individual cells discharge in relation to multiple movements and parameters, are consistent with M1 controlling more global features of movements or synergies (Schieber, 2001).

Examination of the discharge of neurons during natural behaviors involving the hand provides further insight into the control strategy utilized by M1. The modulation of M1 neurons in relation to grasp categories has been explored extensively. For example, power (whole hand) and precision (pinching between index and thumb) grasps represent two global hand shapes that are often utilized in prehension. Neurons in the hand area of M1 are activated during both precision and power grasping (Wannier et al., 1991; Maier et al., 1993; Umilta et al., 2007; Gardner et al., 2007b). Single unit activity (Lemon, 1981; Muir and Lemon, 1983) and local field potentials (Asher et al., 2007; Spinks et al., 2008) in M1 differ between power and precision grips, suggesting that M1 is involved with selection of grasp type. Imaging studies in humans also found activation in M1 is significantly different between precision and power grasps (Kuhtz-Buschbeck et al., 2008), but only when the task requires actual grasping of a physical object (Takasawa et al., 2003). The selectivity of neurons for grasp types suggests that M1 is involved with control of global features of movement rather than specification of individual degrees of freedom.

Power and precision grasp are highly qualitative terms and the exact parameters of hand shape that define these grasp types are not well-described. One can question

whether these descriptions of hand shaping are optimal as various PC analyses have not uncovered patterns that correspond to precision and power grasps in either humans or monkeys (Santello et al., 1998; Mason et al., 2001; Mason et al., 2004; Theverapperuma et al., 2005). Nor do the concepts of power or precision grasp provide any insight into the intrinsic aspects of the finger movements, such as the joint angles or muscle activations. Many configurations of joint angles and muscle activations can be utilized to generate a specific grasp. There is a need to examine whether the firing of M1 neurons is related to other types of synergies or global properties of hand shaping. For example, the firing of primary motor cortical neurons is correlated with groups of functional arm muscles during a simple reaching task (Holdefer and Miller, 2002), suggesting M1s involvement with muscle synergies. Further support for the concept that M1 controls global parameters is the violation of fingertip force synergies during grasping by TMS (Niu et al., 2008). A recent single-unit study of M1 neurons during whole-hand grasping found evidence for encoding of grasp dimension (Hendrix et al., 2009), a global parameter of hand shape. However, the hand shapes tested were limited and hand kinematics were not simultaneously collected with neural recordings. Whether M1 neurons encode kinematic or hand shaping synergies has not been examined.

To test the hypothesis that M1 is involved with global hand shaping, this thesis examines the relationship of motor cortical firing to intrinsic properties of grasping as well as patterns in hand shaping during a reach-to-grasp task. Two rhesus monkeys reached to and grasped a set of 23 different objects that were designed to systematically vary hand shape. Fourteen joint angles and angular velocities of the hand and fingers

were recorded simultaneously with single-unit activity of cells in the hand area of M1. Mahalanobis distances (MDs) are used to examine the relationship between intrinsic properties of hand shaping (i.e. joint angles) and extrinsic properties (i.e. objects). Singular value decomposition (SVD) analyses are used to define patterns in hand shaping based on the joint angles and/or joint angular velocities. Simple linear regressions are used to examine the relationship between joint angles, joint angular velocities, and patterns defined by SVD. Finally, applications for this research as well as future directions are discussed.

Chapter 2: Materials and methods

2.1 Experimental techniques, procedures, and equipment

2.1.1 Paradigm

Two Rhesus monkeys (*Macaca mulatta*; subjects S-6 kg and B-5 kg) were trained to reach and grasp a specially designed set of objects using a power grasp. The forearm of the reaching arm was in a neutral position; the volar surfaces of the fingers in opposition to the palmar surface and thumb were used to grasp the object. The animals were secured in a primate chair with head fixed in the forward direction, viewing a computer monitor (45 cm in front of the animal). The non-task related arm was gently secured to stop the monkey from using the incorrect hand to complete the task. To begin a trial, the monkey placed its hand on the start pad (a flat plate with a force sensor) located to its side. After a variable delay, a visual cue appeared on the computer screen to first instruct the force level of the grasp (Figure 2.1A, *premove epoch*). It was required that a minimal force was maintained on the start pad through the *premove epoch* (random duration 1-1.5 s), after which a second cue was given to signal the monkey to move ("go cue"), initiating the *reach epoch* (Figure 2.1B). The monkey then moved its hand from the start pad to the object (within 2 s of go cue) that was located directly in front (15 cm from start pad). The monkey was required to apply equal force to both sides of the object until the second visual cue reached the bounds of the first cue (force level) and held for a random time period between 2 and 4 s (Figure 2.1C, *grasp epoch*). A set of 23 different objects was used (see 2.1.2 Objects). The objects were randomly selected by the

paradigm and presented in blocks of 5 (subject B) or 10 (subject S) repetitions. In between blocks, objects were manually changed by the experimenter. Because examining the grasp force was not among the aims of the experiment and the contribution of grasp force to the firing of motor cortical neurons was investigated in a previous study (Hendrix et al., 2009), grasp force was kept constant across all trials to remove this potential confounding factor. When the two cues disappeared, the monkey returned its hand to the start pad and maintained force on the sensor for approximately 1 s to minimize extraneous movements and changes in posture (Figure 2.1D, *end epoch*). This signaled the end of the trial and a liquid reward was provided for correct completion. Monkey S completed 43 experimental sessions and Monkey B completed 6 sessions (average of 114 trials and 13 objects per session) during which the firing of motor cortical neurons was recorded (see 2.3 Neural).

A computer program written in Visual C++® presented the paradigm signals (Figure 2.1 A-D) to the monkey on the computer screen, monitored and displayed the force signals from the start pad and grasped object, and rewarded the monkey upon proper completion of a trial. The program also collected the time series information on the amplitude of the forces applied to both the start pad and the grasped object. The former is used to determine onset of movement, and the latter grasp initiation. Finally, the program was also used to collect and display the analog single unit activity of motor cortical cells.

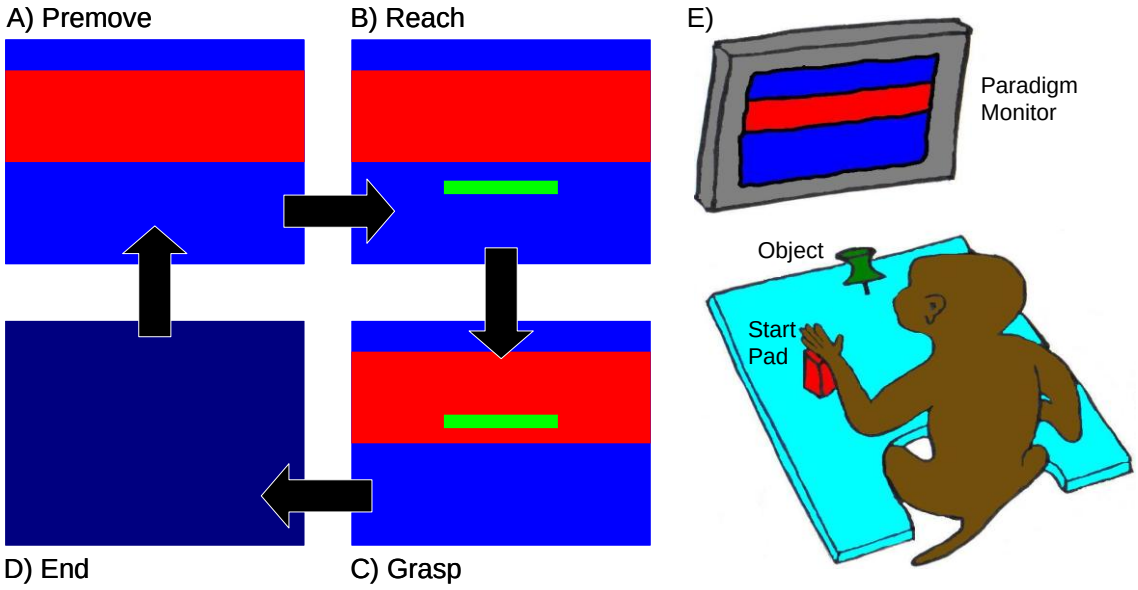

Figure 2.1. The reach-to-grasp task. A) During the *premove epoch*, the red bar appeared instructing the animal about the force range (vertical height of the red box) to be applied to the object. B) The "go cue" (green bar) appeared (1-2 s after instruction) signaling the animal to move, initiating the *reach epoch.* C) Feedback about force exerted on the object was provided to the animal by the green bar moving according to the amount of force applied during the *grasp epoch*. The green bar was required to be maintained in the red box for a random time between 2 and 4 s, after which the cues disappeared and the animal returned to the starting position to receive a reward. D) During the *end epoch* the animal returned to the start pad and was required to maintain force for ~1 s. This allowed for resetting of equipment as well as helped eliminate overlap of neural signals between trials. E) Paradigm setup displaying position of monkey, start pad, object, and computer monitor.

2.1.2 Objects

The goal in the design of the objects was to systematically explore a variety of hand shapes and finger positions during reach and grasp. Previously, 16 objects used in the Ebner laboratory to study reach-to-grasp in the monkey (Mason et al., 2004; Theverapperuma et al., 2005) varied shape, volume, and orientation of objects (Figure 2.2). However, these objects produced limited changes in movements of the fingers and hand shape other than grasp aperture (distance between thumb and forefinger).

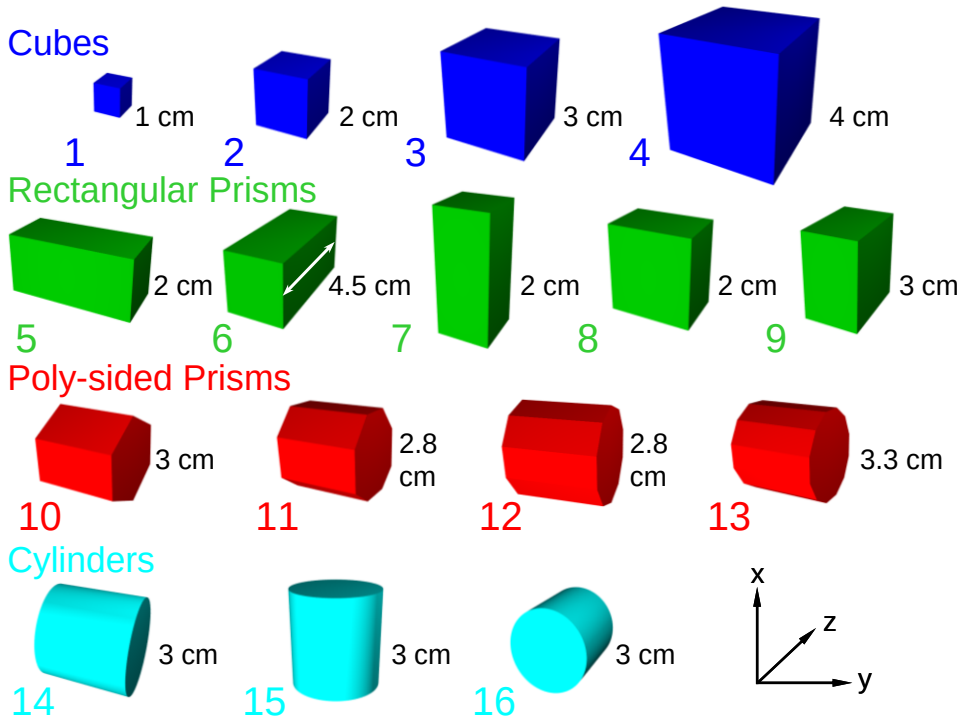

Figure 2.2. Schematic of previously used set of objects. Objects are grouped into four classes—cubes, rectangles, polygons, and cylinders. The grasp dimension (distance between faces of the object where finger contact is made) is labeled next to each object.

The new object set used in these experiments was designed to create a larger and more systematic variation in hand shape to better examine the relationship between kinematics and neural firing. Object set one (Figure 2.3A) contained notched and oval-shaped cylinders, and set two (Figure 2.3B) was made up of wedges varying in base width across the set. Set three (Figure 2.3C) utilized cones differing in diameter and orientation. Finally, set four (Figure 2.3D) was made up of spheres and spindles of differing radii.

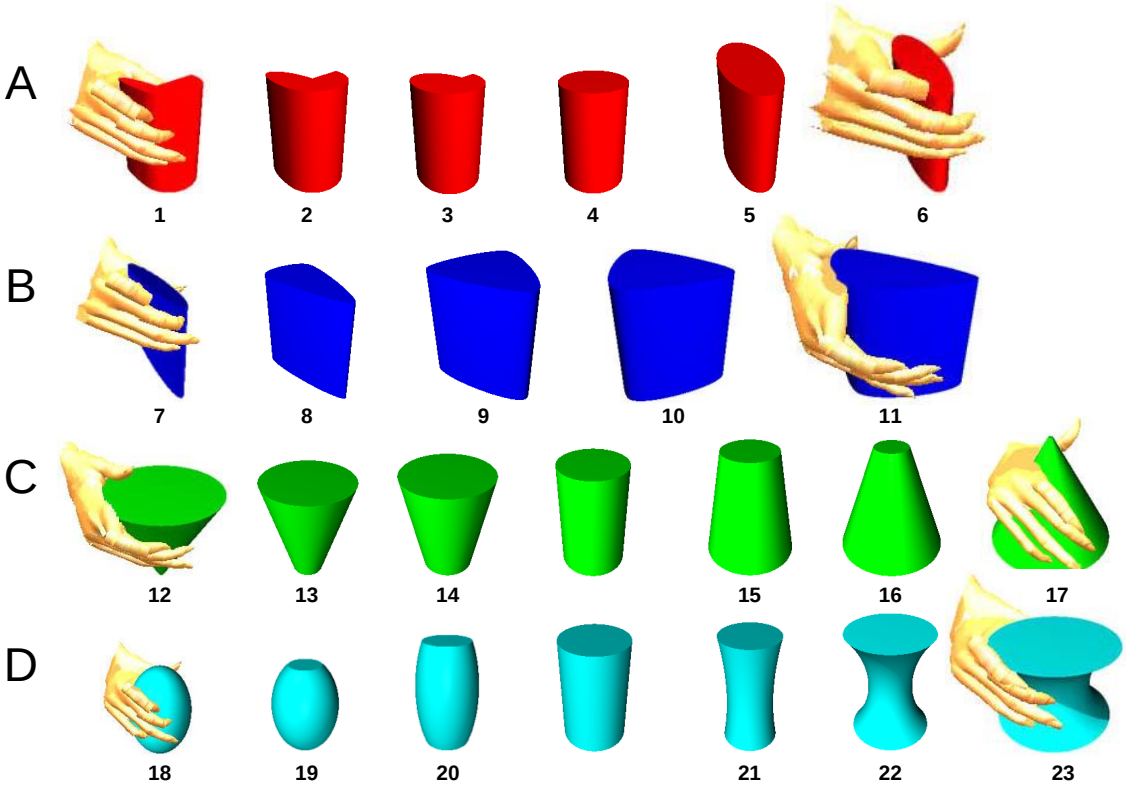

Figure 2.3. Schematic of newly designed set of objects grouped in sets and subsets. A) Set one contains notched and oval-shaped cylinders. B) Set 2 is made up of wedges varying in base width. C) Set 3 contains cones of differing diameter and orientation. D) Set 4 has spheres and spindles of different radii. Example hands reproduced from actual kinematic data are shown grasping representative objects.

The objects were precision-machined from aluminum, cut into 2 or 3 pieces to allow for force sensor placement, and reassembled with set-screws and o-rings to allow maximum sensitivity of touch to the sensors (Figure 2.4). All objects were 3 cm in height and mounted on a 1 cm-diameter metal post and presented so the object was mid-chest level to the animal. In addition, objects were secured to a base that prevented any rotation or translation of the object during grasping.

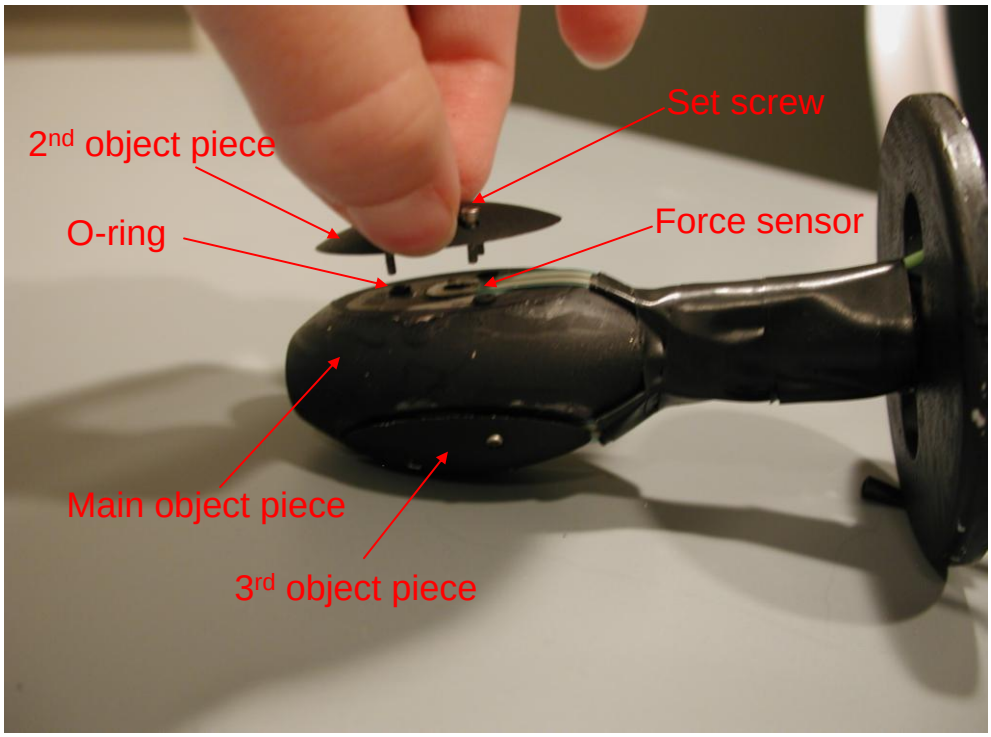

Figure 2.4. Construction of objects. Objects were cut into pieces so that force sensors could be placed below the surface. The pieces were secured to the object using set screws. O-rings between object pieces were used to create maximum sensitivity on the force sensor.

It was important that the monkeys grasped the new objects from the side as opposed to an overhand grasp (Mason et al., 2004; Theverapperuma et al., 2005), to obtain the intended changes in grasp shape. This was accomplished by extensive training (approximately 24 months) and continued monitoring of the monkey during the experimental sessions.

In addition, it was necessary to control for the manner in which force was applied to the objects. Most objects contained two force sensors (Force Sensing Resistors®, Interlink Electronics©, Camarillo, CA). However, the narrow width of three objects (Figure 2.3, objects 1, 6, and 7), allowed for the placement of only one sensor. The force sensors were embedded beneath the surface (Figure 2.4), approximately located where the forces were applied with the finger pads and palm to achieve the desired side grasp. Objects with two sensors had them located on each side of the object. For other objects, the sensor was either located in the center of the object (Figure 2.3, objects 6 and 7), or beneath the outer surface where the palm would make contact (Figure 2.3, object 1). The paradigm required that force be applied to both sensors if two were present. The force sensors required the construction of a non-inverting amplifier circuit to remove noise. Objects were calibrated once a month by adjusting the digital gain until the cursor was maintained inside the force box when a 500 g weight was placed on the object.

2.2 Kinematics

2.2.1 Data collection

The kinematics of the fingers, hand, and wrist were monitored in three dimensions during trials using a video motion capture system (Motion Analysis Corporation® (MAC), Santa Rosa, CA). The system utilized six Hawk digital cameras permanently mounted to frames in the experimental room in triangulated positions to maximize tracking the larger number of markers required to monitor movements of the fingers and wrist. Data collection was automatically initiated when the paradigm provided the instruction cue to the monkey. Video was acquired as LED ring lights illuminated passive reflective markers attached to the monkey's hand. The video signal was then digitized at 120 Hz and processed offline using EVaRT software provided by MAC. In addition, analog data from the object and start pad were simultaneously recorded in EVaRT in order to properly align kinematic and neural data.

Reflective markers were constructed by covering 2 mm-diameter plastic spheres with special reflective tape provided by MAC. After shaving, seventeen reflective markers were glued to the wrist and hand of the subject using SuperGlue® Gel. One marker was placed proximal to the dorsal wrist crease and another at the dorsal wrist crease. Four markers were placed near each long finger metacarpophalangeal (MCP) joint, proximal interphalangeal (PIP) joint, and distal interphalangeal (DIP) joint. A marker was also placed at the thumb carpometacarpal (CMC) joint, and the thumb MCP and IP joints (Figure 2.5). The markers were placed in approximately the same locations

across experimental sessions. At the end of each session, markers were removed by peeling them from the skin and discarded.

Figure 2.5. Placement of reflective markers. Markers were placed close to, but not directly on each joint.

2.2.2 Data processing

The EVaRT software was designed for use with human subjects rather than non-human primates, and the models provided within the program did not always capture and identify the markers properly because of their close proximity and small size. Therefore, the kinematic data collected with the monkeys required a great deal of post-processing.

Each trial (100-400 per session) of each session (71 total sessions) was processed individually. First, markers were identified and named. After determining that the markers were properly named for each frame, any gaps in the data (such as when a marker was occluded by the object, start pad, other fingers, etc.) were filled in using one of two methods. One, if the gap was less than five frames (< 41.5 ms) during movement or any size during static periods, a linear join was used. Two, if the gap was larger than five frames, the gap was filled by extrapolating the placement of the marker by using the location of other nearby markers. While nearly all trials contained small frame gaps, a trial was required to contain 50% of frames for all markers during the reach epoch to be considered for further analysis. Finally, the data was smoothed using a 10 Hz Butterworth filter.

Fourteen joint angles (thumb metacarpophalangeal (THMCP), metacarpophalangeal angles for digits 2-5 (MCP2-5), proximal interphalangeal for digits 2-5 (IP2-5), adduction/abduction 1-4 (ABD1-4), and wrist flexion/extension (WFLEX)) were calculated for later analysis and are referred to as individual elements (IEs). The joint angles were defined by vectors drawn between markers (Figure 2.6). For instance, the MCP joint angle of the first finger was defined as the angle between the vector drawn from the marker at MCP2 and the wrist crease and the vector from MCP2 to IP2. Wrist path was calculated as the distance between the marker at the wrist crease and the start pad.

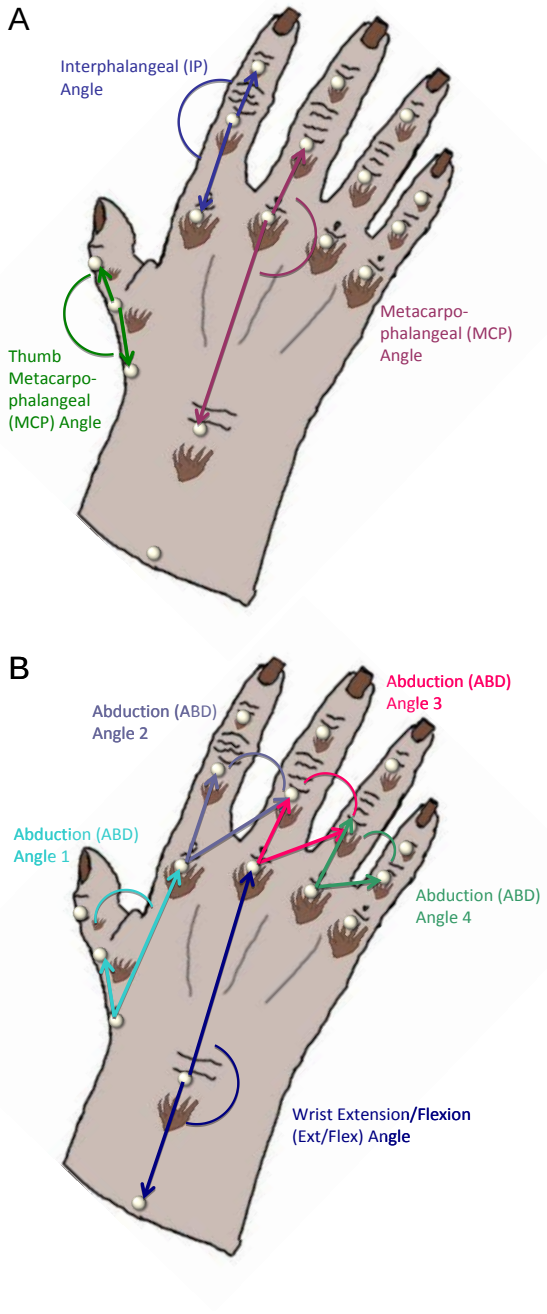

Figure 2.6. Joint angle definition. Vector definitions for THMCP, MCP2-5 and IP2-5 joint angles (A) and ABD1-4 and WFLEX joint angles (B). Each joint angle was defined as the angle between two vectors. Each vector's endpoints corresponded to a marker attached to the surface of the hand or wrist.

A problem encountered using this method for defining joint angles is that the markers were not placed directly at the center of rotation for the joint, and therefore the joint angles were not entirely accurate. To account for this, physical models of the hand were constructed using the dimensions of each subject's hand. Ten models (two monkeys, five digits each) were built consisting of two joints each. All distances between joints for the models were precisely measured to match the dimensions of the monkeys' digits. Markers were glued to the center of each joint as well as the top of the model on the "skin". Data was collected using video motion capture as the model fingers were articulated from 90-180 degrees (measured with a protractor). Figure 2.7 displays the relationship between the measured (surface of hand) and actual (center-of-joint) data. All angles tested had similar linear relationships, but the exact equation for each joint and monkey was used to determine the final angles using MATLAB (Table 2.1). Some equations are similar across monkeys because hand dimensions were the same (i.e. MCP5), and therefore the same model was used to calculate the adjustment. No adjustments were made for ABD1-4 or WFLEX. All joint angles were low-pass filtered using an 83.3 ms sliding-average filter.

Joint angular velocities were calculated by taking the current frame's joint angle, subtracting the previous frame's joint angle, and dividing by the time step (8.33 ms). Joint angular velocities were also filtered using an 83.3 ms sliding-average filter. Wrist speed was calculated in a similar manner.

Table 2.1. Equations used to adjust each joint for each monkey (θ is the measured joint angle).

Joint	Equation for Monkey S	Equation for Monkey B
THMCP	Θ*1.18 - 26.7	Θ*1.18 - 26.7
MCP2	Θ*1.18 - 34.1	Θ*1.24 - 39.4
MCP3	Θ *1.36 - 37.5	Θ*1.36 - 37.5
MCP4	Θ *0.99 + 0.22	Θ*1.11 - 18.6
MCP5	Θ*1.28 - 49.0	Θ*1.28 - 49.0
IP2	Θ*0.77 + 37.7	Θ*1.29 - 39.6
IP3	Θ*1.32 - 49.8	Θ*1.32 - 49.8
IP4	Θ*0.55 + 72.8	Θ*1.45 - 67.5
IP5	Θ*1.45 - 65.3	Θ*1.29 - 43.7

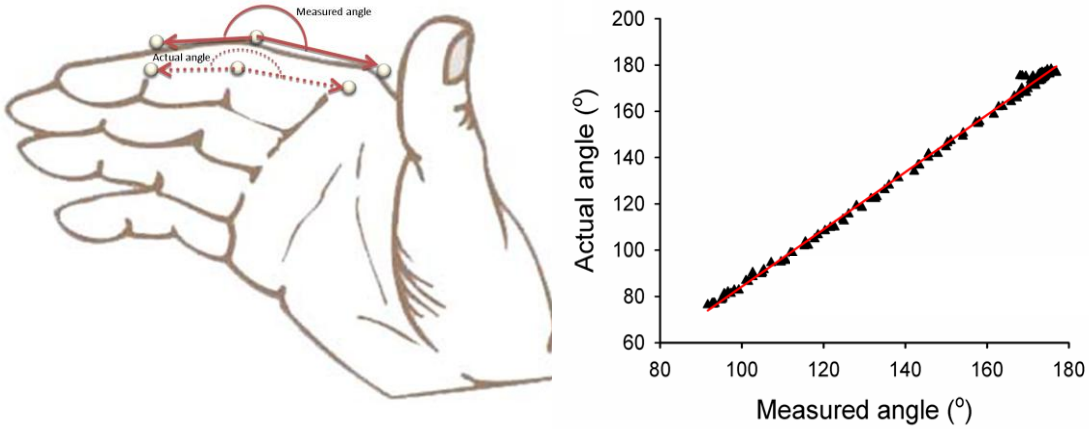

Figure 2.7. Angle adjustment example. Relation between measured (surface of hand) and actual (center-of-joint) joint angles for one joint angle (MCP5). The relationship can be described with a linear equation with more than 90% confidence.

2.2.3 Data analysis

2.2.3.1 Individual elements

The data was divided into three epochs for analysis: *premove*, *reach*, and *grasp*. Analog data from the force sensors embedded in the start pad and objects was collected by both the motion analysis and neural recording systems. The force data were co-

registered so as to align kinematic and neural recordings as well as defining epochs. Reach onset was defined as the time at which the change in force on the start pad first dropped below 10 N/s. Grasp onset was defined as the time at which the change in force on the object first exceeded 10 N/s. In the event that the analog data was not properly recorded with the kinematic system, additional criteria were necessary. Reach and grasp onset times were required to occur between the times at which the absolute value of the wrist velocity first exceeded 12 cm/s and again fell below 12 cm/s. If the reach and grasp onset times defined by the force sensor data did not occur in this range, these times were used instead. All data was aligned on grasp onset. With the exception of the *reach epoch*, epochs used for analysis were abbreviated segments of the task epochs. The *end epoch* was not used for analysis. The *premove epoch* was defined as the 250 ms before reach onset and the *grasp epoch* as the 250 ms after grasp onset. The *reach epoch* was defined as the time between reach and grasp onset (~400 ms).

Several analyses were used to examine the differences in the joint kinematics. First, analysis of variance (ANOVA) evaluated the changes in the joint angles and joint angular velocities across objects for individual sessions. For the ANOVAs, the average magnitude of the joint angles and joint angular velocities at the three centermost bins (25 ms) of each epoch were used. Similarity between sessions was examined by calculating the Pearson correlation coefficient between the average across all trials for each session within subjects and across subjects.

Second, to examine differences in hand shaping across repetitions for each object, the Mahalanobis Distance (MD) from the average hand shape during the *grasp epoch* was

calculated using Equation 2.1 for each session individually (Theverapperuma et al., 2005).

$$MD^2_i = (y_i - u)' A^{-1} (y_i - u) \qquad \textbf{Equation 2.1}$$

Where y_i is the matrix of joint angle data for trial (i) during the *grasp epoch*, u is the average joint angle data across all trials in the *grasp epoch*, and A is the covariance matrix. Because the epoch is static, all time points within the *grasp epoch* were averaged to obtain the joint angle used in the analysis. MDs were then normalized by dividing each value by the maximum for the session. In order to examine the variability within trials for an object, the range of normalized MDs for each object were calculated by subtracting the minimum from the maximum MD for the object. Ranges were averaged across sessions in order to examine the consistency of each object's variability across sessions.

Finally, the colinearity that exists between the fourteen joint angles and joint angular velocities during the reach-to-grasp task was quantified. The correlation coefficient for the entire temporal progression of the joint angles and joint angular velocities was calculated between each pair of elements for each session separately. Similarly, correlations were calculated between all elements and the wrist path and speed. To display the consistency of these correlations, the values obtained were averaged across sessions.

2.2.3.2 Singular value decomposition analysis

Singular value decomposition (SVD) was performed for all trials in each session using the fourteen joint angles and joint angular velocities to identify patterns in hand

shaping and define orthogonal components of the data. SVD is similar to Principal Component Analysis (PCA) in that it identifies patterns and uncorrelated components (or eigenvectors), but SVD also provides the temporal scaling of the patterns (Jolliffe, 2002; Jackson, 2003). SVD was performed by first constructing the X (or data) matrix

$$\mathbf{X}= \begin{vmatrix} IE_1(trial_1, time_1) & IE_2(trial_1, time_1) & \dots & IE_n(trial_1, time_1) \\ IE_1(trial_1, time_2) & IE_2(trial_1, time_2) & \dots & IE_n(trial_1, time_2) \\ \dots & \dots & \dots & \dots \\ IE_1(trial_2, time_1) & IE_2(trial_2, time_1) & \dots & IE_n(trial_2, time_1) \\ IE_1(trial_2, time_2) & IE_2(trial_2, time_2 & \dots & IE_n(trial_2, time_2) \\ .. & \dots & \dots & \dots \\ IE_1(trial_i, time_p) & IE_2(trial_i, time_{p)} & \dots & IE_n(trial_i, time_p) \end{vmatrix}$$

Where *i* is the number of trials, *p* is the number of time bins (8.33 ms), and *n* is the number of individual elements (joint angles or joint angular velocities (IE)) being used in the analysis. As described in Section 2.2.3.1, 250 ms of the *premove* and *grasp epochs* and the entire *reach epoch* (~400 ms) were used in the analysis. Five variations of the SVD analyses were determined for the combination of all analysis epochs (Table 2.2). Joint angles and joint angular velocities were standardized by first subtracting the mean and then dividing by the standard deviation of each joint angle.

Table 2.2. Variations on SVD analysis. Five different SVD analyses were performed using joint angles, joint angular velocities, or the combination.

Input
14 unadjusted joint angles
14 standardized joint angles
14 unadjusted joint angular velocities
14 standardized joint angular velocities
14 standardized joint angles + 14 standardized joint angular velocities

For SVD, matrix X was decomposed into three matrices using $X= U \Sigma V^T$. Matrix U contained the coefficients describing each individual element's contribution to the eigenvector. It is important to note that while eigenvectors may contain both positive and negative coefficients for individual elements, it is not the sign but the relationship between the coefficients that is key to interpreting the data. The matrix V contained the vector scaling explaining the involvement of each eigenvector over the course of time. These temporal weightings (TWs) are used in regression analysis with neural firing. The superscript T indicates the transpose of the matrix. Finally, matrix Σ contained the eigenvalues, or the amount of variance described by each eigenvector.

Similarity of eigenvectors across sessions was examined by calculating the correlation coefficient between the eigenvectors of a model session and each eigenvector of each other session (Ingram et al., 2008; Thakur et al., 2008). A correlation coefficient of 0.5 or greater was required to consider an eigenvector to be similar to the model eigenvector (Ingram et al., 2008).

2.3 Neural

2.3.1 Surgical procedures

To record the activity of primary motor cortical neurons, two survival surgeries were required after training. For both surgeries the animal was first anesthetized using a combination of Ketamine (7 mg/kg IM) and Xylazine (0.6 mg/kg IM), intubated, mechanically respirated, and anesthesia was maintained using isofluorane gas. Heart rate, blood pressure, and oxygen saturation were continuously measured to assure the proper level of anesthesia. In the first surgery, the scalp was opened, the muscles retracted, and four posts were affixed to the exposed skull using titanium screws. After the animal recovered from this surgery, a halo was fastened to the posts and used to fix the animal's head during recording sessions. In the second surgery, the scalp was again pulled back and a circular plug (19 mm diameter) of the skull was removed over the hand area of the motor cortex contralateral to the working hand (right M1 for money B; left and right for monkey S (at separate times)). The M1 hand area was located by both surface landmarks (i.e. sagittal suture) and by stereotaxic coordinates (Monkey S, left M1: 20A, 16.6L; Monkey S, right M1: 15.5A, 18.5L; Monkey B, right M1: 20.3A, 16.6L). Leaving the dura mater intact, a 19 mm internal diameter chamber was placed over the craniotomy, affixed with titanium screws, and sealed with dental acrylic. Postoperatively, the animals were given an analgesic (Buprenorphine 0.06 mg IM bid x 3-4 days) and an antibiotic (Clindamycin 25 mg PO bid x 10 days). While the animal was in its cage, the chamber was filled with agar, treated with antibiotics, and capped.

2.3.2 Data collection

Once the animal recovered from surgery, recording sessions were conducted on a daily basis. During recording sessions, the cap and agar were removed and 1-4 tungsten microelectrodes (FHC, 250 μm, ~3 MΩ) were inserted through the dura into the cortex using an Alpha Omega Electrode Positioning System with a custom-designed coupler to attach to the recording chamber and feed the electrodes. The location of electrode insertion within the chamber varied each session. Electrodes were connected to a four-channel, multispike amplification, filtering, and discrimination system (Alpha Omega Engineering), as well as the paradigm, speaker, and oscilloscope. The system was lowered into the cortex until background cellular activity was audible. After the cortex and electrodes were allowed to "settle" for 30 minutes, single units were isolated by driving each electrode independently in 10 μm intervals (maximum depth of 3 mm) until the waveforms of one or two neurons were clearly visible over the background firing. The monkey was then allowed to complete a few practice trials to test whether the cell was modulated to the task. If the cell was not modulated with the task, the electrode was moved and a new cell was isolated. Analog single unit activity was filtered (25-3000 Hz) and collected for 1-5 task related neurons each session at a 10 kHz sample rate. Collection was initiated when the monkey began a trial by placing its hand on the start pad, and only successful trials were saved. Following each recording session, if the cell was still viable, qualitative examination of the receptive field of each cell was performed by passively moving, stroking, tapping, and gently squeezing various regions of the arm, forearm, hand and fingers.

For a select number of sessions, intracortical microstimulation (ICMS) was performed to verify that the chamber was placed over the hand area of the motor cortex (Weinrich and Wise, 1982; Tanne-Gariepy et al., 2002). The same electrodes in the same position used for recording were used to stimulate over an amplitude range of 5-60 μA during ICMS (35 ms duration train of 12 cathodal pulses, each pulse: 200 μs duration, at 333 Hz). Visual and manual examination was used to assess whether the ICMS evoked limb movements or muscle twitches of the hand and forearm.

2.3.3 Data processing

The single unit waveforms recorded during the sessions were processed offline using Mclust 3.21 (MatLab® special program). Using the peaks, valleys, and time of waveforms, single units were discriminated from the raw data and outputted as a digital signal. All trials were aligned on grasp onset determined from analog data collected from the force sensors embedded in the objects (see Section 2.2.3). Digital spiking information was converted to instantaneous firing rates using fractional intervals binned at 8.33 ms to match the kinematic sampling rate (Taira et al., 1996).

2.3.4 Data analysis

The *premove, reach, and grasp* analysis epochs used for the neural data were the same as used for the kinematic data. A baseline firing rate was determined by averaging the first 300 ms of the trial, prior to any visual cues. Paired student's t-tests were performed between the mean firing of each epoch and the baseline firing, and only cells showing significant differences in at least one epoch were retained for the study. Of the 96 cells recorded, 81 were retained using this criterion. The mean firing rate for a cell

during each epoch was analyzed for differences across objects using ANOVA. Cells were categorized according to the epoch which displayed the highest mean firing rate. For other analyses, the firing rate data was logarithmically transformed to ensure a more normal distribution (Vittinghoff et al., 2005). All analyses were performed on single-trial data that was not averaged.

In order to test for joint parameters that are encoded in the firing of M1 neurons, multiple linear regressions were performed, evaluating the resulting R^2 values and coefficients. Two different types of regression models were used: 1) individual element-based models, and 2) SVD-based models. Thirty individual element-based regressions were performed (i.e., fourteen based on joint angles, fourteen based on joint angular velocities, one based on all angles together, and one based on all joint angular velocities together). The individual element-based model was of the form:

$$F(t) = a_0 + \beta_{IE_n} IE_n(t) \qquad \textbf{Equation 2.2}$$

where F(t) is the firing of the cell at time t, $IE_n(t)$ is the n^{th} individual element of grasping at time t, β_{IEn} is the calculated coefficient, and a_0 is the calculated constant. The equations for the models including all elements (overall models) were similar (Equation 2.3), except that they included the summation of all elements (N) of the model and their calculated coefficients.

$$F(t) = a_0 + \sum_{n=1}^{N} \beta_{IE_n} IE_n(t) \qquad \textbf{Equation 2.3}$$

Fifteen SVD-based regressions were performed (i.e., one based on each of 14 time weight vectors and one based on the model of all time weight vectors together) for each variation of the first four SVD analyses performed (Table 2.2), and 29 regressions

were performed (i.e., one based on each of 28 time weight vectors and one based on the model of all time weight vectors together) for the SVD analysis of the standardized joint angles and joint angular velocities. The SVD-based model was of the form

$$F(t) = a_0 + \beta_{V_m} V_m(t) \qquad \textbf{Equation 2.4}$$

where F(t) is the firing of the cell at time t, $V_m(t)$ is the m^{th} time weight vector of grasping at time t, β_{Vm} is the calculated coefficient, and a_0 is the calculated constant. The equation for the overall model was similar (Equation 2.5), except that it included the summation of all time weight vectors (M) and their calculated coefficients.

$$F(t) = a_0 + \sum_{m=1}^{M} \beta_{V_m} V_m(t) \qquad \textbf{Equation 2.5}$$

Because timing of neural firing and behavior is not simultaneous, the regression was tested for improvement by introducing a delay (τ) as shown in Equation 2.6 (individual elements), Equation 2.7 (individual elements model), Equation 2.8 (time weight vectors), and Equation 2.9 (time weight vectors model). Only physiologically relevant values of τ (between -500 and 500 ms) were considered (Roitman et al., 2005).

$$F(t-\tau) = a_0 + \beta_{IE_n} IE_n(t) \qquad \textbf{Equation 2.6}$$

$$F(t-\tau) = a_0 + \sum_{n=1}^{N} \beta_{IE_n} IE_n(t) \qquad \textbf{Equation 2.7}$$

$$F(t-\tau) = a_0 + \beta_{V_m} V_m(t) \qquad \textbf{Equation 2.8}$$

$$F(t-\tau) = a_0 + \sum_{m=1}^{M} \beta_{V_m} V_m(t) \qquad \textbf{Equation 2.9}$$

Each model was based on a type III sum of squares, which is an order-insensitive regression technique. Each variation on SVD shown in Table 2.1 was regressed and

compared. Standardized coefficients were obtained by subtracting the mean and dividing by the standard deviation of data before inputting it in the regression.

The R^2-values obtained from each regression were averaged across all cells for only regressions that resulted in high correlations ($R^2 \geq 0.138$) (Cohen, 1988). The percentage of cells displaying a high correlation for each regression was also tabulated. Comparisons were made across regression types and cell types. In addition, the number of high regressions for each cell was tallied.

Chapter 3: Reach to grasp behavior

3.1 Individual elements

3.1.1 Results

The first step of the analysis focused on understanding the grasping behavior at the level of the individual joint angles and joint angular velocities which are referred to as individual elements (IEs). Fourteen joint angles (THMCP, MCP2-5, IP2-5, ABD1-4, and WFLEX) and their respective joint angular velocities were examined for three analysis epochs (*premove*, *reach*, and *grasp*). For analysis purposes, only 250 ms of the *premove* and *grasp epoch*s were used, as well as the entire *reach epoch* (391 +/- 25 ms average for monkey S, 417 +/- 16 ms average for monkey B). Each joint angle is shown across all epochs for a model session (Monkey S) in Figure 3.1. The same experimental session is used to demonstrate various analyses throughout Chapter 3. The behavioral population data in the chapter is based on 43 sessions from Monkey S and 6 sessions from Monkey B.

The THMCP, MCP2-5 (Figure 3.1A), IP2-5 (Figure 3.1B), and WFLEX (Figure 3.1C) joint angles increased through the first half of the reach as the hand was opening. The shaping of the hand continued through the second half of the reach when the joint angles decreased as the hand approached and enclosed the object. This temporal progression of hand shaping is typical of previous observations in humans and non-human primates (Jeannerod, 1984; Santello and Soechting, 1998; Roy et al., 2000; Mason et al., 2001; Mason et al., 2004; Hu et al., 2005). The ABD1-2 (Figure 3.1C) joint angles

decreased initially after movement onset, followed by an increase as the hand approached the object. ABD3 generally decreased throughout the reach but had little overall change. ABD 4 decreased as well but included a small increase midway through reach (Figure 3.1C). IP5 and ABD4 displayed a temporal progression that was less stereotypical across trials than other joint angles, similar to findings in humans that the little finger is involved with detailed shaping of the hand to a lesser degree than the remaining fingers (Ansuini et al., 2006). The joint angles were generally tightly clustered for trials until midway through the reach, after which the angles began diverging to accomplish different grasp shapes for different objects (Santello and Soechting, 1998; Mason et al., 2001; Mason et al., 2004; Theverapperuma et al., 2005).

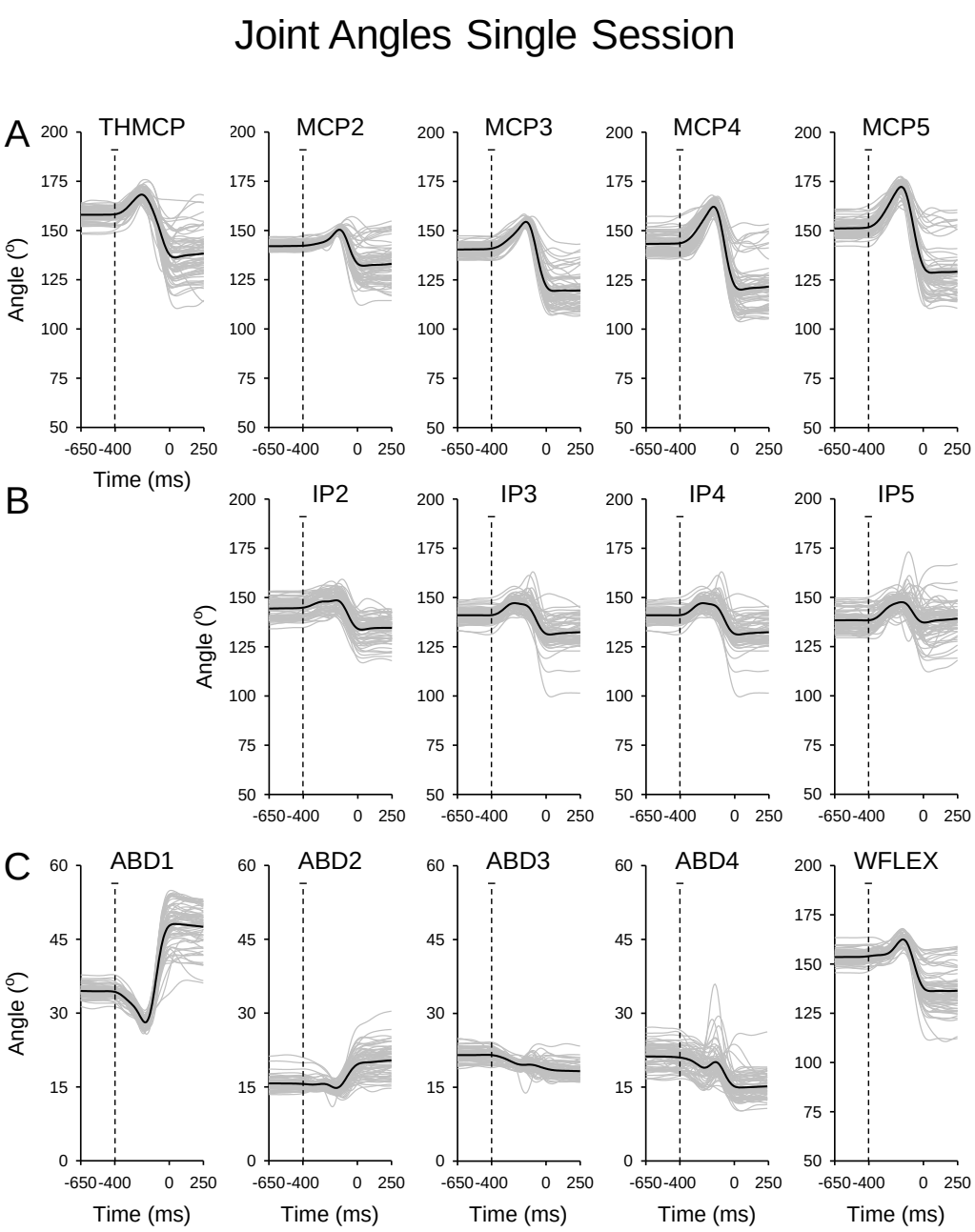

Figure 3.1. Single session joint angles. Plots of joint angles in time for all trials in one session. A) MCP joint angles for thumb (THMCP) and digits 2-5 (MCP2-5). B) IP joint angles for digits 2-5 (IP2-5). C) Abduction/adduction angles between fingers (ABD1-4). D) Wrist flexion/extension angle (WFLEX). Plots are aligned on grasp onset (time = 0 ms). Each gray line is a single trial. Bold line is the average across trials. Dashed vertical line represents mean reach onset and bar above is +/- one standard deviation.

The population data displays similar temporal progressions of increases and decreases in joint angles (Figure 3.2). Similarities across sessions for each joint angle were quantified by calculating the Pearson correlation coefficient (r) between the average across all trials for each session and the average for each other session with each monkey and across monkeys (Figure 3.3). The average temporal progression of most joint angles (13/14 for Monkey S, 8/14 for Monkey B, and 13/14 for both combined) was highly correlated ($r>0.65$) with the average temporal progression of the same joint angle across different sessions. The ABD3 joint angle had the smallest correlation coefficient for comparisons across monkeys ($r=0.53$). Monkey B had smaller correlations across sessions for most joint angles than Monkey S, especially for ABD2 ($r=0.50$), ABD4 ($r=0.46$), and WFLEX ($r=0.49$), emphasizing the larger variability in task performance for the subject. Overall, joint angles were highly similar across sessions both when comparing sessions for the same monkey and comparing sessions across monkeys (Figure 3.3). Some joint angles, however, displayed qualitative differences between monkeys. For example, the THMCP, MCP2-5, and IP2-5 were more flexed at the onset and more extended in the final grasp posture for Monkey B. Therefore, all data used in further analysis was unaveraged across trials, sessions, or monkeys.

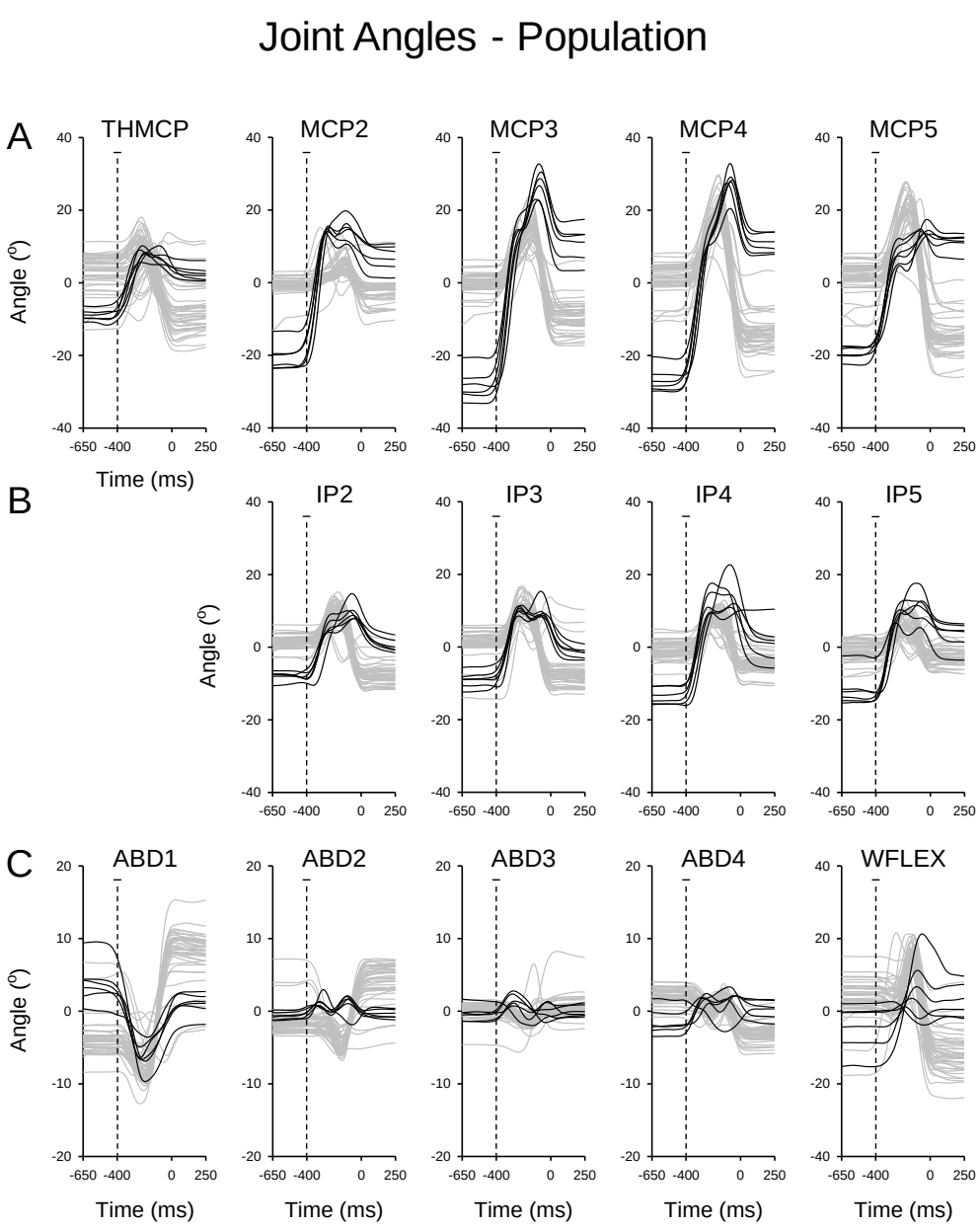

Figure 3.2. Population joint angles. Plots of joint angles in time for all sessions, normalized by subtracting the overall mean of each session. A) MCP joint angles for thumb and digits 2-5 (THMCP and MCP2-5). B) IP joint angles for digits 2-5 (IP2-5). C) Abduction/adduction angles between fingers (ABD1-4). D) Wrist flexion/extension angle (WFLEX). Each gray line is the mean of each session for Monkey S and each black line is the mean of each session for Monkey B. Conventions as in Figure 3.1.

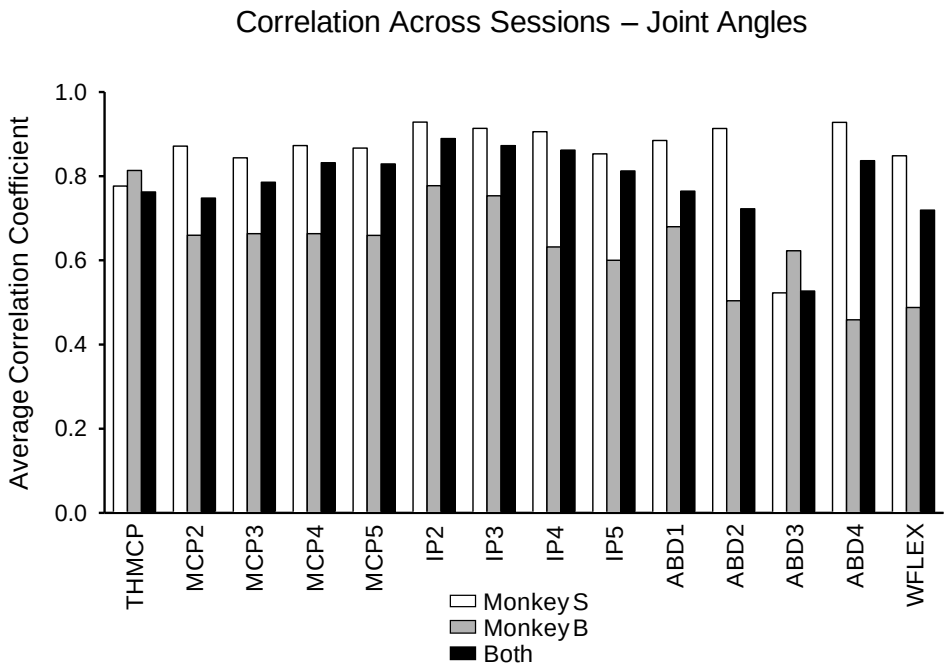

Figure 3.3. Correlation of joint angles across sessions. Bar graph of the average correlation coefficient between the average temporal progression of each joint angle of each session with the average temporal progression of each joint angle of each other session for all Monkey S sessions (white), all Monkey B sessions (gray) and all sessions for both monkeys (black).

Most previous studies of finger movements during grasping only examined joint angles (Santello et al., 1998; Santello and Soechting, 1998; Jerde et al., 2003; Weiss and Flanders, 2004) or other parameters of grasp (Mason et al., 2001; Mason et al., 2004; Theverapperuma et al., 2005; Hendrix et al., 2009). However, the speed and velocity of finger movements is a critical parameter in motor control (Zhang et al., 1998; Mon-Williams and Tresilian, 2001; Braido and Zhang, 2004). Recent studies in humans have argued that joint angular velocity is an important determinant of grasping (Vinjamuri et

al., 2007; Ingram et al., 2008; Vinjamuri et al., 2009). Also, many studies have emphasized that the firing of motor cortical neurons is modulated by speed/velocity (Ashe and Georgopoulos, 1994; Reina et al., 2001), implicating dynamic parameters of movement. No previous study has examined joint angular velocities in depth with non-human primates. Therefore, joint angular velocities were evaluated. Joint angular velocities for the model session are shown in Figure 3.4. For THMCP, MCP2-5 (Figure 3.4A), IP2-5 (Figure 3.4B), and WFLEX (Figure 3.4C), the joint angular velocity increased initially after movement onset, during opening of the hand, then decreased through peak aperture as the hand approached the object (Vinjamuri et al., 2007; Vinjamuri et al., 2009). The angular velocity of ABD1-3 displayed an opposite pattern and the angular velocity of ABD4 displayed a less consistent pattern (Figure 3.4C). As required by the task, the joint angular velocities were approximately zero during the *premove epoch* when the hand was on the start pad, and also for the *grasp epoch* after the hand reached its final posture (~100 ms after grasp onset). As a consequence, the joint angular velocities were generally tightly clustered across trials throughout the *premove* and *grasp epochs*, with much greater variability during the *reach epoch*.

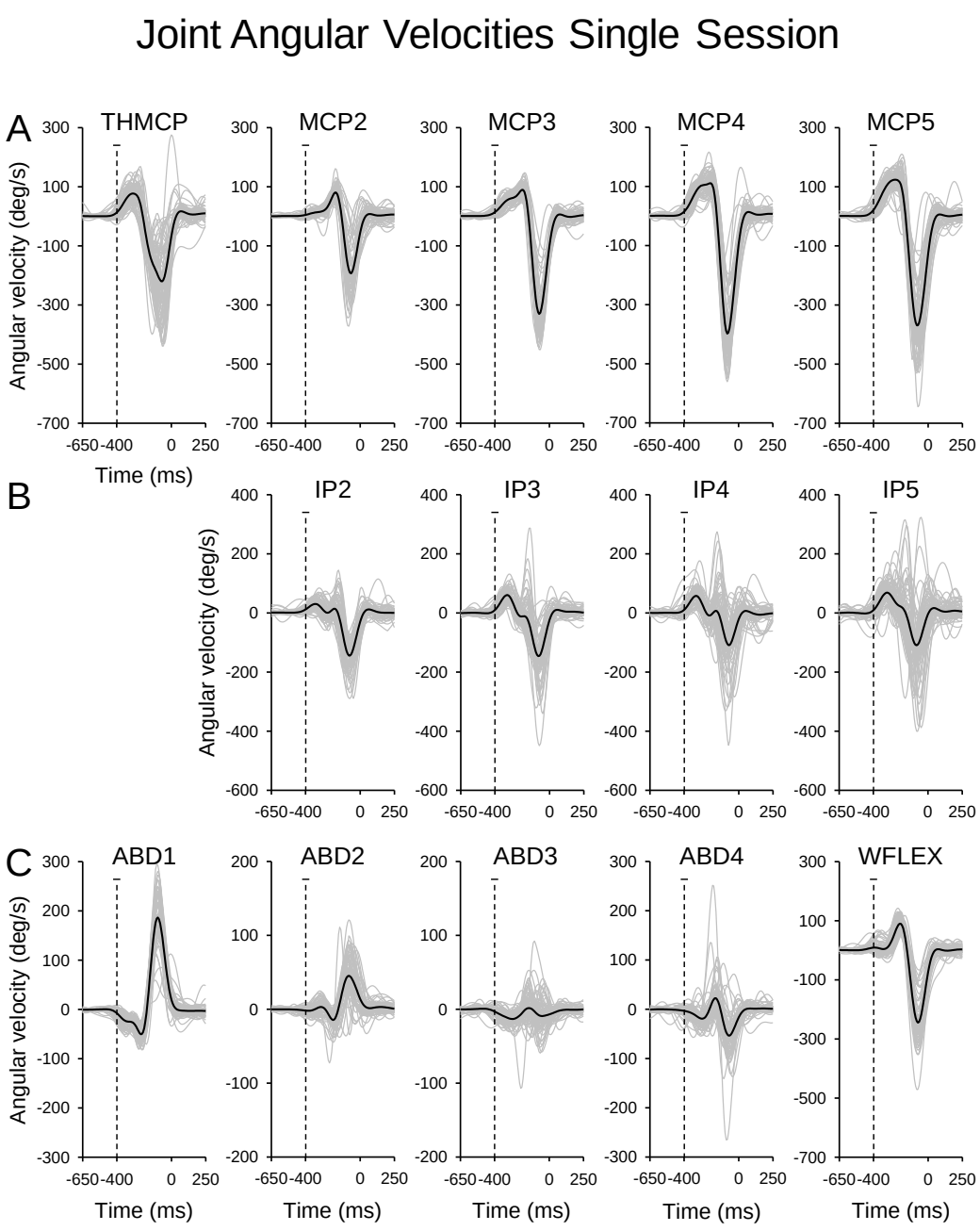

Figure 3.4. Single session joint angular velocities. Plots of joint angular velocities in time for all trials in one session. A) MCP joint angles for thumb and digits 2-5 (THMCP and MCP2-5). B) IP joint angles for digits 2-5 (IP2-5). C) Abduction/adduction angles between fingers (ABD1-4). D) Wrist flexion/extension angle (WFLEX). Conventions as in Figure 3.1.

The population data in Figure 3.5 demonstrates the variability in joint angular velocities across sessions and monkeys. For the majority of joints (11/14 for Monkey S sessions, 10/14 for Monkey B sessions, and 9/14 for all sessions) the velocities were highly correlated across sessions ($r>0.65$) (Figure 3.6). However, some correlations were much lower for the joint angular velocities than for the joint angles. For instance, the average correlations for THMCP and ABD3 joint angular velocities for sessions for Monkey S were 0.48 and 0.50, respectively. The average correlation for the WFLEX joint angular velocity across sessions for Monkey B was only 0.20. Across monkeys, correlations were smaller ($r<0.50$) for THMCP, ABD3, and ABD4. Similar to the joint angles, qualitative examination revealed that some of the joint angular velocity profiles differ between monkeys (Figure 3.5). For instance, THMCP did not have as large of range or decreases in joint angular velocity for Monkey B as Monkey S. In addition, ABD1-4 and WFLEX joint angular velocities for monkey B had an additional peak and were smaller in amplitude compared to those for Monkey S. These differences suggest that the strategies utilized for controlling joint speed differed day to day as well as between monkeys.

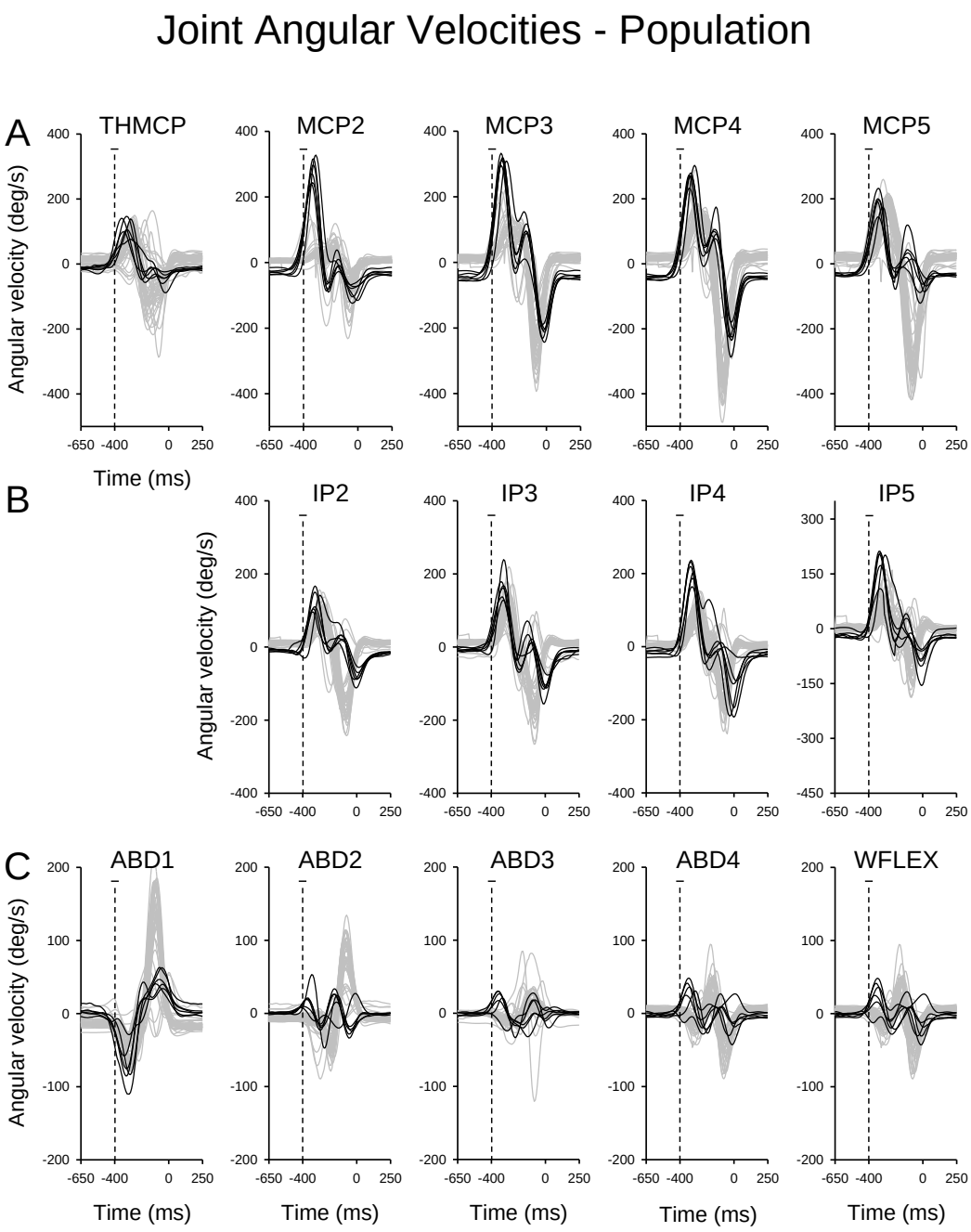

Figure 3.5. Population joint angular velocities. Plots of joint angular velocities in time for all trials for all sessions. A) MCP joint angles for thumb and digits 2-5 (THMCP and MCP2-5). B) IP joint angles for digits 2-5 (IP2-5). C) Abduction/adduction angles between fingers (ABD1-4). D) Wrist flexion/extension angle (WFLEX). Each gray line is the mean of each session for Monkey S and each black line is the mean of each session for Monkey B. Conventions as in Figure 3.1.

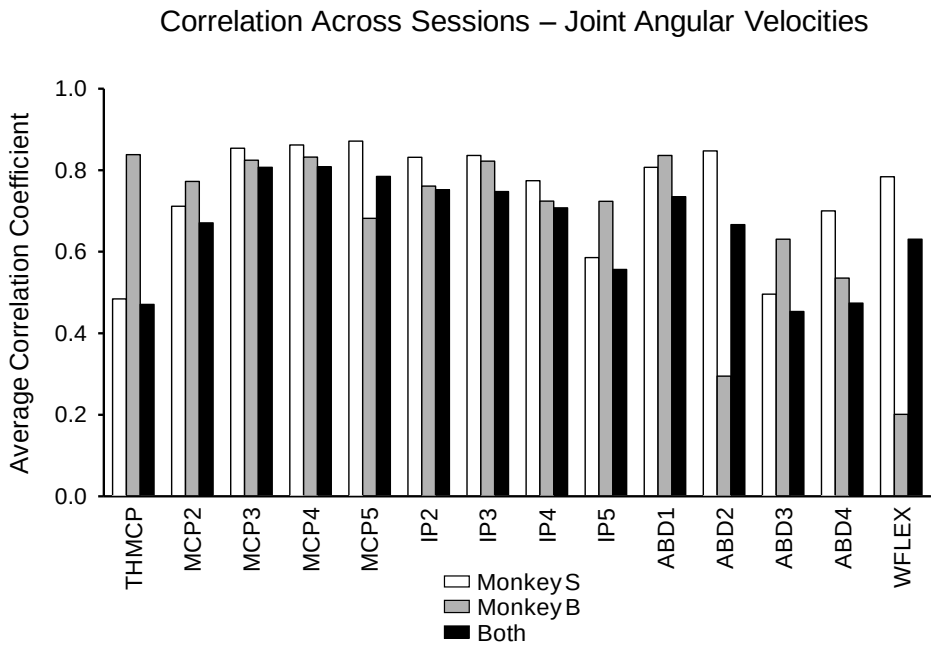

Figure 3.6. Correlation of joint angular velocities across sessions. Bar graph of the average correlation coefficient between the average temporal progression of each joint angular velocity of each session with the average temporal progression of each joint angular velocity of each other session for all Monkey S sessions (white), all Monkey B sessions (gray) and all sessions for both monkeys (black).

Because objects were a controlled variable in the experiment and were designed to create variances in joint kinematics, differences in joint angles and joint angular velocities by object were examined. A multi-way linear-model ANOVA was performed on joint angles and joint angular velocities for the average of the three centermost bins of each epoch. For the model session (Figure 3.1), all joint angles except ABD2, were significantly different across objects during the *grasp epoch* when differences were most expected (Table 3.1). Significant differences were found across objects for 64% (9/14)

and 93% (13/14) of joint angles during the *premove* and *grasp epochs*, respectively. On the other hand, the angular velocity of only one joint (MCP2) showed significant differences across objects during the *premove epoch*, and none were significant during the *grasp epoch* for the model session. Forty-three percent (6/14) of joint angular velocities differed significantly as a function of object during the *reach epoch*.

For Monkey S, the joint angles differed significantly ($p \leq 0.05$) across objects during the *premove epoch* from 33% (IP5 and MCP3) to 61.9% (THMCP) of sessions (Figure 3.7A). The number of sessions displaying significance for joint angles increased during the *reach epoch* (Figure 3.7B; range 40.5% (ABD4) to 83.3% (ABD1)), and was greatest during the *grasp epoch* (Figure 3.7C; range 76.2% (IP5 and ABD1) to 90.5% (MCP5, ABD4, and WFLEX)). This progressive increase in significance across objects exemplifies the preshaping to objects that occurs during reach and grasp (Jeannerod, 1984; Santello and Soechting, 1998; Roy et al., 2000; Mason et al., 2001; Santello et al., 2002; Mason et al., 2004; Hu et al., 2005; Thakur et al., 2008). The results for Monkey B, however, were more variable, with joint angles differing significantly across objects for 20%-100% of sessions during the *premove epoch* (Figure 3.7A), 40%-100% during the *reach epoch* (Figure 3.7B), and 20%-100% during the *grasp epoch* (Figure 3.7C). One factor that may contribute is the fewer number of trials, and therefore objects, completed in each session for Monkey B.

Joint angular velocities were less dependent on the object grasped than were the joint angles. Velocities varied with objects in less than 24% of sessions during the *premove epoch* (Figure 3.7D) and less than 53% during the *grasp epoch* (Figure 3.7F) for

either monkey. This is not unexpected because joint angular velocities were approximately zero during these epochs. The number of sessions displaying significant differences during the *grasp epoch* is greater than the *premove epoch* due to the subjects making small corrections before settling on a final grasp. Similar to the model session, differences across objects for joint angular velocities were greatest during the *reach epoch* (Figure 3.7E; range 20%-80%) when the hand was opening and closing. A previous study found joint angular velocities did not vary with grasp type (Cole and Abbs, 1986), which is not consistent with the large number of sessions displaying significant differences across objects during the *reach epoch* in this study. This shows that joint angular velocities are a critical factor in hand shaping during reach-to-grasp.

Table 3.1. ANOVA by object for joint kinematics of the model session. Resulting p-values from ANOVA by object for joint angles and joint angular velocities during each epoch for the model session.

	Joint angles			Joint angular velocities		
	Premove	**Reach**	**Grasp**	**Premove**	**Reach**	**Grasp**
THMCP	0.007	0.000	0.030	0.204	0.355	0.172
MCP2	0.188	0.085	0.000	0.011	0.082	0.194
MPC3	0.043	0.022	0.000	0.825	0.739	0.724
MCP4	0.000	0.000	0.000	0.733	0.013	0.830
MCP5	0.059	0.000	0.000	0.921	0.011	0.349
IP2	0.000	0.000	0.000	0.334	0.172	0.756
IP3	0.000	0.000	0.000	0.876	0.311	0.570
IP4	0.000	0.000	0.000	0.498	0.525	0.714
IP5	0.000	0.000	0.000	0.873	0.517	0.207
ABD1	0.076	0.004	0.000	0.980	0.009	0.135
ABD2	0.000	0.000	0.056	0.527	0.003	0.999
ABD3	0.545	0.000	0.020	0.728	0.000	0.124
ABD4	0.004	0.000	0.003	0.823	0.173	0.407
WFLEX	0.349	0.050	0.000	0.689	0.000	0.215

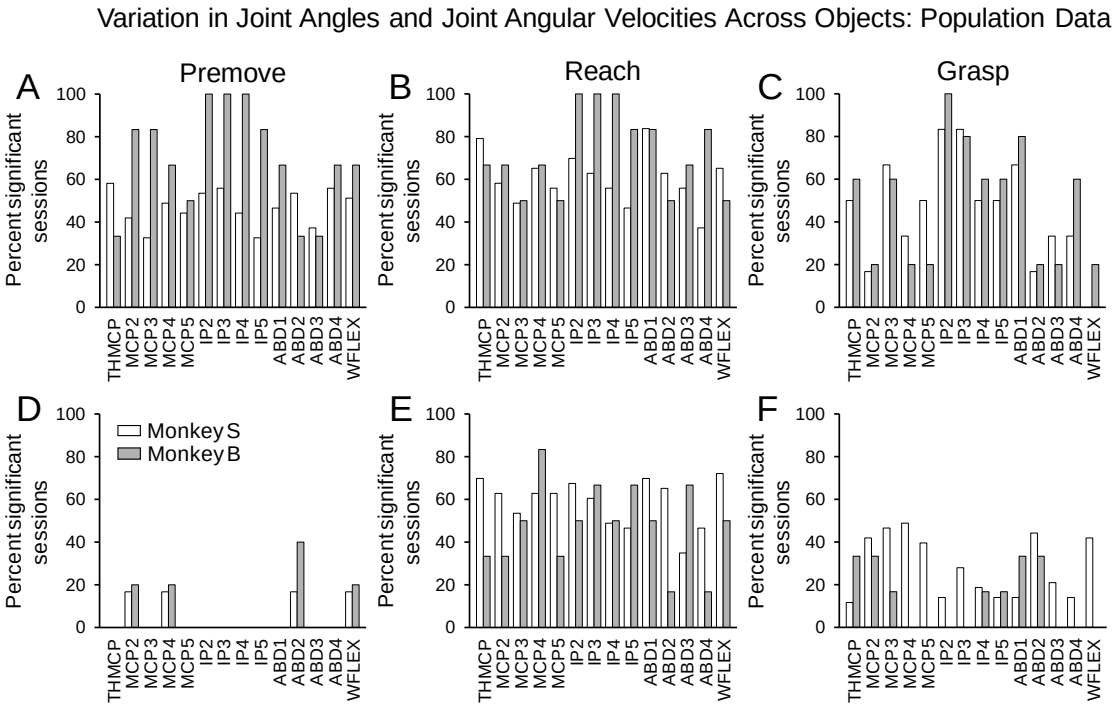

Figure 3.7. Percent of sessions with significant joint angles and joint angular velocities across objects. Bar graphs of the percentage of sessions displaying significant differences across objects in A-C) joint angles and D-F) joint angular velocities for *premove* (A and D), *reach* (B and E), and *grasp* (C and F) *epochs*. White is Monkey S and gray is Monkey B.

In addition to movement of the digits, it is also necessary to examine how the movement of the hand varies within the task. Qualitative examination of the wrist paths (distance from the origin) and speed suggests that variations were small and, when present, were predominantly during the *grasp epoch* (Figure 3.8). However, the wrist path and speed for the model session (Figure 3.8) showed significant differences by object (ANOVA, $p \leq 0.05$) during the *reach* and *grasp epochs* (Table 3.2). Wrist path was significantly different across objects for nearly 50% of sessions during the *premove epoch*, and for almost 80% of sessions during the *reach* and *grasp epochs* (ANOVA,

$p \leq 0.05$; Figure 3.9A) for Monkey S. Monkey B displayed significant differences in wrist path across objects in 60% of sessions during the *premove epoch* and 40% of sessions during the *reach epoch* (ANOVA, $p \leq 0.05$; Figure 3.9A). There were no sessions in which path was significant during the *grasp epoch.* On the other hand, wrist speed was significantly different in very few sessions during the *premove* and *grasp epochs* (less than 50%), and for more than 60% of sessions during the *reach epoch* for either monkey (Figure 3.9B). Previous studies found little significant differences in wrist path or speed as a function of the object grasped, possibly due to the limited finger placement possibilities created by the force sensor placement on the objects (Mason et al., 2004; Theverapperuma et al., 2005; Mason et al., 2006). Because the force sensors were embedded below the surface and the proper forces could be applied in several locations, the current object set allowed the monkey to change hand position.

Table 3.2. ANOVA by object for wrist kinematics of the model session. Resulting p-values from ANOVA by object for wrist path and speed during each epoch for the model session.

	Premove	Reach	Grasp
Path	0.557	0.001	0.000
Speed	0.316	0.000	0.000

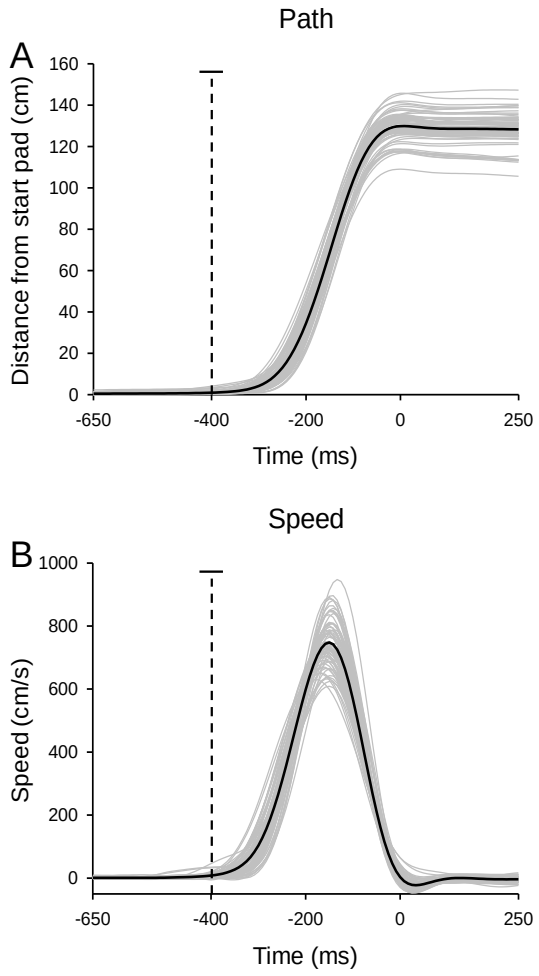

Figure 3.8. Wrist path and speed for the model session. A and B) Plots of wrist crease path (distance from start pad) and wrist crease speed, respectively, in time for all trials within a session. Plots are aligned on grasp onset (time = 0 ms). Each gray line is a single trial. Bold line is the average across trials. Dashed vertical line represents mean reach onset and bar above it is +/- one standard deviation.

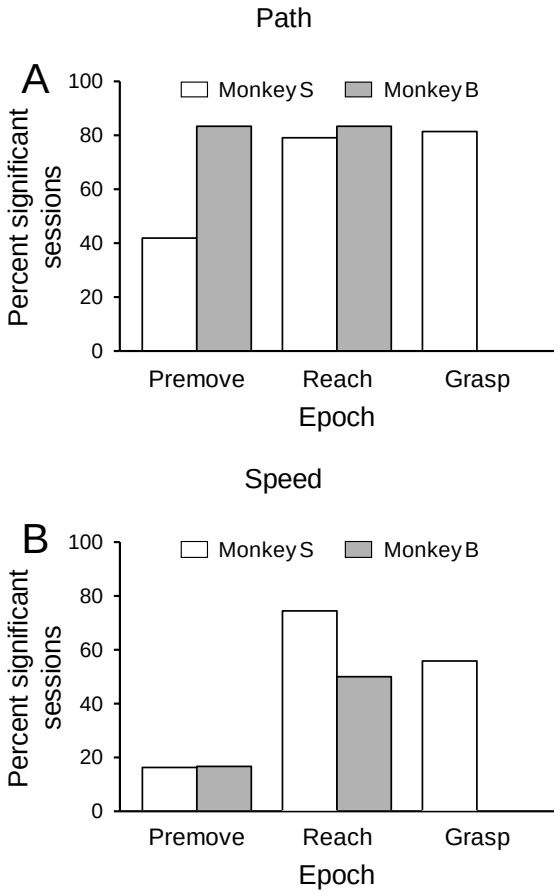

Figure 3.9. Wrist path and speed as a function of objects. Percentage of sessions displaying significant differences across objects in A) wrist path and B) wrist speed for *premove, reach*, and *grasp epochs*.

The kinematic parameter (e.g. grasp aperture) examined with the previous object set (see Figure 2.2) was significantly different across objects for all sessions (Mason et al., 2004; Theverapperuma et al., 2005; Mason et al., 2006). While joint angles varied as a function of objects in most epochs, it was expected that joint angles would be significantly different across objects for all sessions using the new object set. Therefore, the normalized Mahalanobis Distances (MDs) were calculated for each trial within a

session by dividing each value by the maximum for the session to examine for differences from mean hand shape as both a function of object and trials. The MD for each trial during the *grasp epoch* grouped by object is shown in Figure 3.10. For some objects (e.g. 7 and 9), there was considerable variability in the MDs across trials, implying the monkey grasped the object differently over the course of a single session. To examine the variability in hand shape within an object, the range of MDs was calculated by subtracting the minimum MD from the maximum MD for each object within a session, and the range in MDs for each object were averaged across sessions. Several objects had large average ranges in MD across sessions, confirming the variability in the population data (Figure 3.11). One explanation for the greater variability in objects 6-9 and 11-13 is that the shapes were complex and this increased difficulty of grasping. Therefore, average kinematics across objects does not capture the variability present within a session. This provides further support for basing the analyses on single-trial data.

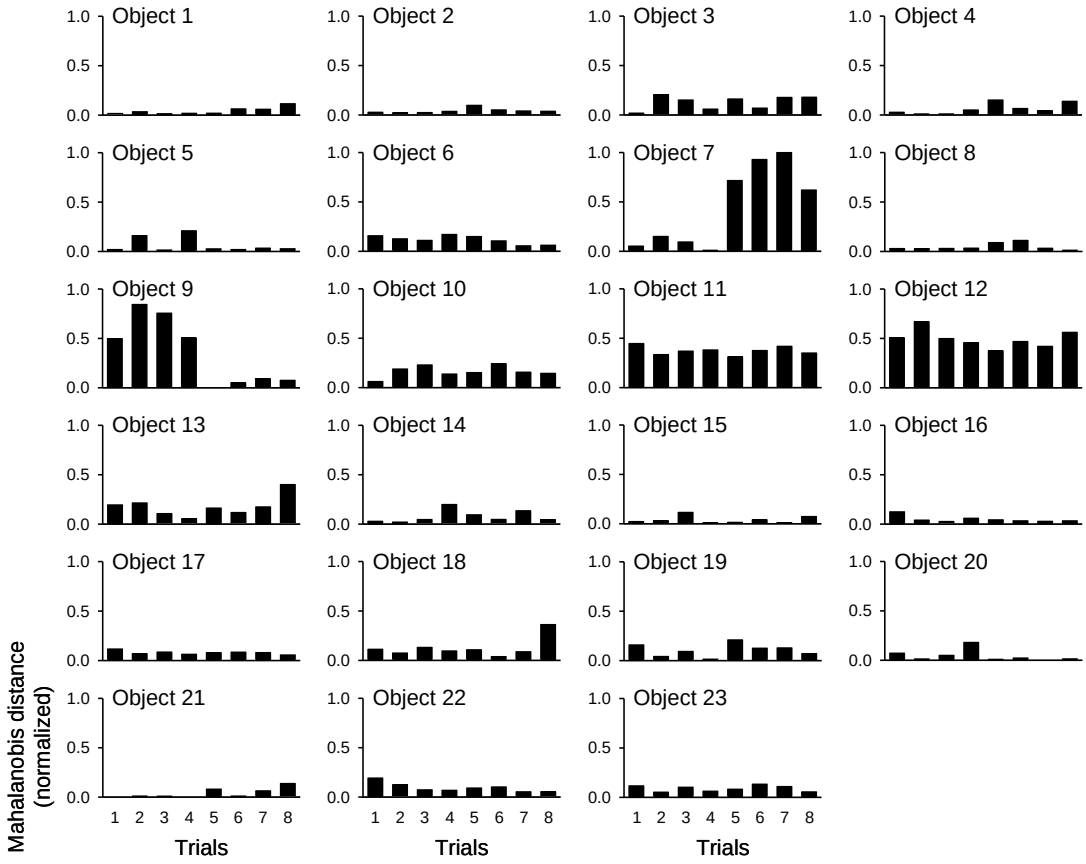

Figure 3.10. Mahalanobis distance as a function of object. Normalized MDs (y-axis) for each trial (x-axis) for a representative session during the *grasp epoch*. MDs are grouped by object (individual plots).

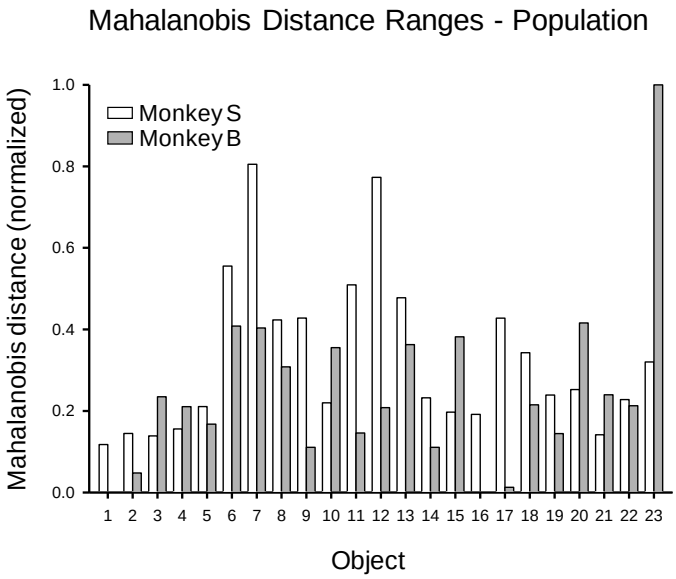

Figure 3.11. Mahalanobis distance population range within an object. Average of the range (maximum-minimum) of normalized MDs (y-axis) for all sessions during the *grasp epoch* for each object (x-axis). Gray is Monkey S and white is Monkey B.

A high degree of correlation among the joint angles has been observed in human grasping (Schieber, 1991; Soechting and Flanders, 1997). This is important not only from the perspective of whether joints are controlled individually or together but also from the perspective of analyzing how motor cortical firing modulates in relation to the joint angles. Therefore, the correlation coefficient for each possible pair of joint angles, and similarly joint angular velocities, was calculated for each epoch and averaged across sessions (Figure 3.12). For the joint angles (Figure 3.12), the MCP2-5 and IP2-5 joint angles were strongly and positively correlated ($r > 0.5$), as observed in human grasp. The THMCP angle was less strongly correlated (0.3 to 0.5) with the MCPs and IPs and had the lowest correlation with MCP2, indicative of independent control of the thumb relative to the long fingers (Schieber, 1991; Soechting and Flanders, 1997). The ABD1-3 angles

were negatively and only weakly coupled to the other joints, and ABD4 had the lowest (0 to 0.3) correlations with all joint angles, displaying the independence often found in the little finger (Ansuini et al., 2006). The WFLEX angle was highly and positively correlated to the MCP and IP joint angles. The joint angular velocities displayed similar correlations (Figure 3.12). However, joint angles and joint angular velocities had little correlation ($-0.25 < r < 0.28$). In addition, wrist path and speed displayed high correlations, both negative and positive, with most joint angles and angular velocities (Figure 3.12).

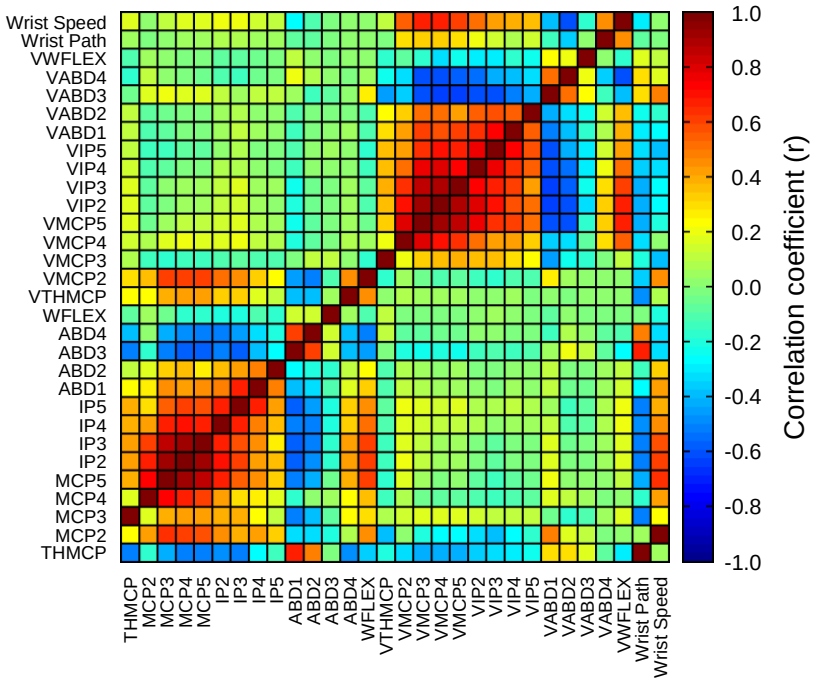

Figure 3.12. Measure of colinearity. Average correlation coefficients between all possible pairs of joint angles and joint angular velocities for all sessions.

One of the goals of developing and using the present set of objects (see Figure 2.3) was to generate a greater range of joint angles and hand shapes than the set of objects

used previously in the Ebner laboratory (see Figure 2.2) (Mason et al., 2001; Mason et al., 2004; Theverapperuma et al., 2005; Hendrix et al., 2009). Figure 3.13 displays the ranges created in the MCP2-5, IP2-5, and ABD1-4 joint angles for the old and new object sets. The new object set resulted in a larger range in the joint angles for the majority of joints, with the exception of MCP2, MCP3, and ABD1. This reflects that the previous object set was designed to vary grasp aperture, which is highly dependent on the MCP2 and ABD1 joints. Because grasp aperture was the focus of the studies using the old object set (Mason et al., 2001; Hendrix et al., 2009), grasp aperture was not explored in this thesis.

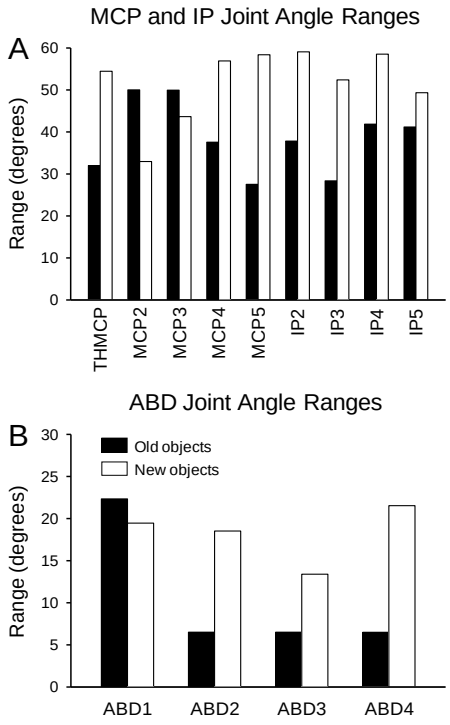

Figure 3.13. Range of angles created during grasp at each joint for new and old object sets. Range (maximum-minimum) of A) THMCP, MCP2-5, and IP2-5 and B) ABD1-4 was usually larger for the new object set compared to the old object set. Data was taken from a representative session for each set.

3.1.2 Discussion of individual elements

During reaching and grasping tasks, humans and non-human primates pre-shape the hand to match properties of the object to be grasped (Jeannerod, 1984; Wing et al., 1986; Paulignan et al., 1991a; Castiello et al., 1993; Santello and Soechting, 1998; Castiello et al., 1998; Roy et al., 2002; Mason et al., 2004). Earlier studies have also established that preshaping begins approximately midway through reach, if not earlier (Santello and Soechting, 1998; Mason et al., 2004). As shown in Figure 3.1, the joint angles are generally the same across trials for the *premove epoch* and first part of the *reach epoch* and begin to diverge towards the end of the *reach epoch.* Large differences in the joint angles are evident during the *grasp epoch*. This evolution in joint angles across epochs is explained by preshaping of the hand involved in grasping of a highly varied set of objects. This is supported by the finding that joint angles are significantly different across objects most often during the *grasp epoch* (Figure 3.7). The IP5 and ABD4 joint angles displayed a much less consistent progression with time, suggesting less involvement with preshaping of the hand for grasp. These observations are generally consistent across sessions and monkeys (Figures 3.2 and 3.3).

Joint angular velocities of the hand have been much less studied. Most joints (THMCP, MCP2-5, IP2-5, WFLEX) followed a typical pattern of a rapid increase in angular velocity followed by a long decrease in velocity through peak aperture (Figure 3.4). This is consistent with a strategy of quickly opening of the hand to maximum aperture and then slowing before contact and producing the final hand shapes (Vinjamuri et al., 2007; Vinjamuri et al., 2009). Similar to the joint angle progressions, the IP5 and ABD4 joint angular velocities displayed a much less consistent pattern in time.

Furthermore, there were fewer instances of significant differences in joint angular velocities across objects than for the joint angles, especially during the *premove* and *grasp* epochs (Figure 3.7). Joint angular velocities and wrist speed increase in variability during the *reach epoch* when the majority of movement occurs (Cole and Abbs, 1986; Vinjamuri et al., 2007). Inconsistency was observed for the velocities of some joints both within and across monkeys, suggesting that the monkeys did not use a consistent strategy to control joint speed from day to day (Figure 3.6).

Neural firing in the hand areas of the premotor and primary motor cortices is related to object grasped (Murata et al., 1997; Mason et al., 2002; Umilta et al., 2007; Hendrix et al., 2009) and orientation of the object (Mason et al., 2002). Object type and orientation are extrinsic properties, related to variables outside the body and are not directly related to the biomechanics of the hand or arm, which are intrinsic properties. The Mahalanobis Distance (MD) from the mean hand shape during grasp provides insight into the relationship between extrinsic and intrinsic properties. The MD for several objects consistently differs from the mean and can vary across trials (Figure 3.10). This variability is also evident across sessions (Figure 3.11). Therefore, in contrast to the relatively invariant extrinsic properties such as object shape, intrinsic properties may vary greatly. These findings have implications for the analyses of this data. Because of the large variability in hand shaping within object blocks, all analyses of the behavior and neural firing was performed on single-trial data rather than averaging within object blocks.

As shown previously in humans (Santello and Soechting, 1998; Mason et al., 2001; Santello et al., 2002; Braido and Zhang, 2004; Thakur et al., 2008), during reach-to-grasp there is a high level of colinearity between joint angles. This is due to biomechanical constraints within the hand, neuroanatomy, as well as the nature of the task. Similarly, in this study the MCP and IP joint angles are highly positively correlated with each other, as well as with wrist extension (Figure 3.12). These joint angles change synchronously in time as the hand first opens and then closes around the object (Theverapperuma et al., 2005). The other joint angles (ABDs) are relatively independent or negatively correlated. The independence of the ABD joint angles with respect to the MCP and IP joint angles indicates that there may be a separate functional group of cells or circuits dedicated to the control of these sets of joints. Similar results were observed for correlations between joint angular velocities (Figure 3.12). However, the lack of correlation between joint angles and joint angular velocities (Figure 3.12) suggests that these parameters are controlled relatively independently through different mechanisms in the CNS. The examination of motor cortical firing in relation to kinematic parameters could reveal groups of cells that coincide with these functional groups. Previous studies of how motor cortical firing is related to joints and velocities of the arm has resulted in conflicting conclusions (Moran and Schwartz, 1999; Reina et al., 2001; Paninski et al., 2004; Wang et al., 2007; Stark et al., 2007a). The high degree of correlation between many of the joint angles, however, is a challenge for analyses of neural firing in relation to individual joint movements. One potential solution is to use a principal component analysis as described in the next section.

3.2 Singular value decomposition analyses

Singular value decomposition (SVD) was performed using the unadjusted joint angles, standardized joint angles, joint angular velocities, and standardized joint angular velocities (see Table 2.2). The unadjusted and standardized data sets were analyzed separately to examine the differences in eigenvectors obtained for each data set. SVD was also completed on the combination of standardized joint angles and standardized joint angular velocities. Standardized data was required for the combined analysis due to the differing units (i.e. mm and mm/sec), and therefore, different variances between joint angles and joint angular velocities (Jolliffe, 2002; Jackson, 2003).

In SVD, the data matrix is decomposed into three matrices. The first matrix contains the eigenvectors that describe orthogonal patterns in the various joint variables. Each individual component of an eigenvector is weighted by a coefficient (Equation 3.1).

$$\begin{aligned} EV = {} & \beta_{THCMP}THMCP + \beta_{MCP2}MCP2 + \beta_{MCP3}MCP3 + \beta_{MCP4}MCP4 + \beta_{MCP5}MCP5 \\ & + \beta_{IP2}IP2 + \beta_{IP3}IP3 + \beta_{IP4}IP4 + \beta_{IP5}IP5 \\ & + \beta_{ABD1}ABD1 + \beta_{ABD2}ABD2 + \beta_{ABD3}ABD3 + \beta_{ABD4}ABD4 + \beta_{WFLEX}WFLEX \end{aligned}$$

Equation 3.1

For example, Figure 3.14A contains the coefficients (βs) for each element for eigenvector 1 (EV1) resulting from SVD with unadjusted joint angles for the model session. These eigenvectors are described in further detail for each SVD in the following sections. The second matrix resulting from SVD contains the eigenvalues. Eigenvalues are the amount of variance the eigenvector shares with all elements in the analysis (Kline, 2005). The eigenvalue associated with the example eigenvector in Figure 3.14A is

displayed in the upper right corner (e.g. 87% for EV1). Finally, the third matrix has the scaling describing the involvement of each eigenvector in hand shaping through time for each trial within the session (Figure 3.14B). The temporal weightings (TWs) for each eigenvector and each analysis method are described further in the chapter, and are also used in the regression analysis of the neural firing.

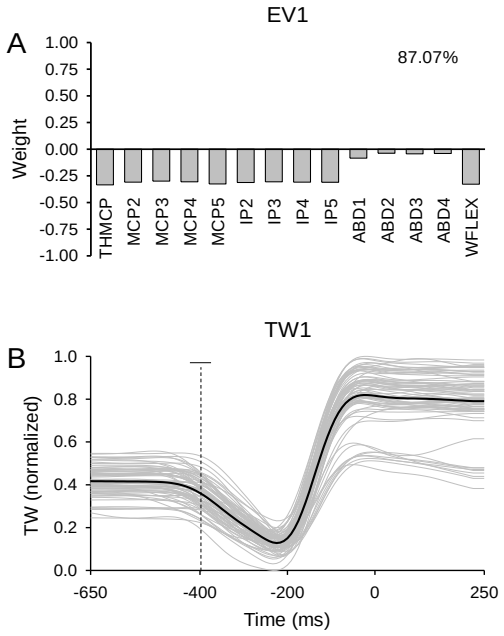

Figure 3.14. SVD example results. A) Weightings of individual joint angles for the first eigenvector (EV1) resulting from SVD analysis. Number in upper right is the eigenvalue. B) Temporal weight (TW1) (normalized) of the first eigenvector for each trial in the model session.

It was important to examine the consistency of the eigenvectors across sessions to compare the hand shaping strategies utilized. When eigenvectors were simply averaged across sessions, many eigenvectors displayed similarities across sessions, but others displayed large variability (described in detail later in the chapter). This was often due to slight changes in the order of eigenvectors having similar eigenvalues. For example, as

displayed in Figure 3.15, EV8 of sessions 7, 8, 18, and 26 had a similar composition as EV9 for sessions 3, 12, 23, and 28, with heavy weightings for IP2 and ABD1. The mean eigenvalue for the examples for EV8 was 3.72% +/- 0.11% and the mean eigenvalue for EV9 was 3.6% +/-0.51%. These eigenvectors were highly correlated, despite having different orders across sessions (r = 0.78 +/- 0.02). Therefore, the correlation coefficient between the eigenvectors from the model session (model eigenvectors) and each eigenvector from all other sessions was used to provide an order invariant analysis of the consistency of these patterns across sessions (Ingram et al., 2008; Thakur et al., 2008). Session eigenvectors with a correlation coefficient greater than 0.5 compared to the model eigenvectors were considered to be displaying "similar" patterns (Ingram et al., 2008). However, not all sessions had eigenvectors similar to all model eigenvectors.

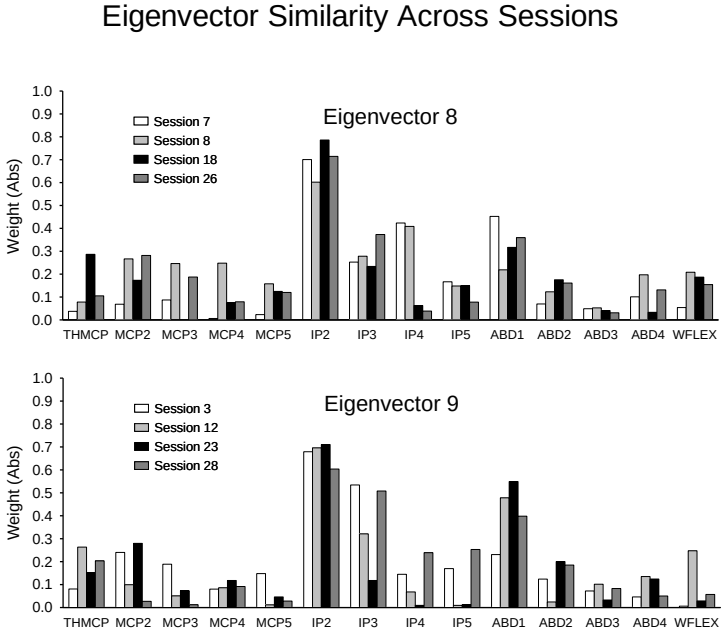

Figure 3.15. Eigenvector similarity across sessions. Eigenvector 8 (top) for certain sessions had similar weightings for the joint elements (x-axis) as Eigenvector 9 (bottom) for other sessions.

3.2.1 Pattern identification and dimensionality

3.2.1.1 Joint angles

For SVD performed on joint angles, the first three eigenvectors (EVs) explained more than 90% of the variability (91% +/- 2%) in hand shaping for most (84%) sessions (Figure 3.16A). In contrast, 10 (+/-1) EVs were needed to reach the same amount of variance for the standardized data (Figure 3.16B). This shows that the average joint angles captured by EV1 in the unadjusted SVD represent a large fraction of the variability.

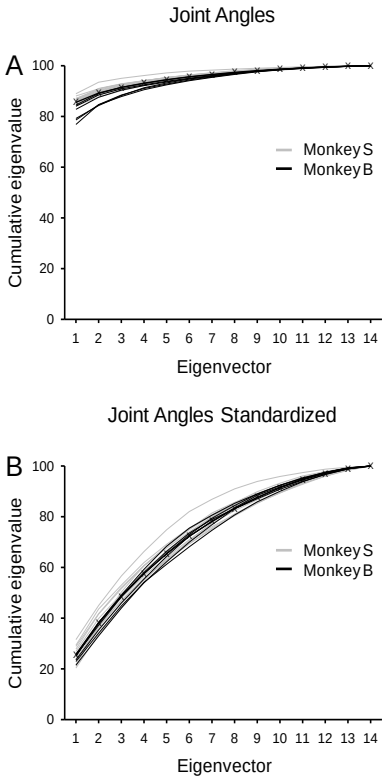

Figure 3.16. Cumulative eigenvalues for all sessions for joint angle SVDs. Cumulative eigenvalues for each session and the average for all sessions for SVD performed using A) joint angles and B) standardized joint angles. Gray lines represent Monkey S sessions, black lines are Monkey B sessions, and the average across sessions is represented with a (+).

The coefficients for the joint angles in each EV for the model session for both unadjusted joint angle and standardized joint angle SVDs are shown in Figure 3.17. The first EV of the unadjusted joint angle SVD (Figure 3.17A) was predominantly weighted for the MCP and IP joints as well as the WFLEX. While all weightings were negative for this eigenvector, the sign of the weighting does not carry significance. Rather, a positive or negative coefficient simply describes the relationship between coefficients within an eigenvector. EV1 represents the average hand shape and describes the overall opening and closing of the hand through extension/flexion of the joints. The first EV explained 87% of the variability in hand shapes. The second EV accounted for a dramatically smaller percent of the variance (4%), and is negatively weighted toward MCP3-5 in synchrony with an increase of IP3-5, as well as an increase in angle between the thumb and forefinger (ABD1) (Figure 3.17A). EV2 captures closing of the hand through the MCPs while the IPs open. Explaining 2% of the variance, EV3 is heavily negatively weighted toward THMCP (Figure 3.17A), and is consistent with the independence of the thumb during reaching and grasping (Schieber, 1991; Soechting and Flanders, 1997). The remaining twelve EVs described other unique details of the shaping of the hand, and accounted for only a total of 7% of the variance. A fundamental question, however, is which of these higher EVs have functional significance and whether there are any neural correlates or representation.

EV1 based on the standardized data for the model session had similar absolute weightings for most joint angles, with IP4-5 and ABD 3 weighted to a slightly lesser extent (Figure 3.17B). This EV, which explained 29% of the variance, described the

opening and closing of the hand through a coordinated increase of the MCP and IP angles, ABD3-4, and WFLEX. EV1 also included a decrease in ABD1 and ABD2. This EV was similar to EV1 obtained with unadjusted data, with the addition of weightings for ABD1-2 (negative) and ABD3-4 (positive). This EV represents the predominant pattern in the joint angles after the mean hand shape has been removed. Standardizing the data equalizes the variability in the elements and results in nearly equal weights for all elements in EV1. EV2 explained 13% of the variance and was weighted toward an increase of the IP joints and a decrease in ABD3 (Figure 3.17B). EV3 accounted for 10% of variance and captured an increase of MCP2 and ABD2, representing the pattern of individuation often observed with the forefinger (Schieber, 1991; Soechting and Flanders, 1997). The fourth EV was highly weighted for the decrease in ABD1-4 and had an eigenvalue (9%) close to that of EV3. The remaining EVs described additional details of hand shaping. Except for EV1 and EV2, there are few similarities between eigenvectors obtained from the unadjusted joint angles versus standardized joint angles. This implies that, while both methods represent the data correctly, the interpretations of the eigenvectors and their relationship to the neural data will be different.

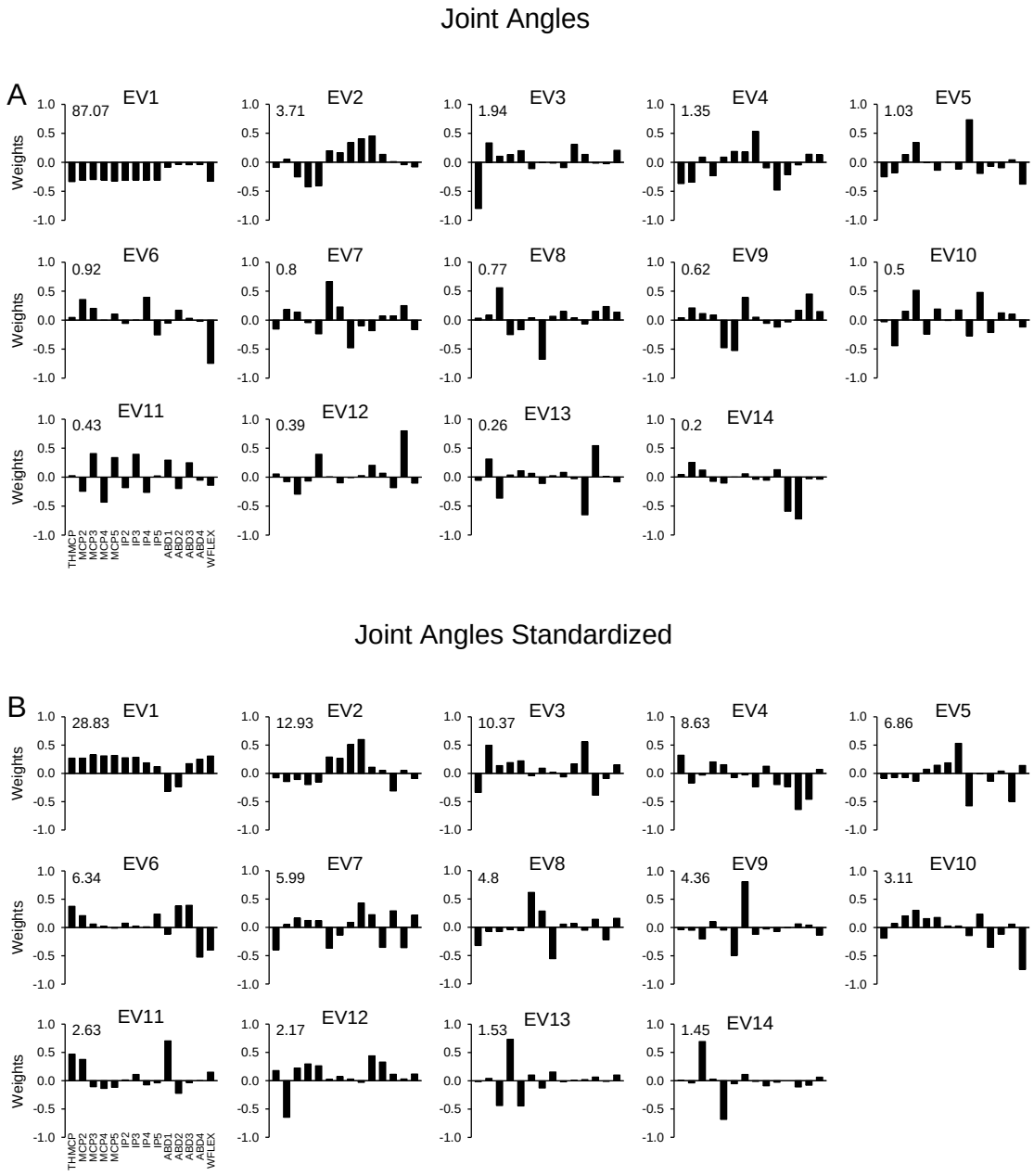

Figure 3.17. Coefficients for eigenvectors for joint angle SVDs for one session. Bar graphs of the of the eigenvector coefficients for the model session for SVD performed using A) joint angles and B) standardized joint angles. Numbers in the upper left are variance explained.

EV1 based on both methods had small standard deviation across sessions (error bar), displaying a consistency in coefficient patterning, while higher-order TWs generally have larger variability (Figure 3.18). On average, the eigenvectors for unadjusted joint angles were similar to the model eigenvectors ($r > 0.5$) in over 60% of sessions (60.9% +/- 18.6% for Monkey S and 83.3% +/- 18.5% for Monkey B, Figure 3.19), emphasizing the consistency in structure of the EVs. EV1 was present in all sessions for both monkeys. For SVD with standardized joint angles, the model eigenvectors were not as consistent across sessions, averaging 63.0% +/- 13.4% for Monkey S and 63.1% +/- 27.9% for Monkey B. EV1 was similar in only 51.2% of sessions for Monkey S and 66.7% of sessions for Monkey B. However, even EVs that display consistency in as low as 50% of sessions suggest a remarkable reproducibility in hand shaping patterns. Overall, there was a high degree of consistency in joint angle EVs across experimental sessions.

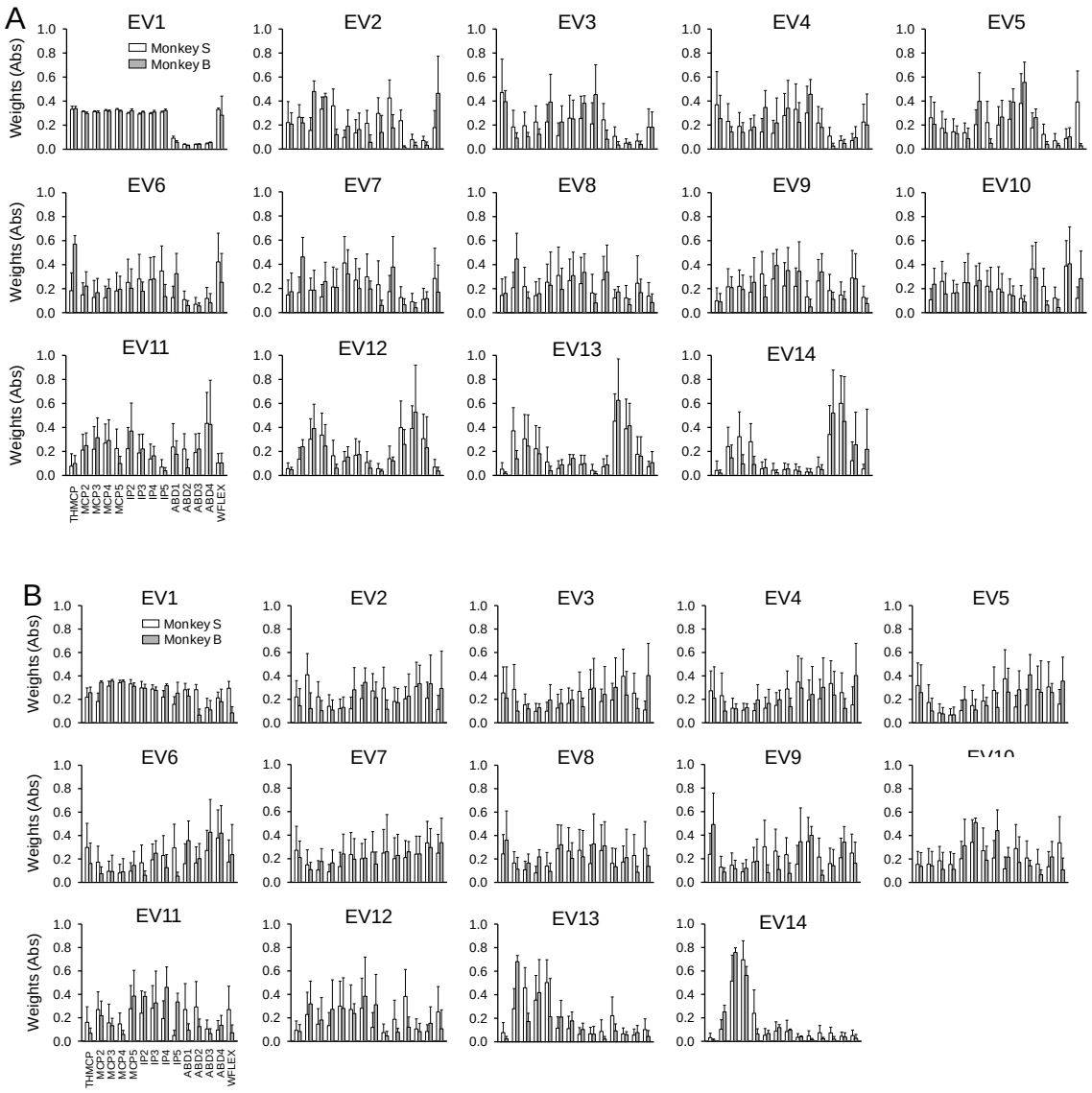

Figure 3.18. Coefficients for eigenvectors for joint angle SVDs for all sessions. Mean across sessions of each eigenvectors' coefficients (absolute value) for individual elements (x-axis) for SVD performed using A) joint angles and B) standardized joint angles for each monkey.

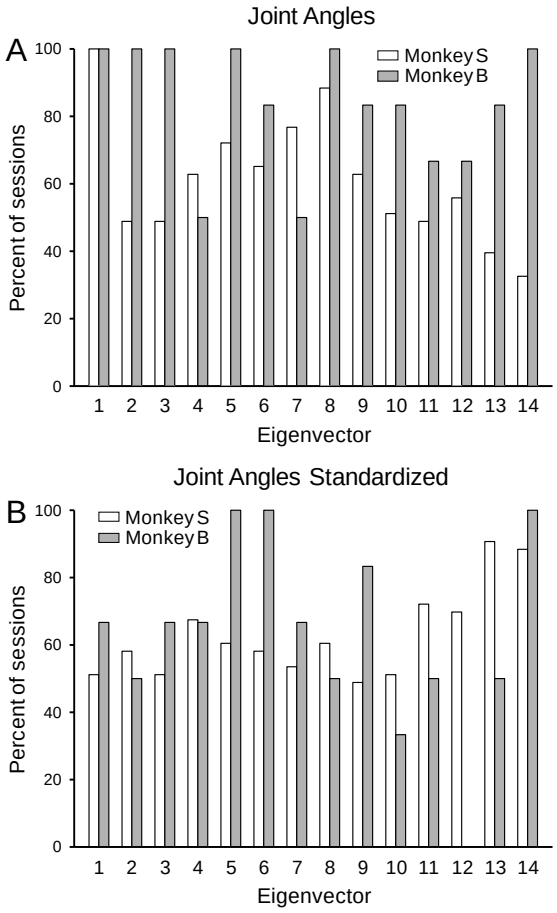

Figure 3.19. Percent of sessions displaying each eigenvector for joint angle SVDs. Correlation coefficients compared a model eigenvector for SVD performed using A) joint angles and B) standardized joint angles with the eigenvectors of each session.

The temporal weightings (TWs) are also of interest as these describe the progression of the eigenvector in time (Figure 3.20). The first TW based on the unadjusted data (Figure 3.20A) was essentially the inverse of the temporal progressions of the MCP and IP joint angles (Figure 3.1). The inverse reflects that the coefficients of the eigenvector have negative values (Figure 3.17). However, as for the joint angles, this negativity has no significance. TW2 had a similar temporal progression as TW1 due to the high degree of colinearity between the unadjusted joint angles (see Section 3.2.2). The third TW decreased for a short duration, increased throughout the first half of the *reach epoch*, and diverged (either increased or decreased for different trials) for the remainder of the epoch. For the standardized joint angles, the first TW had a temporal pattern closely related to that of the majority of the joint angles, increasing with time after movement onset until peak aperture, and decreasing until grasp onset (Figure 3.20B), consistent with the positive weightings of the eigenvectors for most joint angles (Figure 3.17B). TW2 was largely variable across trials. The third TW increased or decreased for different trials at the end of the *reach epoch*. The remaining TWs from both unadjusted joint angle and standardized joint angle data had various temporal patterns and varied greatly across trials.

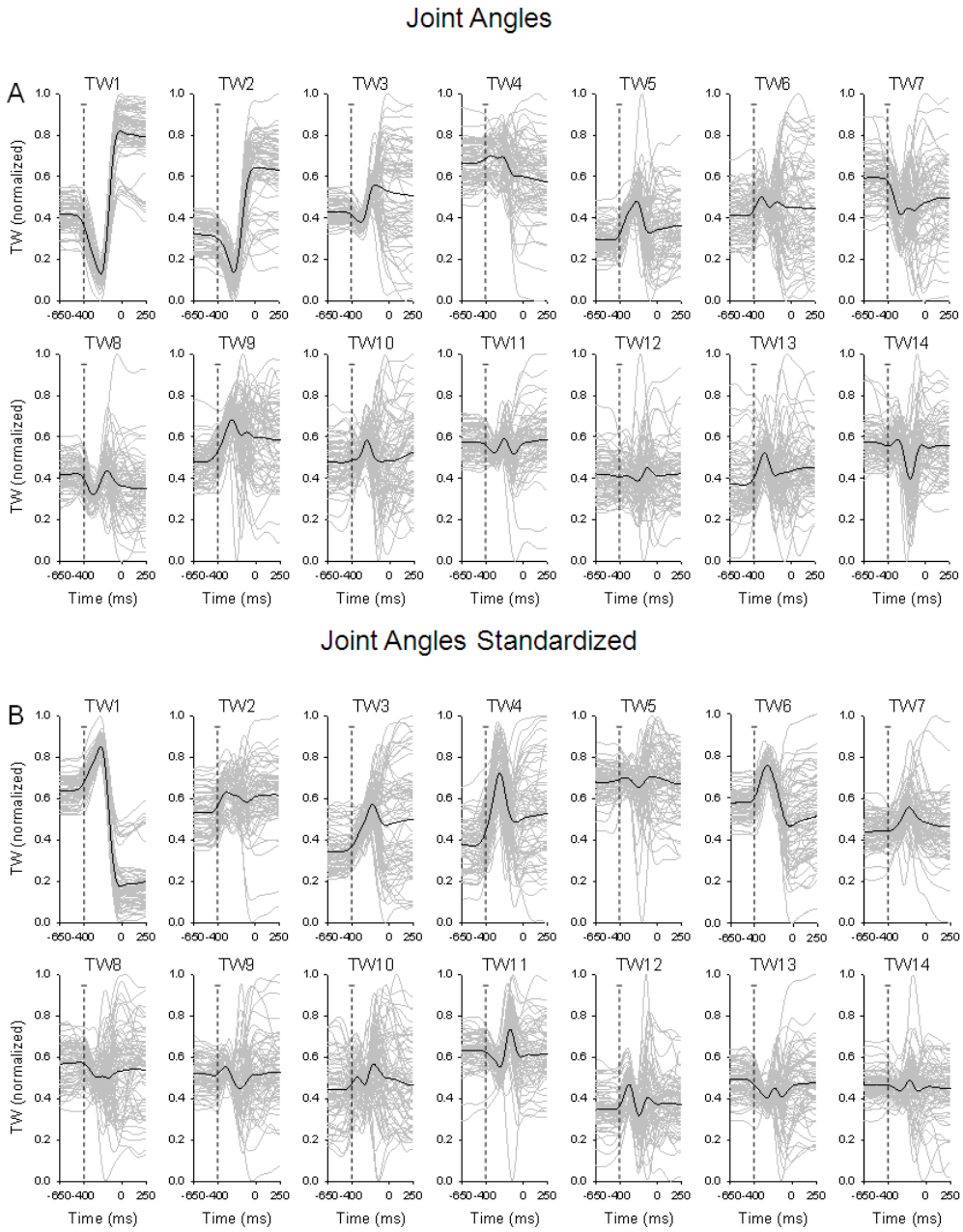

Figure 3.20. Temporal weighting vectors for joint angle SVDs in time for a model session. Plots of normalized temporal weighting vectors (y-axis) with time (x-axis) for each eigenvector (individual plot) across all trials in one session for SVD performed using A) joint angles and B) standardized joint angles. Plots are aligned on grasp onset (time = 0 ms). Each gray line is a single trial. Black line is the average across trials.

3.2.1.2 Joint angular velocities

On average, 10 (+/- 1) eigenvectors were required to account for 90% of the variance in the joint angular velocities, with both unadjusted and standardized data (Figure 3.21). The first EV explained only 34% +/-5% for joint angular velocities and 26% +/- 3% for standardized joint angular velocities. For most sessions (93% for unadjusted data and 74% for standardized data) the eigenvalues were greater than 1% for all eigenvectors. Therefore, the variability in joint angular velocities was greater and less consistent than that for the joint angles.

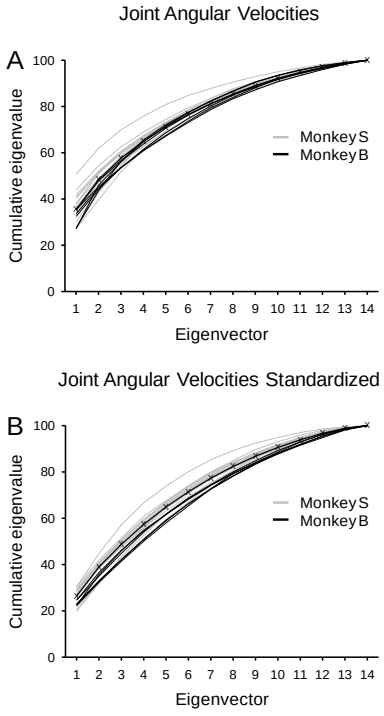

Figure 3.21. Cumulative eigenvalues for all sessions for joint angular velocity SVDs. Cumulative eigenvalues for each session and the average for all sessions for SVD performed using A) joint angular velocities and B) standardized joint angular velocities. Gray lines represent Monkey S sessions, black lines are Monkey B sessions, and the average across sessions is represented with a (+).

For the model session, EV1 accounted for 40% of the variability in the joint angular velocities and had a positive weighting for THMCP, MCP2-5, IP2-5, and WFLEX joint angular velocities, with the larger weightings on MCP3-5 (Figure 3.22A). In addition, EV1 included a negative weighting for the angular velocity of ABD1. This eigenvector, therefore, captures a pattern where THMCP, MCP2-5, and IP2-5 have opposite speeds than ABD1. Explaining 11% of the variance, EV2 was dominated by a decrease in the angular velocities of THMCP and the IPs and increases in MCPs. EV3 also had a large negative weighting for the THMCP and positive weightings for the IP joint angular velocities. The remaining EVs were weighted for various combinations of increases and decreases in joint angular velocities.

The first EV based on standardized joint angular velocities had negative weightings that were similar in magnitude for THMCP, MCP2-5, IP2-5, ABD4, and WFLEX. EV1 also had a positive weighting for the angular velocities of ABD1-2 and had an eigenvalue of 29%. EV2 was dominated by an increase in the joint angular velocity of ABD3, but also contained positive weightings for the angular velocity of MCP2-5 and negative weightings for the velocities of the IP2-5 joints. This EV explained 11% of the variance. EV3 was mainly positively weighted for ABD4 and negatively for THMCP joint angular velocities.

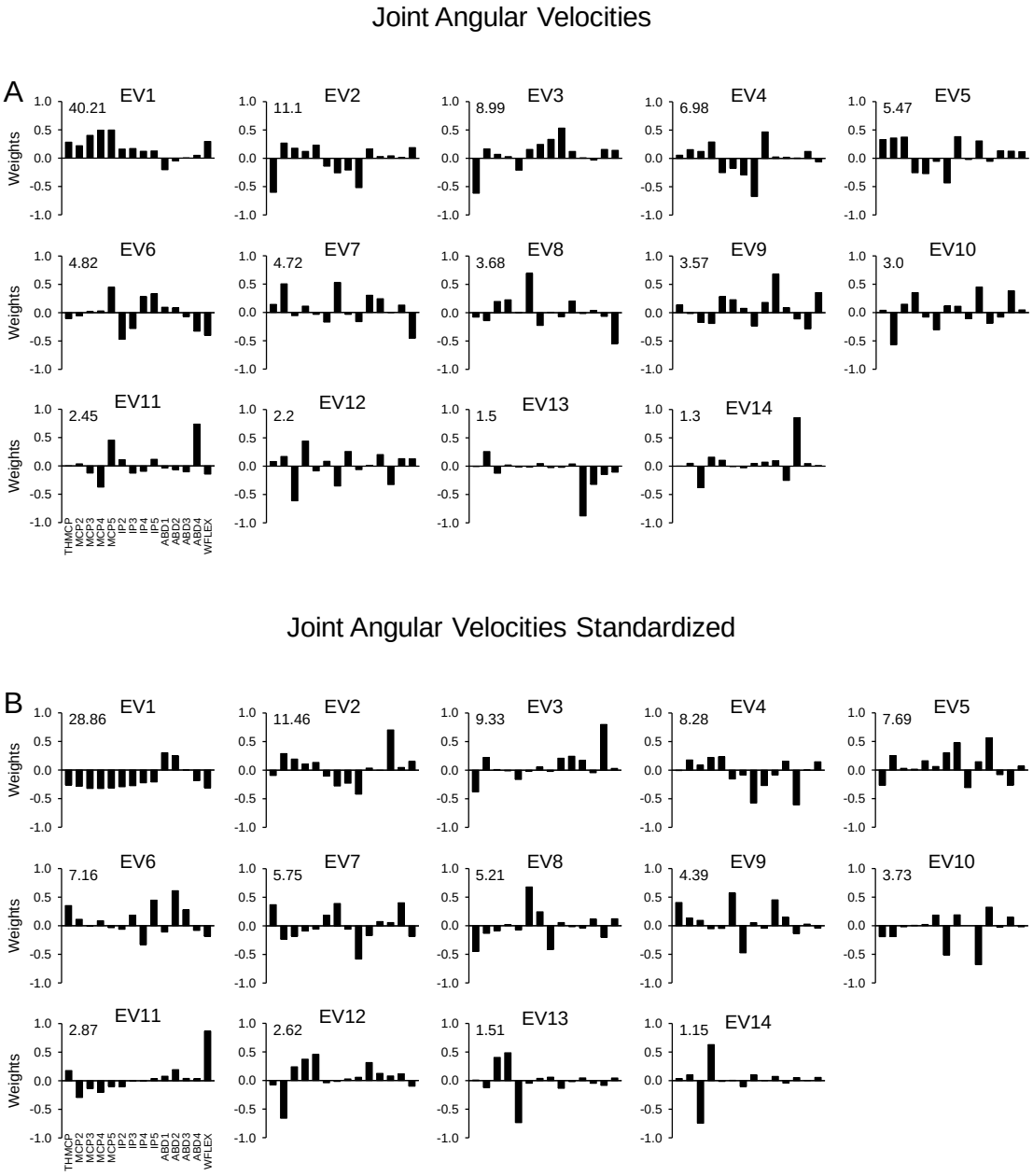

Figure 3.22. Coefficients for eigenvectors for joint angular velocity SVDs for one session. Bar graphs of the eigenvectors' coefficients for the model session for SVD performed using A) joint angular velocities and B) standardized joint angular velocities. Numbers in the upper left are variance explained.

EV1 obtained from both unadjusted and standardized joint angular velocities had small deviations (error bar) across sessions (Figure 3.23). Higher-order EVs, however, exhibited larger variability across sessions. Order invariant analysis revealed that the eigenvectors obtained for the model session were, on average, present ($r > 0.5$) in more than 67% of all sessions for unadjusted joint angular velocities (67.1% +/- 19.6% for Monkey S and 70.2% +/-25.5% for Monkey B). As for joint angles (Figure 3.19), the eigenvectors for standardized joint angular velocities were less consistent across sessions, with the model eigenvectors present in 63.0% +/-16.3% of sessions for Monkey S and 60.7% +/-22.3% for Monkey B (Figure 3.24). The eigenvectors of the joint angular velocities were more variable than those based on joint angles, but were nonetheless largely consistent across sessions.

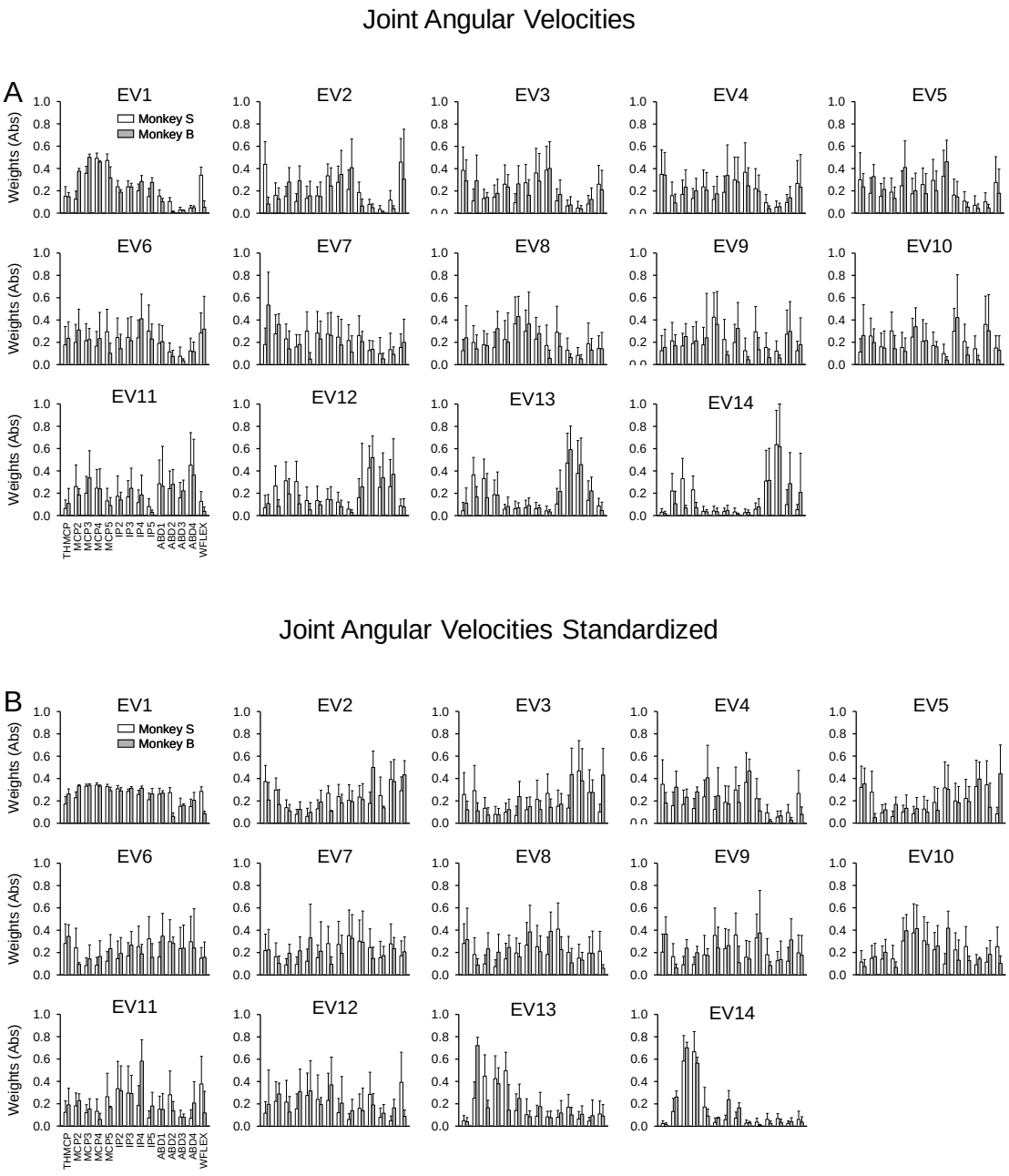

Figure 3.23. Coefficients for eigenvectors for joint angular velocity SVDs for all sessions. Mean across sessions of each eigenvectors' coefficients (absolute value) for individual elements (x-axis) for SVD performed using A) joint angular velocities and B) standardized joint angular velocities for each monkey.

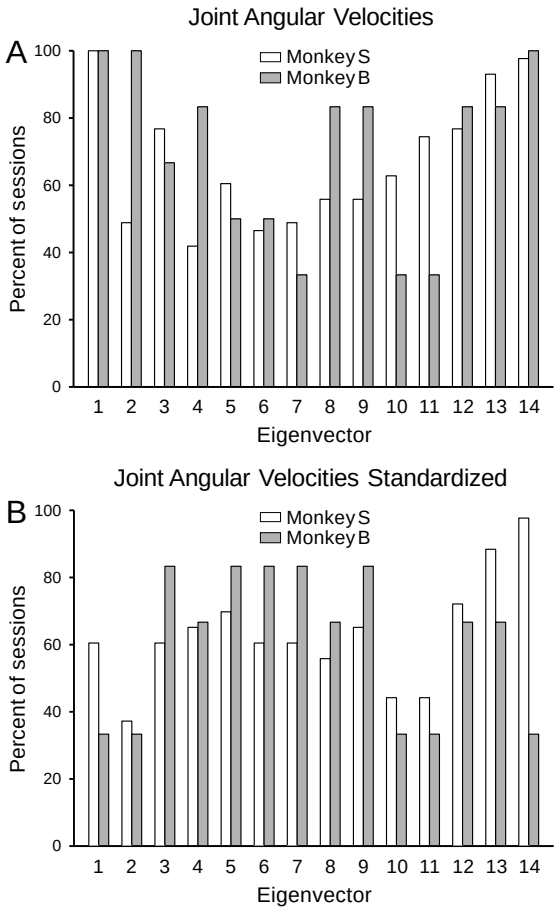

Figure 3.24. Percent of sessions displaying each eigenvector for joint angular velocity SVDs. Correlation coefficients compared a model eigenvector for SVD performed using A) joint angular velocities and B) standardized joint angular velocities with the eigenvectors of each session.

The first TW of the SVD using joint angular velocities increased initially after movement onset, decreased quickly through reach, and increased just before grasp was initiated (Figure 3.25A). This progression is similar to the individual joint angular velocities and reflects that EV1 was positively weighted for most joint angular velocities. The first TW based on the standardized data had the opposite progression resulting from negative weightings for the majority of joint angular velocities. Similar to the TWs for the joint angle data, TW1 for unadjusted and standardized joint angular velocities were tightly grouped across trials. The remainder of the TWs displayed temporal patterns that were more varied across trials.

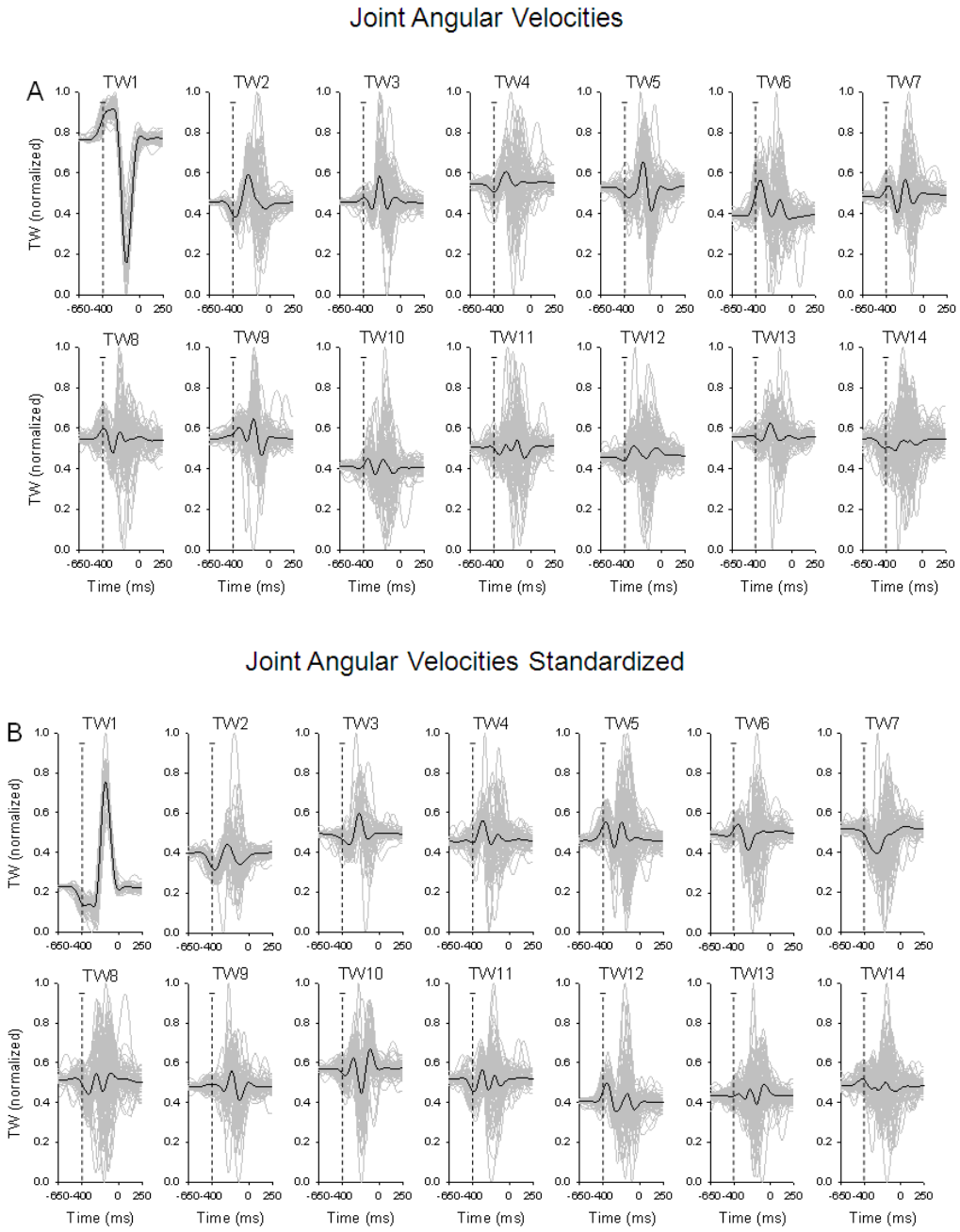

Figure 3.25. Temporal weighting vectors for joint angular velocity SVDs in time for one session. Plots of normalized temporal weighting vectors (y-axis) with time (x-axis) for each eigenvector (individual plot) across all trials in one session for SVD performed using A) joint angular velocities and B) standardized joint angular velocities. Plots are aligned on grasp onset (time = 0 ms). Each gray line is a single trial. Black line is the average across trials.

3.2.1.3 Joint angles and joint angular velocities combined

Because of differing units, a combined SVD analysis of combined joint angles and joint angular velocities required using standardized data. The majority of sessions (72%) achieved a cumulative eigenvalue of 90% with 20 eigenvectors (Figure 3.26). This is similar to results from standardized joint angles, unadjusted joint angular velocities, and standardized joint angular velocities, where 90% of the variance was accomplished with 71.4% (10/14) of the eigenvectors. The first eigenvector accounted for only 14% +/- 2% of the variance. Combining joint angles and angular velocities increases the variability in the data set, naturally decreasing the eigenvalue for EV1.

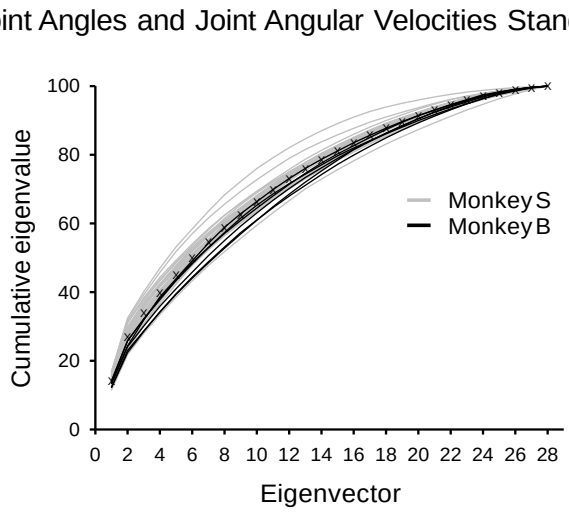

Figure 3.26. Cumulative eigenvalues for all sessions. Cumulative eigenvalues for each session and the average for all sessions for SVD performed with standardized joint angles and joint angular velocities. Gray lines represent Monkey S sessions, black lines are Monkey B sessions, and the average across sessions is represented with a (+).

The first and second EVs for the model session had eigenvalues of 15% and 14%, respectively, and were similar in composition (Figure 3.27). EV1 had similar absolute

weights for all joint angles and angular velocities, with the majority of the weights positive and negative weights for ABD1-2 joint angles and ABD1-3 joint angular velocities. EV1 is comparable to the combination of EV1 from standardized joint angles (Figure 3.17) and the inverse of EV1 from standardized joint angular velocities (Figure 3.22). EV2 was similar to EV1 except the weightings for joint angles were inversed, capturing a different relationship between the angles and angular velocities in hand shaping. In contrast, the third eigenvector had almost no influence from joint angular velocities, and was dominated by the IP joint angles, much like EV3 from standardized joint angles. Several eigenvectors were dominated by either joint angles or joint angular velocities (EV3-4, EV9-12, EV19, and EV22-29). Others displayed high weightings for the same joint in both the angles and angular velocities (e.g. EV6-8, EV14-15). However, these observations are only describing a portion of the weightings in these higher-order EVs. Overall, EV4-28 did not present obvious general patterns.

EV1 and EV2 were highly consistent across sessions, as illustrated by the small standard deviations in Figure 3.28. The composition and order of the remaining eigenvectors were more variable than the lower-orders EVs across sessions. Examination of the correlation coefficient between the model eigenvectors and all eigenvectors of all other sessions revealed that the model eigenvectors were present in 55.1% +/- 18.6% of sessions for Monkey S and 58.9% +/- 23.3% of sessions for Monkey B (Figure 3.29). The eigenvectors based on the combined analysis of joint angles and joint angular velocities were less consistent across sessions than the analysis for the elements separately.

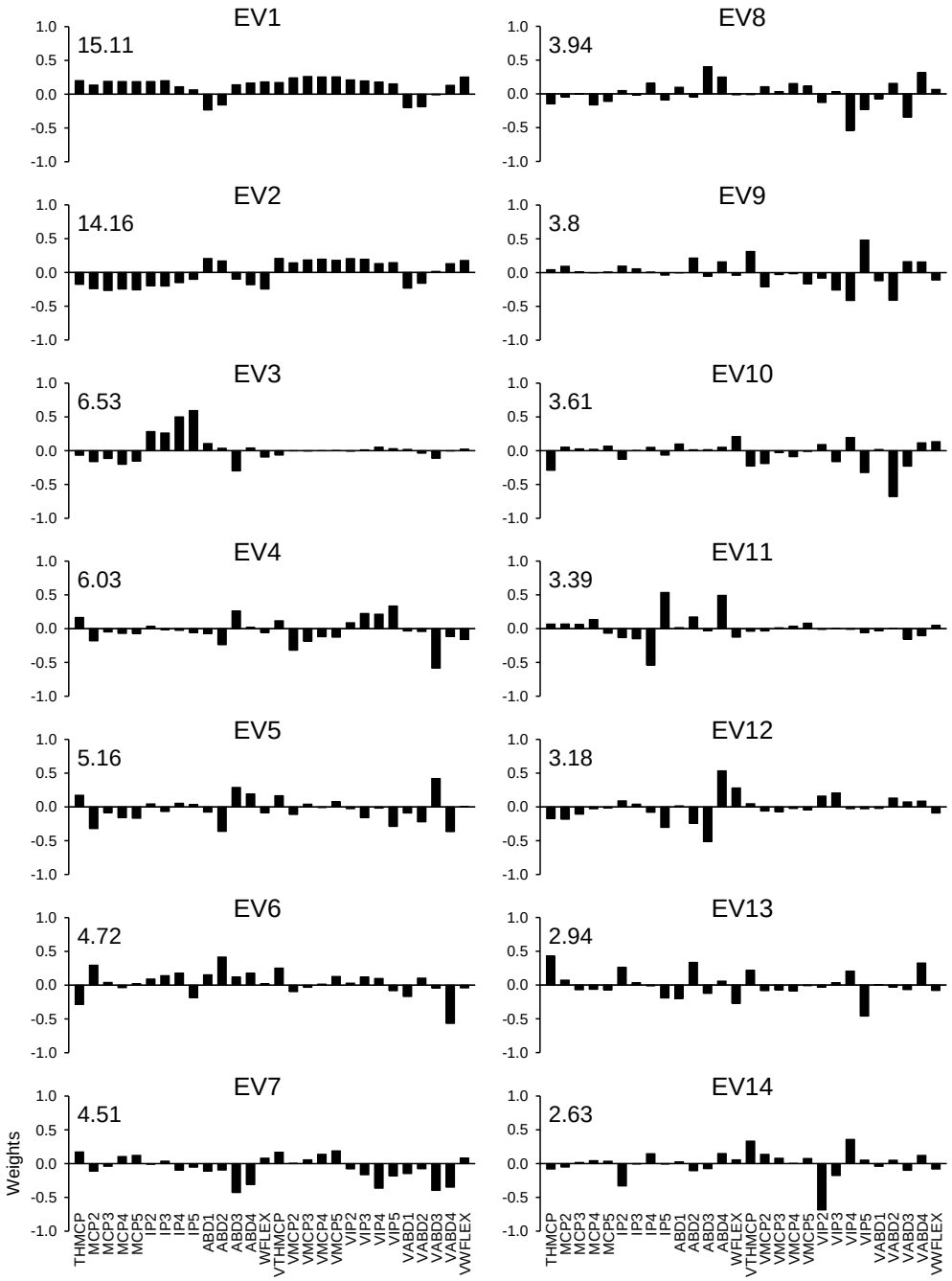
Joint Angles and Joint Angular Velocities Standardized
EV1
15.11
EV2
14.16
EV3
6.53
EV4
6.03
EV5
5.16
EV6
4.72
EV7
4.51
EV8
3.94
EV9
3.8
EV10
3.61
EV11
3.39
EV12
3.18
EV13
2.94
EV14
2.63
Weights
1.0
0.5
0.0
-0.5
-1.0
THMCP
MCP2
MCP3
MCP4
MCP5
IP2
IP3
IP4
IP5
ABD1
ABD2
ABD3
ABD4
WFLEX
VTHMCP
VMCP2
VMCP3
VMCP4
VMCP5
VIP2
VIP3
VIP4
VIP5
VABD1
VABD2
VABD3
VABD4
VWFLEX

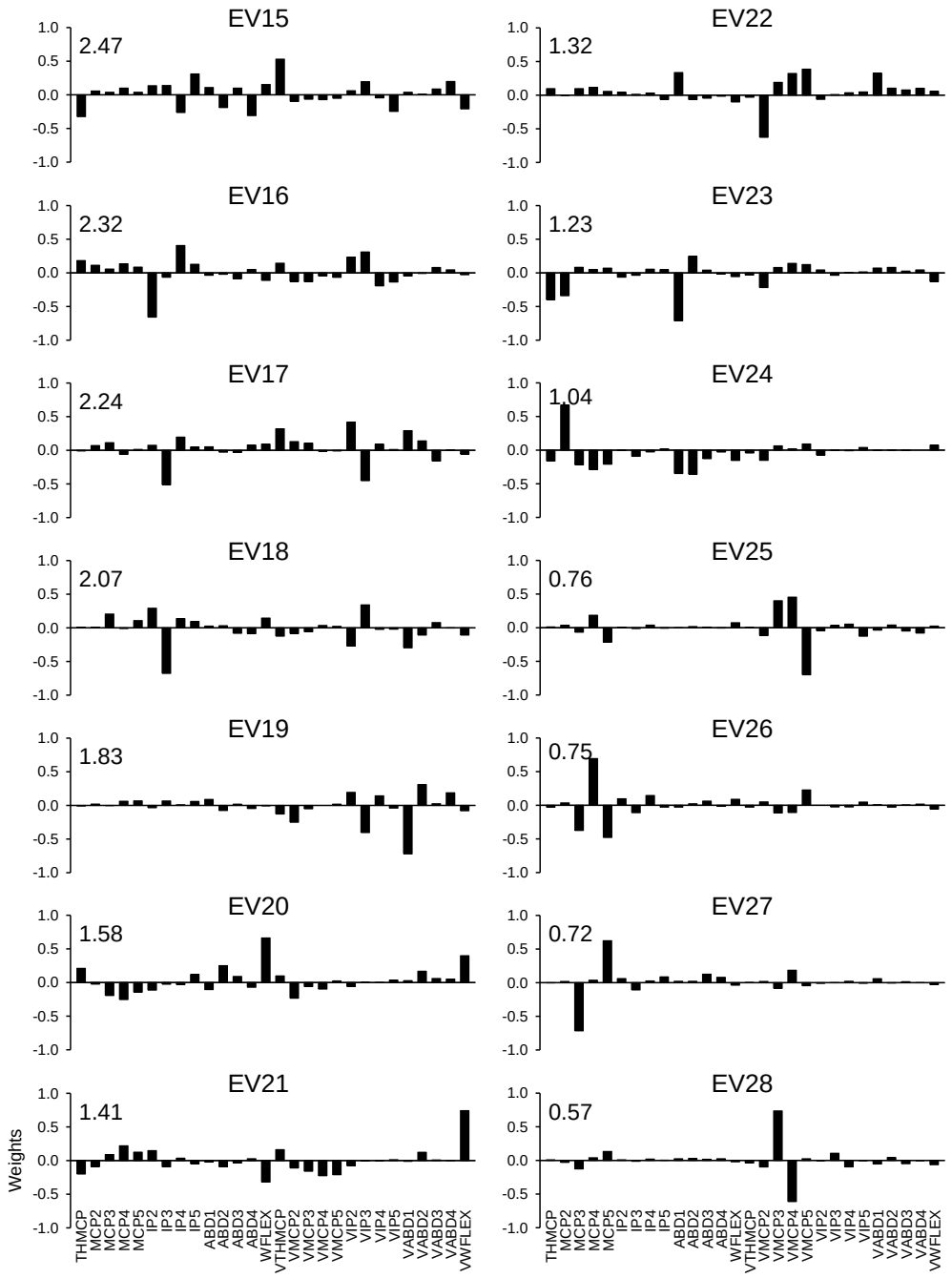

Figure 3.27. Coefficients for eigenvectors for one session. Bar graphs of the eigenvectors' coefficients for the model session for SVD performed with both joint angles and joint angular velocities. Numbers in the upper left are variance explained.

Joint Angles and Joint Angular Velocities Standardized

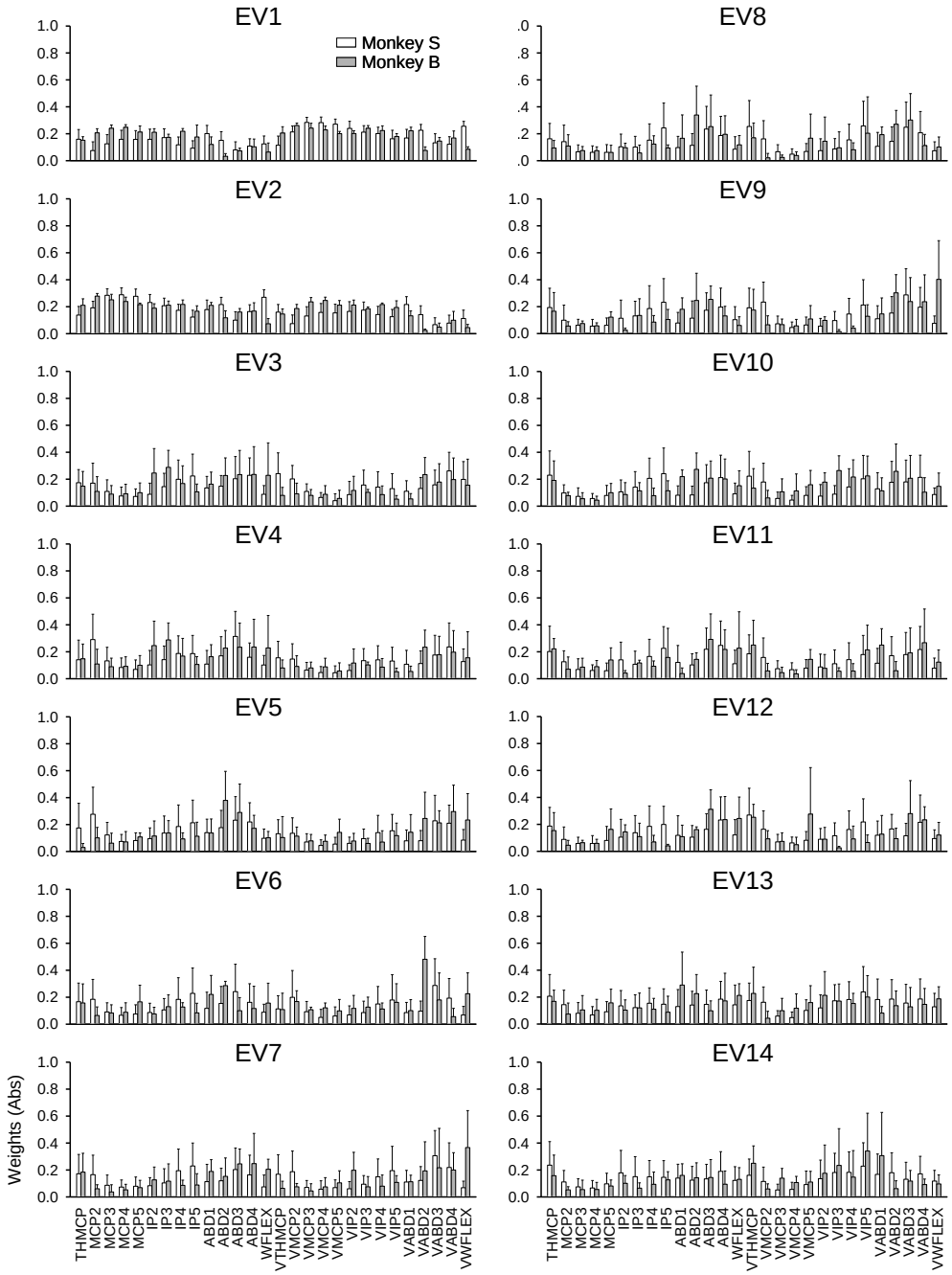

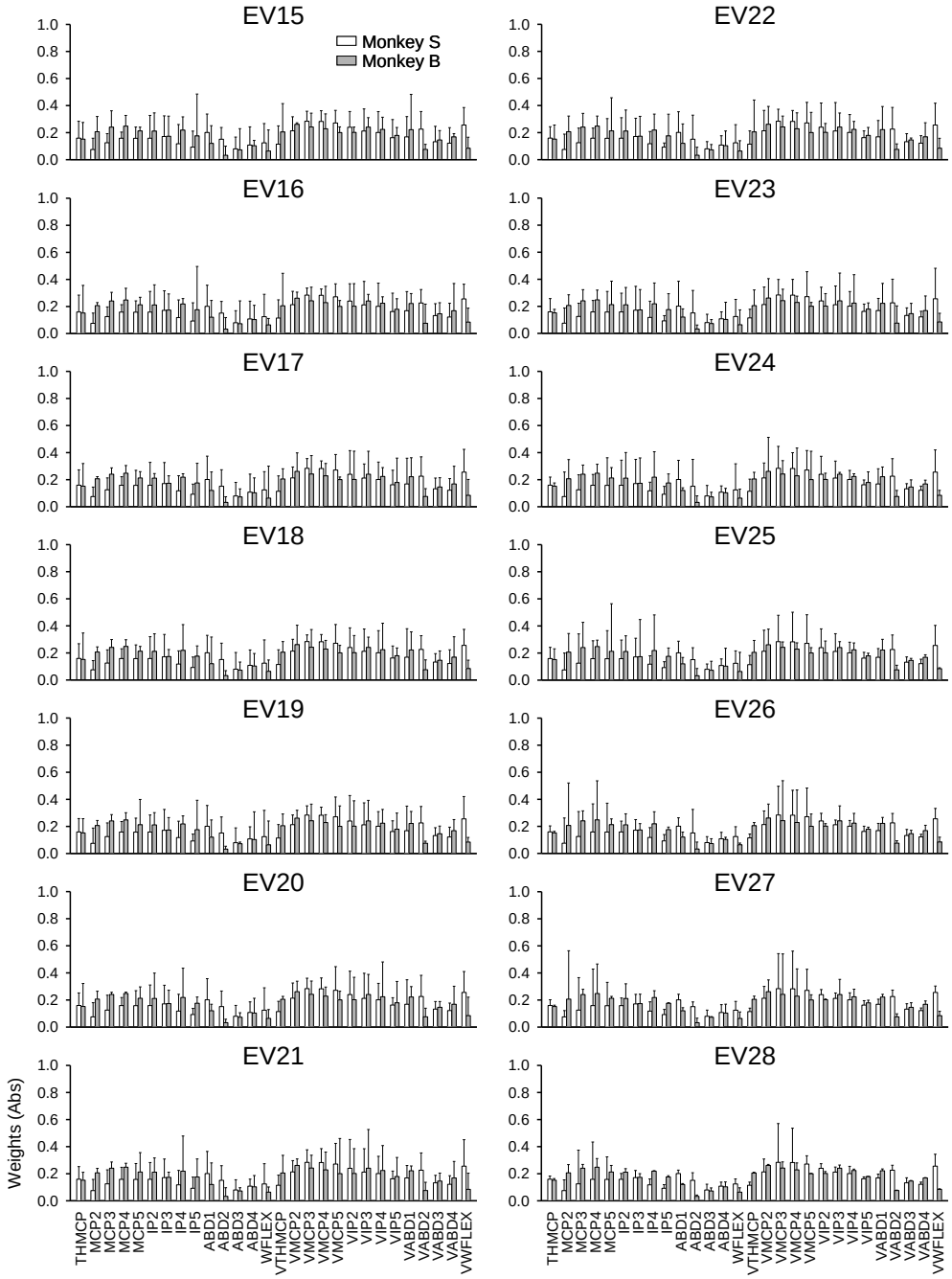

Figure 3.28. Coefficients for eigenvectors for all sessions. Mean across sessions of each eigenvectors' coefficients (absolute value) for individual elements (x-axis) for SVD performed using joint angles and joint angular velocities for each monkey.

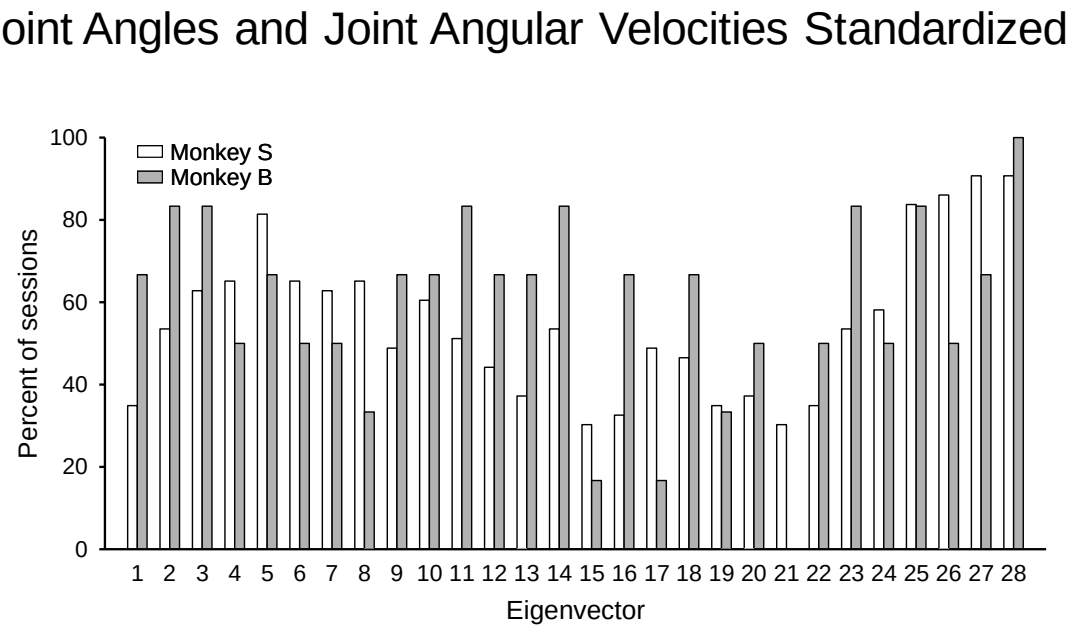

Figure 3.29. Percent of sessions displaying each eigenvector. Correlation coefficients compared a model eigenvector for SVD performed using the combination of standardized joint angles and joint angular velocities with the eigenvectors of each session.

TW1 and TW2 were highly consistent across trials, displaying a slight increase at the beginning of the *reach epoch* followed by a larger decrease (Figure 3.30). The temporal construction is much like the combination of the TWs found for the elements separately, as would be expected based on the EVs. Similarly TW3 was highly similar to TW3 of standardized joint angles, with much divergence across trials during the *grasp epoch*. All other TWs displayed large variability in temporal patterns across trials.

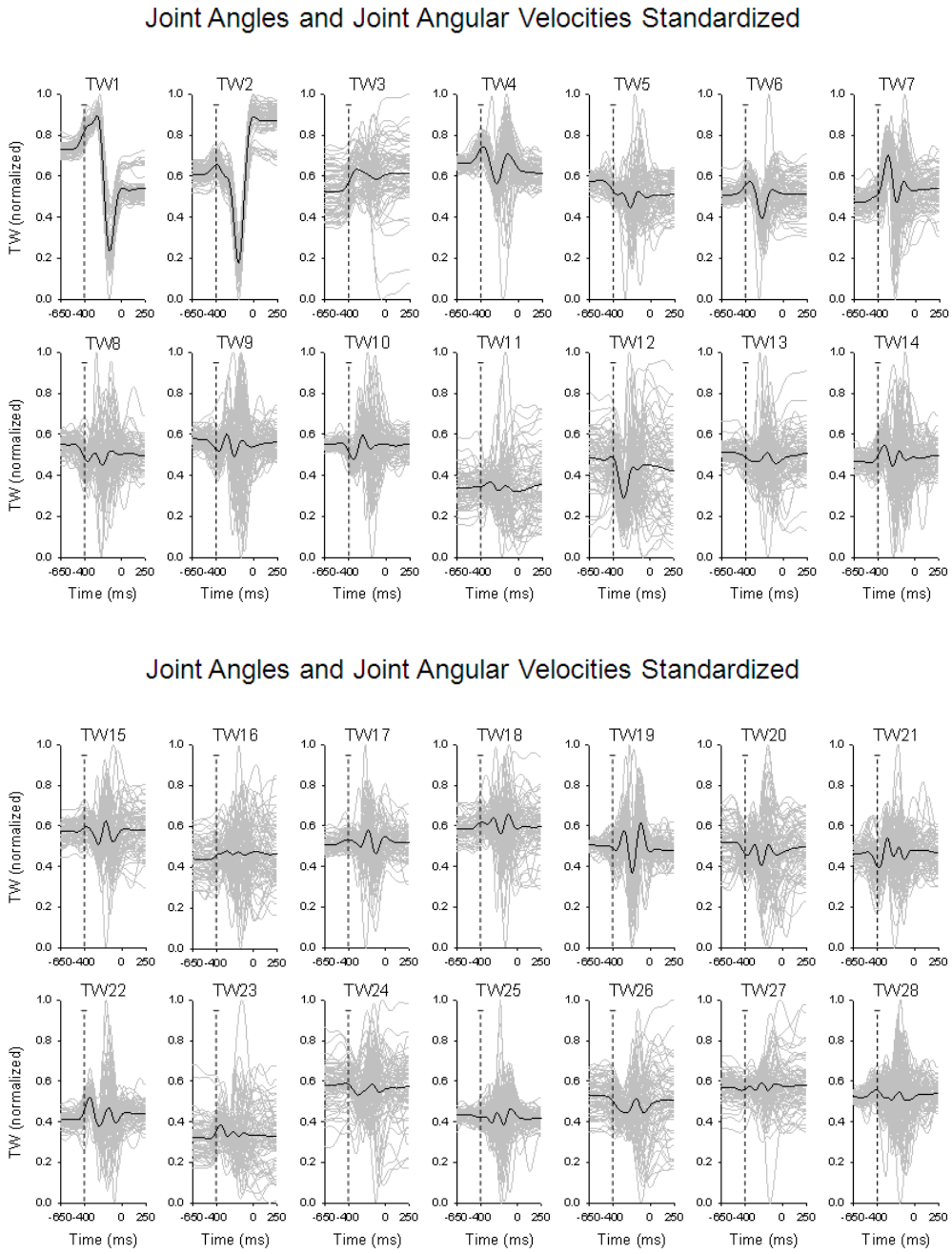

Figure 3.30. Temporal weighting vectors in time for one session. Plots of normalized temporal weighting vectors (y-axis) with time (x-axis) for each eigenvector (individual plot) across all trials in one session for SVD performed using standardized joint angles and joint angular velocities. Plots are aligned on grasp onset (time = 0 ms). Each gray line is a single trial. Black line is the average across trials.

3.2.2 Colinearity of temporal weights

One of the purposes of conducting factor analysis, PCA, or SVD is to eliminate the correlation between elements of a system. The eigenvectors described for each type of SVD performed were uncorrelated ($r \approx 0$) within a session, eliminating the high degree of colinearity observed between the individual elements during hand shaping (Figure 3.12). However, because the temporal weighting vectors are derived through direct multiplication of the eigenvectors to the joint angles and/or angular velocities, some degree of colinearity may exist between TWs within a session (Tabachnick and Fidell, 1996). The average correlation between TWs for most SVD types is approximately zero, with the exception of the first few TWs of SVD with unadjusted joint angles (Figure 3.31A). For the unadjusted joint angles, TW1 and TW2 were typically highly correlated ($r = 0.76 +/- 0.22$). This shows that standardizing data before performing an SVD analysis aids in removal of colinearity among the variables.

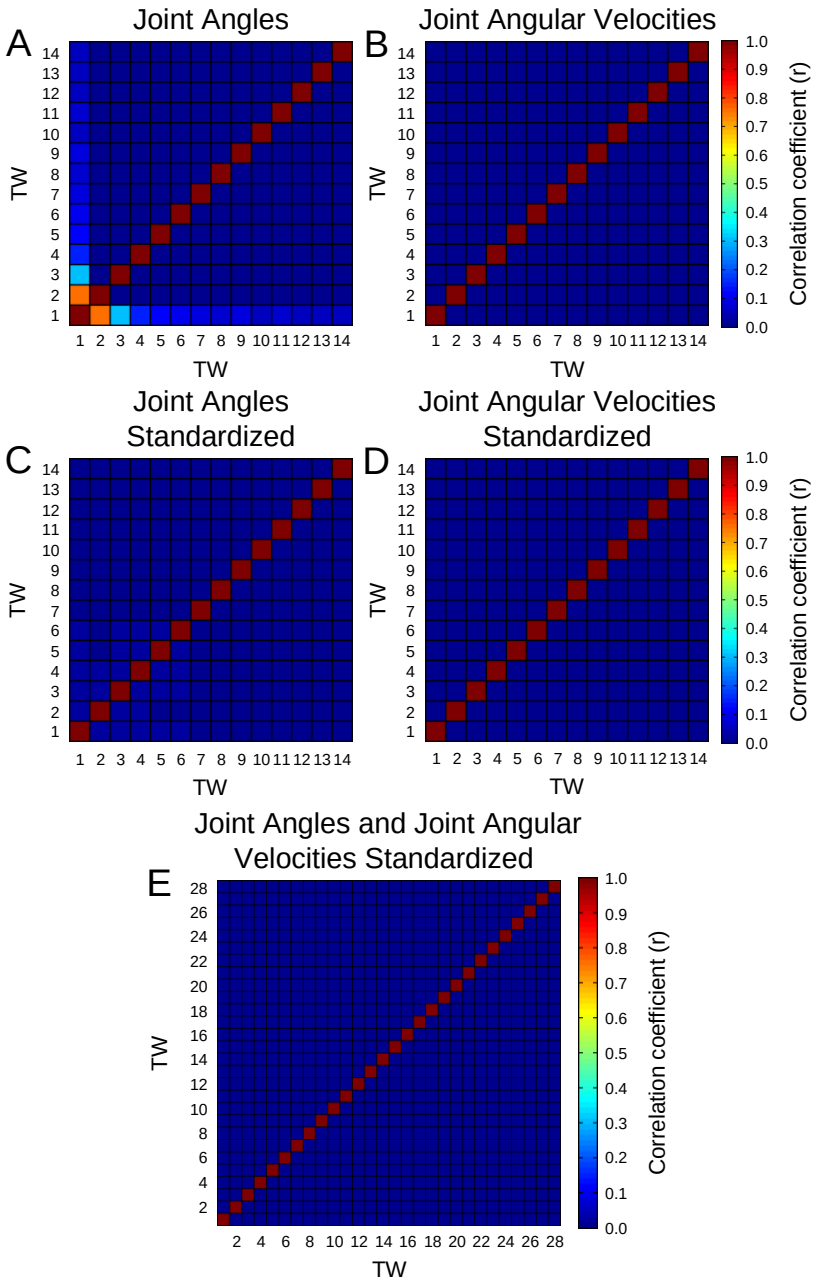

Figure 3.31. Measure of colinearity. Average correlation coefficients (absolute value) between all possible pairs of temporal weighting vectors from SVD using A) unadjusted joint angles, B) unadjusted joint angular velocities, C) standardized joint angles, D) standardized joint angular velocities, and E) standardized joint angles and angular velocities combined.

3.2.3 Discussion of SVD analyses

3.2.3.1 Singular value decomposition analysis

The SVD analysis of the hand kinematics described in this chapter has three goals. The first goal is to identify patterns of hand shaping. Using unadjusted joint angles, the SVD resulted in a dominant hand shaping pattern in the first eigenvector. Irrespective of the analysis method, TW1 is highly consistent across trials within the model session. In addition, for all methods EV1 is highly consistent across sessions (Figures 3.18, 3.23, and 3.28). This suggests that, despite the mean being subtracted for standardized analyses, the first EV represents a pattern that is central for all grasp shapes. This hand shaping pattern is similar across all SVD types and is consistently identified throughout the literature (Santello et al., 1998; Mason et al., 2001; Mason et al., 2004; Braido and Zhang, 2004; Thakur et al., 2008). EV1 predominantly involves the flexion/extension of the MCP and IP joint angles or angular velocities, representing the overall opening and closing of the hand (Figures 3.17, 3.22, and 3.27). For some analysis methods (unadjusted joint angles and standardized joint angle and joint angular velocity combined), the second EV is also tightly grouped across sessions. The remaining vectors capture the differences in hand shaping across and within a task, showing varying temporal weightings across trials. Higher-order EVs display large variability across studies of hand shaping in humans and non-human primates (Santello et al., 1998; Mason et al., 2004; Ingram et al., 2008; Thakur et al., 2008). These differences have been interpreted as the details in hand shaping (Santello et al., 1998; Thakur et al., 2008).

A second goal of SVD is to identify orthogonal components by transforming the data to a new coordinate system in which each component is independent. Due to the nature of the reach-to-grasp task, biomechanical constraints, and neuroanatomy, many joint angles of the hand are highly correlated with one another (Santello et al., 1998; Santello and Soechting, 1998). Colinearity is also present in this task (Figure 3.12), particularly for those joint angles (THMCP, MCP2-5, IP2-5, and WFLEX) that make up the dominant hand shape (Figure 3.17). Through an iterative process, SVD transforms the data into a new coordinate system in which eigenvectors are orthogonal (Tabachnick and Fidell, 1996; Jolliffe, 2002; Jackson, 2003). EVs, however, are static and do not provide temporal information about the new orthogonal system. Therefore, TWs are derived by multiplying the EVs with the original data and eigenvalues in order to describe the contribution of each EV through time (Tabachnick and Fidell, 1996; Jolliffe, 2002; Jackson, 2003; Mason et al., 2004). However, due to the high degree of covariation remaining in unadjusted data, colinearity is also observed between TW1 and TW2 of SVD with unadjusted joint angles (Figure 3.31), albeit to a lesser extent than that observed for the individual elements. By removing or minimizing elemental correlations using SVD, neural firing can be examined in relation to independent components rather than highly correlated individual elements, allowing for a better interpretation of the relationship.

Finally, SVD is used to reduce the degrees of freedom needed to explain a complex system. In this study, the hand was defined by 14 joint angles or joint angular velocities or the combination of the two, resulting in 28 degrees of freedom. SVD

analysis resulted in 14 or 28 orthogonal eigenvectors, corresponding eigenvalues, and temporal weighting vectors. Consistent with previous findings, the first few eigenvectors explain the majority of the variance in hand shaping (Santello et al., 1998; Mason et al., 2001; Mason et al., 2004; Braido and Zhang, 2004; Thakur et al., 2008). Typically, when attempting to reduce the degrees of freedom of a system, eigenvectors with smaller eigenvalues, or that describe less variance, are ignored because they are considered to be less important (Dunteman, 1989; Freund and Littel, 2000; Jolliffe, 2002; Jackson, 2003). Several methods exist for determining the proper number of eigenvectors to retain (Jolliffe, 2002; Jackson, 2003). Using a 90% cumulative variance cutoff value, SVD with unadjusted joint angle data required retaining, on average, only 3 components instead of 14 (Figure 3.16A). For standardized joint angle data, joint angular velocity, and standardized joint angular velocity, the 90% cutoff required retaining 10 components (Figure 3.16B and Figure 3.21). For the combination of standardized joint angles and joint angular velocities, the components could be reduced to 20 from 28 (Figure 3.26). However, because hand shaping is such a complex system, it has been argued that higher-order EVs are critical for the reconstruction of the fine details needed for proper grasp of different objects (Santello et al., 1998; Thakur et al., 2008). This raises the important question as to whether these components have neural representation. Therefore, all EVs will be used in analyzing neural responses. For our purposes, because they describe the majority of the variance in most SVDs, the first three EVs are interpreted as simplified or dominant patterns, while the remaining are considered to capture details of hand shaping.

3.2.3.2 Comparison of unadjusted and standardized joint angle SVD

The most important difference between the unadjusted and standardized joint angle analyses is the first eigenvector. The first EV based on unadjusted joint angles represents the average hand shape; that is, the opening and closing of the hand through extension and flexion of the THMCP, MCP2-5, IP2-5, and WFLEX joint angles (Figure 3.17A). The involvement of the ABDs in the average hand shape is minimal. This hand shape is consistent with results from both human and non-human primates (Santello et al., 1998; Mason et al., 2001; Mason et al., 2004; Braido and Zhang, 2004; Thakur et al., 2008). On average, this pattern accounted for more than 85% of the variance (Figure 3.16A), nearly three times that of the first eigenvector for any other analysis method (Figures 3.16, 3.21, and 3.26). Understandably, the first EV is important for the reconstruction and overall understanding of hand shaping.

While the SVD analysis based on standardized data accurately describes hand shaping patterns, it does not include the average hand shape. EV1 of the standardized joint angle data is significantly weighted for all joint angles, including the ABDs, due to the equalized variance for all variables. In addition, higher-order EVs from unadjusted and standardized joint angles are not comparable. Therefore, care must be taken when using these patterns. For example, if using SVD patterns to reconstruct hand shapes to control a neural prosthesis, it is simplest to use unadjusted data so that the average hand shape is included. However, standardized data may be used for such an application if the average is added back into the data. Another potential use is to examine whether the patterns of hand shaping uncovered are represented in the neural firing of CNS regions involved with controlling prehension. The EVs resulting from unadjusted and

standardized data define different patterns, thus presenting a larger repertoire of possibilities to relate to the neural firing. Chapter 5 investigates this question for the firing of M1 neurons.

3.2.3.3 SVD including joint angular velocities

Joint angular velocities of the fingers have been much less examined than other kinematic parameters of hand shaping. Subsequently, description of patterns of angular velocities has been limited. Patterns in joint angular velocities of the fingers during grasping have been described utilizing a gradient descent algorithm (Vinjamuri et al., 2007), SVD (Vinjamuri et al., 2009), and PCA (Ingram et al., 2008), with varying results. The principal components obtained by Ingram and coworkers (Ingram et al., 2008) are most comparable to the EVs described in this chapter, in which EV1 is highly weighted for the majority of the MCP and IP joint angles (Figure 3.23). Similar to joint angles, EV1 obtained from SVD analysis of joint angular velocities uncovers a dominant pattern that is consistent across sessions (Figure 3.24 and 3.25). Unlike SVD of the joint angles, however, the variance explained by each eigenvector, from both unadjusted and standardized joint angular velocities is distributed across a greater number of eigenvectors. On average, 10 eigenvectors were required to account for 90% of the variability in the joint angular velocity data (Figure 3.21). The higher-order EVs capture details of the joint angular velocities with grasping that are highly variable. Previous studies in humans have described similar trends in variability (Ingram et al., 2008; Vinjamuri et al., 2009). However, these previous studies observed that the contribution of the thumb to these patterns was reserved for higher-order patterns (Ingram et al., 2008;

Vinjamuri et al., 2009), which was not the case for the present data (Figure 3. 23). This likely represents differences in control strategies utilized by humans versus non-human primates, in which the latter employs the thumb for details in hand shaping to a lesser extent. In addition, the extensive practice of the task by the monkeys may have played a role in these differences.

Rather than examining neural control strategies, the intent of others in defining patterns in joint angular velocities was to mathematically integrate the velocities to obtain hand shapes (Vinjamuri et al., 2007; Ingram et al., 2008; Vinjamuri et al., 2009) However, it is possible that joint angular velocities, or patterns in joint angular velocities, are directly controlled by the cortex. In addition, the coordination of position (i.e. joint angles) and velocity may also be a relevant neural control mechanism, yet previous studies have not examined patterns based on combining these two classes of parameters. SVD of standardized joint angles and angular velocities combined resulted in the first two EVs weighted similarly for the majority of joint angles and angular velocities (Figure 3.27), comparable to the first EV of standardized joint angles or angular velocities alone (Figures 3.17 and 3.22). Much like other analyses, these EVs represent global patterns involving the coordination of angular position and velocity that were fairly consistent across sessions (Figure 3.29). Many EVs (i.e. EV1-2) described patterns combining joint angles and angular velocities, especially across similar joints. However, several of the higher EVs were dominated by angles or angular velocities rather than combinations, suggesting that the two parameters have little interaction (Figure 3.27). This is consistent with the joint angle and angular velocity individual elements having low correlation

(Figure 3.12), further supporting the idea that these kinematic parameters are controlled through different mechanisms in the CNS (Stark et al., 2007a). These patterns can be utilized for exploration of neural correlates to both combined angles and angular velocities (i.e. EV1 and EV2) as well as patterns of these parameters separately (i.e. higher-order EVs).

3.3 Summary

Fourteen joint angles and angular velocities were examined as two Rhesus monkeys reached to and grasped 23 different objects that were designed to systematically vary hand shape. Joint angles varied significantly across objects predominantly during the reach and grasp epochs. Variability in the joint angular velocities was mainly during the reach epoch. Joint angles were also highly variable across trials for a single object, as displayed by examining the Mahalanobis distance from average hand shape for each trial. High measures of colinearity were observed between MCP, IP, and WFLEX joint angles. Similar observations were made for joint angular velocities. However, joint angles and angular velocities showed little correlation with each other.

Using SVD, patterns were identified in joint angles, joint angular velocities, or the combination of the two. Results were examined for analysis utilizing unadjusted and standardized data. The first eigenvector for all SVD analyses represented a global pattern that was predominantly weighted for the MCP and IP joint and was highly consistent across sessions. As few as three eigenvectors were required to explain 90% of the variability. Temporal weighting vectors describing the contribution of each eigenvector through time were tightly coupled across trials for lower-order components. The patterns

identified using these analyses provide a useful tool for examining neural control strategies. Correlations between motor cortical firing and joint kinematics as well as temporal weighting vectors from SVD are examined in Chapters 4 and 5, respectively.

Chapter 4: Modulation of motor cortical neurons during prehension

4.1. Neuronal data base and modulation patterns

A total of 238 neurons (84 left chamber monkey S, 77 right chamber monkey S, 77 right chamber monkey B) in the hand area of the motor cortex were recorded as the monkey reached to and grasped the set of 23 objects differing in shape (see Figure 2.3). Due to the difficulty of recording and analyzing the kinematic data, only 96 cells have been examined thus far (75 left chamber monkey S, 8 right chamber monkey S, 13 right chamber monkey B). To be included in the study, a cell was required to have firing significantly different from baseline (paired Student's t-test, $p \leq 0.05$) in at least one analysis epoch (*premove*, *reach*, or *grasp*). Baseline was defined as the average firing rate for the first 300 ms of the trial, prior to any visual cues. A total of 81 cells (63 left chamber monkey S, 6 right chamber monkey S, 12 right chamber monkey B) fulfilled this criterion. On average, each session included 104 +/- 76 trials completed with 13 +/- 6 objects. Several different timing patterns were observed in the cells' firing (Figure 4.1A). Most cells (63/81) showed significant differences in firing from baseline for all epochs (28/81), *premove* and *reach epochs* combined (14/81), or *reach* and *grasp epochs* combined (21/81). A significant change in firing for the *reach* or *grasp epochs* alone was present for some cells (7/81 and 5/81, respectively), and for only a few cells for the *premove epoch* alone or *premove* and *grasp epoch* combined (2/81 and 4/81, respectively).

Cells were categorized according to the epoch which displayed the highest mean firing rate (Figure 4.1B). The majority of cells (57/81) increased firing during the *reach epoch* when transport and the vast majority of movement occurred. Few cells displayed maximum firing during the *premove* and *grasp epochs* (14/81 and 10/81, respectively). It should be stressed that this categorization is based on highest mean firing and many cells (63/81) were significantly modulated during multiple epochs (Figure 4.1A). Therefore, this categorization provides only a first-order examination of the many firing patterns present in the motor cortex.

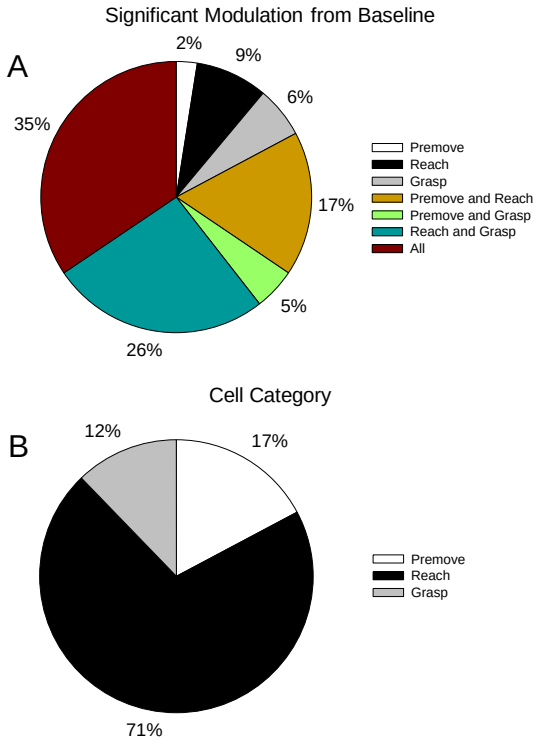

Figure 4.1. Neuronal modulation patterns. A) Percentage of cells with firing significantly different than baseline during each epoch or combination of epochs. B) Percentage of cells with maximal firing during the *premove, reach,* or *grasp epochs*.

The results of passive manipulation and intracortical microstimulation (ICMS) support that the cells recorded were in the hand area of M1. If a cell remained well isolated at the end of a session, qualitative examination of the receptive field was performed by passively moving, stroking, tapping, and gently squeezing various regions of the arm, forearm, hand and fingers. Testing for receptive fields was performed on 112 of the 244 cells recorded (40 right chamber Monkey S, 32 left chamber Monkey S, and 40 right chamber Monkey B). Seventy-five percent (84/112) responded to passive movement/manipulation of the hand, fingers, or thumb, 28.6% (32/112) to the wrist, 20.5% (23/112) to the elbow or shoulder, and <1% (1/112) to other areas (Figure 4.2). ICMS during two sessions resulted in twitches of the thumb, hand, and wrist at a threshold between 30 and 35 μA, also consistent with stimulation within the primary motor cortex (Weinrich and Wise, 1982; Tanne-Gariepy et al., 2002). These findings strongly support that the chamber was placed over the hand region of the primary motor cortex.

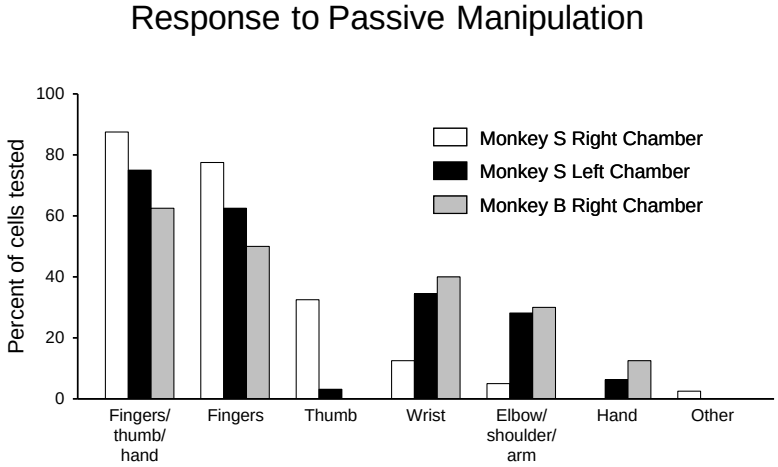

Figure 4.2. Passive manipulation testing results. Percentage of cells that were modulated in response to passive movement for each chamber placement.

The firing of primary motor cortical neurons was highly dependent on the object grasped, as found in previous studies (Picard and Smith, 1992a; Mason et al., 2002; Hendrix et al., 2009). Analysis of variance (ANOVA, $p \leq 0.05$) across objects showed that mean firing was significantly different across objects for 40.7% (33/81) of cells during the *premove epoch*, 65.4% (53/81) during the *reach epoch*, and 51.9% (42/80) during the *grasp epoch* (Figure 4.3). The firing of 76.5% percent of cells varied as a function of objects for one or more epochs. As the hand and reach kinematics also varied as a function of objects (see Chapter 3), this suggests that M1 cells modulate with hand shape.

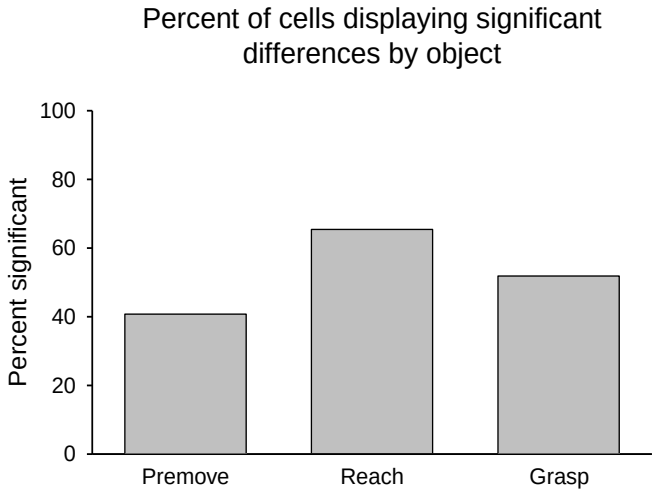

Figure 4.3. Analysis of variance on neural firing for each epoch. Percentage of cells displaying significance across objects in mean firing rate during each epoch (*premove, reach,* and *grasp*).

As described above, cells were classified based on the epoch in which highest firing occurred. Several firing patterns were observed. Examples of cells from each category (premove, reach, or grasp) are depicted in Figures 4.4-4.6. The motor cortical

cell in Figure 4.4 (T011) increased firing on average 150 ms before reach onset and had highest firing during the *premove epoch*. Through most of the *reach epoch*, the firing remained elevated but decreased below baseline 167 ms (average) before grasp onset, and the firing rate fell below baseline during the *grasp epoch* (Figure 4.4). This firing pattern was observed for all objects. However, the strongest modulation occurred for objects 6, 9, 13, 14, 19, and 20, with less modulation for objects 3, 15, and 23 (Figure 4.4B).

The cell shown in Figure 4.5 (T022) modulated predominantly during the *reach epoch*. While the majority of firing occurred during the *reach epoch*, firing increased an average of 83 ms before movement onset and returned to baseline just as grasp was initiated (Figure 4.5). The average amplitude and overall temporal profile of firing was similar for all objects (Figure 4.5B). Examination of the average firing across objects, however, provides only a first-order observation of the relation of the cells' modulation to kinematics of grasp.

An example of a motor cortical cell firing primarily during the *grasp epoch* is shown in Figure 4.6 (T088). Firing gradually increased near the end of the *reach epoch* and continued to increase throughout the *grasp epoch* for most objects (Figure 4.6). However, for objects 7 and 12, the firing pattern differed, displaying an early peak either in the *reach* (object 12) or *grasp epoch* (object 7). As noted earlier, one common aspect of the three example cells is that the modulation was not confined to a single epoch.

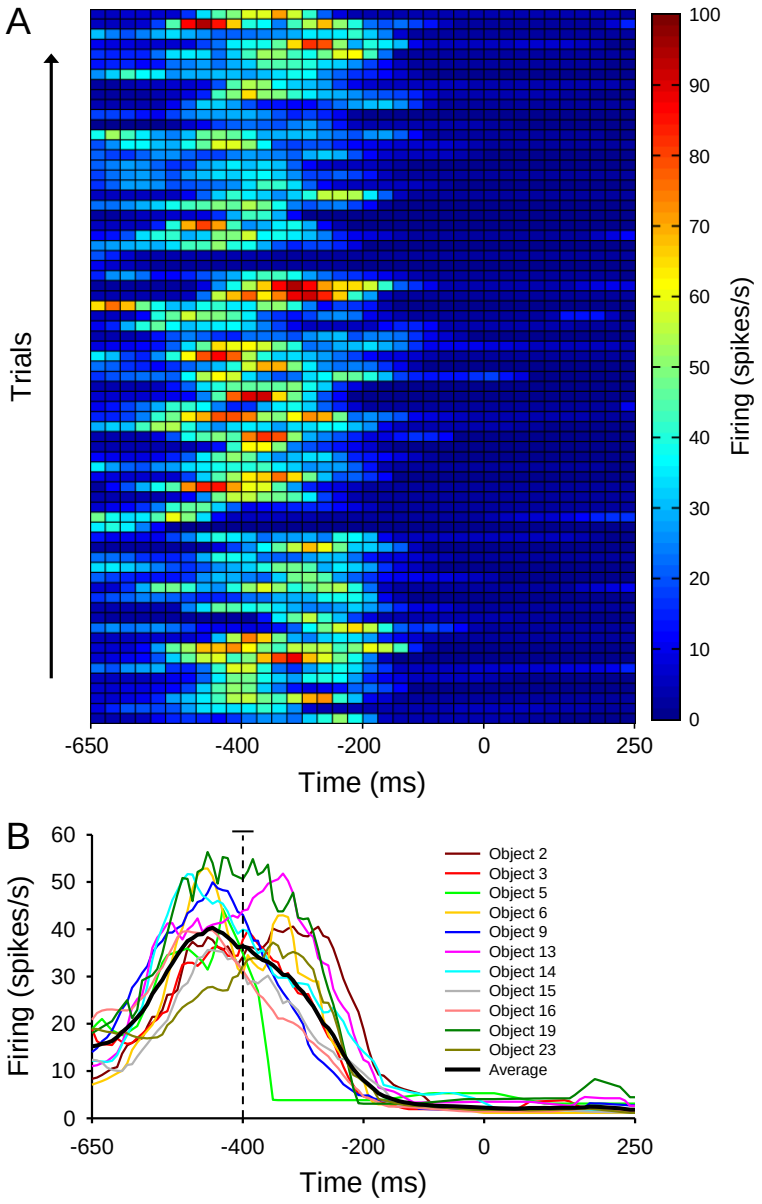

Figure 4.4. Example of cell with maximal firing during the premove epoch (T011). A) Color plot of the instantaneous firing rates over time (x-axis; 25 ms bins) for all trials (y-axis) of an example cell that had maximal firing during the *premove epoch*. The trials are shown in temporal order with the first trial at the bottom. Color bar on the right is spikes/sec. B) Average firing across all trials for an object (13 total objects) and average across all trials for the entire session (bold) over time (x-axis). Dashed vertical line denotes average reach onset and horizontal line on top denotes the standard deviation in reach onset time.

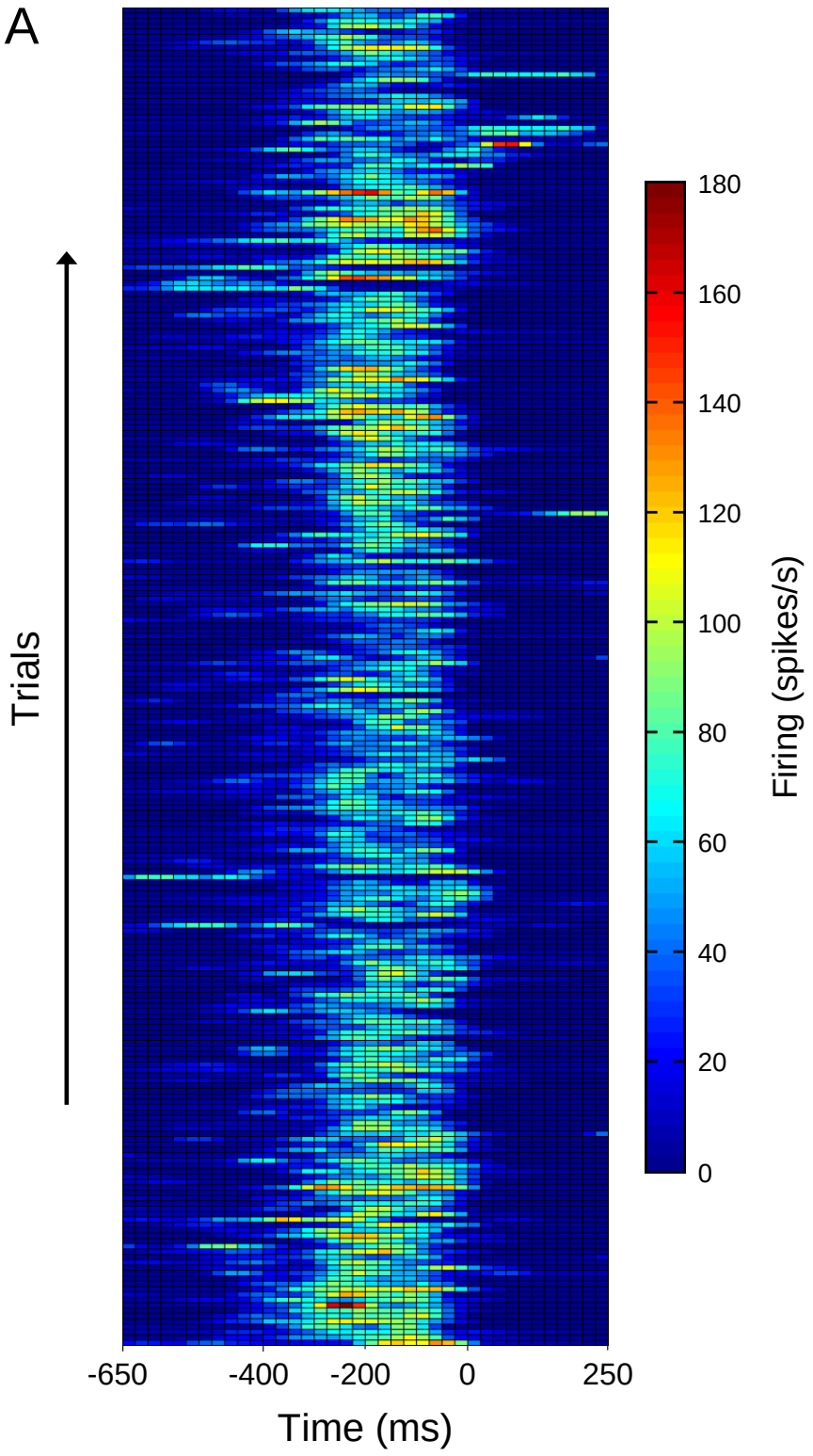
A
Trials
-650
-400
-200
0
250
Time (ms)
180
160
140
120
100
80
60
40
20
0
Firing (spikes/s)

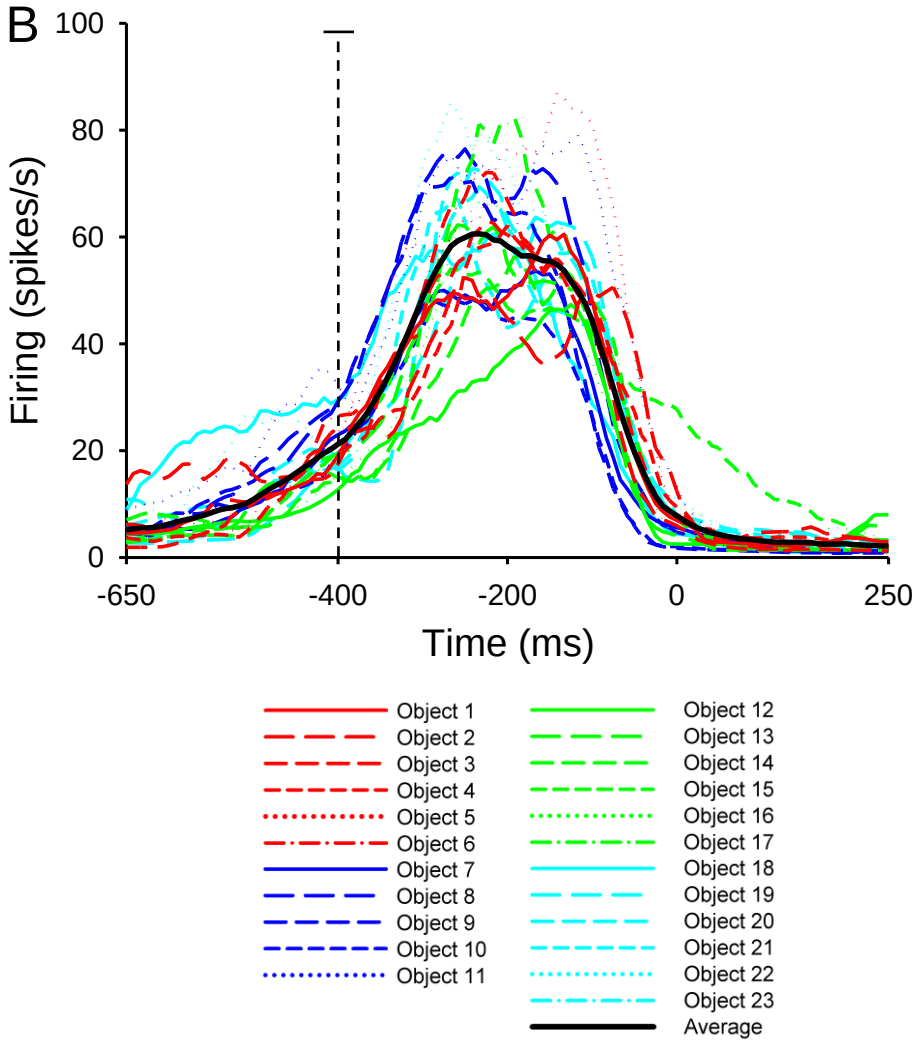

Figure 4.5. Example of cell with maximal firing during the reach epoch (T022). A) Color plot of the instantaneous firing rates over time (x-axis; 25 ms bins) for all trials (y-axis) of an example cell that had maximal firing during the *reach epoch*. B) Average firing across all trials for an object and average across all trials for the entire session (bold) over time (x-axis). Conventions as in Figure 4.4.

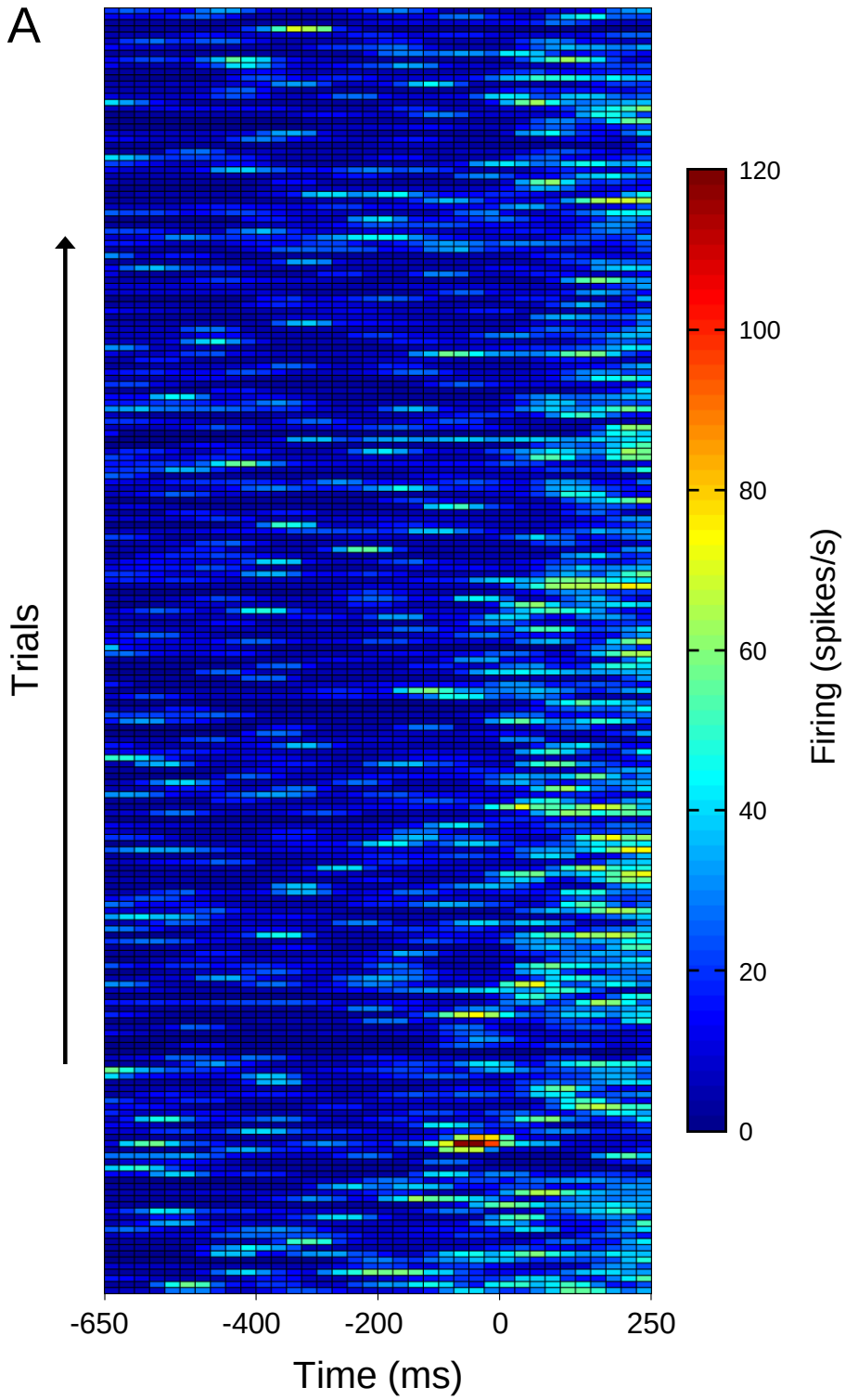
A
Trials
-650
-400
-200
0
250
Time (ms)
120
100
80
60
40
20
0
Firing (spikes/s)

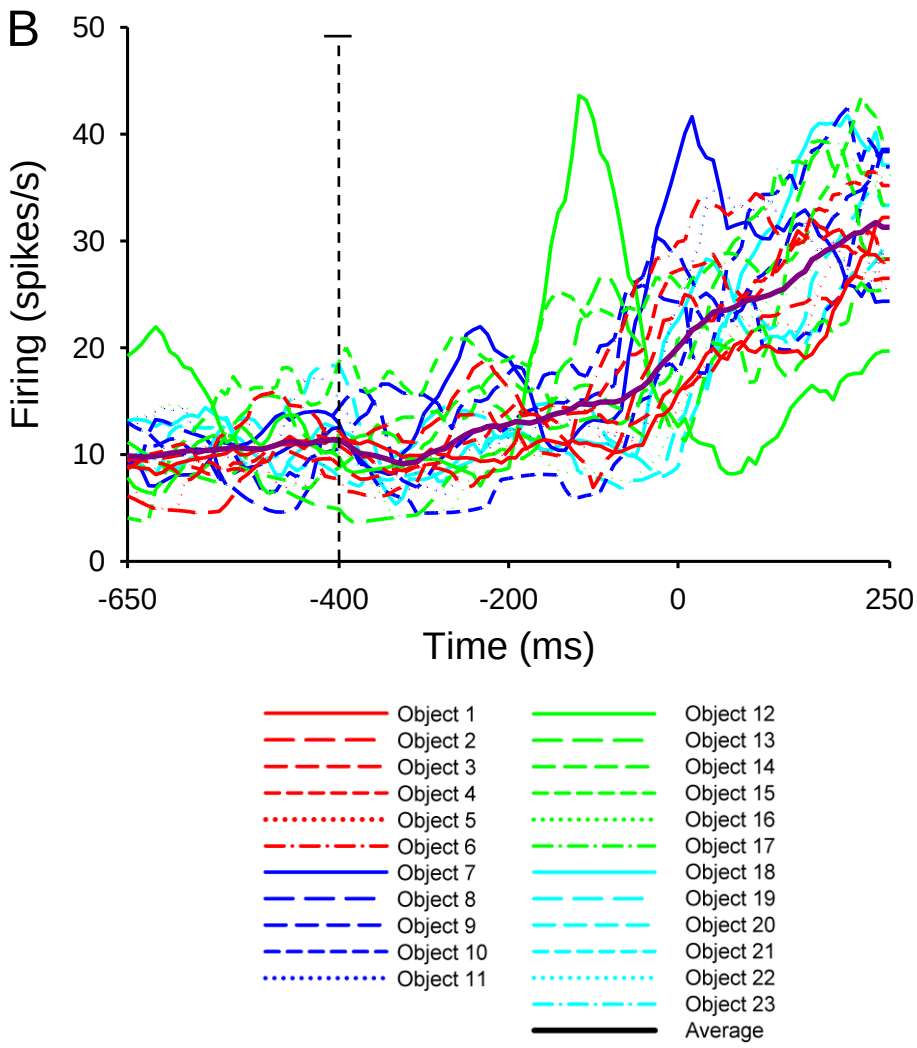

Figure 4.6. Example of cell with maximal firing during the grasp epoch (T088). A) Color plot of the instantaneous firing rates over time (x-axis; 25 ms bins) for all trials (y-axis) of an example cell that had maximal firing during the *grasp epoch*. B) Average firing across all trials for an object and average across all trials for the entire session (bold) over time (x-axis). Conventions as in Figure 4.4.

4.2 Linear regression analysis of firing to individual elements

To test whether the firing of the motor cortical neurons was correlated to the kinematics of the individual joints, a linear regression analysis was performed based on Equation 2.2 (see section 2.3.4 Data Analysis). Using single-trial data, the firing was fit to each individual element (joint angles and joint angular velocities) as well as wrist path and speed for all epochs. Firing was also fit to an overall model that combined all 14 joint angles or all 14 joint angular velocities (see Equation 2.4). Data was not averaged in order to examine cortical activity in relation to the entire variability in the natural reach-to-grasp behavior. Therefore, resulting R^2-values may appear smaller compared to studies utilizing averaged data. In addition, it has been suggested that R^2-values obtained from linear regression analyses with physiological or behavioral data are naturally lower and should be interpreted on an individual-study basis (Cohen, 1988). The goal of this analysis was twofold. First, to provide a survey of correlation between the firing with finger joint and reach kinematics. This has not been undertaken for joint angles and joint angular velocities in a reach-to-grasp task. Second, to assess the validity of the regression approach for a task as complex as reach-to-grasp.

Cells that fired predominantly during the *premove* or *reach epochs* were often highly correlated to several joint angles. For example, cell B056 increased firing beginning in the *premove epoch* and peaked during the *reach epoch* (Figure 4.7 E and F). The cell displayed high correlations ($R^2 \geq 0.138$) (Cohen, 1988) to MCP2-5 joint angles (Figure 4.7A). However, as shown in Figure 3.12, the movements of the MCPs are highly correlated during this task. Therefore, it is not unexpected that the firing would be

correlated with each of the MCPs. These high correlations reflect that the temporal profiles of the firing and MCP joint angles are similar (Figure 4.7C). The overall model R^2-value for the joint angles was also high (R^2=0.28), but was only slightly larger than the R^2-value for MCP3 (R^2=0.26) (see Section 4.4). The firing showed little correlation to the joint angular velocities, with the exception of that for ABD1 (Figure 4.7 B and D). The cell also displayed a high R^2 for wrist path but not wrist speed (Figure 4.8 A and B).

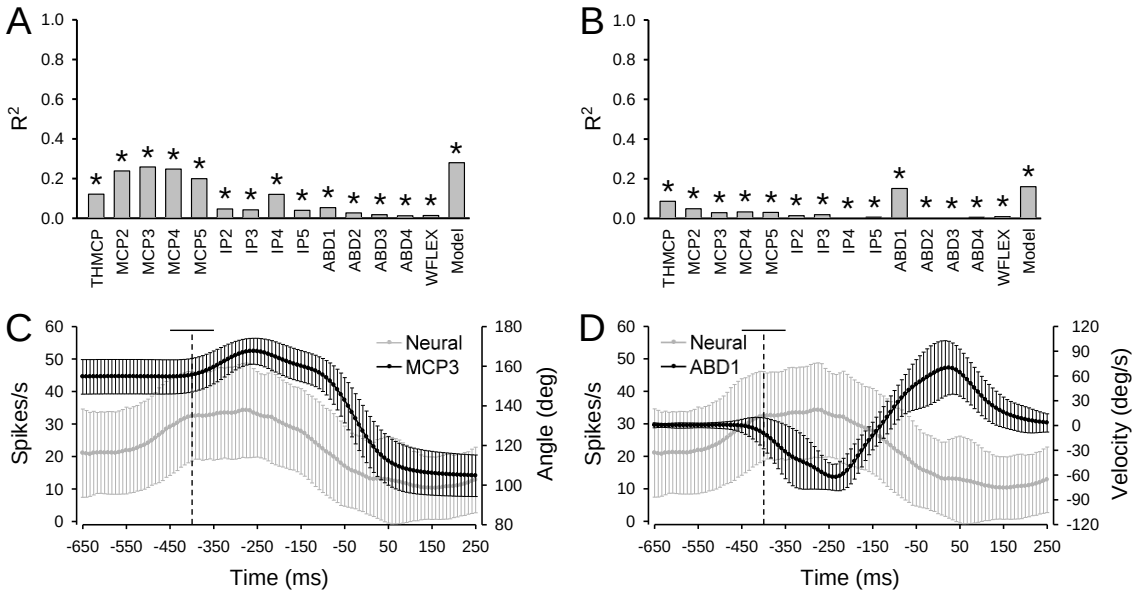

Figure 4.7. Regression analysis of neural firing with individual joint angle elements (B056). A-B) R^2 for neural firing regressed with individual joint angles (A) and joint angular velocities (B) for all epochs. Star denotes significance ($p \leq 0.05$). C-D) Average firing (+/- standard deviation) across all trials over time (x-axis) and mean (+/- standard deviation) of the most significant joint angle (C) and joint angular velocity (D). Dashed vertical line denotes average reach onset and horizontal line on top denotes the standard deviation in reach onset time.

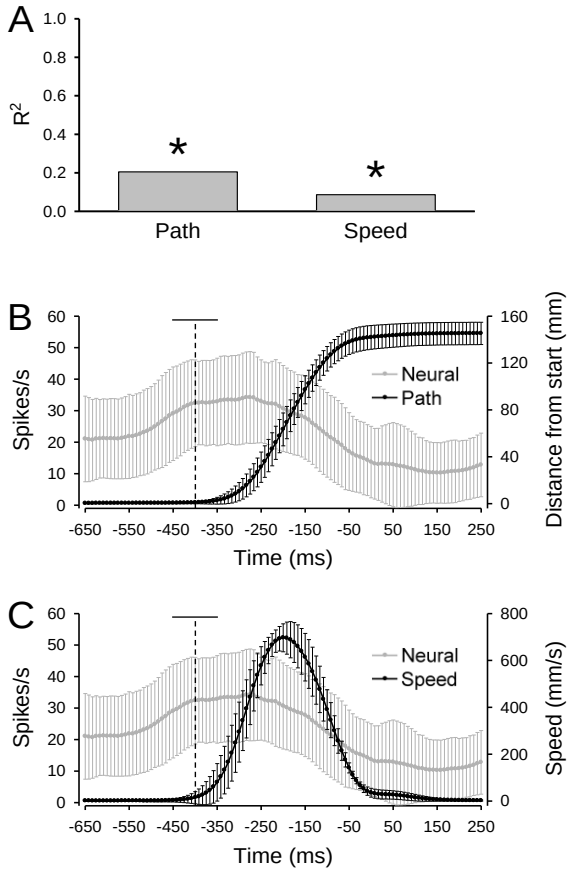

Figure 4.8. Regression analysis of neural firing with wrist path and speed (B056). A) R^2 for neural firing regressed with wrist path (left) and speed (right) for all epochs. B-C) Average firing (+/- standard deviation) across all trials over time (x-axis) and mean (+/- standard deviation) wrist path (B) or speed (C). Conventions as in Figure 4.7.

Cells with different firing patterns than that observed for B056 displayed varying relationships to the individual elements. Cell T081 increased firing at the end of the *reach epoch* and maintained firing above baseline through the *grasp epoch* (Figure 4.9 C and D). High R^2s were obtained for regressions with THMCP, ABD1, ABD2, ABD4, and WFLEX (Figure 4.9A), a unique combination of joint angles. The overall model for joint angles had a large R^2-value (R^2=0.54) that was more than twice as large as that for

any other individual element. As for cell B056, the regressions of firing with joint angular velocities had low R^2s, even for the overall model (Figure 4.9B). Similarly, the cell had a high correlation with the wrist path but not to wrist speed (Figure 4.10 A and B).

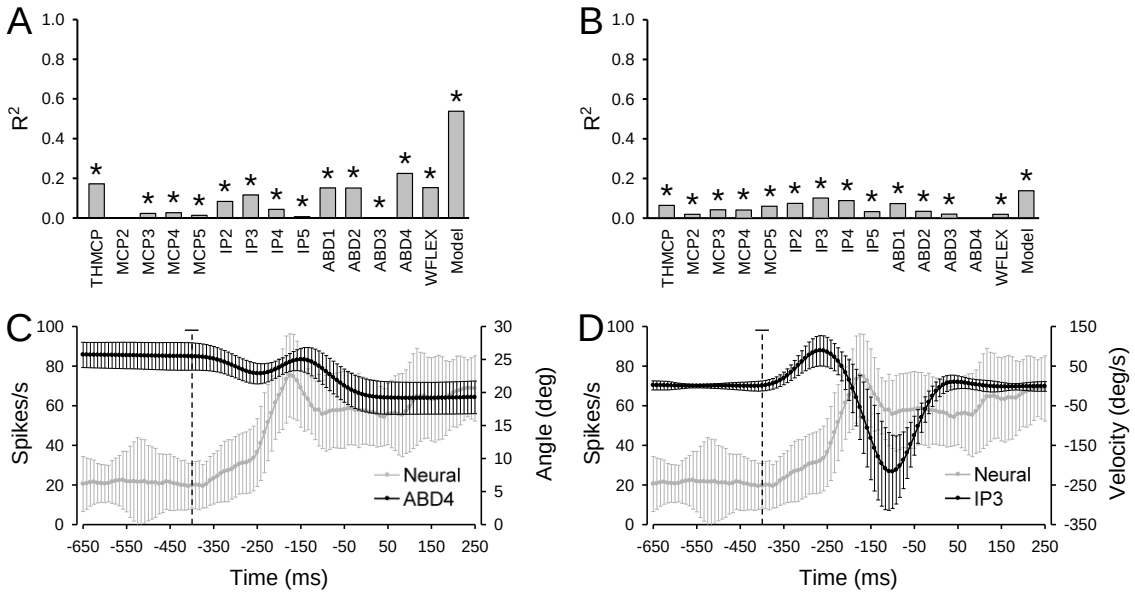

Figure 4.9. Regression analysis of neural firing with individual joint angle elements (T081). A-B) R^2 for neural firing regressed with joint angles (A) and joint angular velocities (B) for all epochs. C-D) Average firing (+/- standard deviation) across all trials over time (x-axis) and mean +/- standard deviation of the most significant joint angle (C) and joint angular velocity (D). Conventions as in Figure 4.7.

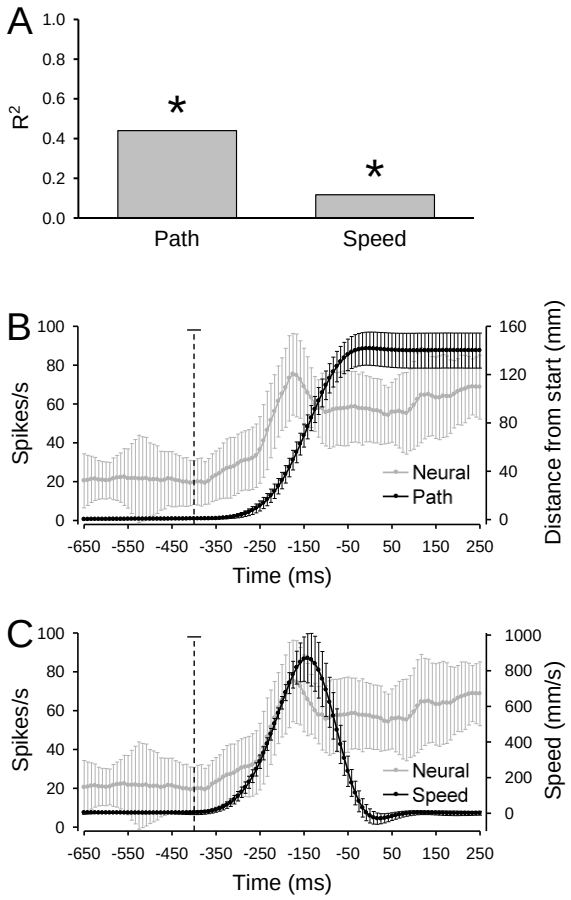

Figure 4.10. Regression analysis of neural firing with wrist path and speed (T081). A) R^2 for neural firing regressed with wrist path (left) and speed (right) for all epochs. B-C) Average firing (+/- standard deviation) across all trials over time (x-axis) and mean (+/- standard deviation) wrist path (B) or speed (C). Conventions as in Figure 4.7.

For a small group of cells, the regression of firing to the individual elements resulted in strong fits for joint angular velocities. Cell B015 displayed peak firing just before grasp onset (Figure 4.11 C and D), and was highly correlated to MCP2-5 joint angular velocities (Figure 4.11B). The overall model R^2 for joint angular velocities was the same as that obtained for the WFLEX angular velocity alone (R^2=0.33). Similar to

the joint angles, the joint angular velocities were highly correlated with one another (see Figure 3.12). The high R^2s for these regressions are due to the peak firing corresponding to the minimum of the joint angular velocities (Figure 4.11D). The only joint angle with a high R^2 was ABD4 (Figure 4.11A). However, the overall model for the joint angles also had a high R^2-value (R^2=0.29). The firing was also highly correlated to the wrist path (Figure 4.12A).

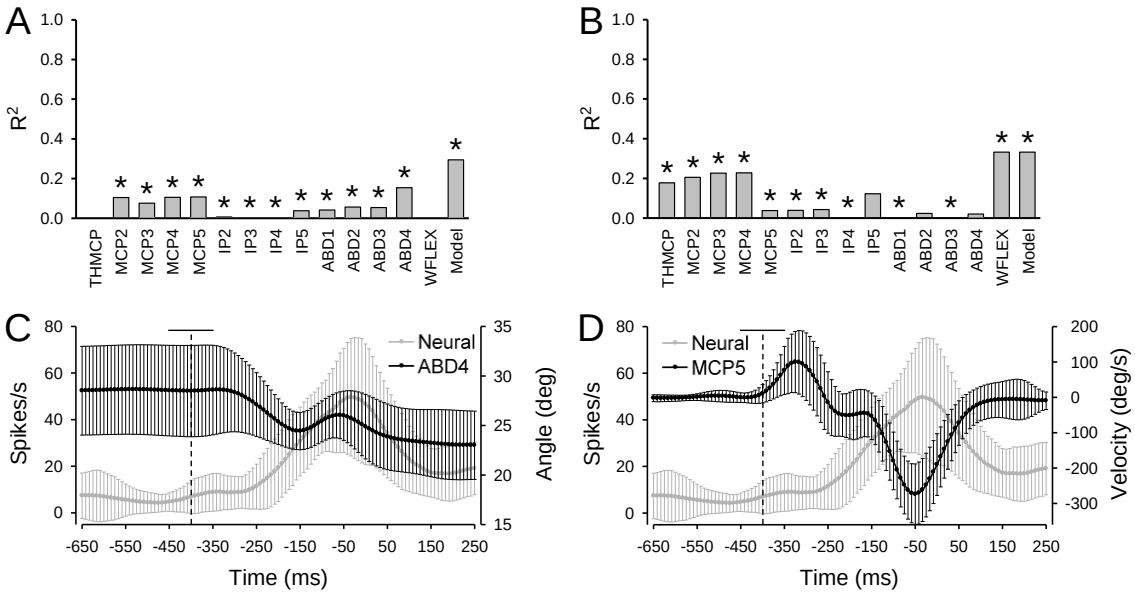

Figure 4.11. Regression analysis of neural firing with individual joint angle elements (B015). A-B) R^2 for neural firing regressed with joint angles (A) and joint angular velocities (B) for all epochs. C-D) Average firing (+/- standard deviation) across all trials over time (x-axis) and mean +/- standard deviation of the most significant joint angles (C) and joint angular velocities (D). Conventions as in Figure 4.7.

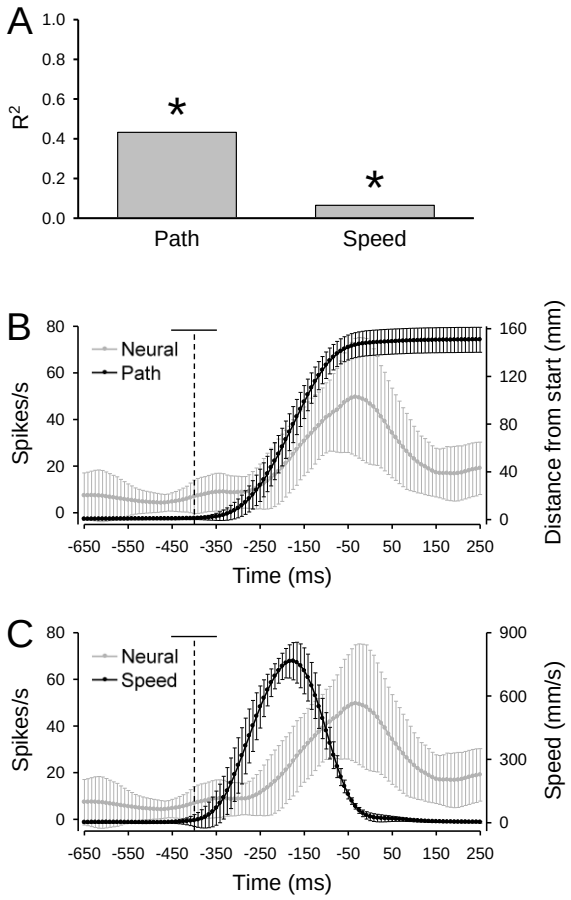

Figure 4.12. Regression analysis of neural firing with wrist path and speed (B015). A) R^2 for neural firing regressed with wrist path (left) and speed (right) for all epochs. B-C) Average firing (+/- standard deviation) across all trials over time (x-axis) and mean (+/- standard deviation) wrist path (B) or speed (C). Conventions as in Figure 4.7.

The R^2-values were averaged for the population by category (maximal firing during *premove*, *reach*, or *grasp* epochs). Only high ($R^2 \geq 0.138$) (Cohen, 1988) and significant ($p \leq 0.05$) correlations were included in the average to prevent skewing by low correlations. In general, the average R^2s for joint angles were similar across cell category and joint (Figure 4.13A). The population average R^2-values for the overall

model were only slightly higher than those for the individual joints. However, only premove or reach cells had high correlations with IP4 or IP5. The similarity of averages across cell types and joints implies that no particular joint angles were preferred by the population of cells recorded (Figure 4.13A). An average of 15.4% of premove cells and 17.3% of grasp cells had high R^2s for regressions between neural firing and joint angles (Figure 4.13C). Reach cells, however, were more often correlated to joint angles than premove or grasp cells. Between 35.1% and 38.6% of reach cells were highly correlated with MCP3-5, while IP2 and IP3 were highly correlated with 21.1% and 26.3% of reach cells, respectively. The percentage of cells with high correlations was widely distributed across the joint angles with the exception of IP3-5 and ABD3 (Figure 4.13C). In addition, most cells (28.6% premove, 35.1% reach, 30% grasp) displayed high R^2-values for more than three joint angles (Figure 4.14A). The percentage of cells with high R^2-values for the overall model, between 57.1% and 80% of each cell category, was much larger than for the joint angles regressed independently.

The average R^2s for joint angular velocities as well as the overall model for angular velocities, when present, were similar to the averages for joint angles (Figure 4.13B). However, the percentage of cells displaying high and significant correlations was much smaller for joint angular velocities (Figure 4.13D). Less than 15% of any cell type were highly correlated to velocities, and there were no cells in which the firing was highly correlated to IP5, ABD3, or ABD4 (Figure 4.13D). There were no obvious preferences for specific joints, but the small number of cells with high correlations makes conclusions difficult (Figure 4.14B). High correlations were observed, however, for the

overall model of joint angular velocities in a much larger number of cells (up to 54.4% for reach cells). Overall, the correlation of the neural firing to joint angular velocities was less robust than to joint angles.

Population averages for correlations between neural firing and wrist trajectory or speed were high ($\overline{R^2} = 0.31$ or $\overline{R^2} = 0.27$, respectively). The firing for all cell types was highly correlated to wrist trajectory, on average, 40.1% of the time. Interestingly, reach cells were correlated with wrist speed (49.1%) far more often than they were for wrist trajectory (17.5%), while premove and grasp cells had the opposite trend. The firing of the majority of grasp cells (60%) had high R^2-values for wrist trajectory, but was not related to wrist speed (0%). However, wrist path and speed were both highly correlated with the joint angles and angular velocities of the fingers (see Figure 3.12). Therefore, the firing of these M1 cells was correlated with a mixture of wrist and finger joint signals.

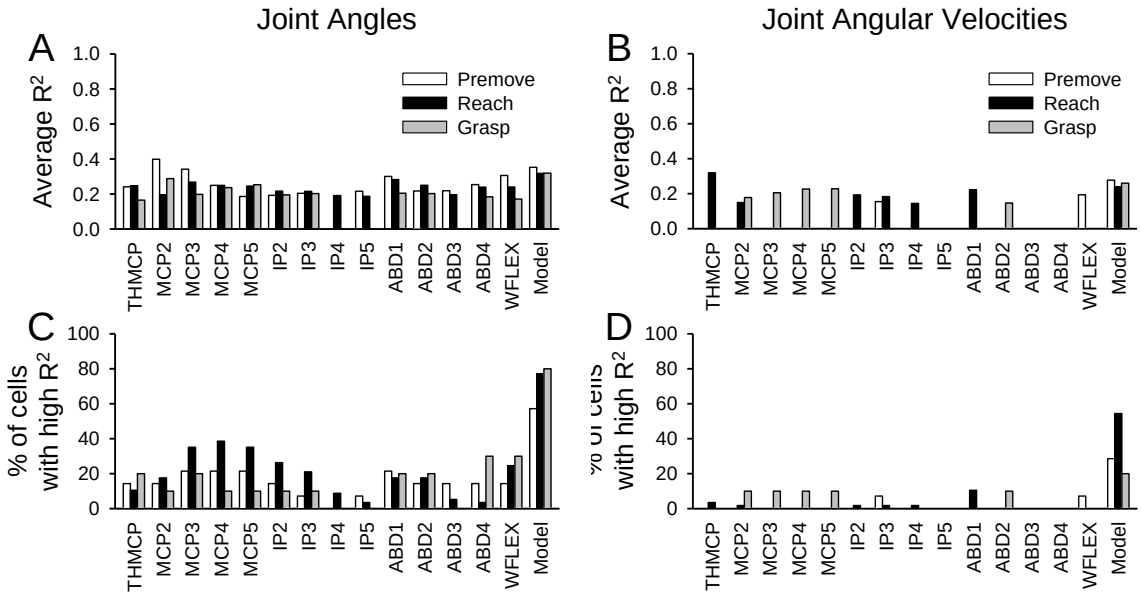

Figure 4.13. Population results obtained during regression analysis of neural firing with individual joint angle elements. A and B) Mean R^2 for neural firing regressed with joint angles (A) and joint angular velocities (B) for all epochs for each category of cells. Only cells with high ($R^2 \geq 0.138$) and significant R^2-values were included. Standard deviations were not included to prevent crowding. C and D) Percentage of cells with $R^2 \geq 0.138$ for neural firing regressed with joint angles (C) and joint angular velocities (D) for all epochs for each category of cells.

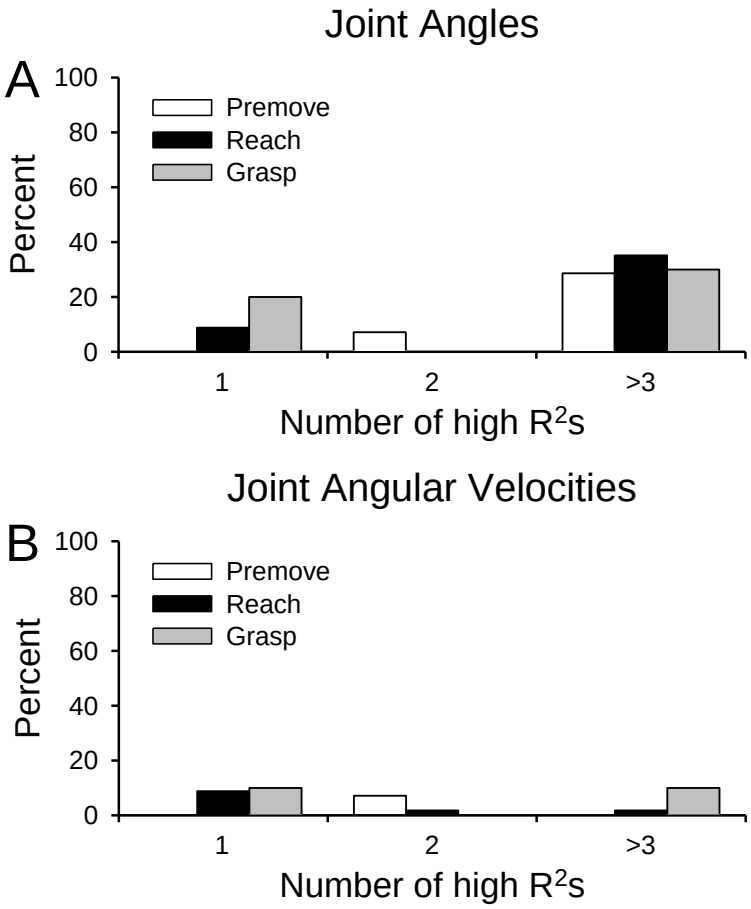

Figure 4.14. Percentage of cells displaying high correlations to each number of individual elements. A-B) Percentage of cells displaying $R^2 \geq 0.138$ for 1, 2, or >3 joint angles (A) or joint angular velocities (B) for all epochs for each category of cells.

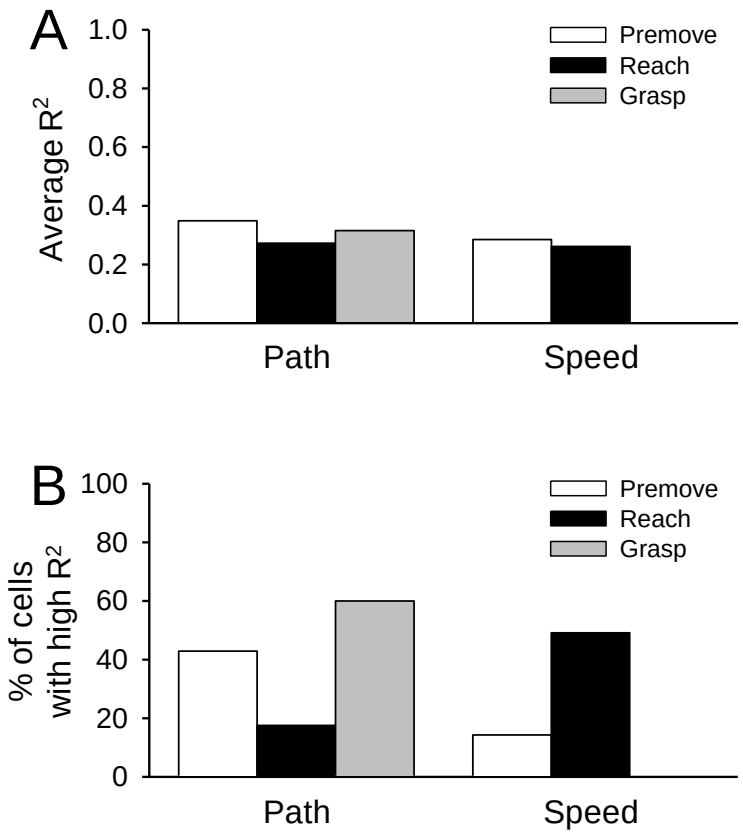

Figure 4.15. Population results obtained during regression analysis of neural firing with wrist trajectory and speed. A) Mean R^2 for neural firing regressed with wrist trajectory and speed for all epochs for each category of cells. Only cells with high ($R^2 \geq 0.138$) and significant R^2-values were included. Standard deviations were not included for consistency. B) Percentage of cells with $R^2 \geq 0.138$ for neural firing regressed with wrist trajectory and speed for all epochs for each category of cells.

4.3 Time-shifted linear regression analysis of firing to individual elements

An inherent problem in the previous regression analysis is that it assumed no lead or lag between the cell firing and the kinematics. To examine the improvements from introducing a temporal lead or lag for each cell, regressions were examined after shifting the neural firing +/- 500 ms (in 8.33 ms increments) for all epochs. The resulting R^2-values for each individual element at each lead or lag are displayed in Figure 4.16 for example cell T081. The predominantly single-peak profiles obtained suggest that utilizing these temporal shifts is a valid approach with a clearly defined lead or lag. For cell T081, the time-shift increased R^2-values by an average of 0.13 for joint angles and 0.06 for joint angular velocities (Figure 4.17 A and B). The largest increases in the R^2s were for MCP3-5 joint angles and joint angular velocities, as well as the ABD3 joint angle or ABD4 joint angular velocity. For all but one joint angle (IP5), the best fit occurred at a lead. However, the correlation of neural firing to IP5 was minimal even with a temporal shift. The maximum correlations were obtained by utilizing a lead (positive τ) in the neural firing ($\bar{\tau} = 162.5$ +/- 198.2 ms for joint angles and $\bar{\tau} = 85.7$ +/- 17.1 ms for joint angular velocities) (Figure 4.17 C and D).

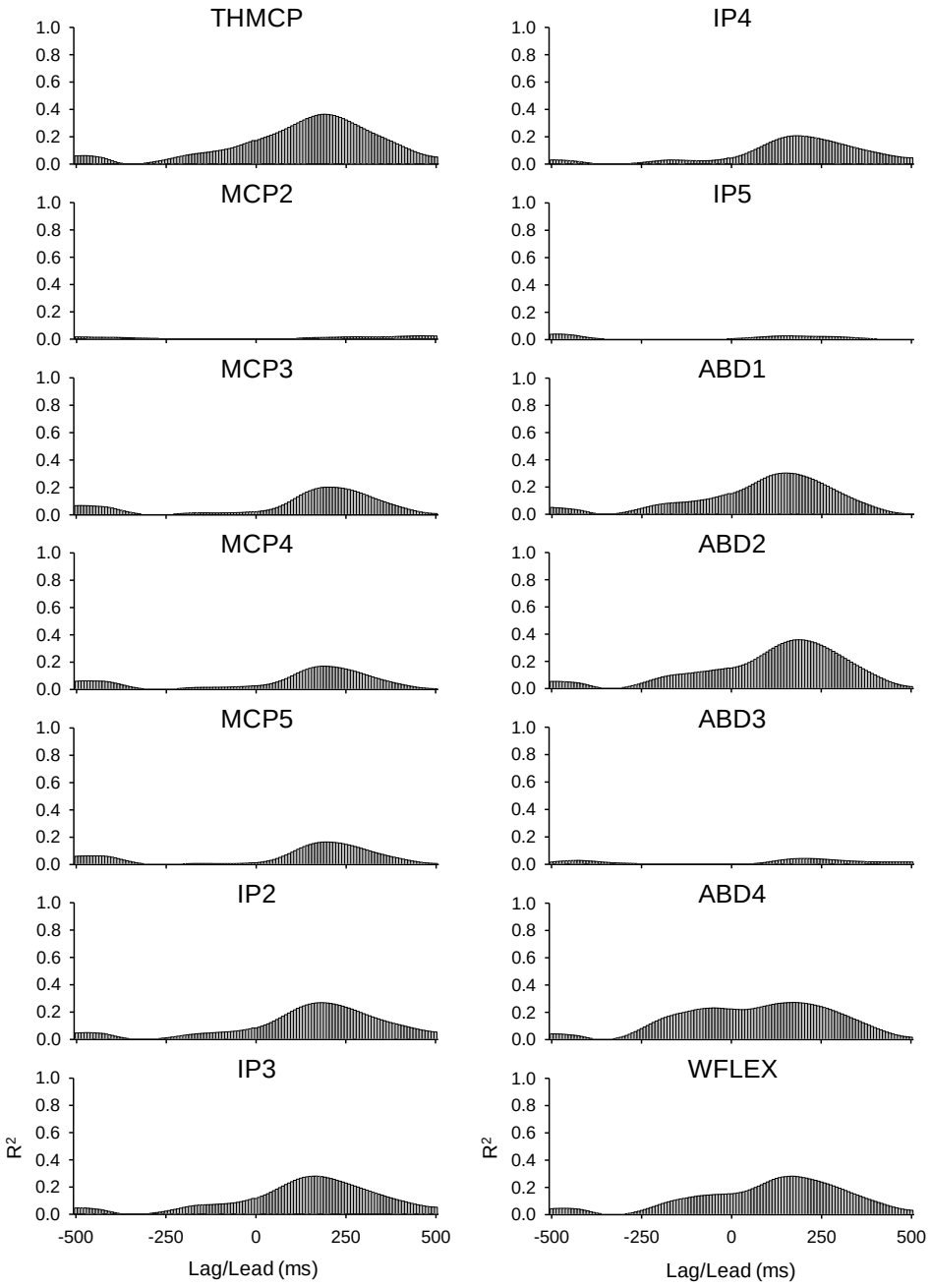
THMCP
IP4
MCP2
IP5
MCP3
ABD1
MCP4
ABD2
MCP5
ABD3
IP2
ABD4
IP3
WFLEX
1.0
0.8
0.6
0.4
0.2
0.0
R2
-500
-250
0
250
500
Lag/Lead (ms)

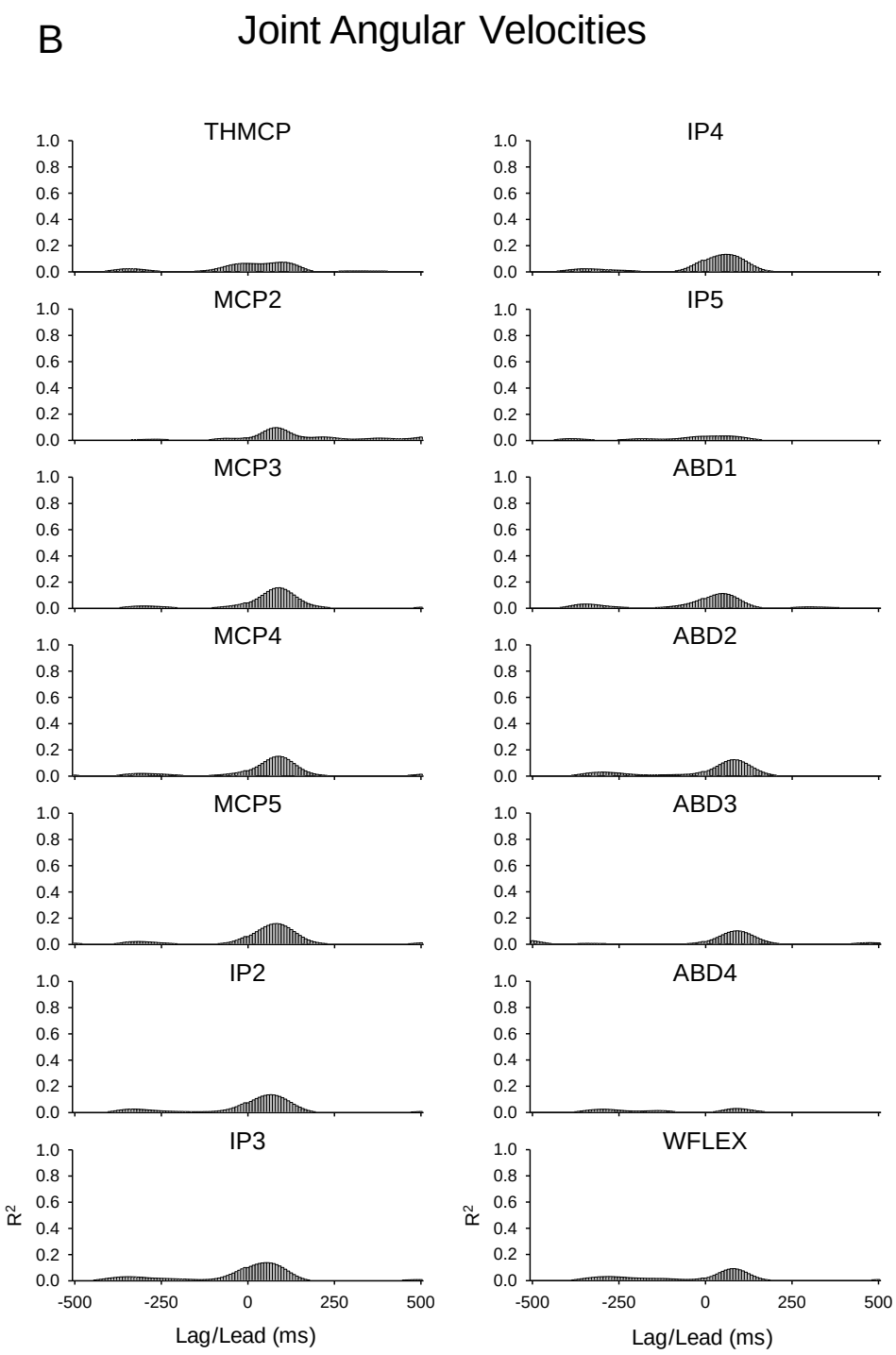

Figure 4.16. R^2-values obtained for each lead and lag. A and B) Resulting R^2-values for regression analysis of the firing of cell T081 with A) joint angles and B) joint angular velocities at each neural time-shift between -500 ms and 500 ms in 8.33 ms increments.

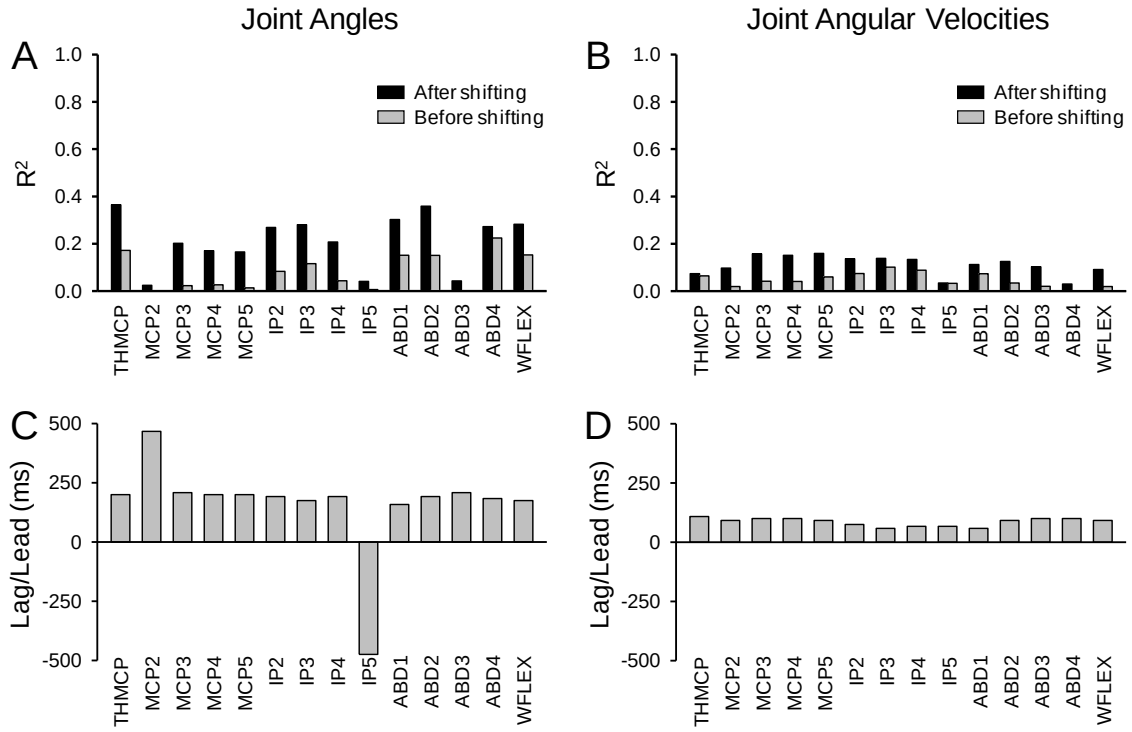

Figure 4.17. Resulting R^2-values and corresponding lead or lag for regression with temporally shifted data for model cell (T081). R^2-values from regressions with each A) joint angle and B) joint angular velocity before and after incorporating shift (τ) in neural firing. C and D) Temporal shift corresponding to the highest R^2-value (between -500 and 500 ms) for joint angles (C) and joint angular velocities (D).

The population data for the time shifted regressions were analyzed similarly to the regressions without a shift, in which only regressions that resulted in an $R^2 \geq 0.138$ were included (Cohen, 1988). The average correlations for joint angles were higher after incorporating a temporal shift (Figure 4.18A) compared to no shift (Figure 4.13A). For example, for premove cells the average R^2-values for the MCP2 joint angle increased from 0.31 to 0.40. The correlations with joint angular velocities, however, showed the

most improvement (Figures 4.13 B and 4.18B). For THMCP joint angular velocity, the average R^2-value increased from 0.20 before shifting to 0.32 after for reach cells.

For all cell types, the percentage of cells displaying a high R^2 increased for most joint angles and joint angular velocities after incorporating the time-shift (Figure 4.18 C and D). For example, the percentage of reach cells that were highly correlated with MCP4 increased from 38.6% (Figure 4.13 C) before a temporal shift to 57.9% after (Figure 4.18C). Regressions with joint angular velocities also increased in the percentage of cells that were highly correlated, but the percentages remained lower than those for joint angles. These percentages also increased for the overall models, with up to 90% of cells in a category displaying significant and high correlation to the model (Figure 4.18 C and D). The percentages of cells displaying high R^2s with more than 3 elements also increased markedly for both joint angles and angular velocities (Figure 4.19). R^2-values between neural firing and wrist path and speed increased by an average of 0.13 and 0.08, respectively, compared to regressions without a temporal shift (Figures 4.15 A and 4.20A). This was mirrored by an increase in cells displaying significant R^2-values (Figures 4.15 B and 4.20B).

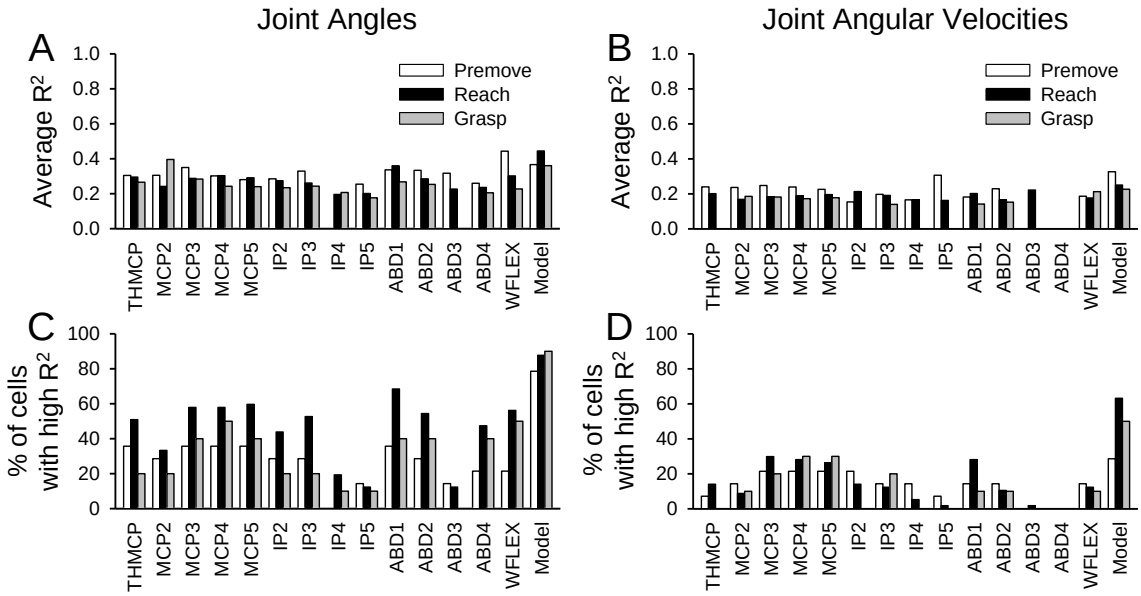

Figure 4.18. Population results of the time-shifted regressions. A and B) Mean R^2 for the time-shifted regressions of neural firing with joint angles (A) and joint angular velocities (B) for all epochs for each category of cells. Only cells with high ($R^2 \geq 0.138$) and significant R^2-values were included. Standard deviations were not included to prevent crowding. C and D) Percentage of cells with $R^2 \geq 0.138$ for the time-shifted regressions with joint angles (C) and joint angular velocities (D) for all epochs for each category of cells.

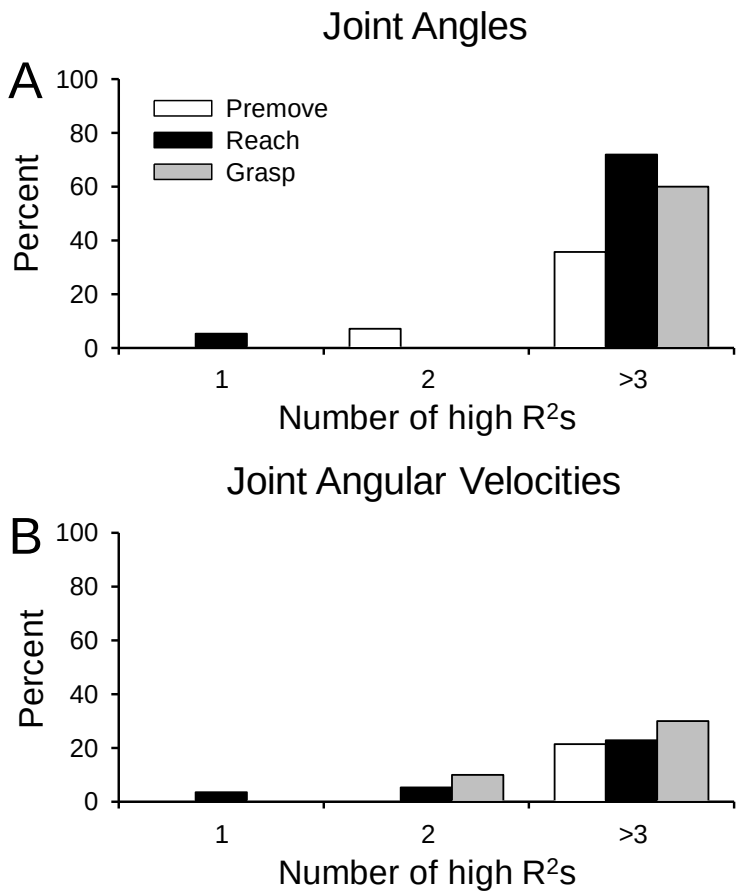

Figure 4.19. Percentage of cells displaying high correlations to each number of individual elements for temporally shifted data. A-B) Percentage of cells displaying $R^2 \geq 0.138$ for 1, 2, or >3 joint angles (A) or joint angular velocities (B) for all epochs for each category of cells.

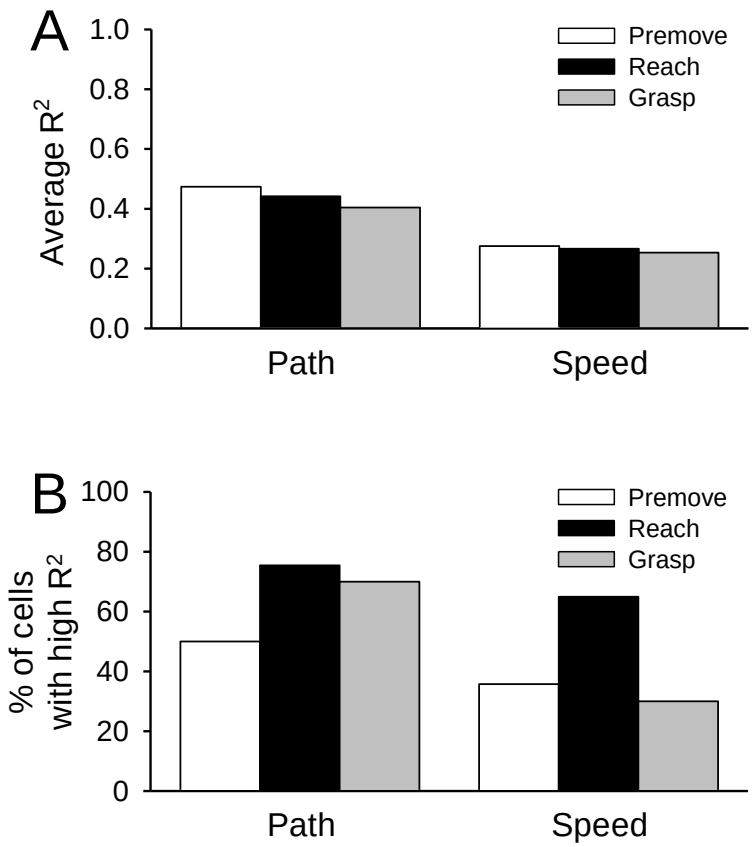

Figure 4.20. Population results of the time-shifted regressions with wrist trajectory and speed. A) Mean R^2 for time-shifted regressions of neural firing with wrist trajectory and speed for all epochs for each category of cells. Only cells with high ($R^2 \geq 0.138$) and significant R^2-values were included. Standard deviations were not included for consistency. B) Percentage of cells with $R^2 \geq 0.138$ for the time-shifted regressions with wrist trajectory and speed for all epochs for each category of cells.

The majority of shifts for the population of cells were for a lead between 151 and 200 ms for regressions with joint angles and between 251 and 300 ms for joint angular velocities (Figure 4.21). The majority (90.2% for joint angles and 96.3% for joint angular velocities) of shifts for premove cells were leads. Reach and grasp cells were distributed more evenly between lags (40.2% reach, 38.2% grasp) and leads (59.8% reach, 61.8% grasp) for regressions with joint angles, but were nonetheless dominated by leads. Results were similar for regressions of firing with joint angular velocities. On average, joint angles displayed a lead of 115.7 +/- 224.3 ms and joint angular velocities a lead of 91.9 +/- 151.6 ms. Wrist trajectory and speed, on the other hand, had nearly equal numbers of leads (average of 53.5% and 48.2%, respectively) and lags (average of 46.5% and 51.7%, respectively) (Figure 4.22). Most shifts were between 1 and 50 ms lag for wrist trajectory or 151 and 200 ms lead for wrist speed, and the overall average for each was 62.4 +/- 237.1 ms and 26.1 +/-116.2 ms, respectively.

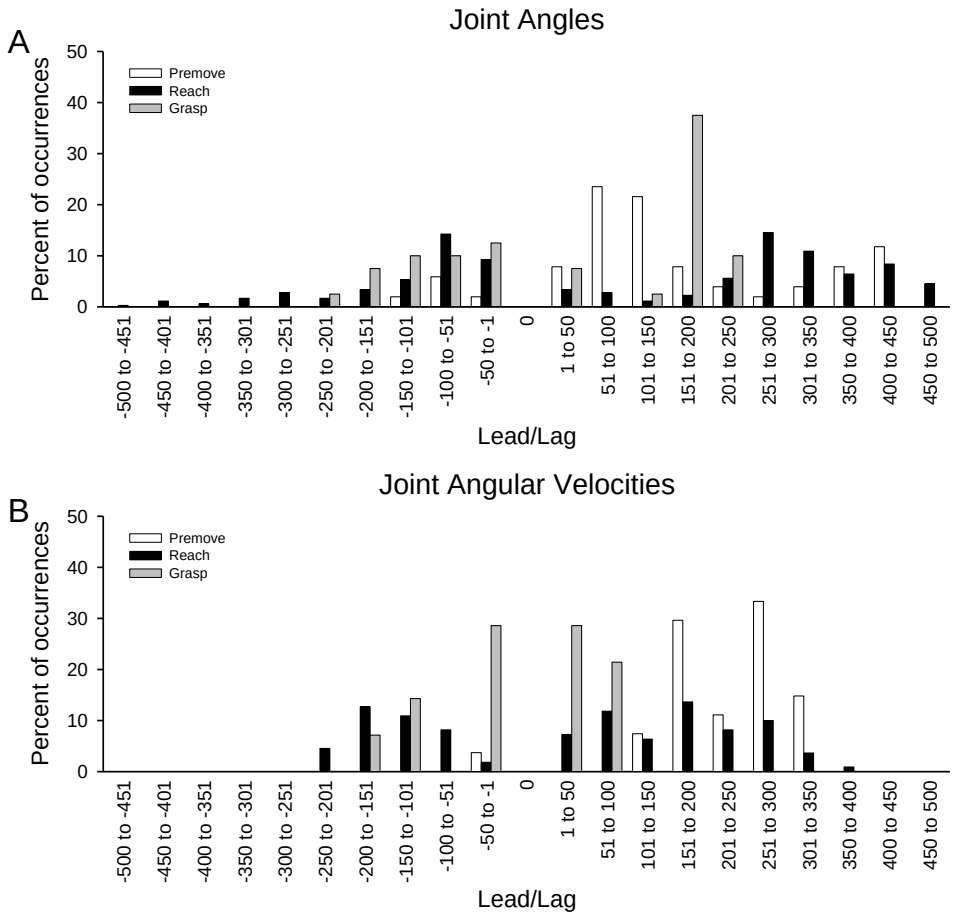

Figure 4.21: Population lead/lag shifts for individual elements. The percentage of occurrences of each range of leads or lags for joint angles and angular velocities for each category of cells.

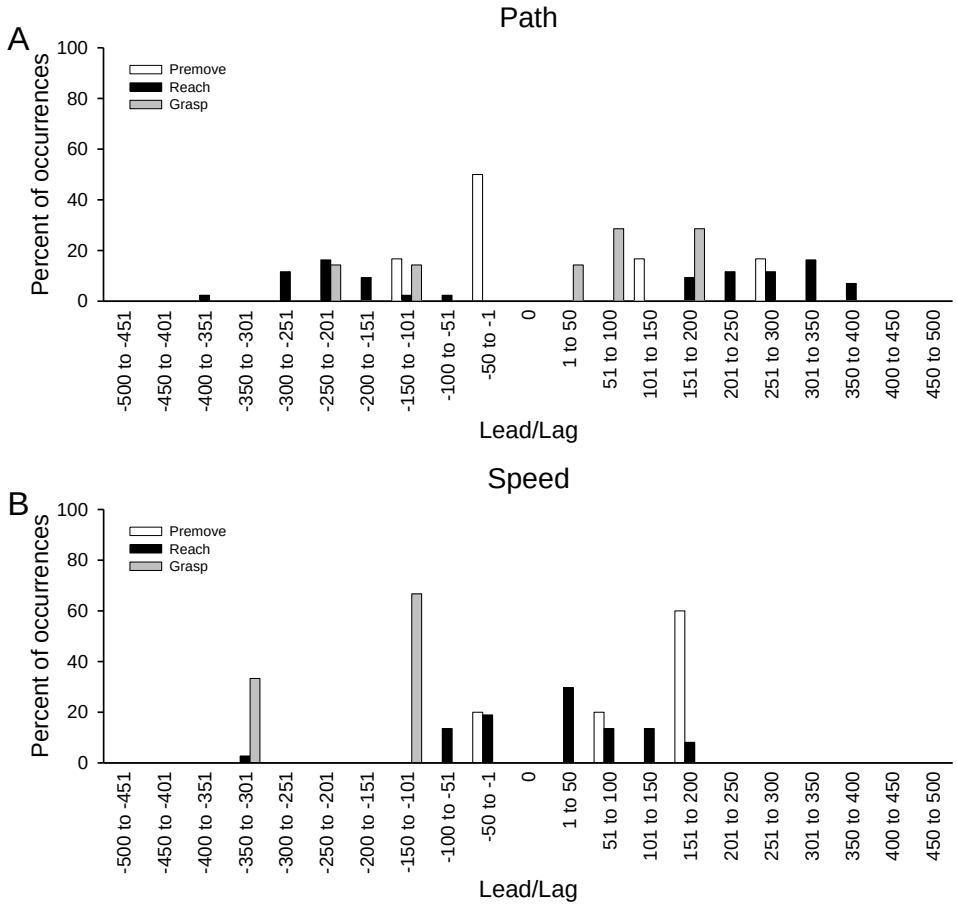

Figure 4.22. Population lead/lag shifts for wrist path and speed. The percentage of occurrences of each range of leads or lags for wrist trajectory and speed for each category of cells.

4.4 Limitations of linear regression analysis

While the firing of most cells was significantly correlated to individual joint elements, the interpretation of these correlations is not straight-forward. Due to the nature of the task as well as biomechanical constraints, the temporal profiles of several of the joint angles and angular velocities were highly correlated (see Figure 3.12). Comparing the regression results based on the individual elements versus the overall models reveals several major problems. First, the R^2-value for the overall model improved only marginally over the R^2 of the individual elements (Figures 4.7, 4.9, 4.11). For example cell B015 (Figure 4.23), the overall model R^2 for the joint angular velocities was 0.29, which is only 6.7% higher than the R^2-value for the MCP5 (0.23) joint angular velocity regressed alone (Figure 4.23B). Similarly, the sum of the R^2-values of the regression of firing to joint angles (R^2=0.74) is considerably larger than the overall model (R^2=0.33; Figure 4.23A). For regressions of independent parameters, the summation of the R^2s for individual regressions should be approximately equal to the R^2 for the overall model. This failure of the R^2-values for the individual components to sum was true for 79% (64/81) of cells for joint angles and 75% (61/81) of cells for joint angular velocities. On average, the summation of the R^2s for individual regressions was 0.67 larger than the model for joint angles and 0.18 for joint angular velocities. This suggests that the high R^2-values obtained for the individual elements that have a high degree of colinearity (i.e. MCPs, IPs, and WFLEX) are inflated.

The difficulty of interpreting the regression results is reinforced by comparing the coefficients obtained from the overall models (Figure 4.23 C and D) with the regressions

of the elements individually (Figure 4.23 E and F). The regression coefficients from a multiple linear regression describe how much the dependent variable (e.g. neural firing) changes when an independent variable (e.g. MCP2) changes while the remaining independent variables are held constant (Berry and Feldman, 1985). When the independent variables of a multiple linear regression are orthogonal, the regression coefficients for each parameter are the same as the coefficients obtained for separate regressions (Abdi, 2003). In other words, the coefficient describes the slope between the dependent variable and the independent variable. As the degree of colinearity between independent variables increases, the values of the multiple regression coefficients and the independent regression coefficients diverge. When the colinearity between independent variables is high, as is the case between most joint angles or angular velocities, the regression coefficients obtained from a multiple regression model do not compare to the coefficients from a single parameter model (Abdi, 2003). As shown in Figure 4.23, few similarities exist between the coefficients obtained for individual and multiple linear regressions of the joint angles or joint angular velocities. Whether the coefficients were positive or negative also varied between the individual element and overall model regressions. For example, the coefficients for MCP2 and MCP4 are positive for the individual element regressions and negative for the overall model. Therefore, the regression coefficients from the overall model do not accurately describe the relationship between the neural firing and each individual element separately.

The significance (p-value) of each coefficient is also misleading due to their instability. An unstable regression coefficient has a confidence interval that is wide or

includes zero, as defined by Student's t-tests (Berry and Feldman, 1985; Freund and Wilson, 1998; Cohen et al., 2003), indicating that a small change in the independent variable can result in large changes in the dependent variable. Unstable coefficients are often inaccurate at defining the relationship between the independent variable and dependent variable in the absence of the other model parameters. Instability leads to improper definition of significance of a regression coefficient. Cell B015, for example, had several coefficients from the individual element regressions that were significant, yet the same predictors were insignificant for the overall regression model (Figure 4.23 A and B). Specifically, the coefficient for the MCP2 angular velocity was insignificant (Figure 4.23D), despite having a large R^2-value that was significant when regressed individually (Figure 4.23F). These inconsistencies suggest the presence of unstable regression coefficients. Therefore, the ability to explain the neural firing in relation to each element separately using the coefficients from the multiple regression is greatly limited. However, if all parameters are used together, the ability for the overall model to predict the neural firing is accurately represented by the model coefficients, and the power of that prediction is properly represented by the R^2-values (Berry and Feldman, 1985; Freund and Wilson, 1998; Cohen et al., 2003).

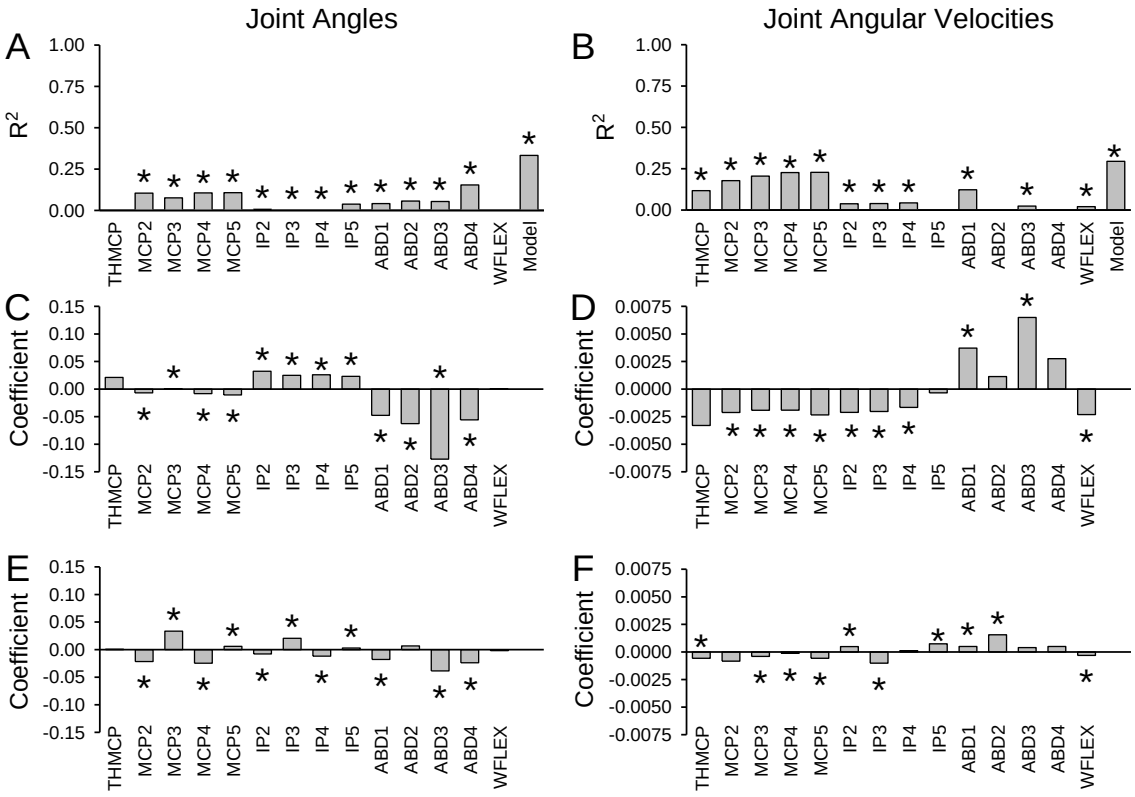

Figure 4.23. Analysis of regression coefficients (B015). A-B) R^2-values resulting from regressions between neural firing and individual joint angles (A) or joint angular velocities (B). C-D) Coefficients from the regression of all joint angles combined (C) or joint angular velocities combined (D). E-F) Coefficients from the regression of each joint angle (E) or joint angular velocity (F) individually. Star denotes significance ($p \leq 0.05$).

4.5 Discussion

It is well established that the firing of M1 neurons modulates in relation to several properties of reach-to-grasp. For instance, M1 discharge is correlated to extrinsic properties of reach, including movement direction (Georgopoulos et al., 1986; Caminiti et al., 1990; Fu et al., 1993; Georgopoulos et al., 1999), amplitude (Kalaska, 1991; Fu et al., 1993), force (Wannier et al., 1991; Georgopoulos et al., 1992; Cramer et al., 2002; Hendrix et al., 2009), and velocity (Reina et al., 2001). In addition, motor cortical cells are correlated with extrinsic properties of grasp, including weight and texture of the object being grasped (Picard and Smith, 1992a), as well as volume, orientation, size, and type of object (Mason et al., 2002; Hendrix et al., 2009).

The firing of M1 cells analyzed in this thesis was also modulated in relation to extrinsic properties. A large percentage of the cells had high correlations to the wrist path (up to 75.4%) and wrist speed (up to 64.9%), which are extrinsic reach properties. The majority of the 81 M1 neurons analyzed, from 3 separate chamber locations in 2 monkeys, also displayed significant differences in firing across objects (Figure 4.3), an extrinsic property of grasp. However, intrinsic properties such as joint angles were shown to vary across trials for the same object (see Figure 3.10 and 3.11). Therefore, ANOVA by object does not capture a cell's relationship to time-varying intrinsic properties of grasp. Variation in modulation across objects, while not the focus of this investigation, provides a foundation for examination of the correlation of the firing of motor cortical cells with other parameters.

The discharge of M1 neurons is also correlated to intrinsic properties of grasping such as joint angles of the fingers (Schieber and Hibbard, 1993; Georgopoulos et al., 1999; Poliakov and Schieber, 1999). These previous studies used individuated finger movements. This thesis is the first study examining the relationship of M1 to joint angles and angular velocities during reach-to-grasp, a more natural behavior in humans and non-human primates requiring the coordination of complex movements of the arm, hand, and fingers. Simple linear regressions were used to examine the relationship between motor cortical firing and kinematics of reaching and grasping. Many neurons exhibited high correlations with the various movement kinematics examined. In particular, several cells were highly correlated with joint angles of the hand. Between 29.6% and 32.1% of the cells displayed high R^2-values for regressions with MCP3-5 (Figure 4.13C), which increased to 51.9%-53.1% after incorporating a temporal shift (Figure 4.18C). With the exception of IP4-5 and ABD3, joint angles were highly correlated to the firing of more than 30% of cells when a lead or lag was included (Figure 4.18C). In addition, the firing of most cells led the joint angles (Figure 4.21A). The population average R^2-values were greater than 0.28 for all cells, and several joint angles (MCP2, MCP3, ABD1, and WLEX) had averages R^2s over 0.30 (Figure 4.18A). These correlations are remarkable considering the analysis was performed utilizing unaveraged, single-trial data. Also, the discharge of M1 cells was correlated with the movements of the wrist parameters of the reach. Therefore, the discharge of M1 cells signals many components of reaching and grasping. As suggested by others, these neurons are encoding complex, multidimensional information (Johnson et al., 2001; Aflalo and Graziano, 2006; Jackson et al., 2007).

The firing of M1 cells was also correlated to joint angular velocity, but to a lesser extent than joint angles (Figure 4.13). Other researchers found significant correlations between motor cortical firing and joint angular velocities of the arm during reaching (Reina et al., 2001), but none have examined the relationship of M1 neuronal discharge to joint angular velocities of the digits. Correlations with joint angular velocities were most evident in the time-shifted regression analysis (Figure 4.18 B and D). Before incorporating a lead or lag, a maximum of 10.5% of reach cells displayed high R^2-values for any one joint velocity, and IP5 and ABD3-4 joint angular velocities were not related to the firing of any cell (Figure 4.13D). In the time-shifted regressions, up to 30% of grasp cells were highly correlated to angular velocities (Figure 4.18D). Similar to joint angles, the firing of most cells led joint angular velocities (Figure 4.21B). However, there were no instances of M1 cells correlated to ABD4. On average, R^2-values were 0.20, which is lower than those for joint angles (Figure 4.13 A and C), but still high for single-trial behavioral data. These results further support M1s involvement with several components of grasping but emphasizes that different parameters are represented to differing degrees.

Also of interest is the timing between neural firing and the parameters of reaching and grasping. In this and previous studies (Hendrix et al., 2009), neurons in M1 exhibited several firing patterns, including being modulated during the *premove*, *reach*, and *grasp epochs* as well as combinations of the three (Figure 4.1A and B). Cells most modulated during reach had the strongest correlation with joint angles, in which an average of 18.9% of reach cells had high R^2s for joint angles compared to 15.4% and

17.3% for premove and grasp cells, respectively (Figure 4.13C). After incorporating a lead or lag, the percentage of neurons with high R^2s increased to 28.0%, 44.7%, and 30.8% of premove, reach, and grasp cells, respectively (Figure 4.18C). Premove and reach cells most commonly had high correlations with MCP and IP joint angles (Figures 4.7), suggesting involvement in overall opening and closing of the hand. In contrast, joint angular velocities were, on average, most highly correlated to premove (7.14%) and grasp cells (10%) rather than reach cells (3.5%) (Figure 4.13D). However, for the time shifted regressions these averages were nearly equal (13.3% premove, 13.8% reach, and 10.0% grasp) (Figure 4.18D). These results indicate that motor cortical cells are involved with several stages of prehension, including grasp planning, preshaping during the reach, and actual grasp (Gardner et al., 2007b; Spinks et al., 2008; Scott, 2008; Hendrix et al., 2009).

Most cells did not display a preference for a single joint angle or angular velocity (Figure 4.14 and 4.19). This conclusion must be tempered by the high degree of colinearity among joint angles or joint angular velocities (see Figure 3.12) that characterizes this and other reach-to-grasp tasks (Santello and Soechting, 1998; Mason et al., 2001; Santello et al., 2002; Braido and Zhang, 2004; Thakur et al., 2008). However, cells in M1 are correlated to multiple joints even when the instructed task is to individuate movements (Schieber and Hibbard, 1993; Georgopoulos et al., 1999; Poliakov and Schieber, 1999). It is expected that M1 cells having preferences to single joints would be rare. These results suggest that M1 is involved with instructing patterns in movement rather than individual degrees of freedom. Therefore, Chapter 5 examines

the correlation between the firing of M1 neurons and the patterns of hand shaping defined by the SVD analysis in Chapter 3.

In addition to finger joint kinematics, M1 cells were also highly correlated with wrist path and speed (Figure 4.15 and 4.20). This is not unexpected, as movements of the hand and arm are tightly coupled during prehension (Jeannerod, 1981; Jeannerod, 1984; Arbib et al., 1985). Changes in task parameters related to grasp, such as object size, subsequently result in changes in various components of reaching (Paulignan et al., 1991a; Paulignan et al., 1991b; Castiello et al., 1993). Both wrist path and speed were highly correlated with many of the finger joints and joint angular velocities (see Figure 3.12). For example, the temporal profile of the wrist speed was similar to THMCP, MCP2-5, IP2-5, increasing until approximately midway through the *reach epoch* followed by a decrease until grasp onset (see Chapter 3). The high correlations of these cells to components of both reaching and grasping further suggest that these neurons play a role in the coordination of the reach and grasp aspects of prehension.

Finally, it is important to discuss the neuroengineering implications of the regression analyses. The high R^2s obtained from the linear regressions with the separate individual elements suggest that neural firing could be predicted, with some degree of error, by knowing the state of only one of these elements. In turn, an algorithm utilizing these relationships could be developed to control individual joint angles or angular velocities of a robotic or virtual hand using single cell firing as an input signal. For instance, based on the highest R^2-values from these individual element regressions, the firing from cells B056, T081, and B015 could be used to control MCP3, ABD4, or MCP5

joint angular velocity, respectively (Figures 4.7, 4.9, and 4.11). However, a single cell would not be sufficient to precisely control each parameter. The level of precision in such a model would be improved by utilizing more than one cell to control each joint. In addition, the high degree of colinearity between the individual elements suggests that the model could be improved by incorporating parameters that quantitatively define the interrelationship between the elements.

Motor cortical firing was also examined using a multiple linear regression model including all joint angles or angular velocities. The regression coefficients from a multiple linear regression represent the effect of each individual parameter on the dependent variable with all other variables held constant (Berry and Feldman, 1985). While the R^2-values were larger for the overall models than for the individual joint element regressions (Figures 4.7, 4.9, and 4.11), the regression coefficients from the overall model cannot accurately predict the neural firing with respect to the separate individual elements (see Section 4.4) (Berry and Feldman, 1985; Freund and Wilson, 1998; Cohen et al., 2003). The regression coefficients from the overall model are only valid when using all parameters together to predict the neural firing. Therefore, it is extremely difficult to use these models to develop control algorithms for each kinematic parameter utilizing the firing of a single cell. For example, the firing in time (F(t)) for cell B015 can be described using the equation

$$F(t)= -0.02MCP2(t)+0.03MCP3(t)-0.02MCP4(t)-0.01IP4(t) \\ -0.02ABD1(t)-0.04ABD3(t)-0.02ABD4(t)$$

Equation 4.1

in which the firing rate is dependent on a combination of each joint angle in time as defined by the regression coefficients (Figure 4.23C). However, this equation cannot be reversed to predict each joint angle separately from the neural firing without holding all other parameters of the equation constant. Due to the high degree of colinearity of the joint angles and resulting unstable regression coefficients, these predictions would be inaccurate. Investigating neural firing in relation to the patterns described by SVD (Chapter 3) may provide a better substrate for producing command algorithms for technologies (Chapter 5).

Chapter 5: Primary motor cortical relation of patterns of prehension

5.1. Linear regression analysis of firing to temporal weightings from SVD analysis

The results of various SVD analyses provide a means for examining the relationship of the firing of motor cortical cells to both dominant as well as detailed hand shaping patterns. For example, the first eigenvector using unadjusted joint angle data represents the average hand shape and overall opening and closing of the hand. While the eigenvectors obtained from the SVD based on standardized data do not represent the mean, the first few eigenvectors explain the majority of the variability, suggesting that these eigenvectors also represent major patterns of hand shaping. In contrast, the higher-order eigenvectors characterize the more detailed movements of the hand because of the smaller amount of variance captured (Santello et al., 1998; Thakur et al., 2008). For our purposes, the first three temporal weightings (TWs) are considered to be "lower-order", or dominant patterns, and the remaining "higher-order", or details. The fundamental question is whether these hand shaping patterns are represented in the firing of the primary motor cortex or other central motor structures.

Linear regression analysis was used to quantify the correlation between the instantaneous firing, at the single-trial level, of each motor cortical cell and the hand shaping patterns derived from SVD. The relationship between cell firing and these patterns are easier to interpret than the individual element regressions (Chapter 4) due to the elimination or reduction of colinearity among the parameters assessed. Each cell's

firing was regressed against the TWs from each of the five SVD analyses described in Chapter 3 (see Table 2.2) individually as well as combined in an overall model (Equations 2.4 and 2.5; see Section 2.3.4 Data Analysis). The R^2-values for the TW regressions for the example cells from Chapter 4.2 are displayed in Figures 5.1-5.3.

The most common pattern of correlation observed between motor cortical firing and the TWs from SVD were high R^2-values for one or two lower-order TWs. The firing of the first example cell (B056) was highly correlated to only four TWs from all SVD types (Figure 5.1). For unadjusted joint angles, the regressions with TW1 and TW2 had high R^2s (R^2= 0.24 and R^2=0.22, respectively; Figure 5.1A). TW1 was highly negatively weighted for the THMCP, MCP, and IP joint angles (Figure 5.1E). TW2 had high positive weightings for MCP3-4 as well as high negative weightings for IP2-3 and IP5. Strong correlations were also found for TW1 of SVD of standardized joint angles (Figure 5.1A; R^2=0.24) and the combination of standardized joint angles and angular velocities (Figure 5.1C; R^2=0.26). As for the unadjusted data, these TWs were also dominated by the THCMP, MCP, and IP joint angles (Figure 5.1F and G). The correlations with these TWs reflect the high R^2-values obtained for THMCP, MCP2-5, and IP4 from the individual element regressions (see Figure 4.7).

The firing of cell B056 had minimal correlations with higher-order TWs (Figure 5.1A-C; R^2<0.06). Furthermore, the firing had limited correlations with TWs obtained from the joint angular velocities (Figure 5.1B, R^2<0.06). This latter finding mirrored the low correlations obtained for the individual joint angular velocities (see Figure 4.7). The TWs with high correlations had temporal profiles similar to the MCP and IP joint angles;

that is, an initial increase followed by a large decrease in the weight, similar to the temporal firing pattern of the cell (Figure 5.1D). For the unadjusted joint angle data, the temporal profile of TW1 was inverted (decrease followed by an increase) (Figure 5.1D). The overall models for the joint angle SVDs had R^2-values of 0.27 (unadjusted and standardized), 0.16 for joint angular velocities (unadjusted and standardized), and 0.33 for the combination of joint angles and joint angular velocities. The high degree of correlation with the lower-order TWs weighted for THMCP, MCPs, and IPs suggests involvement of cell B056 in the dominant patterns of hand shaping. Conversely, this cell does not signal the finer details of grasping (higher-order TWs) or joint angular velocity.

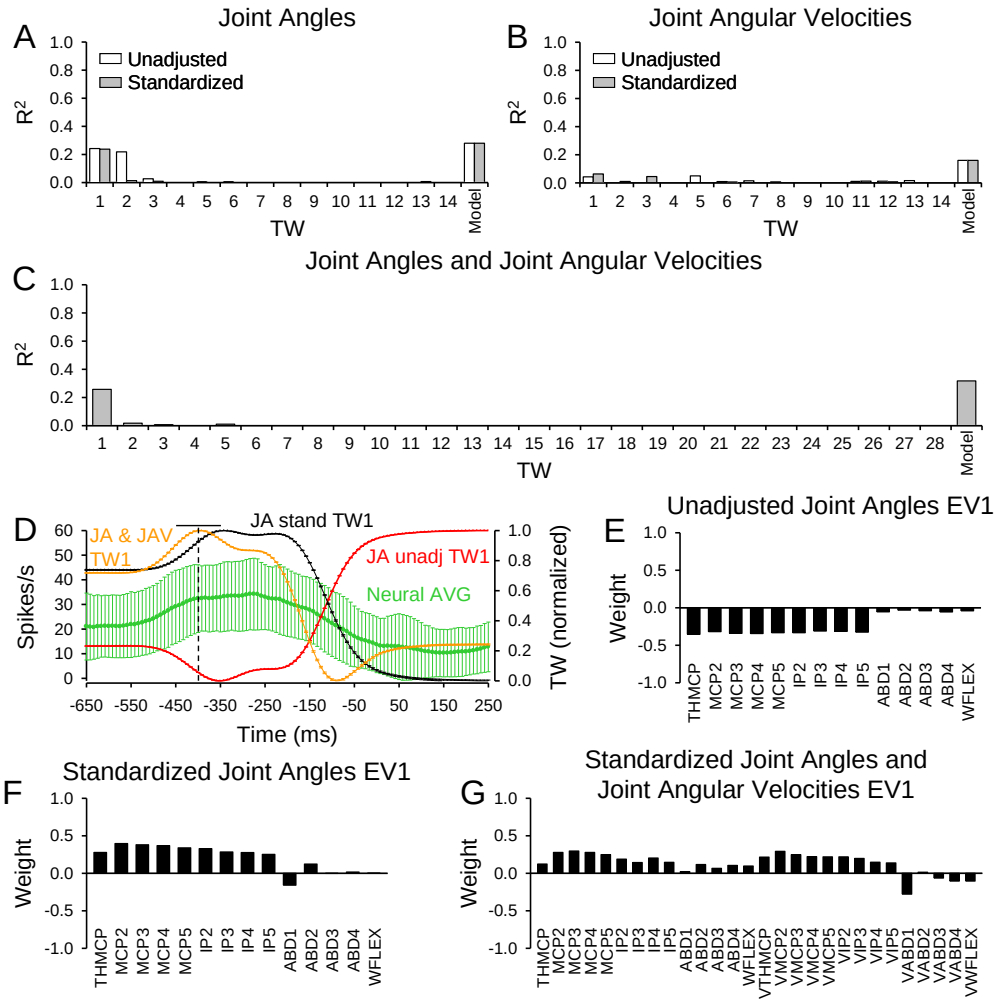

Figure 5.1: Regression analysis of neural firing with temporal weightings for an example cell (B056). A-C) R^2 for neural firing regressed with temporal weightings resulting from SVD with unadjusted and standardized joint angles (A), unadjusted and standardized joint angular velocities (B) and standardized joint angles and joint angular velocities combined (C) for all epochs. D) Average firing (+/- standard deviation) across all trials for the model cell over time (x-axis) and mean (+/- standard deviation) of the most significant TWs, TW1 of standardized joint angles and angular velocities combined, TW1 of unadjusted joint angles, and TW1 of standardized joint angles. Dashed line denotes average reach onset and bar above is +/- standard deviation of reach onset. E-G) Bar graphs of the of the eigenvector coefficients for the session for those with highest correlations to neural firing.

Although the majority of cells displayed high correlations to a small number of lower-order TWs, some cells were related to higher-order TWs. An example is cell T081 shown in Figure 5.2. In general, the R^2s for the regressions with individual TWs were smaller than for cell B056. The highest correlation was for TW4 obtained from the SVD with unadjusted joint angles (Figure 5.2A; R^2=0.15). The cell was also highly correlated with TW1 of standardized joint angles and angular velocities combined (R^2=0.14). Interestingly, this cell had R^2-values for several TWs that were only slightly lower than the specified high threshold. This included TW2 of unadjusted joint angles (Figure 5.2A; R^2=0.11), TW1-2 and TW6 of standardized joint angles (Figure 5.2A; R^2=0.09, R^2=0.09, and R^2=0.10, respectively), and TW3-4 of standardized joint angles and angular velocities combined (Figure 5.2C; R^2=0.09). The correlations with TWs obtained from joint angular velocity SVDs were small (Figure 5.2B; R^2<0.06).

The eigenvector associated with TW4 of unadjusted joint angles was primarily weighted for THMCP, MCPs, and IPs, with the exception of MCP2 and IP4 (Figure 5.2E). The weights were both positive and negative. The small eigenvalue for EV4 (1.38%) suggests that TW4 signals finer details in hand shaping. The temporal profiles of the TWs with high R^2s were similar to the neural firing, whether directly or inversely (Figure 5.2D). However, the neural firing tended to lag the TWs to which it was most highly correlated. The components of the TWs from all SVDs with high R^2s were not identical to the individual element regressions with high correlations (see Figure 4.9A). This suggests the cell is correlated with hand shapes not captured by the individual element analysis. For the overall models of joint angles or combined joint angles and

joint angular velocities the R^2-values were large (R^2=0.54 and R^2=0.59, respectively), while the R^2 for the overall model of joint angular velocities was much smaller (R^2=0.14). The relationships to multiple higher-order TWs suggests that cell T081 is related to complex details of hand shaping.

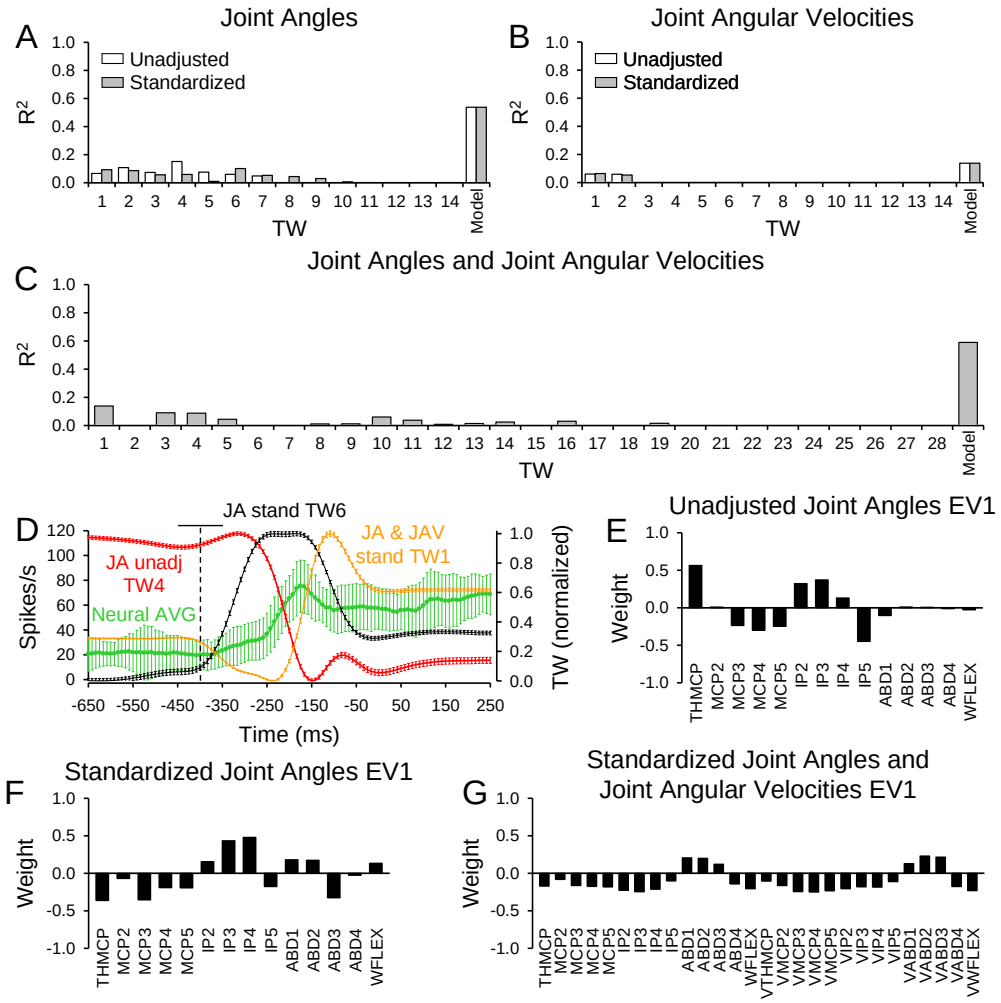

Figure 5.2. Regression analysis of neural firing with temporal weightings for an example cell (T081). A-C) R^2 for neural firing regressed with temporal weightings resulting from SVD with unadjusted and standardized joint angles (A), unadjusted and standardized joint angular velocities (B) and standardized joint angles and joint angular velocities combined (C) for all epochs. D) Average firing (+/- standard deviation) across all trials for the model cell over time (x-axis) and mean (+/- standard deviation) of the most significant TWs, TW1 of standardized joint angles and angular velocities combined, TW4 of unadjusted joint angles, and TW6 of standardized joint angles. Conventions as in Figure 5.1. E-G) Bar graphs of the of the eigenvector coefficients for those with highest correlations to neural firing.

A small percentage of cells were highly correlated to TWs from SVD of joint angular velocities. This is illustrated in the final example cell (B015) that had high R^2-values for the regressions of firing to the TWs derived from joint angular velocities (Figure 5.3). For this cell, the highest R^2-values were obtained for TW1 from the unadjusted and standardized joint angular velocities (R^2=0.21 and R^2=0.19, respectively; Figure 5.3B), and TW1 of standardized joint angles and angular velocities combined (R^2=0.23; Figure 5.3C). The eigenvectors for these TWs were primarily weighted for the MCP and IP joint angular velocities, with EV1 of standardized data also weighted for THMCP (Figure 5.2 E-G). This is not unexpected, as the firing of this cell was highly correlated to the THMCP and MCP2-5 joint angular velocities in the individual element regressions (see Figure 4.11). The cell also had high correlations with TW2 of unadjusted and standardized joint angles (R^2=0.13 and R^2=0.17, respectively; Figure 5.3A). The R^2s for the overall models of joint angles (R^2=0.33 for both) were larger than those for the overall models of joint angular velocities (R^2=0.29 for both). The temporal profiles of the TWs with the highest correlations to neural firing exhibited multiple increases and decreases during the *reach epoch* (Figure 5.3D), but generally matched the temporal profile of the neural firing. These findings suggest that this motor cortical cell signals a combination of joint position and velocity.

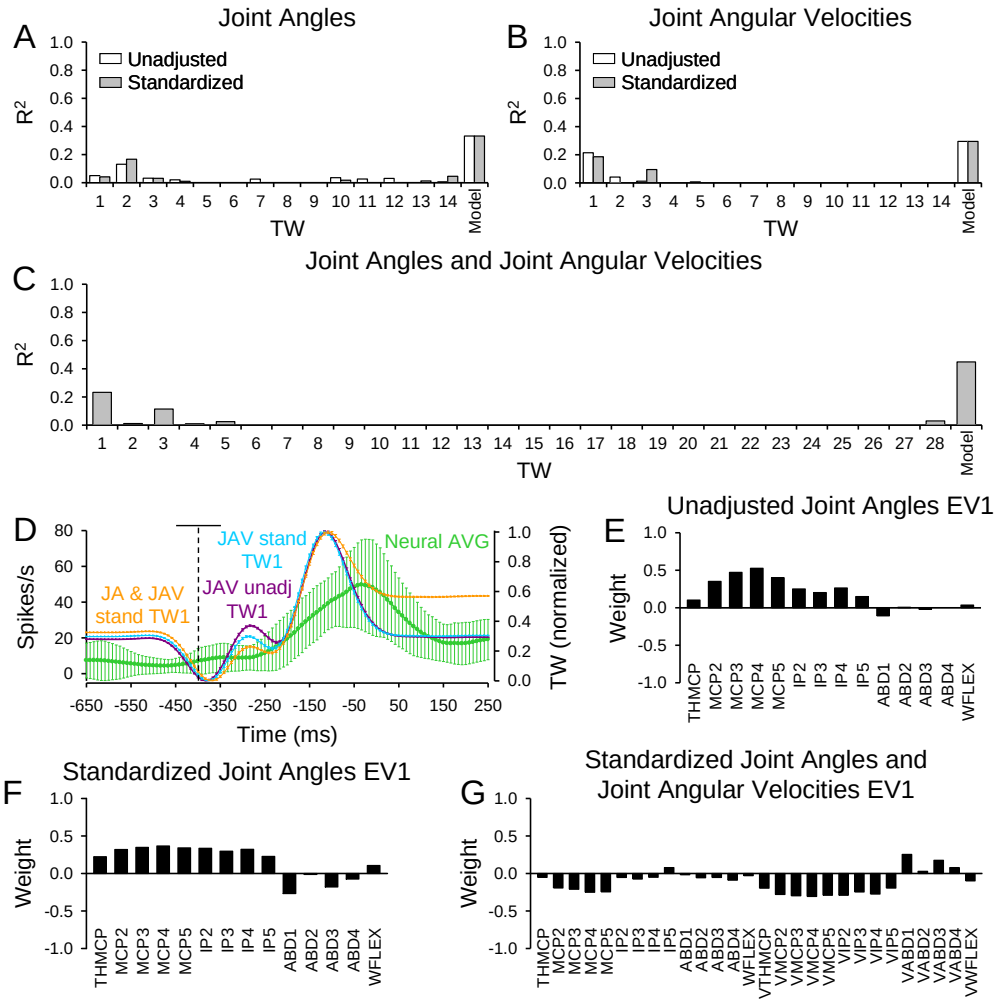

Figure 5.3. Regression analysis of neural firing with temporal weightings for an example cell (B015). A-C) R^2 for neural firing regressed with temporal weightings resulting from SVD with unadjusted and standardized joint angles (A), unadjusted and standardized joint angular velocities (B) and standardized joint angles and joint angular velocities combined (C) for all epochs. D) Average firing (+/- standard deviation) across all trials for the model cell over time (x-axis) and mean (+/- standard deviation) of the most significant TWs, TW1 of standardized joint angles and angular velocities, TW1 of unadjusted joint angular velocities, and TW of standardized joint angular velocities. Conventions as in Figure 5.1. E-G) Bar graphs of the of the eigenvector coefficients for those with highest correlations to neural firing.

To examine how the population of cells are related to the TWs, the R^2-values were averaged by category (maximal firing during *premove*, *reach*, or *grasp* epochs) and are displayed in Figure 5.4. Only high ($R^2 \geq 0.138$) (Cohen, 1988) and significant ($p \leq 0.05$) correlations were included in the average to prevent skewing. In general, the population average R^2s for the individual TWs were similar across SVDs and cell types (Figure 5.4). Averages ranged from 0.14 (TW4 standardized joint angular velocities and TW6 standardized joint angles) to 0.40 (TW2 standardized joint angles and angular velocities combined). In addition, the average R^2s for the overall model were similar to those for the individual TWs. This similarity in the R^2-values obtained from the individual and overall model implies that for most cells, the high correlations were restricted to one or two TWs (see below).

A striking observation is that the high correlations were almost exclusively obtained for the regressions to TW1-3, irrespective of the type of SVD (Figure 5.5). Very few premove or grasp cells (up to 30%) yielded high R^2-values from regressions with TWs. However, up to 40.4% of reach cells were highly correlated with TWs. In addition, most cells were highly correlated with the overall models (up to 86% for standardized joint angles and angular velocities combined). A small percentage of cells displayed high R^2-values for higher-level TWs for reach cells (3 cells for SVD with unadjusted joint angles, 2 cells for SVD with standardized joint angles, and 1 cell for SVD with standardized joint angles and angular velocities combined), but no other cell types were highly correlated to TWs 5-14. Overall, the firing of these motor cortical cells

was correlated to dominant patterns in hand shaping. The firing of only a small number of cells was related to details in hand shaping.

An additional observation is that cells displayed high correlations to only a small number (1-3) of TWs. For unadjusted joint angles, cells were equally related to one (17.3%) or two TWs (22.2%) (Figure 5.6A). Most often (89% of cases), these were the first and second TWs (Figure 5.6 F), suggesting that these cells are related to the average hand shape and one additional dominant pattern. The majority of cells were highly correlated to only one TW derived from the standardized joint angles (35.8%) (Figure 5.6C), or standardized joint angles and angular velocities combined (34.6%) (Figure 5.6E). Few cells were found to be highly correlated with TWs for unadjusted (3.7%) or standardized (6.2%) joint angular velocities and these correlations were limited to a single TW (Figure 5.6 B and D).

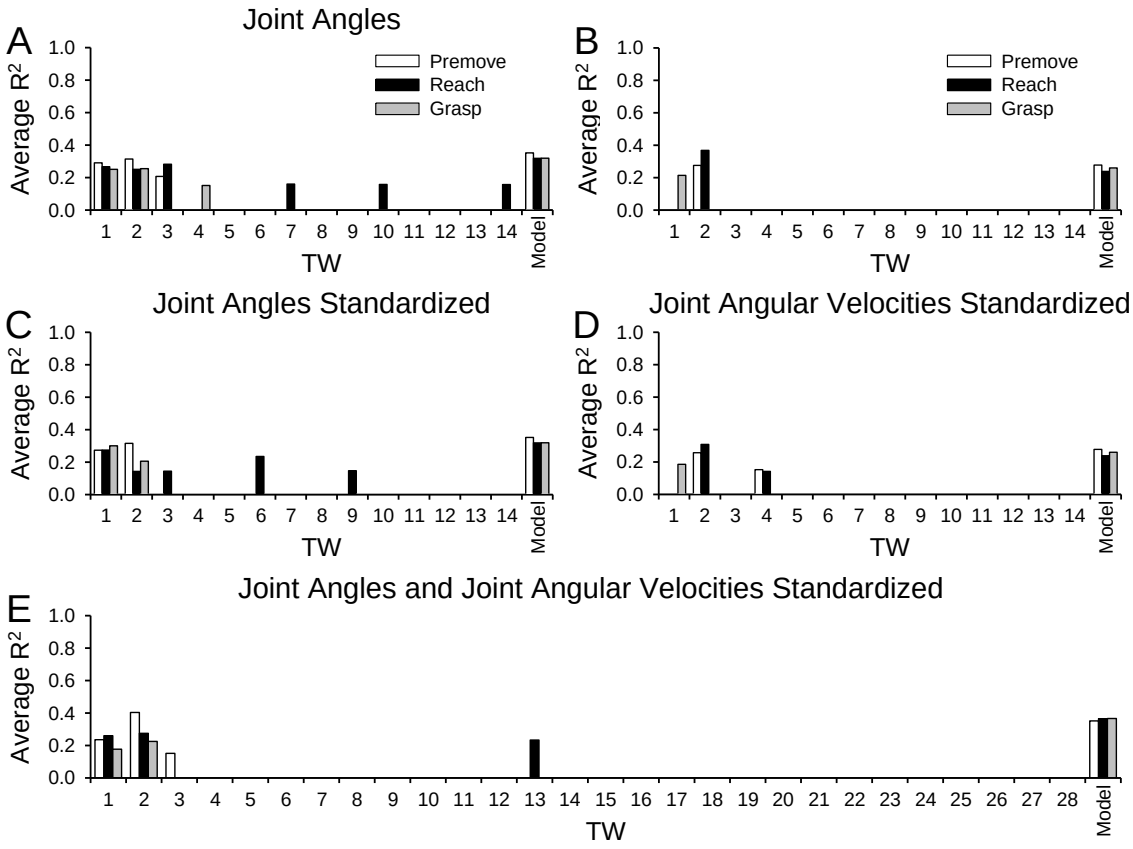

Figure 5.4. Population average R^2-values obtained from the regression analysis of neural firing with temporal weightings. A-E) Mean R^2 for neural firing regressed with temporal weightings (TWs) resulting from SVD with unadjusted (A) and standardized joint angles (C), unadjusted (B) and standardized (D) joint angular velocities, and standardized joint angles and angular velocities (E) for all epochs for each category of cells. Only cells with high ($R^2 \geq 0.138$) and significant R^2-values were included. Standard deviations were not included to prevent crowding.

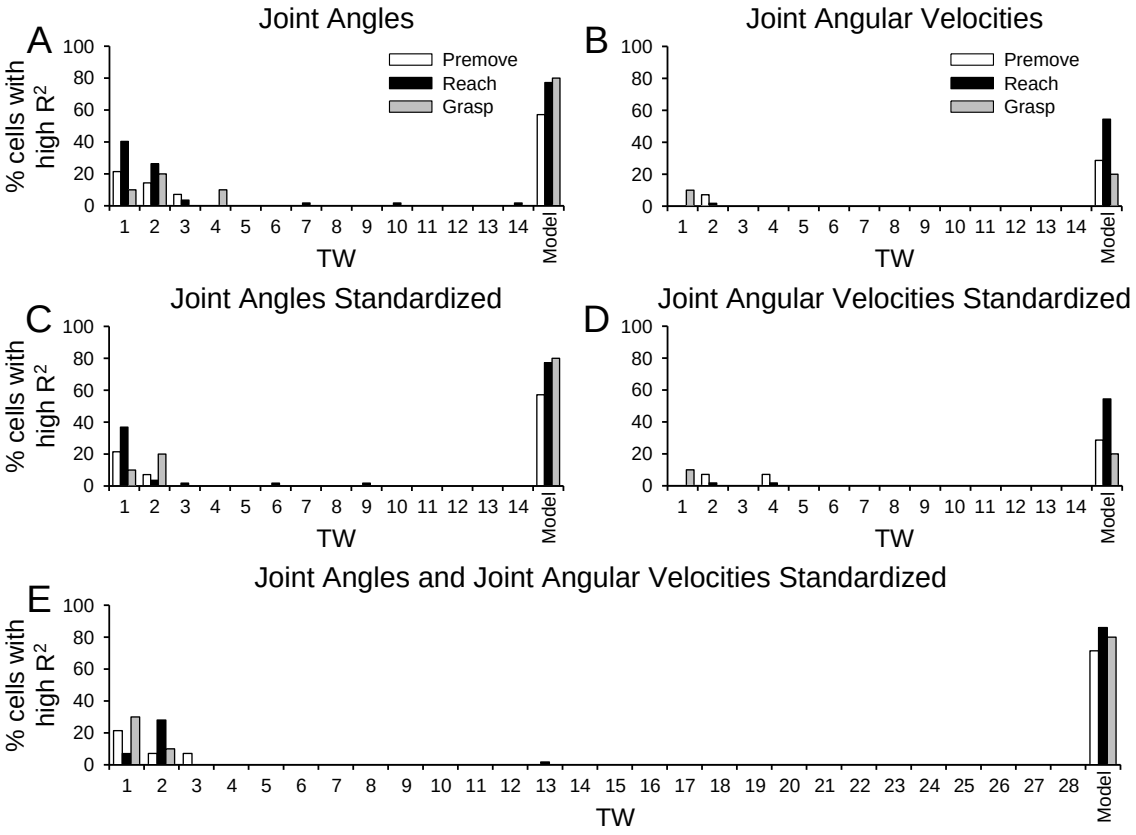

Figure 5.5. Percentage of cells displaying high correlations to temporal weightings. A-E) Percentage of cells displaying high R^2-values ($R^2 \geq 0.138$) when regressed with temporal weightings (TWs) resulting from SVD with unadjusted (A) and standardized joint angles (C), unadjusted (B) and standardized (D) joint angular velocities, and standardized joint angles and angular velocities (E) for all epochs for each category of cells.

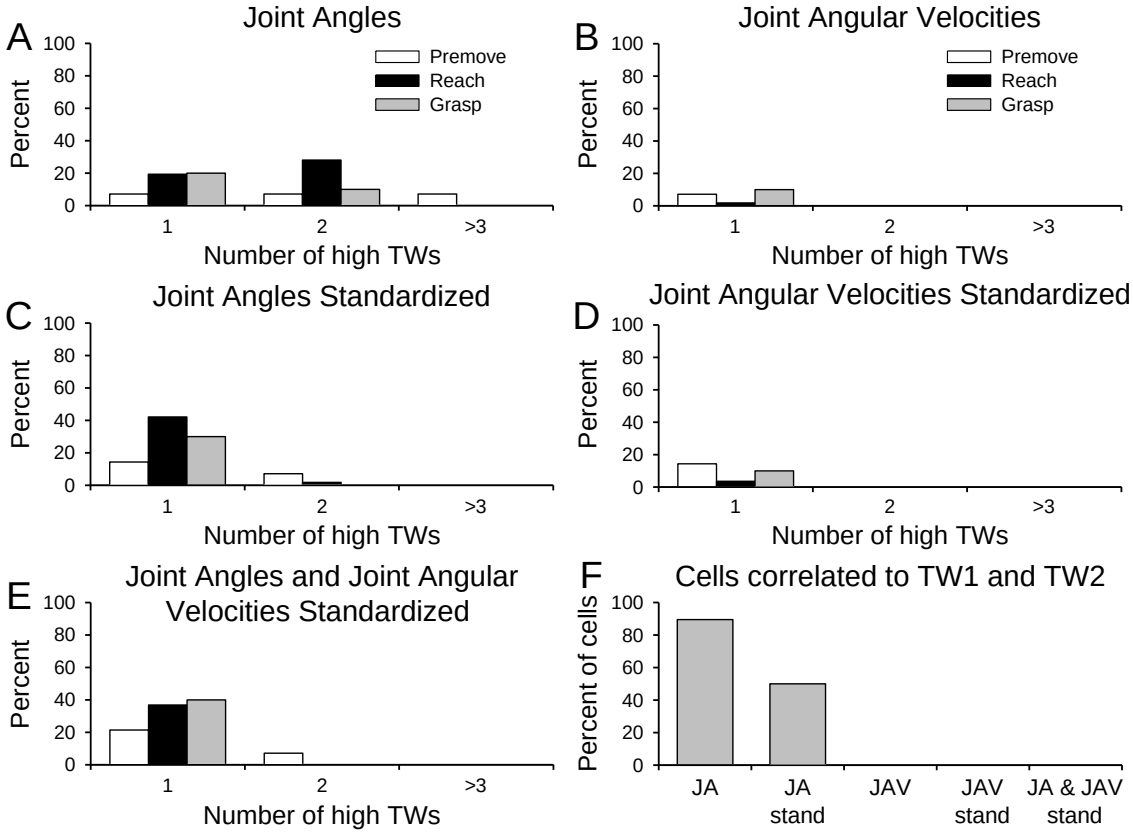

Figure 5.6. Percentage of cells displaying high correlations to each number of temporal weightings. A-E) Percentage of cells displaying high R^2-values ($R^2 \geq 0.138$) for 1, 2, or >3 temporal weightings (TWs) resulting from SVD with unadjusted (A) and standardized joint angles (C), unadjusted (B) and standardized (D) joint angular velocities, and standardized joint angles and angular velocities (E) for all epochs for each category of cells. F) Of the cells that were highly correlated to two or more TWs, the percentage of cells highly correlated to TW1 and TW2.

5.2 Time-shifted linear regression analysis of firing to temporal weightings from SVD analysis

The effect of a lead or lag (τ) was examined to maximize the relationship of the neural firing to TWs from SVD. As for the regression analysis with the individual elements, the ranges examined for lead/lag were limited to +/- 500 ms in 8.33 ms increments. Similar to other population analyses, only high ($R^2 \geq 0.138$) (Cohen, 1988) and significant results were included. After incorporating a temporal shift (Figure 5.7), the average R^2-values increased primarily for the higher-order TWs. However, for many TWs the average remained zero because of the failure to reach the high correlation criterion. The largest average R^2s remained concentrated for the regressions to TW1-3 for all SVDs (Figure 5.7), and the averages for the overall models were only slightly higher than for TWs individually.

The percentage of cells displaying high correlations after including a temporal shift nearly doubled for most TWs and SVD types (Figure 5.8). For example, the percentage of premove cells that had correlations with TW1 or TW2 of SVD with unadjusted joint angles increased from 14.3% to 28.6%. In contrast to the small number of premove and grasp cells with high correlations to TWs before time-shifting, up to 42.8% (TW2 unadjusted joint angles) of premove or 60% (TW1 of unadjusted or standardized joint angles) of grasp cells were highly correlated to individual TWs after incorporating a lead or lag (Figure 5.8). Almost all cells displayed high R^2s for overall models of TWs from joint angle (78.6%-90%), joint angular velocity (28.6%-63.2%), and combined joint angle and angular velocity SVDs (78.6%-90%). In addition, the number of occurrences of high correlations for higher-order joint angle TWs increased from 6 to

17 (e.g. TWs 4-7, 9-11, and 14; Figure 5.8). However, the percentage of cells with firing correlated to these TWs remained small in comparison to lower-order TWs, reinforcing that the firing profiles reflected the patterns of hand shaping that describe the most variance. Finally, the percentage of cells with high correlations for TWs derived from joint angular velocities remained considerably smaller than for joint angles, irrespective of the type of SVD or model.

After incorporating the temporal shift, most cells were related to two TWs for SVD with standardized joint angles (40.7%) and joint angles and angular velocities combined (30.9%) (Figure 5.9 C and E). For SVD with unadjusted joint angles, most cells were correlated with three or more TWs (35.8%) (Figure 5.9 A). Similar to unshifted data, most cells (95.9%) with correlation to multiple TWs typically had high R^2-values for TW1 and TW2 (Figure 5.9 F). The percentage of cells with high R^2s for joint angular velocity TWs increased compared to unshifted data, but most cells were still only related to one TW (Figure 5.9 B and D).

The average temporal shifts for all cell types were similar across SVDs (Table 5.1). Consistent with regressions for individual elements, the average shifts were leads (Chapter 4), but varied greatly by cell type and the SVD (Figure 5.10). For example, most shifts (63.6%) for grasp cells with TWs from standardized joint angles were lags, while the majority (60%) of shifts obtained for premove cells were leads (Figure 5.10C). On the other hand, the shifts obtained for the regressions with TWs from unadjusted joint angles were more heavily distributed as leads for all cell types. For both unadjusted and standardized joint angular velocities the shifts varied greatly across cell types. However,

due to the small number of regressions displaying high and significant R^2-values (range 1-5), it is difficult to generalize whether the relationship of the population to these TWs is a lead or lag.

Table 5.1. Population average lead or lag. The average (mean and standard deviation) for all cells for each SVD.

	Mean	Standard Deviation
Unadjusted joint angles	93.5 ms	255.2 ms
Standardized joint angles	60.6 ms	262.0 ms
Unadjusted joint angular velocities	51.9 ms	175.3 ms
Standardized joint angular velocities	80.5 ms	165.2 ms
Standardized joint angles and angular velocities	61.3 ms	233.7 ms

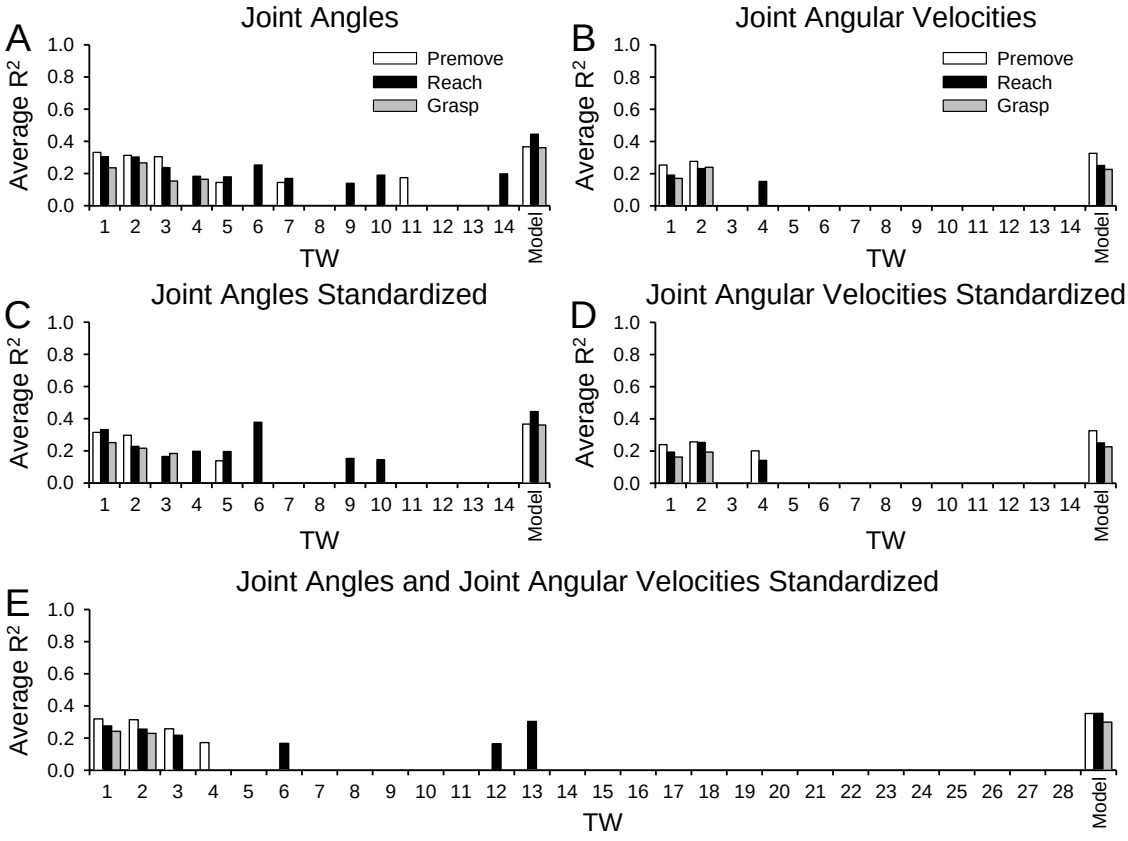

Figure 5.7. Population results obtained from the regression analysis of SVD temporal weights with neural firing after incorporating a lead or lag. Bar graphs of the mean R^2 for shifted neural firing regressed with TWs from SVD with unadjusted joint angles (A), unadjusted joint angular velocities (B), standardized joint angles (C), standardized joint angular velocities (D), and standardized joint angles and angular velocities combined for all epochs for each category of cells. Only cells with high ($R^2 \geq 0.138$) and significant R^2-values were included. Standard deviations were not included to prevent crowding.

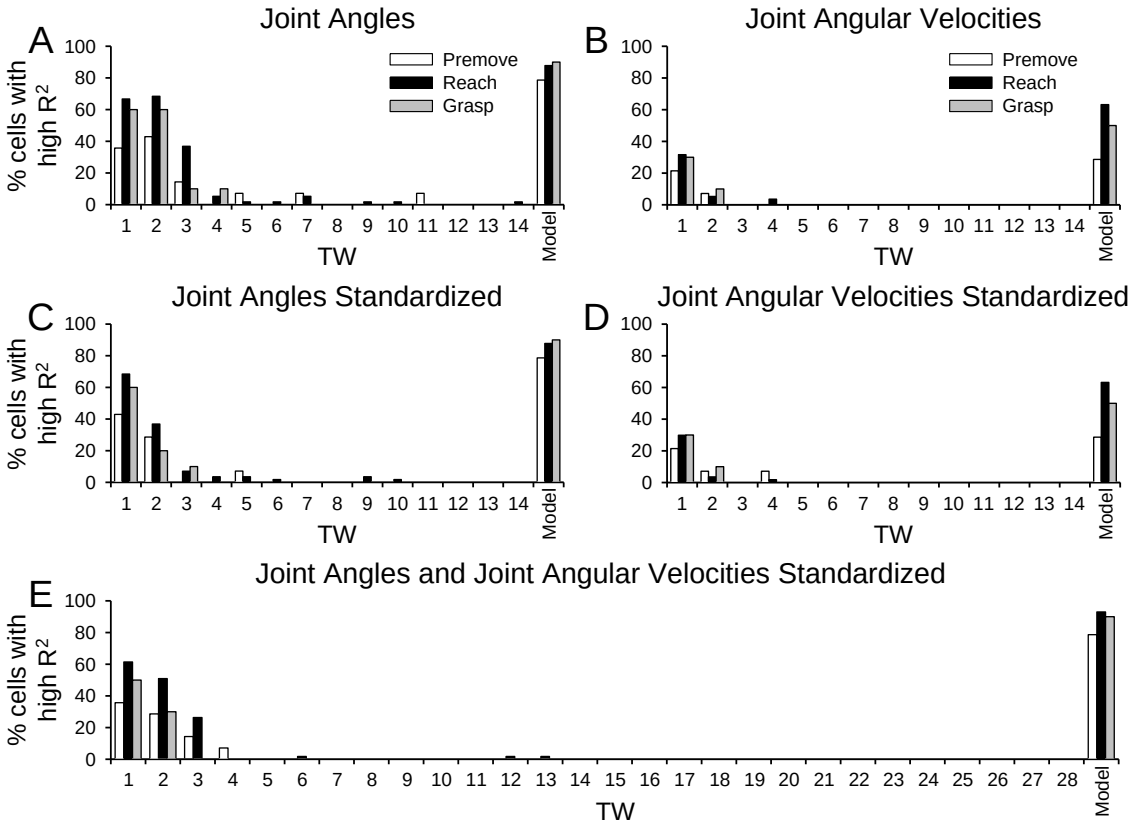

Figure 5.8. Percentage of cells with high and significant correlations obtained during regression analysis of SVD temporal weights with neural firing after incorporating a lead or lag. Bar graph of the percentage of cells with $R^2 \geq 0.138$ and that were significant ($p \leq 0.05$) for shifted neural firing regressed with TWs from SVD with unadjusted joint angles (A), unadjusted joint angular velocities (B), standardized joint angles (C), standardized joint angular velocities (D), and standardized joint angles and angular velocities combined for all epochs for each category of cells.

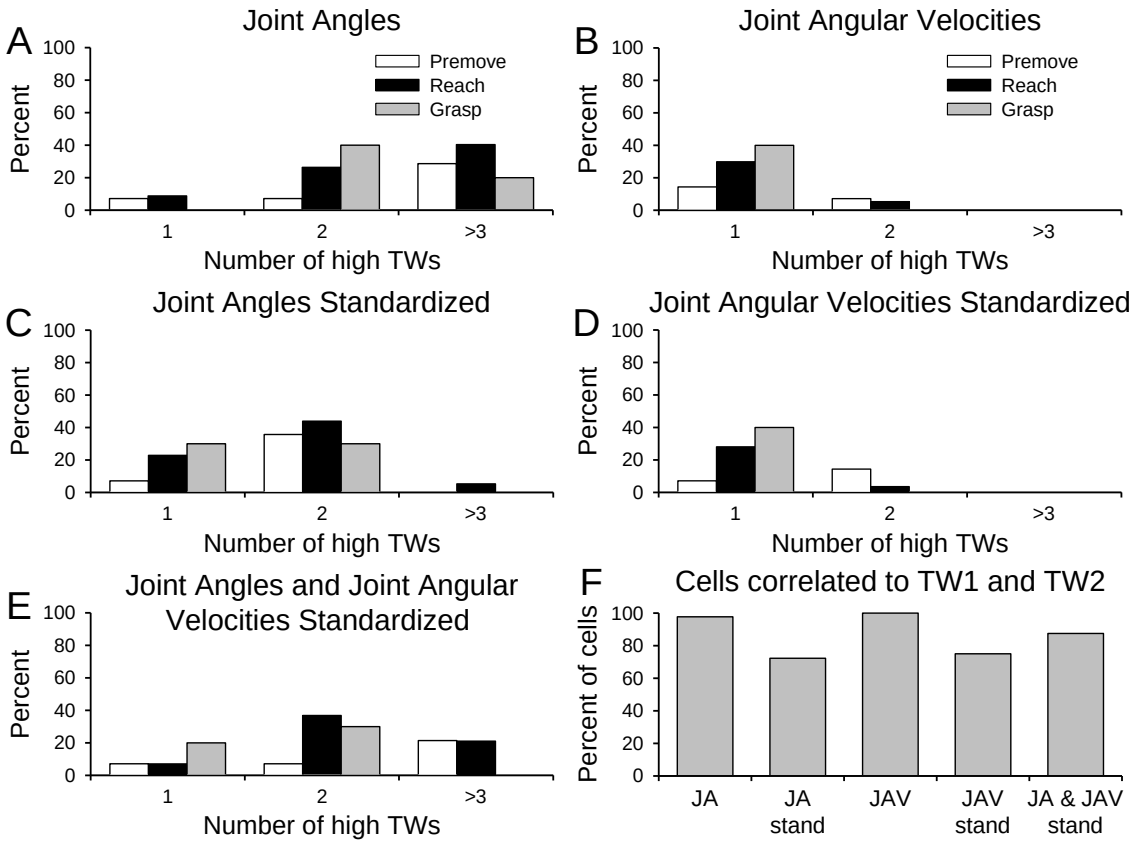

Figure 5.9: Percentage of cells displaying high correlations to each number of temporal weightings. A-E) Percentage of cells displaying each number of high R^2-values ($R^2 \geq 0.138$) for temporal weightings (TWs) resulting from SVD with unadjusted (A) and standardized joint angles (C), unadjusted (B) and standardized (D) joint angular velocities, and standardized joint angles and angular velocities (E) for all epochs combined for each category of cells. F) Of the cells that were highly correlated to two or more TWs, the percentage of cells highly correlated to TW1 and TW2.

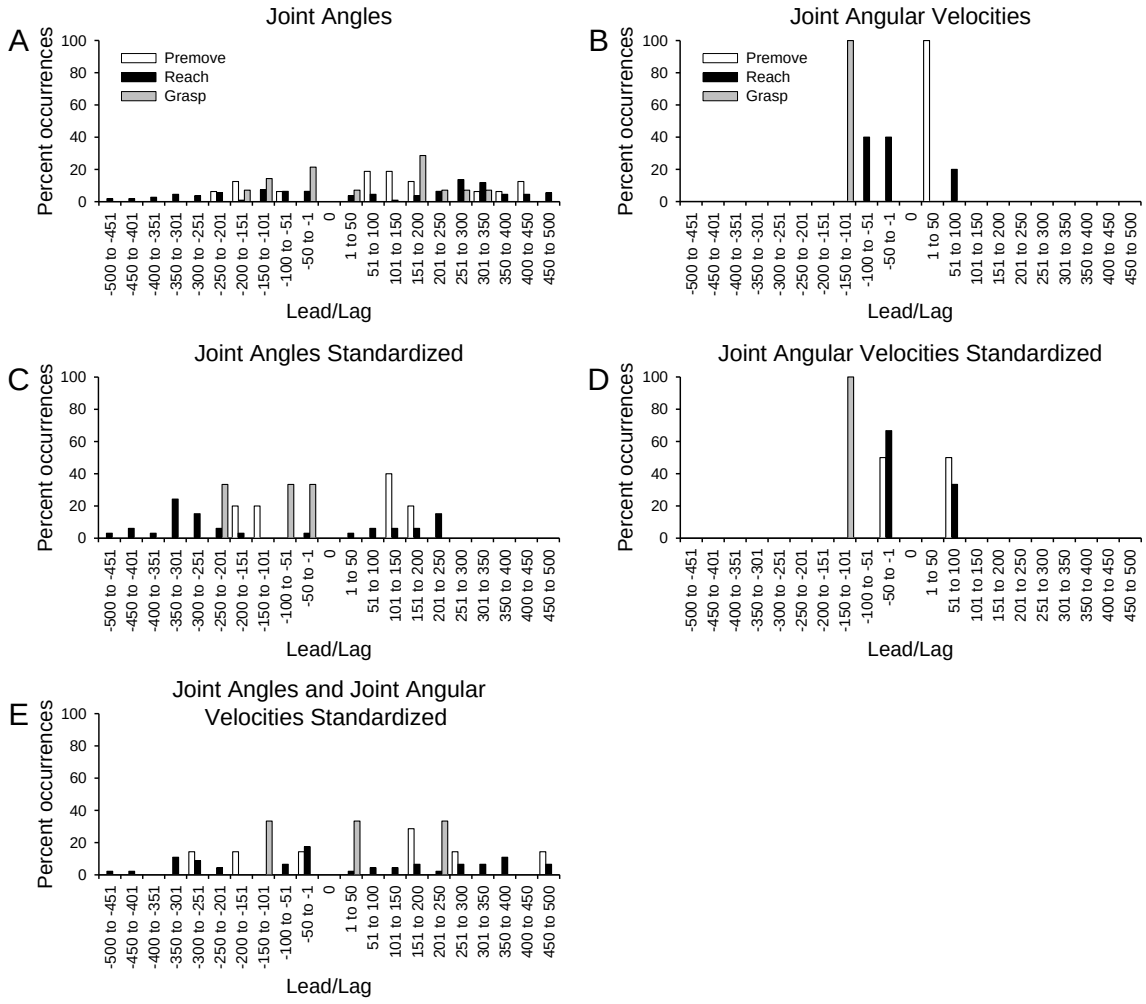

Figure 5.10: Population lead/lag shifts. The percentage of occurrences of each range of leads or lags (+/- 500 ms) for each category of cells for regressions of neural firing and TWs from SVD of A) unadjusted joint angles, B) unadjusted joint angular velocities, C) standardized joint angles, D) standardized joint angular velocities, and E) standardized joint angles and joint angular velocities.

5.3 Limitations of linear regression analysis

The limitations of the linear regression analyses with the individual joint angles and angular velocities is eliminated or minimized by using the TWs from SVD. This can be appreciated by examining the resulting regression coefficients (Figure 5.11). As explained in Chapter 4, regression coefficients from a multiple linear regression describe how much the dependent variable changes with an incremental change in the independent variable while the remaining parameters are held constant (Berry and Feldman, 1985; Abdi, 2003). For completely orthogonal variables, the regression coefficients represent the slope between the dependent variable and the independent variable (Abdi, 2003). When there is colinearity between the variables, however, the coefficients will differ between the multiple and individual linear regressions with varying degrees that depend on the amount of colinearity. In addition, colinearity results in unstable regression coefficients (see Section 4.4). These problems with the regression coefficients were a major limitation in the regression of firing to joint angles and joint angular velocities (see Figure 4.23).

The coefficients resulting from regressions with the TWs of unadjusted joint angles or joint angular velocities were similar between the individual regressions and the multiple regressions (Figure 5.11 A and B). The major dissimilarity is between the coefficients for TW1 and TW2 of unadjusted joint angles, where the coefficient for TW1 individually was 0.13 and for the model 0.21, and for TW2 individually was 0.21 and 0.05 for the model. These differences are due to the degree of colinearity between these two parameters (see Figure 3.31). The coefficients for the regressions for TWs from

standardized data were identical between the individual and multiple regressions (Figure 5.11 C, D, E). Overall, both the individual and multiple linear regressions result in coefficients that can accurately explain the neural firing in relation to each TW. In addition, in contrast to the regressions with the individual elements, the R^2s are a more reasonable estimate of the variability in firing that can be explained by individual TWs.

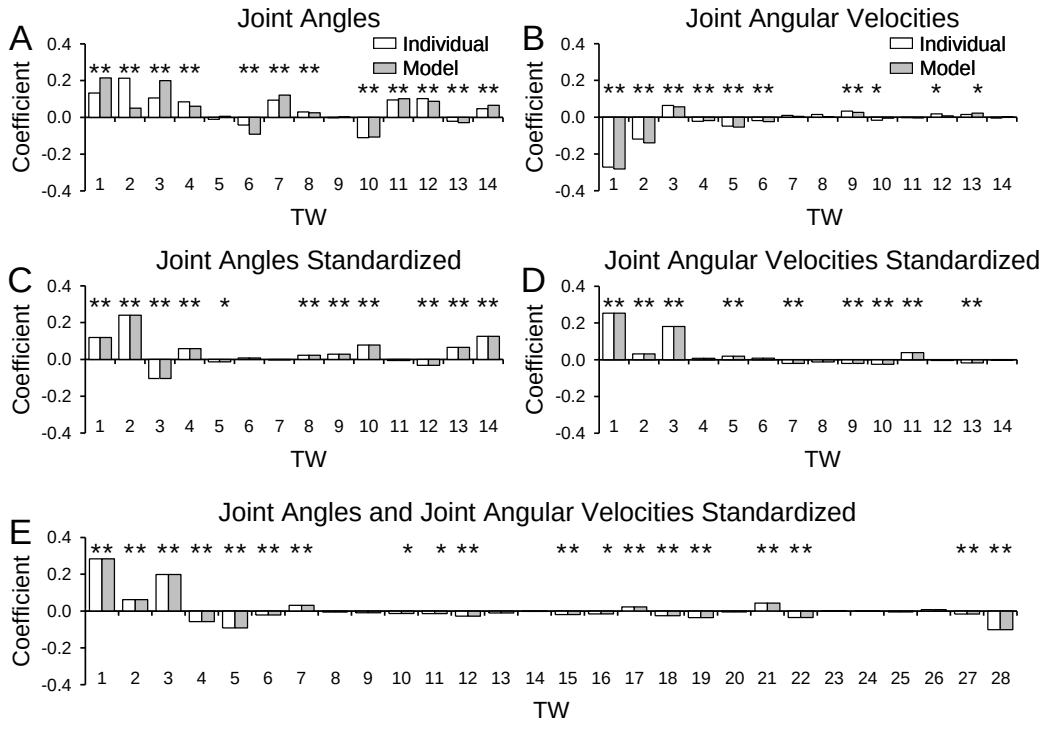

Figure 5.11. Analysis of regression coefficients (B015). Coefficients from the regressions with TWs individually or as the overall model of A) unadjusted joint angles, B) unadjusted joint angular velocities, C) standardized joint angles, D) standardized joint angular velocities, and E) standardized joint angles and joint angular velocities. Star denotes significance ($p \leq 0.05$).

5.4 Discussion

Numerous studies have striven to define patterns or synergies in hand shaping (Santello and Soechting, 1998; Hager-Ross and Schieber, 2000; Mason et al., 2001; Holdefer and Miller, 2002; Jerde et al., 2003; Shim et al., 2004; Mason et al., 2004; Weiss and Flanders, 2004; Brochier et al., 2004; Braido and Zhang, 2004; Theverapperuma et al., 2005; Gao et al., 2005; Shim et al., 2005; Vinjamuri et al., 2007; Klein et al., 2007; Ingram et al., 2008; Niu et al., 2008; Vinjamuri et al., 2009). Synergies have been defined by using forms of principal component analysis as well as other covariation techniques and have resulted in both dominant as well as detailed hand shaping patterns. Inherent assumptions behind these studies are that the resulting patterns and the reduction in dimensionality reflect the underlying strategies used by the CNS to control hand shaping. A logical extension of these assumptions is that these hand shaping patterns or synergies will be reflected in the neuronal firing patterns of motor structures controlling hand movements. Ingram and coworkers argued these hand shaping patterns are represented by separate neuronal populations that are responsible for each type of movement (Ingram et al., 2008). This chapter provides the first direct test of these assumptions for neurons in M1.

The firing of M1 cells analyzed had the highest correlations for the first few TWs of each SVD (Figure 5.5 and 5.8). Only after incorporating a temporal shift did the firing of M1 cells have high R^2-values with higher-order TWs (Figure 5.7). However, even with the time shift, far fewer cells (up to 10%) were related to TWs 4-28 compared to TWs 1-3 (up to 68.4%) (Figure 5.8). The limited correlation with higher-order TWs was

found for both the joint angles and joint angular velocities. The high correlations with higher-order TWs were predominantly with premove (6 of 24) and reach cells (17 of 24) after incorporating a temporal shift (Figures 5.4 and 5.8). However, no grasp cells were found to have high R^2s for higher-order TWs. At best, a small population of cells in M1 may be related to details in hand shaping as described by higher-order TWs of SVD with joint angles. As described in Chapter 3, lower-order TWs represent dominant hand shaping patterns that encompass the covariation of many joints of the hand and fingers and are highly consistent across sessions (see Figures 3.19, 3.24, and 3.29). In turn, higher-order TWs represent details in hand shaping (Santello et al., 1998; Thakur et al., 2008), which is supported by the small amount of variability described by the patterns (see Figures 3.16, 3.21, and 3.26). However, the lack of representation in M1 of higher-order TWs is not surprising, as these are derived from complex mathematical calculations. One could argue that it is highly unlikely that the CNS has explicit representation of these patterns of hand shaping. While the CNS must control these finer aspects of hand shaping, the present data suggests that the primary motor cortex does not accomplish this by generating representations of higher-order principle component-like elements.

The firing of M1 neurons is correlated to arm velocity during reaching and tracking movements (Moran and Schwartz, 1999; Reina et al., 2001; Paninski et al., 2004; Stark et al., 2007b), as well as joint angular velocities of the arm (Reina et al., 2001). However, the present results suggest that motor cortical cells are only weakly correlated to joint angular velocities of the fingers during reach-to-grasp. Most M1 cells

showed little relationship for TWs from the SVDs derived from joint angular velocities (Figure 5.5 and 5.8). These observations are consistent with the small number of cells with firing that was highly correlated to the joint angular velocities as individual elements (see Chapter 4), suggesting that the motor cortex does not explicitly control or signal this parameter in grasping.

It has been shown that muscles controlling the hand are best aligned with multiple hand shaping patterns (Weiss and Flanders, 2004). Because of the many direct connections between M1 and spinal motor neurons (Asanuma et al., 1978; Shinoda et al., 1979; Lemon, 1988; Palmer and Ashby, 1992; Bortoff and Strick, 1993; Maier et al., 1997; Park et al., 2004; Rathelot and Strick, 2006; Rathelot and Strick, 2009), it is natural to hypothesize that the firing of motor cortical neurons would have a similar relationship to patterns of hand shaping. For unshifted data, most cells were highly correlated to only one TW (Figure 5.6), in contrast to the findings for individual elements, in which several joint angles or angular velocities were often highly correlated to the firing of a single cell (see Chapter 4). However, after incorporating a time shift, most cells were highly correlated with two or more TWs (Figure 5.9), providing support for the concept that individual M1 cells are involved with several patterns in grasping. In addition, Weiss and Flanders found that muscles controlling the hand are most often related to the first two hand shaping PCs (Weiss and Flanders, 2004). Therefore, both muscle activity and firing of M1 cells reflect lower-order PCs.

The R^2-values obtained for regressions with TWs were similar to those resulting from regressions with the individual elements. Cell T081, for example, had a maximum

R^2-value of 0.36 for THMCP (Figure 4.16), and 0.30 for TW2 of unadjusted joint angles after a time shift. The population averages show a similar relationship between the R^2-values of the individual elements and TWs. For instance, the maximum average R^2-value for reach cells was 0.36 for individual joint angles, 0.30 for unadjusted joint angles, and 0.38 for standardized joint angle TWs. However, as described in Section 4.4, the R^2s for individual joint elements are inflated. Change in motor cortical firing captures significant amounts of variability in both the individual joint angle elements and the TWs derived from SVD, but the strength of the correlations with TWs are more accurate than those with individual elements.

Some cell types showed an increase in percentage of cells with high correlations when comparing TW regressions to those with individual elements. For example, a maximum of 50% of grasp cells had high R^2s for an individual joint angle, where up to 60% of cells were highly correlated with a TW from joint angles. The maximum percentages of high correlations were also increased for premove cells with TWs from joint angles and reach cells for TWs from joint angular velocities. The overall model R^2s for the regressions with individual elements and TWs were identical and were high for the same percentage of cells due to both regressions stemming from the same databases.

TWs describe patterns in joint angles, angular velocities, or the combination of the two, that have minimal colinearity. Unlike regressions obtained for the individual elements, the coefficients from either the individual or the multiple regressions with TWs are valid estimates of the slopes of the firing with the parameter (see Section 5.3). Therefore, a single algorithm may be developed to accurately control any combination of

the TWs from the modulation of a motor cortical cell. In a BMI application, for example, this algorithm could be used to drive the joints of a robotic or virtual hand. Due to the similarity across sessions (see Chapter 3), a pre-established set of eigenvectors and eigenvalues could be defined for the system. Then, once a TW has been predicted by using this algorithm, the joint angle or joint angular velocity can be calculated by utilizing the eigenvector and eigenvalue for the TW. A system controlling TWs rather than individual elements is more efficient because it also utilizes the natural interaction between the parameters. Depending on the necessary skill-level of a given task, the number of cells required to precisely control a hand shape, and therefore complete a task utilizing a neural prosthetic, could be minimized by using cells of different firing patterns and relationships to different parts of grasp development, similar to the population vector method described by Georgopoulos and colleagues (Georgopoulos et al., 1986). It is possible that M1 utilizes a similar strategy to control the hand. However, irrespective of the mechanism used by M1, these SVD and regression analyses offer a strategy for extracting signals that can be used in neuroengineering applications (Schwartz, 2004; Schwartz, 2007; Velliste et al., 2008).

Chapter 6: Summary, future directions, and applications

6.1 Summary

This thesis is the first study utilizing a large object set that was designed to provide large variation in the joint angles of all of the digits during grasping in monkeys. The majority of the joint angles of the fingers and hand evolved in a highly predictable manner during the reach-to-grasp task performed by monkeys. The joint angles varied significantly across object during the *reach* and *grasp epoch*. This preshaping for the joints of the hand during prehension are well documented (Jeannerod, 1984; Santello and Soechting, 1998; Roy et al., 2000; Mason et al., 2001; Mason et al., 2004; Hu et al., 2005). Joint angles of the little finger were less predictable, reflecting their independence from the other digits. This observation mirrors findings in humans that the little finger is involved less with detailed shaping of the hand than the remaining fingers (Ansuini et al., 2006). The joint angular velocities were also consistent with previous findings in humans (Vinjamuri et al., 2007; Vinjamuri et al., 2009). However, joint angular velocities exhibited greater variability than the joint angles and also were significantly different across object predominantly during the *reach epoch*. Overall, the reach-to-grasp behavior presented in this thesis is consistent with the prehension literature.

As reviewed in Chapter 1, the hand is a highly complex biomechanical system with a large number of degrees of freedom as well as a high level of covariation of the many joints. Many researchers have described patterns in hand shaping that can be used to reduce the degrees of freedom of the system (Santello et al., 1998; Valero-Cuevas, 2000; Mason et al., 2001; Santello et al., 2002; Jerde et al., 2003; Mason et al., 2004;

Weiss and Flanders, 2004; Braido and Zhang, 2004; Theverapperuma et al., 2005; Klein et al., 2007; Ingram et al., 2008; Thakur et al., 2008; Vinjamuri et al., 2009). In this thesis, five different SVD analyses (unadjusted and standardized joint angles, unadjusted and standardized joint angular velocities, and standardized joint angles and angular velocities combined) were used to define independent patterns (eigenvectors) of the hand shaping kinematics. The eigenvectors described were highly consistent across sessions and subjects within an SVD type. For all analysis types, the first eigenvector depicted the coordinated extension/flexion of the MCP and IP joints, represented the overall opening and closing of the hand, and described the majority of the variance (Santello et al., 1998; Mason et al., 2001; Mason et al., 2004; Theverapperuma et al., 2005). This dominant hand shape has been described in human and non-human primate grasping (Santello et al., 1998; Mason et al., 2001; Mason et al., 2004; Braido and Zhang, 2004; Thakur et al., 2008). Temporal weighting vectors were derived to assess each pattern's contribution to the hand shape through time for each trial within a session (Mason et al., 2004). Used as measures of the hand shaping patterns defined by the SVD analyses, the correlation between the TWs and the neural firing was examined.

This is the first study to analyze simultaneous recordings of several joints of the fingers and hand with single units recorded from the primary motor cortex. Previous studies have shown that the firing of M1 neurons is highly correlated to joint angles of the fingers (Schieber and Hibbard, 1993; Georgopoulos et al., 1999; Poliakov and Schieber, 1999; Theverapperuma et al., 2005). However, these studies utilized individuated finger movements rather than the natural behavior of reaching and grasping.

In this study, the firing of M1 neurons was highly correlated to joint angles and, to a lesser extent, angular velocities as a function of time throughout reach and grasp. The regression fits were improved by incorporating a time-shift in which the firing leads the kinematics, indicating the involvement of M1 with control of kinematics rather than feedback. In addition, the firing of a majority of cells was highly correlated with multiple elements. This is not unexpected, as joint angles and angular velocities are highly colinear both during reach-to-grasp (Santello and Soechting, 1998; Mason et al., 2001; Santello et al., 2002; Braido and Zhang, 2004; Thakur et al., 2008) and individuated movements (Schieber and Hibbard, 1993; Georgopoulos et al., 1999; Poliakov and Schieber, 1999). The linear relationship between the firing of M1 neurons and individual parameters could provide a useful algorithm for neuroprosthetics. However, a more efficient tool might also harness the relationships between the joints.

Several have suggested that the CNS, at some level, represents the patterns of hand shaping derived from analyses that strive to reduce the degrees of freedom (Ingram et al., 2008). To address this question, the firing of M1 cells was regressed with TWs from the SVD analyses. The majority of M1 cells were highly correlated with the first few TWs of each SVD. However, the TWs for joint angular velocities were represented to a much lesser extent. After incorporating a time-shift, additional cells were correlated with higher-order TWs, however the number of cells correlated with these TWs remained small. The firing of most M1 cells was highly correlated with more than one TW, consistent with the relationship between muscle and postural synergies (Weiss and Flanders, 2004). Therefore, both muscle activity and firing of M1 cells reflect dominant

patterns of hand shaping. These SVD and regression analyses provide a basis for algorithms to control neuroprosthetics that is more efficient than those utilizing individual joint kinematic parameters (Schwartz, 2004; Schwartz, 2007; Velliste et al., 2008).

6.2 Future directions

The information presented in this thesis opens the door for several additional analyses of the current data set. First, although the majority of the R^2-values obtained in the regression analyses were large considering the data was not averaged, the regression model could be improved by utilizing vector autoregressions (VARs) (Sims, 1980). VARs are models that capture the interdependencies between multiple time series parameters, explaining the evolution of each variable based on their own leads and lags as well as the leads and lags of all other parameters in the model. A VAR would allow the examination of the dependence of an individual kinematic parameter on its own previous time frames as well as the current and previous time frames of the other kinematic parameters. In turn, the neural firing could be examined in relation to previous time frames and all combinations of kinematic parameters. Because joint movements of the hand are tightly coupled, implementing a VAR approach would likely yield a much more robust model to explain the relationships between neural firing and joint kinematics.

The high degree of correlation between firing of M1 neurons and lower-order TWs suggests that an algorithm could be developed to predict hand shape from the neuronal population. Previously, a population vector method that used the weighted sum

of the firing rates of individual M1 cells and their preferred directions was used to predict the overall movement direction of the arm (Georgopoulos et al., 1986). The population vector approach has been used widely to understand the information encoded in neuronal populations (Lee et al., 1988; Vogels, 1990; Zohary, 1992) and have proven highly useful in neuroprosthetics (Taylor et al., 2002; Schwartz et al., 2006; Schwartz, 2007; Velliste et al., 2008). This method was also extended to individuated finger and wrist movements (Georgopoulos et al., 1999). A population vector could be defined for the current data in 14 or 28-dimensional TW space. However, the number of dimensions used could likely be reduced. The majority of the variability in the joint kinematics was explained by the first few eigenvectors and the firing of the majority of M1 cells was highly correlated only with the first few TWs. Therefore, it is likely that a population vector could be defined utilizing only 3 or 4 dimensions in the TW space.

The hand is an extremely complex system that is capable of performing both simple tasks such as using a tool or picking up a small piece of food, as well as highly sophisticated actions such as typing, playing a musical instrument, or communicating with sign language. Despite the significant differences in joint kinematics of the hand observed during reaching and grasping (see Chapter 3), the task mainly captures the simplistic behavior of the hand. In humans, the reconstruction of hand shapes for intricate movements, such as pinch hand shapes or American Sign Language postures, were not completely accurate when using PCs defined from reaching and grasping tasks (Thakur et al., 2008; Vinjamuri et al., 2009). Detailed patterns in hand shaping necessary to complete intricate tasks, and subsequently the correlation of the firing of M1 neurons

with these intricate details, might not be captured with the current analyses. Therefore, a task where simple reaching and grasping is combined with more intricate behavior would aid in defining both dominant and detailed patterns in hand shaping. For example, a set of objects could be designed that contains keys and/or switches at each finger that allows a large range of angular deviations of each digit. First, the monkey would reach to and grasp the object. Second, additional cues would instruct the monkey to press individual keys or combinations of keys on the object. This task would permit the examination of both the development of hand shape during reach-to-grasp and individuated movements of the fingers in the same motor cortical neurons. The goal is to further understand the mechanisms and strategies M1 uses to plan and execute hand movements.

6.3 Applications

Understanding the detailed kinematics of the hand is important for both the diagnosis and treatment of hand motor deficits. Typically, motor impairments are assessed by comparing the level of movement of the patient to normal subjects (Nagi, 1991; Wuolle et al., 1994). For example, finger tapping tests are used to quantify upper extremity disability in Parkinson's disease (Okuno et al., 2007). Early examinations of hand shaping served to diagnose workplace hand injuries (Griffiths, 1943; Slocum and Pratt, 1946; Napier, 1956). In addition, stroke victims often have marked impairment in distal motor function, often characterized by spontaneous flexion of the fingers (Carey, 1990). A thorough understanding of both the behavior and the neural control strategies of complex movements of the hand and fingers is pertinent for refining the diagnosis and treatments for disorders of hand function.

Therapeutic techniques for hand function rehabilitation have focused on repetitive exercises for isolated movements (Nudo and Friel, 1999; Liepert et al., 2001; Nelson et al., 2002), and several devices have been developed to aid in this technique (Jack et al., 2001; Ochoa et al., 2009; Durfee et al., 2009). However, recent work with the lower extremities has found that functional exercises are more effective than repetition of isolated movements (Nelson et al., 2002; Conti and Schepens, 2009). The success of these techniques is likely due to their similarity to the control strategies utilized by the CNS. This suggests that therapies based on the re-establishment of functional hand synergies, such as those described by SVD, might provide more effective rehabilitation of hand motor deficit (Vinjamuri et al., 2009).

Synergies may provide a more computationally efficient model for real-time control of robots than a model that utilizes individual degrees of freedom. The concept of synergies has been used to develop a simplified control algorithm for arm movements (Popovic and Popovic, 2001). Vinjamuri and coworkers are currently working on an algorithm for the real-time control of a virtual hand using synergies (Vinjamuri et al., 2009). These approaches utilize biologically inspired patterns of movement but lack input from the CNS. Control algorithms utilizing neural input could be defined, for example, using the population vector method described in the previous section. The present data could aid in bridging the control of robotics through synergies and neuroprosthetics. Studies displaying the control of a computer cursor from decoding motor cortical signals in humans provide hope the restoration of movement to humans

with paralysis or amputated limbs will someday be possible (Truccolo et al., 2008; Kim et al., 2008).

In conclusion, this thesis showed that the firing of neurons in the primary motor cortex is highly correlated to individual joint angles of the fingers as well as their joint angular velocities, albeit to a much lesser extent. The cell firing was most often related to several elements. Cells were also highly correlated with lower-order temporal weighting vectors describing hand shaping patterns in time, but high correlations with higher-order patterns were lacking. This suggests that M1 is involved with the control of dominant hand shaping patterns rather than explicitly controlling individual details. These results could be used to develop improved algorithms for controlling neuroprosthetic hands.

References

1. Abdi H, 2003. Partial Regression Coefficients. In: The Sage Encyclopedia of Social Sciences Research Methods (Lewis-Beck M, Bryman A, Futing T, eds), Thousand Oaks: Sage Publications, Inc.

2. Aflalo TN, Graziano MSA, 2006. Partial tuning of motor cortex neurons to final posture in a free-moving paradigm. Proceedings of the National Academy of Sciences 103: 2909-2914.

3. Alberts JL, Tresilian JR, Stelmach GE, 1998. The co-ordination and phasing of a bilateral prehension task. The influence of Parkinson's disease. Brain 121 (Pt 4): 725-742.

4. Alexander GE, Crutcher MD, 1990. Neural representations of the target (goal) of visually guided arm movements in three motor areas of the monkey. J Neurophysiol 64: 164-178.

5. Ansuini C, Giosa L, Turella L, Altoe G, Castiello U, 2008. An object for an action, the same object for other actions: effects on hand shaping. Exp Brain Res 185: 111-119.

6. Ansuini C, Santello M, Massaccesi S, Castiello U, 2006. Effects of end-goal on hand shaping. J Neurophysiol 95: 2456-2465.

7. Arbib MA, Iberall T, Lyons D, 1985. Coordinated control programs for movements of the hand. Exp Brain Res 10: 111-129.

8. Armbruster C, Spijkers W, 2006. Movement planning in prehension: do intended actions influence the initial reach and grasp movement? Motor Control 10: 311-329.

9. Asanuma H, Hongo T, Jankowska E, Marcus S, Shinoda Y, Zarzecki P, 1978. Pattern of projections of individual pyramidal tract neurons to the spinal cord of the monkey. J Physiol (Paris) 74: 235-236.

10. Asanuma H, Rosen I, 1972. Topographical organization of cortical efferent zones projecting to distal forelimb muscles in the monkey. Exp Brain Res 14: 243-256.

11. Ashe J, 1997. Force and the motor cortex. Behav Brain Res 86: 1-15.

12. Ashe J, Georgopoulos AP, 1994. Movement parameters and neural activity in motor cortex and area 5. Cereb Cortex 4: 590-600.

13. Asher I, Stark E, Abeles M, Prut Y, 2007. Comparison of direction and object selectivity of local field potentials and single units in macaque posterior parietal cortex during prehension. J Neurophysiol 97: 3684-3695.

14. Bastian AJ, Martin TA, Keating JG, Thach WT, 1996. Cerebellar ataxia: abnormal control of interaction torques across multiple joints. J Neurophysiol 76: 492-509.

15. Battaglia-Mayer A, Ferraina S, Marconi B, Bullis JB, Lacquaniti F, Burnod Y, Baraduc P, Caminiti R, 1998. Early motor influences on visuomotor transformations for reaching: a positive image of optic ataxia. Exp Brain Res 123: 172-189.

16. Beisteiner R, Windischberger C, Lanzenberger R, Edward V, Cunnington R, Erdler M, Gartus A, Streibl B, Moser E, Deecke L, 2001. Finger somatotopy in human motor cortex. NeuroImage 13: 1016-1026.

17. Berry WD, Feldman S, 1985. Multiple Regression in Practice. Thousand Oaks, CA: Sage Publications, Inc.

18. Binkofski F, Dohle C, Posse S, Stephan KM, Hefter H, Seitz RJ, Freund HJ, 1998. Human anterior intraparietal area subserves prehension: a combined lesion and functional MRI activation study. Neurology 50: 1253-1259.

19. Bootsma RJ, Marteniuk RG, MacKenzie CL, Zaal FT, 1994. The speed-accuracy trade-off in manual prehension: effects of movement amplitude, object size and object width on kinematic characteristics. Exp Brain Res 98: 535-541.

20. Bortoff GA, Strick PL, 1993. Corticospinal terminations in two new-world primates: further evidence that corticomotoneuronal connections provide part of the neural substrate for manual dexterity. J Neurosci 13: 5105-5118.

21. Braido P, Zhang X, 2004. Quantitative analysis of finger motion coordination in hand manipulative and gestic acts. Hum Mov Sci 22: 661-678.

22. Brochier T, Boudreau MJ, Pare M, Smith AM, 1999. The effects of muscimol inactivation of small regions of motor and somatosensory cortex on independent finger movements and force control in the precision grip. Exp Brain Res 128: 31-40.

23. Brochier T, Spinks RL, Umilta MA, Lemon RN, 2004. Patterns of muscle activity underlying object-specific grasp by the macaque monkey. J Neurophysiol 92: 1770-1782.

24. Brochier T, Umilta MA, 2007. Cortical control of grasp in non-human primates. Curr Opin Neurobiol 17: 637-643.

25. Burstedt MK, Flanagan JR, Johansson RS, 1999. Control of grasp stability in humans under different frictional conditions during multidigit manipulation. J Neurophysiol 82: 2393-2405.

26. Buys EJ, Lemon RN, Mantel GW, Muir RB, 1986. Selective facilitation of different hand muscles by single corticospinal neurones in the conscious monkey. J Physiol 381: 529-549.

27. Cabel DW, Cisek P, Scott SH, 2001. Neural activity in primary motor cortex related to mechanical loads applied to the shoulder and elbow during a postural task. J Neurophysiol 86: 2102-2108.

28. Caminiti R, Johnson PB, Burnod Y, Galli C, Ferraina S, 1990. Shift of preferred directions of premotor cortical cells with arm movements performed across the workspace. Exp Brain Res 83: 228-232.

29. Carey JR, 1990. Manual stretch: effect on finger movement control and force control in stroke subjects with spastic extrinsic finger flexor muscles. Arch Phys Med Rehabil 71: 888-894.

30. Castiello U, Begliomini C, 2008. The cortical control of visually guided grasping. Neuroscientist 14: 157-170.

31. Castiello U, Bennett K, Chambers H, 1998. Reach to grasp: the response to a simultaneous perturbation of object position and size. Exp Brain Res 120: 31-40.

32. Castiello U, Bennett KM, Stelmach GE, 1993. Reach to grasp: the natural response to perturbation of object size. Exp Brain Res 94: 163-178.

33. Cheney PD, Fetz EE, 1980. Functional classes of primate corticomotoneuronal cells and their relation to active force. J Neurophysiol 44: 773-791.

34. Cheney PD, Fetz EE, 1985. Comparable patterns of muscle facilitation evoked by individual corticomotoneuronal (CM) cells and by single intracortical microstimuli in primates: evidence for functional groups of CM cells. J Neurophysiol 53: 786-804.

35. Cheyne D, Kristeva R, Deecke L, 1991. Homuncular organization of human motor cortex as indicated by neuromagnetic recordings. Neurosci Lett 122: 17-20.

36. Chieffi S, Gentilucci M, 1993. Coordination between the transport and the grasp components during prehension movements. Exp Brain Res 94: 471-477.

37. Chouinard PA, Leonard G, Paus T, 2005. Role of the primary motor and dorsal premotor cortices in the anticipation of forces during object lifting. J Neurosci 25: 2277-2284.

38. Cohen J, 1988. Statistical power analysis for the behavioral sciences. Hillsdale, NJ; Lawrence Earlbaum Associates.

39. Cohen J, Cohen P, West SG, Aiken LS, 2003. Applied Multiple Regression/Correlation Analysis for the Behavioral Sciences, Third Edition. Mahwah, NJ: Lawrence Erlbaum Associates, Inc.

40. Cole KJ, Abbs JH, 1986. Coordination of three-joint digit movements for rapid finger-thumb grasp. J Neurophysiol 55: 1407-1423.

41. Coltz JD, Johnson MT, Ebner TJ, 1999. Cerebellar Purkinje cell simple spike discharge encodes movement velocity in primates during visuomotor arm tracking. J Neurosci 19: 1782-1803.

42. Conti GE, Schepens SL, 2009. Changes in hemiplegic grasp following distributed repetitive intervention: a case series. Occup Ther Int 16: 204-217.

43. Cramer SC, Weisskoff RM, Schaechter JD, Nelles G, Foley M, Finklestein SP, Rosen BR, 2002. Motor cortex activation is related to force of squeezing. Hum Brain Mapp 16: 197-205.

44. Crutcher MD, Alexander GE, 1990. Movement-related neuronal activity selectively coding either direction or muscle pattern in three motor areas of the monkey. J Neurophysiol 64: 151-163.

45. D'Avella A, Saltiel P, Bizzi E, 2003. Combinations of muscle synergies in the construction of a natural motor behavior. Nature Neuroscience 6: 300-308.

46. Davare M, Andres M, Clerget E, Thonnard JL, Olivier E, 2007. Temporal dissociation between hand shaping and grip force scaling in the anterior intraparietal area. J Neurosci 27: 3974-3980.

47. Davare M, Montague K, Olivier E, Rothwell JC, Lemon RN, 2009. Ventral premotor to primary motor cortical interactions during object-driven grasp in humans. Cortex 45: 1050-1057.

48. DeFelipe J, Jones EG, 1985. Vertical organization of gamma-aminobutyric acid-accumulating intrinsic neuronal systems in monkey cerebral cortex. J Neurosci 5: 3246-3260.

49. DeLong MR, 1973. Putamen: activity of single units during slow and rapid arm movements. Science 179: 1240-1242.

50. DeLong MR, Crutcher MD, Georgopoulos AP, 1983. Relations between movement and single cell discharge in the substantia nigra of the behaving monkey. J Neurosci 3: 1599-1606.

51. Donoghue JP, Leibovic S, Sanes JN, 1992. Organization of the forelimb area in squirrel monkey motor cortex: representation of digit, wrist, and elbow muscles. Exp Brain Res 89: 1-19.

52. Dubrowski A, Roy EA, Black SE, Carnahan H, 2005. Unilateral basal ganglia damage causes contralesional force control deficits: a case study. Neuropsychologia 43: 1379-1384.

53. Dum RP, Strick PL, 2002. Motor areas in the frontal lobe of the primate. Physiol Behav 77: 677-682.

54. Dum RP, Strick PL, 2005. Frontal lobe inputs to the digit representations of the motor areas on the lateral surface of the hemisphere. J Neurosci 25: 1375-1386.

55. Dunnett SB, Torres EM, Annett LE, 1998. A lateralised grip strength test to evaluate unilateral nigrostriatal lesions in rats. Neurosci Lett 246: 1-4.

56. Dunteman GH, 1989. Principal Components Analysis (Quantitative Applications in the Social Sciences). Newburgy Park, CA: SAGE Publications, Inc.

57. Durfee W, Carey J, Nuckley D, Deng J, 2009. Design and implementation of a home stroke telerehabilitation system. Conf Proc IEEE Eng Med Biol Soc 1: 2422-2425.

58. Ebner TJ, Pasalar S, 2008. Cerebellum predicts the future motor state. Cerebellum 7: 583-588.

59. Ehrsson HH, Kuhtz-Buschbeck JP, Forssberg H, 2002. Brain regions controlling nonsynergistic versus synergistic movement of the digits: a functional magnetic resonance imaging study. J Neurosci 22: 5074-5080.

60. Espinoza E, Smith AM, 1990. Purkinje cell simple spike activity during grasping and lifting objects of different textures and weights. J Neurophysiol 64: 698-714.

61. Evarts EV, 1968. Relation of pyramidal tract activity to force exerted during voluntary movement. J Neurophysiol 31: 14-27.

62. Evarts EV, Fromm C, Kroller J, Jennings VA, 1983. Motor Cortex control of finely graded forces. J Neurophysiol 49: 1199-1215.

63. Fellows SJ, Noth J, Schwarz M, 1998. Precision grip and Parkinson's disease. Brain 121 (Pt 9): 1771-1784.

64. Fetz EE, Cheney PD, 1980. Postspike facilitation of forelimb muscle activity by primate corticomotoneuronal cells. J Neurophysiol 44: 751-772.

65. Flanagan JR, Burstedt MK, Johansson RS, 1999. Control of fingertip forces in multidigit manipulation. J Neurophysiol 81: 1706-1717.

66. Flash T, 1990. The organization of human arm trajectory control. In: Multiple muscle systems: Biomechanics and movement organization (Winters JM, Woo SLY, eds), pp 282-301. New York: Springer.

67. Fortier PA, Kalaska JF, Smith AM, 1989. Cerebellar neuronal activity related to whole-arm reaching movements in the monkey. J Neurophysiol 62: 198-211.

68. Fraser C, Wing AW, 1981. A case study of reaching by a user of a manually-operated artificial hand. Prosthet Orthot Int 5: 151-156.

69. Freund RJ, Littel RC, 2000. SAS System for Regression. John Wiley & Sons, Inc.

70. Freund RJ, Wilson WJ, 1998. Regression Analysis, Statistical Modeling of a Response Variable. San Diego, CA: Academic Press.

71. Fu QG, Mason CR, Flament D, Coltz JD, Ebner TJ, 1997. Movement kinematics encoded in complex spike discharge of primate cerebellar Purkinje cells. NeuroReport 8: 523-529.

72. Fu QG, Suarez JI, Ebner TJ, 1993. Neuronal specification of direction and distance during reaching movements in the superior precentral premotor area and primary motor cortex of monkeys. J Neurophysiol 70: 2097-2116.

73. Gallese V, Murata A, Kaseda M, Niki N, Sakata H, 1994. Deficit of hand preshaping after muscimol injection in monkey parietal cortex. NeuroReport 5: 1525-1529.

74. Galletti C, Fattori P, Kutz DF, Battaglini PP, 1997. Arm movement-related neurons in the visual area V6A of the macaque superior parietal lobule. Eur J Neurosci 9: 410-413.

75. Galletti C, Kutz DF, Gamberini M, Breveglieri R, Fattori P, 2003. Role of the medial parieto-occipital cortex in the control of reaching and grasping movements. Exp Brain Res 153: 158-170.

76. Gao F, Latash ML, Zatsiorsky VM, 2005. Internal forces during object manipulation. Exp Brain Res 165: 69-83.

77. Gardner EP, Babu KS, Ghosh S, Sherwood A, Chen J, 2007a. Neurophysiology of prehension. III. Representation of object features in posterior parietal cortex of the macaque monkey. J Neurophysiol 98: 3708-3730.

78. Gardner EP, Ro JY, Babu KS, Ghosh S, 2007b. Neurophysiology of prehension. II. Response diversity in primary somatosensory (S-I) and motor (M-I) cortices. J Neurophysiol 97: 1656-1670.

79. Gelfand IM, Gurfinkel VS, Tsetlin ML, Shik ML, 1971. Some problems in the analysis of movements. In: Models of the structural-functional organization of certain biological systems (Gelfand IM, Gurfinkel VS, Fomin SV, Tsetlin ML, eds), pp 329-345. Cambridge, MA: MIT Press.

80. Gentilucci M, Negrotti A, 1999. Planning and executing an action in Parkinson's disease. Mov Disord 14: 69-79.

81. Gentilucci M, Toni I, Chieffi S, Pavesi G, 1994. The role of proprioception in the control of prehension movements: a kinematic study in a peripherally deafferented patient and in normal subjects. Exp Brain Res 99: 483-500.

82. Georgopoulos AP, 1991. Higher order motor control. Ann Rev Neurosci 14: 361-377.

83. Georgopoulos AP, Ashe J, Smyrnis N, Taira M, 1992. The motor cortex and the coding of force. Science 256: 1692-1695.

84. Georgopoulos AP, Caminiti R, Kalaska JF, 1984. Static spatial effects in motor cortex and area 5: quantitative relations in a two-dimensional space. Exp Brain Res 54: 446-454.

85. Georgopoulos AP, DeLong MR, Crutcher MD, 1983. Relations between parameters of step-tracking movements and single cell discharge in the globus pallidus and subthalamic nucleus of the behaving monkey. J Neurosci 3: 1586-1598.

86. Georgopoulos AP, Pellizzer G, Poliakov AV, Schieber MH, 1999. Neural coding of finger and wrist movements. J Comput Neurosci 6: 279-288.

87. Georgopoulos AP, Schwartz AB, Kettner RE, 1986. Neuronal population coding of movement direction. Science 233: 1416-1419.

88. Gordon AM, Forssberg H, Johansson RS, Westling G, 1991. Visual size cues in the programming of manipulative forces during precision grip. Exp Brain Res 83: 477-482.

89. Gould HJ, Cusick CG, Pons TP, Kaas JH, 1986. The relationship of corpus callosum connections to electrical stimulation maps of motor, supplementary motor, and the frontal eye fields in owl monkeys. J Comp Neurol 247: 297-325.

90. Gribble PL, Scott SH, 2002. Overlap of internal models in motor cortex for mechanical loads during reaching. Nature 417: 938-941.

91. Griffiths HE, 1943. Treatment of the injured workman. Lancet 244: 729-733.

92. Grol MJ, Majdandzic J, Stephan KE, Verhagen L, Dijkerman HC, Bekkering H, Verstraten FA, Toni I, 2007. Parieto-frontal connectivity during visually guided grasping. J Neurosci 27: 11877-11887.

93. Hager-Ross C, Schieber MH, 2000. Quantifying the independence of human finger movements: comparisons of digits, hands, and movement frequencies. J Neurosci 20: 8542-8550.

94. Hamada I, DeLong MR, Mano N, 1990. Activity of identified wrist-related pallidal neurons during step and ramp wrist movements in the monkey. J Neurophysiol 64: 1892-1906.

95. He SQ, Dum RP, Strick PL, 1995. Topographic organization of corticospinal projections from the frontal lobe: motor areas on the medial surface of the hemisphere. J Neurosci 15: 3284-3306.

96. Hendrix CM, Mason CR, Ebner TJ, 2009. Signaling of grasp dimension and grasp force in dorsal premotor cortex and primary motor cortex neurons during reach to grasp in the monkey. J Neurophysiol 102: 132-145.

97. Hepp-Reymond M, Kirkpatrick-Tanner M, Gabernet L, Qi HX, Weber B, 1999. Context-dependent force coding in motor and premotor cortical areas. Exp Brain Res 128: 123-133.

98. Hoffman DS, Strick PL, 1995. Effects of a primary motor cortex lesion on step-tracking movements of the wrist. J Neurophysiol 73: 891-895.

99. Holdefer RN, Miller LE, 2002. Primary motor cortical neurons encode functional muscle synergies. Exp Brain Res 146: 233-243.

100. Holsapple JW, Preston JB, Strick PL, 1991. The origin of thalamic inputs to the "hand" representation in the primary motor cortex. J Neurosci 11: 2644-2654.

101. Hu Y, Osu R, Okada M, Goodale MA, Kawato M, 2005. A model of the coupling between grip aperture and hand transport during human prehension. Exp Brain Res 167: 301-304.

102. Hummel F, Cohen LG, 2005. Improvement of motor function with noninvasive cortical stimulation in a patient with chronic stroke. Neurorehabil Neural Repair 19: 14-19.

103. Humphrey DR, 1986. Representation of movements and muscles within the primate precentral motor cortex: historical and current perspectives. Fed Proc 45: 2687-2699.

104. Huntley GW, Jones EG, 1991. Relationship of intrinsic connections to forelimb movement representations in monkey motor cortex: a correlative anatomic and physiological study. J Neurophysiol 66: 390-413.

105. Illert M, Lundberg A, Tanaka R, 1977. Integration in descending motor pathways controlling the forelimb in the cat. 3. Convergence on propriospinal neurones transmitting disynaptic excitation from the corticospinal tract and other descending tracts. Exp Brain Res 29: 323-346.

106. Ingram JN, Kording KP, Howard IS, Wolpert DM, 2008. The statistics of natural hand movements. Exp Brain Res 188: 223-236.

107. Ingvarsson PE, Gordon AM, Forssberg H, 1997. Coordination of manipulative forces in Parkinson's disease. Exp Neurol 145: 489-501.

108. Jack D, Boian R, Merians AS, Tremaine M, Burdea GC, Adamovich SV, Recce M, Poizner H, 2001. Virtual reality-enhanced stroke rehabilitation. Ieee Transactions on Neural Systems and Rehabilitation Engineering 9: 308-318.

109. Jackson A, Mavoori J, Fetz EE, 2007. Correlations between the same motor cortex cells and arm muscles during a trained task, free behavior, and natural sleep in the macaque monkey. J Neurophysiol 97: 360-374.

110. Jackson JE, 2003. A user's guide to principal components. Hoboken, N.J: Wiley.

111. Jackson SR, Jackson GM, Harrison J, Henderson L, Kennard C, 1995. The internal control of action and Parkinson's disease: a kinematic analysis of visually-guided and memory-guided prehension movements. Exp Brain Res 105: 147-162.

112. Jacobs KM, Donoghue JP, 1991. Reshaping the cortical motor map by unmasking latent intracortical connections. Science 251: 944-947.

113. Jakobson LS, Goodale MA, 1991. Factors affecting higher-order movement planning: a kinematic analysis of human prehension. Exp Brain Res 86: 199-208.

114. Jeannerod M, 1981. Intersegmental coordination during reaching at natural visual objects. In: Attention and Performance IX (Long J., Baddeley A, eds), pp 153-169. Hillsdale, N.J: L. Erlbaum Associates.

115. Jeannerod M, 1984. The timing of natural prehension movements. J Mot Behav 16: 235-254.

116. Jeannerod M, Arbib MA, Rizzolatti G, Sakata H, 1995. Grasping objects: the cortical mechanisms of visuomotor transformation. Trends Neurosci 18: 314-320.

117. Jerde TE, Soechting JF, Flanders M, 2003. Coarticulation in fluent fingerspelling. J Neurosci 23: 2383-2393.

118. Jeyasingham RA, Baird AL, Meldrum A, Dunnett SB, 2001. Differential effects of unilateral striatal and nigrostriatal lesions on grip strength, skilled paw reaching and drug-induced rotation in the rat. Brain Res Bull 55: 541-548.

119. Johansson RS, Westling G, 1988. Coordinated isometric muscle commands adequately and erroneously programmed for the weight during lifting task with precision grip. Exp Brain Res 71: 59-71.

120. Johnson MT, Ebner TJ, 2000. Processing of multiple kinematic signals in the cerebellum and motor cortices. Brain Research Reviews 33: 155-168.

121. Johnson MT, Mason CR, Ebner TJ, 2001. Central processes for the multiparametric control of arm movements in primates. Curr Opin Neurobiol 11: 684-688.

122. Jolliffe IT, 2002. Principal component analysis. New York: Springer-Verlag.

123. Jones EG, Coulter JD, Hendry SH, 1978. Intracortical connectivity of architectonic fields in the somatic sensory, motor and parietal cortex of monkeys. J Comp Neurol 181: 291-347.

124. Kakei S, Hoffman DS, Strick PL, 1999. Muscle and movement representations in the primary motor cortex. Science 285: 2136-2139.

125. Kalaska JF, 1991. What parameters of reaching are encoded by discharges of cortical cells? In: Motor Control: Concepts and Issues (Humphrey DR, Freund H-J, eds), pp 307-330. Somerset, NJ: Wiley.

126. Kalaska JF, Caminiti R, Georgopoulos AP, 1983. Cortical mechanisms related to the direction of two-dimensional arm movements: relations in parietal area 5 and comparison with motor cortex. Exp Brain Res 51: 247-260.

127. Kalaska JF, Cohen DA, Hyde ML, Prud'homme M, 1989. A comparison of movement direction-related versus load direction-related activity in primate motor cortex, using a two-dimensional reaching task. J Neurosci 9: 2080-2102.

128. Kalaska JF, Crammond DJ, 1992. Cerebral cortical mechanisms of reaching movements. Science 255: 1517-1523.

129. Kalaska JF, Scott SH, Cisek P, Sergio LE, 1997. Cortical control of reaching movements. Curr Opin Neurobiol 7: 849-859.

130. Kawato M, 1999. Internal models for motor control and trajectory planning. Curr Opin Neurobiol 9: 718-727.

131. Kawato M, Gomi H, 1992. A computational model of four regions of the cerebellum based on feedback-error learning. Biol Cybern 68: 95-103.

132. Kawato M, Kuroda T, Imamizu H, Nakano E, Miyauchi S, Yoshioka T, 2003. Internal forward models in the cerebellum: fMRI study on grip force and load force coupling. Prog Brain Res 142: 171-188.

133. Keen DA, Fuglevand AJ, 2003. Role of intertendinous connections in distribution of force in the human extensor digitorum muscle. Muscle Nerve 28: 614-622.

134. Keller A, Asanuma H, 1993. Synaptic relationships involving local axon collaterals of pyramidal neurons in the cat motor cortex. J Comp Neurol 336: 229-242.

135. Kilbreath SL, Gorman RB, Raymond J, Gandevia SC, 2002. Distribution of the forces produced by motor unit activity in the human flexor digitorum profundus. J Physiol 543: 289-296.

136. Kim SP, Simeral JD, Hochberg LR, Donoghue JP, Black MJ, 2008. Neural control of computer cursor velocity by decoding motor cortical spiking activity in humans with tetraplegia. J Neural Eng 5: 455-476.

137. Kinoshita H, Oku N, Hashikawa K, Nishimura T, 2000. Functional brain areas used for the lifting of objects using a precision grip: a PET study. Brain Res 857: 119-130.

138. Kirkwood PA, 1979. On the use and interpretation of cross-correlations measurements in the mammalian central nervous system. J Neurosci Methods 1: 107-132.

139. Klatzky RL, McCloskey B, Doherty S, Pellegrino J, Smith T, 1987. Knowledge about hand shaping and knowledge about objects. J Mot Behav 19: 187-213.

140. Klein B, Simura KJ, Flanders M, 2007. Timing of muscle activation in a hand movement sequence. Cereb Cortex 17: 803-815.

141. Kline T, 2005. Psychological Testing: A Practical Approach to Design and Evaluation. Thousand Oaks, California: Sage Publications, Inc.

142. Kuhtz-Buschbeck JP, Gilster R, Wolff S, Ulmer S, Siebner H, Jansen O, 2008. Brain activity is similar during precision and power gripping with light force: an fMRI study. Neuroimage 40: 1469-1481.

143. Kujirai T, Caramia MD, Rothwell JC, Day BL, Thompson PD, Ferbert A, Wroe S, Asselman P, Marsden CD, 1993. Corticocortical inhibition in human motor cortex. J Physiol 471: 501-519.

144. Kwan HC, MacKay WA, Murphy JT, Wong YC, 1978. Spatial organization of precentral cortex in awake primates. II. Motor outputs. J Neurophysiol 41: 1120-1131.

145. Lacquaniti F, Caminiti R, 1998. Visuo-motor transformations for arm reaching. Eur J Neurosci 10: 195-203.

146. Landry P, Labelle A, Deschenes M, 1980. Intracortical distribution of axonal collaterals of pyramidal tract cells in the cat motor cortex. Brain Res 191: 327-336.

147. Lang CE, Bastian AJ, 1999. Cerebellar subjects show impaired adaptation of anticipatory EMG during catching. J Neurophysiol 82: 2108-2119.

148. Latash ML, Scholz JP, Schoner G, 2002. Motor control strategies revealed in the structure of motor variability. Exerc Sport Sci Rev 30: 26-31.

149. Lawrence DG, 1994. Central neural mechanisms of prehension. Can J Physiol Pharmacol 72: 580-582.

150. Lawrence DG, Kuypers HG, 1968. The functional organization of the motor system in the monkey. I. The effects of bilateral pyramidal lesions. Brain 91: 1-14.

151. Lee C, Rohrer WH, Sparks DL, 1988. Population coding of saccadic eye movements by neurons in the superior colliculus. Nature 332: 357-360.

152. Lemon R, 1988. The output map of the primate motor cortex. Trends Neurosci 11: 501-506.

153. Lemon RN, 1981. Functional properties of monkey motor cortex neurones receiving afferent input from the hand and fingers. J Physiol 311: 497-519.

154. Lemon RN, 2008. Descending pathways in motor control. Annu Rev Neurosci 31: 195-218.

155. Lemon RN, Johansson RS, Westling G, 1995. Corticospinal control during reach, grasp, and precision lift in man. J Neurosci 15: 6145-6156.

156. Lemon RN, Mantel GW, Muir RB, 1986. Corticospinal facilitation of hand muscles during voluntary movement in the conscious monkey. J Physiol 381: 497-527.

157. Li ZM, Latash ML, Zatsiorsky VM, 1998. Force sharing among fingers as a model of the redundancy problem. Exp Brain Res 119: 276-286.

158. Liepert J, Uhde I, Graf S, Leidner O, Weiller C, 2001. Motor cortex plasticity during forced-use therapy in stroke patients: a preliminary study. J Neurol 248: 315-321.

159. MacKenzie CL, Iberall T, 1994. The grasping hand. Amsterdam: North-Holland.

160. Mai N, Bolsinger P, Avarello M, Diener HC, Dichgans J, 1988. Control of isometric finger force in patients with cerebellar disease. Brain 111: 973-998.

161. Maier MA, Bennett KM, Hepp-Reymond MC, Lemon RN, 1993. Contribution of the monkey corticomotoneuronal system to the control of force in precision grip. J Neurophysiol 69: 772-785.

162. Maier MA, Olivier E, Baker SN, Kirkwood PA, Morris T, Lemon RN, 1997. Direct and indirect corticospinal control of arm and hand motoneurons in the squirrel monkey (Saimiri sciureus). J Neurophysiol 78: 721-733.

163. Marteniuk RG, Leavitt JL, MacKenzie CL, Athenes S, 1990. Functional relationships between grasp and transport components in a prehension task. Hum Mov Sci 9: 149-176.

164. Martini FH, Ober WC, Garrison CW, Welch K, Hutchings RT, 2006. Fundamentals of Anatomy & Physiology, Seventh Edition. San Francisco: Pearson Education/Benjamin Cummings.

165. Mason CR, Gomez JE, Ebner TJ, 2001. Hand synergies during reach-to-grasp. J Neurophysiol 86: 2896-2910.

166. Mason CR, Gomez JE, Ebner TJ, 2002. Primary motor cortex neuronal discharge during reach-to-grasp: controlling the hand as a unit. Arch Ital Biol 140: 229-236.

167. Mason CR, Hendrix CM, Ebner TJ, 2006. Purkinje cells signal hand shape and grasp force during reach-to-grasp in the monkey. J Neurophysiol 95: 144-158.

168. Mason CR, Miller LE, Baker JF, Houk JC, 1998. Organization of reaching and grasping movements in the primate cerebellar nuclei as revealed by focal muscimol inactivations. J Neurophysiol 79: 537-554.

169. Mason CR, Theverapperuma LS, Hendrix CM, Ebner TJ, 2004. Monkey hand postural synergies during reach-to-grasp in the absence of vision of the hand and object. J Neurophysiol 91: 2826-2837.

170. McKiernan BJ, Marcario JK, Karrer JH, Cheney PD, 1998. Corticomotoneuronal postspike effects in shoulder, elbow, wrist, digit, and intrinsic hand muscles during a reach and prehension task. J Neurophysiol 80: 1961-1980.

171. Messier J, Kalaska JF, 2000. Covariation of primate dorsal premotor cell activity with direction and amplitude during a memorized-delay reaching task. J Neurophysiol 84: 152-165.

172. Mon-Williams M, Tresilian JR, 2001. A simple rule of thumb for elegant prehension. Curr Biol 11: 1058-1061.

173. Moran DW, Schwartz AB, 1999. Motor cortical representation of speed and direction during reaching. J Neurophysiol 82: 2676-2692.

174. Muir RB, Lemon RN, 1983. Corticospinal neurons with a special role in precision grip. Brain Res 261: 312-316.

175. Muller F, Dichgans J, 1994. Dyscoordination of pinch and lift forces during grasp in patients with cerebellar lesions. Exp Brain Res 101: 485-492.

176. Murata A, Fadiga L, Fogassi L, Gallese V, Raos V, Rizzolatti G, 1997. Object representation in the ventral premotor cortex (area F5) of the monkey. J Neurophysiol 78: 2226-2230.

177. Murata A, Gallese V, Luppino G, Kaseda M, Sakata H, 2000. Selectivity for the shape, size, and orientation of objects for grasping in neurons of monkey parietal area AIP. J Neurophysiol 83: 2580-2601.

178. Nagi SZ, 1991. Disability Concepts Revisited: Implications for Prevention. In: Disability in America: Toward a National Agenda for Prevention (Pope AM, Tarlov AR, eds), pp 307-327. Washington, D.C.: National Academy Press.

179. Nakajima K, Maier MA, Kirkwood PA, Lemon RN, 2000. Striking differences in transmission of corticospinal excitation to upper limb motoneurons in two primate species. J Neurophysiol 84: 698-709.

180. Nambu A, Yoshida S, Jinnai K, 1988. Projection on the motor cortex of thalamic neurons with pallidal input in the monkey. Exp Brain Res 71: 658-662.

181. Napier JR, 1956. The prehensile movements of the human hand. J Bone Joint Surg Br 38-B: 902-913.

182. Nelson DL, Cipriani DJ, Thomas JJ, 2002. Physical therapy and occupational therapy: Partners in rehabilition for persons with movement impairments. Occupational Therapy in Health Care 15: 35-57.

183. Niu X, Zatsiorsky VM, Latash ML, 2008. Stability of the multi-finger prehension synergy studied with transcranial magnetic stimulation. Exp Brain Res 190: 225-238.

184. Nowak DA, Hermsdorfer J, 2002. Coordination of grip and load forces during vertical point-to-point movements with a grasped object in Parkinson's disease. Behav Neurosci 116: 837-850.

185. Nudo RJ, Friel KM, 1999. Cortical plasticity after stroke: implications for rehabilitation. Rev Neurol (Paris) 155: 713-717.

186. Nudo RJ, Jenkins WM, Merzenich MM, Prejean T, Grenda R, 1992. Neurophysiological correlates of hand preference in primary motor cortex of adult squirrel monkeys. J Neurosci 12: 2918-2947.

187. Ochoa J, Dev Narasimhan YJ, Kamper DG, 2009. Development of a portable actuated orthotic glove to facilitate gross extension of the digits for therapeutic training after stroke. Conf Proc IEEE Eng Med Biol Soc 1: 6918-6921.

188. Okuno R, Yokoe M, Fukawa K, Sakoda S, Akazawa K, 2007. Measurement system of finger-tapping contact force for quantitative diagnosis of Parkinson's disease. Conf Proc IEEE Eng Med Biol Soc 2007: 1354-1357.

189. Pagowski S, Piekarski K, 1977. Biomechanics of metacarpophalangeal joint. J Biomech 10: 205-209.

190. Palmer E, Ashby P, 1992. Corticospinal projections to upper limb motoneurones in humans. J Physiol 448: 397-412.

191. Paninski L, Fellows MR, Hatsopoulos NG, Donoghue JP, 2004. Spatiotemporal tuning of motor cortical neurons for hand position and velocity. J Neurophysiol 91: 515-532.

192. Park MC, Belhaj-Saif A, Cheney PD, 2004. Properties of primary motor cortex output to forelimb muscles in rhesus macaques. J Neurophysiol 92: 2968-2984.

193. Paulignan Y, Jeannerod M, MacKenzie C, Marteniuk R, 1991a. Selective perturbation of visual input during prehension movements. 2. The effects of changing object size. Exp Brain Res 87: 407-420.

194. Paulignan Y, MacKenzie C, Marteniuk R, Jeannerod M, 1990. The coupling of arm and finger movements during prehension. Exp Brain Res 79: 431-435.

195. Paulignan Y, MacKenzie C, Marteniuk R, Jeannerod M, 1991b. Selective perturbation of visual input during prehension movements. 1. The effects of changing object position. Exp Brain Res 83: 502-512.

196. Penfield W, Rasmussen T, 1950. The Cerebral Cortex of Man: A Clinical Study of Localization and Function. New York: MacMillan.

197. Petit LS, Pegna AJ, Harris IM, Michel CM, 2006. Automatic motor cortex activation for natural as compared to awkward grips of a manipulable object. Exp Brain Res 168: 120-130.

198. Picard N, Smith AM, 1992a. Primary motor cortical activity related to the weight and texture of grasped objects in the monkey. J Neurophysiol 68: 1867-1881.

199. Picard N, Smith AM, 1992b. Primary motor cortical responses to perturbations of prehension in the monkey. J Neurophysiol 68: 1882-1894.

200. Poliakov AV, Schieber MH, 1999. Limited functional grouping of neurons in the motor cortex hand area during individuated finger movements: A cluster analysis. J Neurophysiol 82: 3488-3505.

201. Popovic M, Popovic D, 2001. Cloning biological synergies improves control of elbow neuroprosthesis. IEEE Eng Med Biol Mag 20: 74-81.

202. Popovic MB, 2003. Control of neural prostheses for grasping and reaching. Med Eng Phys 25: 41-50.

203. Prodoehl J, Corcos DM, Vaillancourt DE, 2009. Basal ganglia mechanisms underlying precision grip force control. Neurosci Biobehav Rev 33: 900-908.

204. Rand MK, Shimansky Y, Stelmach GE, Bracha V, Bloedel JR, 2000. Effects of accuracy constraints on reach-to-grasp movements in cerebellar patients. Exp Brain Res 135: 179-188.

205. Raos V, Umilta MA, Gallese V, Fogassi L, 2004. Functional properties of grasping-related neurons in the dorsal premotor area F2 of the macaque monkey. J Neurophysiol 92: 1990-2002.

206. Rathelot JA, Strick PL, 2006. Muscle representation in the macaque motor cortex: an anatomical perspective. Proc Natl Acad Sci U S A 103: 8257-8262.

207. Rathelot JA, Strick PL, 2009. Subdivisions of primary motor cortex based on cortico-motoneuronal cells. Proc Natl Acad Sci U S A 106: 918-923.

208. Rearick MP, Casares A, Santello M, 2003. Task-dependent modulation of multi-digit force coordination patterns. J Neurophysiol 89: 1317-1326.

209. Reilly KT, Nordstrom MA, Schieber MH, 2004. Short-term synchronization between motor units in different functional subdivisions of the human flexor digitorum profundus muscle. J Neurophysiol 92: 734-742.

210. Reina GA, Moran DW, Schwartz AB, 2001. On the relationship between joint angular velocity and motor cortical discharge during reaching. J Neurophysiol 85: 2576-2589.

211. Rizzolatti G, Camarda R, Fogassi L, Gentilucci M, Luppino G, Matelli M, 1988. Functional organization of inferior area 6 in the macaque monkey. II. Area F5 and the control of distal movements. Exp Brain Res 71: 491-507.

212. Rizzolatti G, Gentilucci M, Fogassi L, Luppino G, Matelli M, Ponzoni-Maggi S, 1987. Neurons related to goal-directed motor acts in inferior area 6 of the macaque monkey. Exp Brain Res 67: 220-224.

213. Roitman AV, Pasalar S, Ebner TJ, 2009. Single trial coupling of Purkinje cell activity to speed and error signals during circular manual tracking. Exp Brain Res 192: 241-251.

214. Roitman AV, Pasalar S, Johnson MT, Ebner TJ, 2005. Position, direction of movement, and speed tuning of cerebellar Purkinje cells during circular manual tracking in monkey. J Neurosci 25: 9244-9257.

215. Rosenbaum DA, Vaughan J, Barnes HJ, Jorgensen MJ, 1992. Time course of movement planning: selection of handgrips for object manipulation. J Exp Psychol Learn Mem Cogn 18: 1058-1073.

216. Rouiller EM, Yu XH, Moret V, Tempini A, Wiesendanger M, Liang F, 1998. Dexterity in adult monkeys following early lesion of the motor cortical hand area: the role of cortex adjacent to the lesion. Eur J Neurosci 10: 729-740.

217. Roy AC, Paulignan Y, Farne A, Jouffrais C, Boussaoud D, 2000. Hand kinematics during reaching and grasping in the macaque monkey. Behav Brain Res 117: 75-82.

218. Roy AC, Paulignan Y, Meunier M, Boussaoud D, 2002. Prehension movements in the macaque monkey: effects of object size and location. J Neurophysiol 88: 1491-1499.

219. Sakata H, Taira M, Murata A, Mine S, 1995. Neural mechanisms of visual guidance of hand action in the parietal cortex of the monkey. Cereb Cortex 5: 429-438.

220. Salenius S, Portin K, Kajola M, Salmelin R, Hari R, 1997. Cortical control of human motoneuron firing during isometric contraction. J Neurophysiol 77: 3401-3405.

221. Saltzman E, 1979. Levels of sensorimotor representation. Journal of Mathematical Psychology 91-163.

222. Sanes JN, Donoghue JP, Thangaraj V, Edelman RR, Warach S, 1995. Shared neural substrates controlling hand movements in human motor cortex. Science 268: 1775-1777.

223. Santello M, Flanders M, Soechting JF, 1998. Postural hand synergies for tool use. J Neurosci 18: 10105-10115.

224. Santello M, Flanders M, Soechting JF, 2002. Patterns of hand motion during grasping and the influence of sensory guidance. J Neurosci 22: 1426-1435.

225. Santello M, Soechting JF, 1998. Gradual molding of the hand to object contours. J Neurophysiol 79: 1307-1320.

226. Savelsbergh GJP, Steenbergen B, van der Kamp J, 1996. The role of fragility information in the guidance of the precision grip. Human Movement Science 15: 115-127.

227. Scarpa M, Castiello U, 1994. Perturbation of a prehension movement in Parkinson's disease. Mov Disord 9: 415-425.

228. Schabrun SM, Ridding MC, Miles TS, 2008. Role of the primary motor and sensory cortex in precision grasping: a transcranial magnetic stimulation study. Eur J Neurosci 27: 750-756.

229. Schieber MH, 1991. Individuated finger movements of rhesus monkeys: a means of quantifying the independence of the digits. J Neurophysiol 65: 1381-1391.

230. Schieber MH, Hibbard LS, 1993. How somatotopic is the motor cortex hand area? Science 261: 489-492.

231. Schieber MH, Poliakov AV, 1998. Partial inactivation of the primary motor cortex hand area: effects on individuated finger movements. J Neurosci 18: 9038-9054.

232. Schieber MH, 2001. Constraints on Somatotopic Organization in the Primary Motor Cortex. J Neurophysiol 86: 2125-2143.

233. Schwartz AB, 2004. Cortical neural prosthetics. Annu Rev Neurosci 27: 487-507.

234. Schwartz AB, 2007. Useful signals from motor cortex. J Physiol 579: 581-601.

235. Schwartz AB, Cui XT, Weber DJ, Moran DW, 2006. Brain-controlled interfaces: movement restoration with neural prosthetics. Neuron 52: 205-220.

236. Schweitzer TP, Rayan GM, 2004. The terminal tendon of the digital extensor mechanism: Part I, anatomic study. J Hand Surg [Am] 29: 898-902.

237. Scott SH, 2008. Inconvenient truths about neural processing in primary motor cortex. J Physiol 586: 1217-1224.

238. Scott SH, Kalaska JF, 1997. Reaching movements with similar hand paths but different arm orientations. I. Activity of individual cells in motor cortex. J Neurophysiol 77: 826-852.

239. Sears TA, Stagg D, 1976. Short-term synchronization of intercostal motoneurone activity. J Physiol 263: 357-381.

240. Sergio LE, Kalaska JF, 1997. Systematic changes in directional tuning of motor cortex cell activity with hand location in the workspace during generation of static isometric forces in constant spatial directions. J Neurophysiol 78: 1170-1174.

241. Serrien DJ, Wiesendanger M, 1999. Grip-load force coordination in cerebellar patients. Exp Brain Res 128: 76-80.

242. Serrien DJ, Wiesendanger M, 2000. Temporal control of a bimanual task in patients with cerebellar dysfunction. Neuropsychologia 38: 558-565.

243. Shim JK, Latash ML, Zatsiorsky VM, 2004. Finger coordination during moment production on a mechanically fixed object. Exp Brain Res 157: 457-467.

244. Shim JK, Latash ML, Zatsiorsky VM, 2005. Prehension synergies: trial-to-trial variability and principle of superposition during static prehension in three dimensions. J Neurophysiol 93: 3649-3658.

245. Shinoda Y, Yokota J, Futami T, 1981. Divergent projection of individual corticospinal axons to motoneurons of multiple muscles in the monkey. Neurosci Lett 23: 7-12.

246. Shinoda Y, Zarzecki P, Asanuma H, 1979. Spinal branching of pyramidal tract neurons in the monkey. Exp Brain Res 34: 59-72.

247. Sims CA, 1980. Macroeconomics and Reality. Econometrica 48: 1-48.

248. Slocum DB, Pratt DR, 1946. Disability evaluation for the hand. J Bone Joint Surgery 28: 491-501.

249. Smith AM, Bourbonnais D, 1981. Neuronal activity in cerebellar cortex related to control of prehensile force. J Neurophysiol 45: 286-303.

250. Soechting JF, Flanders M, 1997. Flexibility and repeatability of finger movements during typing: analysis of multiple degrees of freedom. J Comput Neurosci 4: 29-46.

251. Spinks RL, Kraskov A, Brochier T, Umilta MA, Lemon RN, 2008. Selectivity for grasp in local field potential and single neuron activity recorded simultaneously from M1 and F5 in the awake macaque monkey. J Neurosci 28: 10961-10971.

252. Spraker MB, Yu H, Corcos DM, Vaillancourt DE, 2007. Role of individual basal ganglia nuclei in force amplitude generation. J Neurophysiol 98: 821-834.

253. Stark E, Asher I, Abeles M, 2007a. Encoding of reach and grasp by single neurons in premotor cortex is independent of recording site. J Neurophysiol 97: 3351-3364.

254. Stark E, Drori R, Asher I, Ben-Shaul Y, Abeles M, 2007b. Distinct movement parameters are represented by different neurons in the motor cortex. Eur J Neurosci 26: 1055-1066.

255. Strick PL, Kim CC, 1978. Input to primate motor cortex from posterior parietal cortex (area 5). I. Demonstration by retrograde transport. Brain Res 157: 325-330.

256. Strick PL, Preston JB, 1978. Multiple representation in the primate motor cortex. Brain Res 154: 366-370.

257. Tabachnick BG, Fidell LS, 1996. Using Multivariate Statistics. New York: HarperCollins College Publishers.

258. Taira M, Boline J, Smyrnis N, Georgopoulos AP, Ashe J, 1996. On the relations between single cell activity in the motor cortex and the direction and magnitude of three-dimensional static isometric force. Exp Brain Res 109: 367-376.

259. Taira M, Mine S, Georgopoulos AP, Murata A, Sakata H, 1990. Parietal cortex neurons of the monkey related to the visual guidance of hand movement. Exp Brain Res 83: 29-36.

260. Takasawa M, Oku N, Osaki Y, Kinoshita H, Imaizumi M, Yoshikawa T, Kimura Y, Kajimoto K, Sasagaki M, Kitagawa K, Hori M, Hatazawa J, 2003. Cerebral and cerebellar activation in power and precision grip movements: an H2 15O positron emission tomography study. J Cereb Blood Flow Metab 23: 1378-1382.

261. Tanne-Gariepy J, Rouiller EM, Boussaoud D, 2002. Parietal inputs to dorsal versus ventral premotor areas in the macaque monkey: evidence for largely segregated visuomotor pathways. Exp Brain Res 145: 91-103.

262. Taylor DM, Tillery SI, Schwartz AB, 2002. Direct cortical control of 3D neuroprosthetic devices. Science 296: 1829-1832.

263. Thach WT, 1978. Correlation of neural discharge with pattern and force of muscular activity, joint position, and direction of intended next movement in motor cortex and cerebellum. J Neurophysiol 41: 654-676.

264. Thakur PH, Bastian AJ, Hsiao SS, 2008. Multidigit movement synergies of the human hand in an unconstrained haptic exploration task. J Neurosci 28: 1271-1281.

265. Theverapperuma LS, Hendrix CM, Mason CR, Ebner TJ, 2005. Finger movements during reach-to-grasp in the monkey: amplitude scaling of a temporal synergy. Exp Brain Res 169: 433-448.

266. Timmann D, Richter S, Bestmann S, Kalveram KT, Konczak J, 2000. Predictive control of muscle responses to arm perturbations in cerebellar patients. J Neurol Neurosurg Psychiatry 69: 345-352.

267. Timmann D, Watts S, Hore J, 1999. Failure of cerebellar patients to time finger opening precisely causes ball high-low inaccuracy in overarm throws. J Neurophysiol 82: 103-114.

268. Tokuno H, Tanji J, 1993. Input organization of distal and proximal forelimb areas in the monkey primary motor cortex: a retrograde double labeling study. J Comp Neurol 333: 199-209.

269. Truccolo W, Friehs GM, Donoghue JP, Hochberg LR, 2008. Primary motor cortex tuning to intended movement kinematics in humans with tetraplegia. J Neurosci 28: 1163-1178.

270. Turner RS, Anderson ME, 1997. Pallidal discharge related to the kinematics of reaching movements in two dimensions. J Neurophysiol 77: 1051-1074.

271. Umilta MA, Brochier T, Spinks RL, Lemon RN, 2007. Simultaneous recording of macaque premotor and primary motor cortex neuronal populations reveals different functional contributions to visuomotor grasp. J Neurophysiol 98: 488-501.

272. Vaillancourt DE, Yu H, Mayka MA, Corcos DM, 2007. Role of the basal ganglia and frontal cortex in selecting and producing internally guided force pulses. Neuroimage 36: 793-803.

273. Valero-Cuevas FJ, 2000. Predictive modulation of muscle coordination pattern magnitude scales fingertip force magnitude over the voluntary range. J Neurophysiol 83: 1469-1479.

274. van Kan PLE, Horn KM, Gibson AR, 1994. The importance of hand use to discharge of interpositus neurones of the monkey. J Physiol 480 (Pt 1): 171-190.

275. Velliste M, Perel S, Spalding MC, Whitford AS, Schwartz AB, 2008. Cortical control of a prosthetic arm for self-feeding. Nature 453: 1098-1101.

276. Vinjamuri R, Mao ZH, Sclabassi R, Sun M, 2007. Time-varying synergies in velocity profiles of finger joints of the hand during reach and grasp. Conf Proc IEEE Eng Med Biol Soc 2007: 4846-4849.

277. Vinjamuri R, Sun M, Chang CC, Lee H, Sclabassi R, Mao Z, 2009. Dimensionality Reduction in Control and Coordination of the Human Hand. IEEE Trans Biomed Eng.

278. Vittinghoff E, Glidden DV, Shiboski SC, McCulloch CE, 2005. Regression Methods in Biostatistics: Linear, Logistic, Survival, and Repeated Measures Models. New York, NY: Springer.

279. Vogels R, 1990. Population coding of stimulus orientation by striate cortical cells. Biol Cybern 64: 25-31.

280. Wang W, Chan SS, Heldman DA, Moran DW, 2007. Motor cortical representation of position and velocity during reaching. J Neurophysiol 97: 4258-4270.

281. Wannier TM, Maier MA, Hepp-Reymond MC, 1991. Contrasting properties of monkey somatosensory and motor cortex neurons activated during the control of force in precision grip. J Neurophysiol 65: 572-589.

282. Weinrich M, Wise SP, 1982. The premotor cortex of the monkey. J Neurosci 2: 1329-1345.

283. Weir PL, MacKenzie CL, Marteniuk RG, Cargoe SL, Frazer MB, 1991. The effects of object weight on the kinematics of prehension. J Mot Behav 23: 192-204.

284. Weiss EJ, Flanders M, 2004. Muscular and postural synergies of the human hand. J Neurophysiol 92: 523-535.

285. Wenzelburger R, Zhang BR, Poepping M, Schrader B, Muller D, Kopper F, Fietzek U, Mehdorn HM, Deuschl G, Krack P, 2002. Dyskinesias and grip control

in Parkinson's disease are normalized by chronic stimulation of the subthalamic nucleus. Ann Neurol 52: 240-243.

286. Wing AM, Turton A, Fraser C, 1986. Grasp size and accuracy of approach in reaching. J Mot Behav 18: 245-260.

287. Winges SA, Weber DJ, Santello M, 2003. The role of vision on hand preshaping during reach to grasp. Exp Brain Res 152: 489-498.

288. Wise SP, Boussaoud D, Johnson PB, Caminiti R, 1997. Premotor and parietal cortex: corticocortical connectivity and combinatorial computations. Annu Rev Neurosci 20: 25-42.

289. Woolsey CN, 1958. Organization of somatic sensory and motor areas of the cerebral cortex. In: Biological and Biochemical Bases of Behavior (Harlow HF, Woolsey CN, eds), pp 63-81. Madison: University of Wisconsin Press.

290. Wuolle KS, Van Doren CL, Thrope GB, Keith MW, Peckham PH, 1994. Development of a quantitative hand grasp and release test for patients with tetraplegia using a hand neuroprosthesis. J Hand Surg Am 19: 209-218.

291. Zackowski KM, Thach WT, Jr., Bastian AJ, 2002. Cerebellar subjects show impaired coupling of reach and grasp movements. Exp Brain Res 146: 511-522.

292. Zhang X, Kuo AD, Chaffin DB, 1998. Optimization-based differential kinematic modeling exhibits a velocity-control strategy for dynamic posture determination in seated reaching movements. J Biomech 31: 1035-1042.

293. Zohary E, 1992. Population coding of visual stimuli by cortical neurons tuned to more than one dimension. Biol Cybern 66: 265-272.